
Radionuclide Interaction and Transport in Representative Geologic Media

Fuel Cycle Research & Development

*Prepared for
U.S. Department of Energy
Used Fuel Disposition Program*

*Annie Kersting, Mavrik Zavarin, Pihong Zhao,
Zurong Dai, and Susan Carroll (LLNL)*

Yifeng Wang, Andrew Miller, Scott James, (SNL)

Paul Reimus (LANL)

*Liange Zheng, Lianchong Li, Jonny Rutqvist,
Huihai Liu and Jens Birkholzer (LBNL)*

*June 20, 2012
FCRD-UFD-2012-000154*



DISCLAIMER

This information was prepared as an account of work sponsored by an agency of the U.S. Government. Neither the U.S. Government nor any agency thereof, nor any of their employees, makes any warranty, expressed or implied, or assumes any legal liability or responsibility for the accuracy, completeness, or usefulness, of any information, apparatus, product, or process disclosed, or represents that its use would not infringe privately owned rights. References herein to any specific commercial product, process, or service by trade name, trade mark, manufacturer, or otherwise, does not necessarily constitute or imply its endorsement, recommendation, or favoring by the U.S. Government or any agency thereof. The views and opinions of authors expressed herein do not necessarily state or reflect those of the U.S. Government or any agency thereof.

FCT Quality Assurance Program Document

FCT Document Cover Sheet

Name/Title of Deliverable/Milestone Radionuclide Interaction and Transport in Representative Geologic Media
 Work Package Title and Number FT-12LL080707- Generic Natural Systems Evaluations
 Work Package WBS Number 1.02.08.07 Milestone Number M2FT-12LL0807071
 Responsible Work Package Manager Yifeng Wang 6-20-12
 (Name/Signature) (Date Submitted)

Quality Rigor Level for Deliverable/Milestone	<input type="checkbox"/> QRL-3	<input type="checkbox"/> QRL-2	<input type="checkbox"/> QRL-1 <input type="checkbox"/> Nuclear Data	<input checked="" type="checkbox"/> N/A*
---	--------------------------------	--------------------------------	---	--

This deliverable was prepared in accordance with Lawrence Livermore/Sandia National Laboratories
 (Participant/National Laboratory Name)

QA program which meets the requirements of
 DOE Order 414.1 NQA-1-2000 Other: _____

This Deliverable was subjected to:

<input checked="" type="checkbox"/> Technical Review	<input type="checkbox"/> Peer Review
Technical Review (TR)	Peer Review (PR)
Review Documentation Provided	Review Documentation Provided
<input type="checkbox"/> Signed TR Report, or TR Report No.: _____	<input type="checkbox"/> Signed PR Report, or PR Report No.: _____
<input type="checkbox"/> Signed TR Concurrence Sheet (attached), or	<input checked="" type="checkbox"/> Signed PR Concurrence Sheet (attached), or
<input checked="" type="checkbox"/> Signature of TR Reviewer(s) below	<input type="checkbox"/> Signature of PR Reviewers below

Name and Signature of Reviewers

Carlos Jove-Colon/

6/19/2012

(Name/Signature)

(Date)

*Note: In some cases there may be a milestone where an item is being fabricated, maintenance is being performed on a facility, or a document is being issued through a formal document control process where it specifically calls out a formal review of the document. In these cases, documentation (e.g., inspection report, maintenance request, work planning package documentation, or the documented review of the issued document through the document control process) of the completion of the activity along with the Document Cover Sheet is sufficient to demonstrate achieving the milestone. QRL for such milestones may also be marked N/A in the work package provided the work package clearly specifies the requirement to use the Document Cover Sheet and provide supporting documentation.

Contents

Executive Summary	vi
Chapter 1. Introduction	1
1.1 References	2
Chapter 2. Sorption Behavior and Morphology of Plutonium in the Presence of Goethite at 25 and 80°C	3
2.1 Introduction	3
2.2 Materials and Methods	5
2.2.1 Pu stock solution	6
2.2.2 Goethite	6
2.2.3 Batch Experiments	6
2.2.4 Pu analysis	7
2.2.5 TEM sample preparation and analysis	8
2.3 Results and Discussion	8
2.3.1 Pu behavior in the absence of goethite	8
2.3.2 Pu behavior in the presence of goethite	9
2.3.3 TEM observation of Pu morphology	10
2.4 Conclusions.....	15
2.5 References	15
Chapter 3. Stability of Plutonium(IV) Intrinsic Colloids in the Presence of Montmorillonite at 25 and 80°C .	19
3.1 Introduction	19
3.2 Experimental Approach	20
3.3 Materials and Methods	21
3.3.1 Pu stock solution.....	21
3.3.2 Montmorillonite	22
3.3.3 Batch dialysis experiments	22
3.4 Results and Discussion	23
3.4.1 Stability of Pu intrinsic colloids in the absence of clay at 25 and 80°C	23
3.4.2 Dissolution of Pu intrinsic colloids in the presence of clay at 25°C and 80 °C.	24
3.4.3 Aqueous Pu(IV) sorption onto montmorillonite at 25 °C and 80 °C	25
3.4.4 Temperature effects on the sorption K_d	27
3.5 Conclusions	27
3.6 References	28
Chapter 4. Quantifying Weak Interactions between Iodide and Clay Minerals	31
4.1 Introduction	31
4.2 Experimental Methods	32
4.2.1 Clay minerals and purification	32
4.2.2 Titration experiments	32
4.2.3 CEC determination	33
4.2.4 Iodide sorption experiments	33
4.3 Results	34
4.3.1 pKa distributions	34
4.3.2 CEC and surface area	35
4.3.3 Iodide batch uptake experiments	36
4.4 Discussion	37
4.4.1 Titrations	37
4.4.2 CEC and iodide uptake	41
4.5 Conclusions and Future Work	43
4.6 References	43
Chapter 5. Laboratory Testing Complementing Grimsel Field Work: Conservative Tracer Screening and Preliminary Radionuclide Transport Experiments	45

5.1	Introduction	45
5.2	Field Tracer Screening Experiments	45
5.2.1	Materials and methods	45
5.2.2	Results of field tracer screening experiments	48
5.2.3	Conclusions from field tracer screening studies	51
5.3	Preliminary Results from Uranium and Neptunium Transport Experiments in Grimsel Granite	52
5.3.1	Experimental plans for interrogating radionuclide adsorption and desorption rate distributions	52
5.3.2	Preliminary experiments and experimental results	55
5.4	Conclusions	58
5.5	References	58
Chapter 6. Summary of Fieldwork at the Grimsel Field Site: Interpretations and Inferences from CFM Tracer Tests 10-01 through 12-02		59
6.1	Introduction	59
6.2	Colloid-Homologue Tracer Test 10-03, and Comparison to Tracer Test 10-01	60
6.3	Inferences about Shear Zone Flow Pathways from Conservative Tracer Responses in Tracer Tests 10-01 through 12-02	66
6.4	Conclusions	71
6.5	References	72
Chapter 7. Modeling Radionuclide Transport in Clays		73
7.1	Introduction	73
7.2	Technical Approaches	73
7.2.1	Simulator	73
7.2.2	An elastic model for chemical-mechanical coupling	74
7.2.3	Chemical model	75
7.3	Model Setup	81
7.3.1	Model domain	81
7.3.2	Initial and boundary conditions	81
7.4	Modeling Results	85
7.4.1	THM Evolutions	85
7.4.2	Reactive transport simulation results	90
7.5	Conclusions and Future Work	99
7.6	References	101
Chapter 8. Advanced Parameter Uncertainty Quantification Using Null Space Latin Hypercube Sampling: Application to Uranium and Neptunium Transport Experiments		105
8.1	Introduction	105
8.2	Experimental Background	106
8.3	Numerical Modeling	106
8.4	Model Calibration	108
8.5	Linear Uncertainty Analysis	111
8.6	Nonlinear Uncertainty Analyses	115
8.7	References	117
Chapter 8 Appendix: PEST NSLHS Utility Codes		119
General	119
LHS2PEST – Level 1	120
LHS2PEST – Level 2	121
LHS2PEST – Level 3	121
General	123
Parameter Probability Distributions	123
PEST2LHS Usage Details	124
Chapter 9: Summary and Conclusions		129

Executive Summary

The work package of natural system evaluation and tool development directly supports the following Used Fuel Disposition Campaign (UFDC) objectives:

- Develop a fundamental understanding of disposal-system performance in a range of environments for potential wastes that could arise from future nuclear-fuel-cycle alternatives through theory, simulation, testing, and experimentation.
- Develop a computational modeling capability for the performance of storage and disposal options for a range of fuel-cycle alternatives, evolving from generic models to more robust models of performance assessment.

In the Research and Development (R&D) plan for this work package (Wang, 2011), a total of 27 research topics have been identified, based on the UFDC R&D roadmap (DOE, 2011). This report documents the work that has been conducted in fiscal year 2012 on:

- Topic #P10: Better understanding of radionuclide interaction with geomeedia.
- Topic #P11: New perspectives on colloid-facilitated radionuclide transport.

The work scope for FY12 includes five major tasks: (1) The stability and sorption behavior of plutonium to common colloid minerals at ambient and elevated temperatures, (2) evaluation of iodide sorption to environmentally relevant clay minerals, (3) development and design of conservative tracer tests for radionuclide transport experiments for the Grimsel Test Site, Colloid Formation and Migration Program, (4) modeling radionuclide transport in clays, and (5) developing methods for parameter uncertainty analysis. The work supporting the five major tasks was performed in collaboration among four national laboratories and presented as separate chapters below.

The major accomplishments for FY12 are summarized as follows:

- Plutonium sorption experiments have demonstrated that monomeric Pu and intrinsic Pu colloids have a strong affinity to goethite (FeOOH). Intrinsic Pu colloids attached to goethite by epitaxial growth distorts the intrinsic Pu structure causing a stronger attachment than to other minerals. This behavior is observed at both 25 and 80°C, and is stable on the time scale of 3 months.
- The weak stability of intrinsic Pu colloids coupled with the strong sorption of Pu to both montmorillonite and goethite colloids at concentrations below Pu solubility suggests that monomeric sorption may be the dominant process controlling migration in the far-field.
- Experimental interaction between iodide and a suite of clay minerals has shown that iodide appears to accumulate in the interlayer regions of clay minerals. This counter intuitive result can be explained through ion-pair formation. Ion-pair formation is not currently considered in geochemical simulations of nuclear waste disposal.
- Mini-column test results have indicated that there was no measurable adsorption of uranium onto Grimsel granite in synthetic Grimsel groundwater. These results are consistent with the formation of neutral and negatively charged uranyl-carbonate complexes in solution. Similarly, several fluorescent tracers showed no measurable adsorption to Grimsel granite or FEBEX bentonite, indicating positive attributes as conservative tracers for field characterization. The lack of sorption does not explain the apparent tracer loss in field scale tests at Grimsel.
- The combined analysis of shear-zone residence times as a function of injection and extraction flow rates in colloid migration tracer tests suggests a two-pathway conceptual model for flow in the shear zone between the injection borehole and the Pinkel surface packer.

- The TOUGHREACT-FLAC3D simulator developed in Zheng et al. (2011) was further enhanced by incorporation of the two-site protolysis non-electrostatic surface complexation and cation exchange model. The enhanced model was used to evaluate the THMC impacts on U(VI) transport. It is shown that chemical-mechanical coupling based on linear elastic swelling model leads to a 5% difference in effective stress compared with the model that ignores such coupled effects. Ca and bicarbonate concentrations have a significant effect on U(VI) transport by aqueous complexation. Surface complexation dominates sorption processes, while cation exchange plays a diminished role. For the modeled system, the effect of mechanical processes on the migration of U(VI) seems to be insignificant at distances >10m from the emplaced waste.
- Linear and nonlinear parameter uncertainty quantification using PEST provided robust estimates of parameter identifiability and uncertainty distributions, as well as information on how each data set contributes to uncertainty reduction in each model parameter. The parameter estimation method was applied to uranium and neptunium column-scale transport data. This method can inform the design of future experiments to minimize parameter uncertainty.

In FY13, we will continue the current work on radionuclide interactions with clay and granite materials and start experimental data synthesis and interpretation to support total system and subsystem performance assessment calculations. The existing iodine sorption experiment will expand to include compacted clay samples. More uranium and neptunium sorption on granite materials will be performed. Models that couple thermo-hydrologic-mechanical-chemical processes in the near field of a clay repository will be further improved and tested against experimental data. The advanced parameter estimation and uncertainty quantification developed in FY12 will be extended to other systems and applications.

DOE, 2011. *Used Fuel Disposition Campaign Disposal Research and Development Roadmap*, FCR&D-USED-2011-000065, Rev. 0.

Wang, Y., 2011. *Research & Development (R&D) Plan for Used Fuel Disposition Campaign (UFDC) Natural System Evaluation and Tool Development*.

Chapter 1. Introduction

This report summarizes work accomplished in FY12 to support the natural system evaluation and tool development within the Used Fuel Disposition Campaign (UFDC). The work directly supports the following objectives:

- Develop a fundamental understanding of disposal system performance in a range of environments for potential wastes that could arise from future nuclear fuel cycle alternatives through theory, simulation, testing, and experimentation.
- Develop a computational modeling capability for the performance of storage and disposal options for a range of fuel cycle alternatives, evolving from generic models to more robust models of performance assessment.

This reports documents the work that has been conducted in fiscal year 2012 on two topics that were identified based on the UFDC R&D roadmap (Wang, 2011).

- Topic #P10: Better understanding of radionuclide interaction with geomedial.
- Topic #P11: New perspective of colloid-facilitated radionuclide transport.

As radionuclides are released from the engineered barrier they will move through and interact with the natural system. The transport behavior of the radionuclides can and will change due to complex physical and chemical interactions with the surrounding geologic media. Existing models generally assume that radionuclide retention in the natural system can be described with a linear, equilibrium K_d approach. The reality is much more complex. Tasks under topic P10 are designed to carry out experiments to help support model development to improve our ability to predict how radionuclides migrate in the subsurface. Tasks under topic P11 support experiments and model development in the following areas:

- Thermodynamics and kinetics of radionuclide sorption/desorption from representative mineral (e.g., different clay minerals).
- Radionuclide behaviors in high rock/water ratio environments, especially in nanopores and interlayers.
- Coupling of redox reactions with radionuclide sorption.
- Complexation of radionuclides with natural organic matter.
- Radionuclide sorption in the presence of competing species, high ionic strength media, or at elevated temperatures.
- Extrapolation from simple system measurements to complex systems.
- Radionuclide transport in low permeability media (e.g., membrane effect of clay formation).

The second topic (P11) identified based on the UFDC Natural System R&D Plan is designed to determine when colloid-facilitated transport is important under given repository conditions. Colloid facilitated transport (CFT) may have been overestimated in previous performance assessments because many aspects of CFT are not well constrained, thus making pessimistic bounding assumptions necessary. CFT is also an important issue for confidence building of a performance assessment model. Important uncertain processes and parameters associated with CFT include: desorption processes and rates, colloid immobilization processes and associated parameters, the degree to which colloids behave as heterogeneous populations in the subsurface, the role of chemical and flow transients in mobilizing and

immobilizing colloids, and colloid generation processes. This task focuses on two key aspects of the CFT: (1) colloid particle formation and transport in porous geologic media and (2) radionuclide partitioning among pore water, colloid particles, and stationary substrates.

In recent years, much progress has been made in nanoscience and nanotechnology and as a result, it is important to re-examine CFT mechanisms taking into account new advances in nanoscience and nanotechnology. For example, we do not currently know if geochemical processes that are relevant at high concentrations in near-field environments are the same as at low concentrations expected in the far-field. In addition, new technology allows us to investigate colloid processes occurring at low, environmentally relevant concentrations. The work under task P11 will involve laboratory measurements, model development, and field testing. Novel in-situ colloid characterization techniques will be explored. Specific activities include the following:

- Better understanding of colloid-radionuclide-stationary mineral phase interactions.
- Development of novel in-situ techniques for characterizing CFT.
- Development of modeling capabilities for simulating CFT.

The work supporting topics P10 and P11 was performed in the collaboration among four national laboratories (SNL, LLNL, LBNL, LANL) and is presented as seven self-contained but interrelated chapters:

- Chapter 2 evaluates of the sorption behavior of plutonium with goethite colloids at 25 and 80°C at both high and low plutonium concentrations. (LLNL)
- Chapter 3 evaluates of the stability of intrinsic plutonium colloids at 25 and 80°C in the presence of clay minerals. (LLNL)
- Chapter 4 determines iodide uptake to seven environmentally relevant clay minerals. (SNL)
- Chapter 5 presents the development and design of conservative tracer tests with radionuclide transport experiments for the Grimsel Test Site, Colloid Formation and Migration Program. (LANL)
- Chapter 6 synthesizes the fieldwork at the Grimsel Test Site, Colloid Formation and Migration Program. (LANL)
- Chapter 7 demonstrates a coupled THMC model of U(VI) transport in clays. (LBNL)
- Chapter 8 presents a method for uncertainty quantification modeling applied to U and Np transport experiments. (SNL/LANL)

1.1 References

Wang, Y., 2011. *Research & Development (R&D) Plan for Used Fuel Disposition Campaign (UFDC) Natural System Evaluation and Tool Development.*

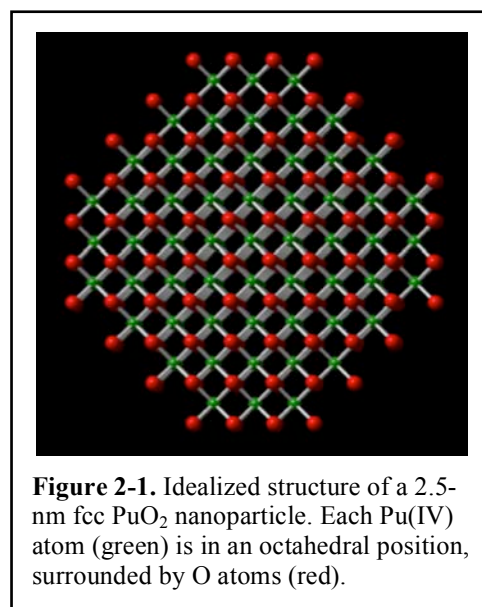
Chapter 2. Sorption Behavior and Morphology of Plutonium in the Presence of Goethite at 25 and 80°C

2.1 Introduction

Plutonium (Pu) has been identified as a dominant long-term dose contributor under certain nuclear waste repository scenarios (Kaszuba and Runde, 1999; Office of Civilian Radioactive Waste Office of Civilian Radioactive Waste Management, 2002). The transport of Pu will likely occur by association with natural or anthropogenic colloids or as intrinsic colloids that migrate through the engineered barrier system and host rock. The dominant anthropogenic colloids may be iron oxides produced as a result of steel corrosion (Office of Civilian Radioactive Waste Management, 2002) or intrinsic colloids formed at relatively high actinide concentrations. The mineralogy of natural colloids will be a function of the host rock mineralogy or backfill material. Host rock minerals such as smectite and iron oxide are known to sorb Pu (Bertetti et al., 1998; Keeney-Kennicutt and Morse, 1985; Kozai et al., 1996; Kozai et al., 1993; Lujaniene et al., 2007; Powell et al., 2004, 2005; Powell et al., 2008; Sabodina et al., 2006; Sanchez et al., 1985; Turner et al., 1998), which will result in actinide immobilization or retention. However, actinide sorption to these same minerals, as colloids, may also result in colloid-facilitated transport (e.g., Kersting et al., (1999).

A major challenge in predicting the mobility and transport of actinides in the natural environment is determining the dominant geochemical processes that control their transport behavior. The reaction chemistry of Pu (i.e., aqueous speciation, solubility, sorptivity, redox chemistry, and affinity for colloidal particles, both abiotic and microbially mediated) is particularly complicated. Its migration is known to be oxidation-state dependent and facilitated by transport on particulate matter (i.e., colloidal particles). Despite the recognized importance of colloid-facilitated transport, little is known about the geochemical and biochemical mechanisms controlling Pu-colloid (intrinsic or pseudo-colloid) formation and stability, particularly under relevant environmental conditions. At high concentrations ($>10^{-9}$ M), Pu tends to form intrinsic nano-colloids (Neck et al., 2007); it is not known whether these nano-colloids are produced or are stable at very low (e.g., $<10^{-9}$ M) concentrations. Future radioactive waste repositories will likely involve environments at elevated temperatures. Thus, the effect of elevated temperature on the stability and sorptivity of monomeric and colloidal Pu is relevant as well.

The structure of Pu precipitates and nano-colloids has been investigated for many years, particularly from the standpoint of sol-gel processes relevant to the production of dense forms of PuO_2 (Lloyd and Haire, 1968). Early electron microscopy studies by Haire et al. (1971) concluded that fresh Pu(IV) precipitates are composed of nanoparticles <2.5 nm in size (Figure 2-1). The degree of crystallinity could be increased (based on x-ray diffraction line broadening) by “aging” the precipitates for a few hours in $<100^\circ\text{C}$ water. However, the fundamental size of these nanoparticles is not affected. Importantly, these nanoparticles were found to aggregate and were not considered stable in solution. Peptization (formation of a stable dispersion of Pu colloids in water) occurred when these precipitates were heated and reacted with $\sim 0.2\text{M}$ HNO_3 . The colloidal products of this peptization have a Pu: NO_3 ratio of ~ 1 . Larger crystallites (4–10 nm) could be produced only upon heating (250°C or greater), which also reduced the NO_3^-

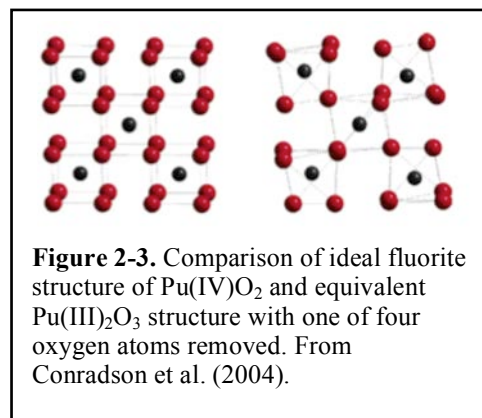
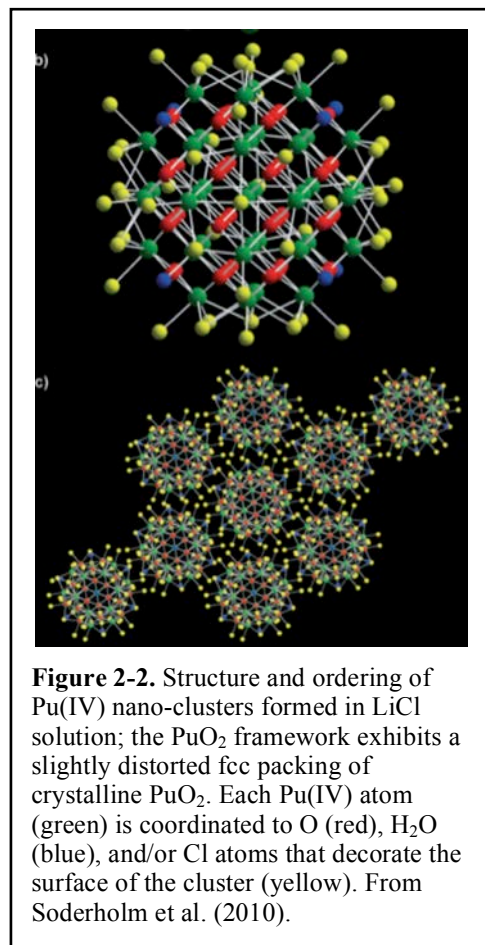


/Pu ratio of the colloids from ~1 to ~0.1 (Lloyd and Haire, 1968).

More recently, Soderholm et al. (2008) examined the structure and formation of stable colloidal suspensions of Pu precipitates in HCl/LiCl solutions. Upon evaporation from high-salt solutions (2 M LiCl), a novel precipitate was formed in which PuO₂-like nano-clusters, “decorated” by Cl⁻ anions, formed a crystalline superstructure (Figure 2-1). Unlike the earlier suggestions of Conradson et al. (2004), the presence of H₂O or OH⁻ or Pu(V)O₂⁺ in these nano-clusters was not identified. However, the stabilization of Pu sols in high ionic strength solutions is consistent with historical schemes developed as part of the sol-gel process. The unique scientific contribution of the Soderholm et al. (2008) work was the identification of well-ordered Pu nanoclusters that is in direct contrast to the traditional assumptions of poorly ordered polymeric or amorphous Pu(IV) precipitates. It also suggests that the <2.5-nm sols produced by Haire et al. (1971) in dilute HNO₃ with a Pu:NO₃ ratio of ~1 may be morphologically related to these nano-clusters (Pu:Cl ratio of 0.7). However, the stability relationship between these nano-clusters and larger nano-colloids produced upon aging and heating of Pu(IV) precipitates/sols has yet to be understood.

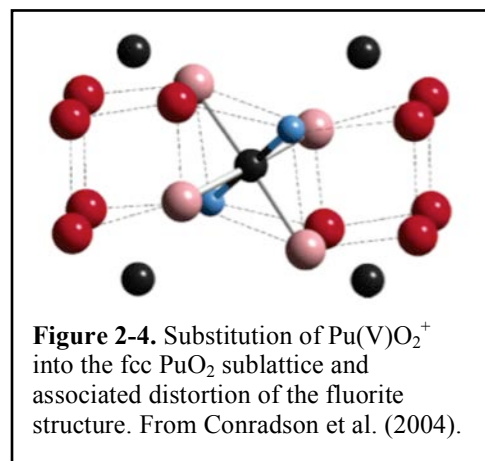
The structure of PuO₂ precipitates and colloids is complicated by the fact that Pu(IV) is susceptible to both reduction to Pu(III) and oxidation to Pu(V) and Pu(VI). Crystallographic studies of partially substituted Pu(IV)O₂ precipitates has been the subject of ongoing research. Conradson et al. (2004) described the structural difference between Pu(IV)O₂ and Pu(III)₂O₃ as an equivalent sublattice with Pu₂O₃ having one of four oxygen atoms removed from the basic PuO₂ fluorite structure (Figure 2-3). Partial removal of oxygen atoms from Pu(IV)O₂ can also produce an intermediate oxidation-state precipitate, Pu₄O₇ (Petit et al., 2003).

A more controversial topic of ongoing research has been the structure of the partially oxidized form of Pu(IV)O₂, namely PuO_{2+x} (Conradson et al., 2004; Haschke et al., 2000; Penneman and Paffett, 2005; Petit et al., 2003). The position of the additional oxygen atoms was initially proposed to be in the octahedral vacancies in the fluorite structure. However, Conradson et al. (2004) characterized multiple preparations of PuO_{2+x} and determined that a more formal description of this phase should be PuO_{2+x-y}(OH)_{2y}*zH₂O in which OH⁻ and H₂O are structurally incorporated into the PuO₂ sublattice and the oxidized Pu is most likely Pu(V) with two -yl oxygens (Figure 2-4). This formulation was not



observed in nano-clusters characterized by Soderholm et al. (2010).

In their recent work, Powell et al. (2011) examined the behavior of Pu(IV) surface precipitates and colloids in the presence of goethite and quartz. Transmission electron microscopy (TEM) was used to characterize the morphology of Pu associated with these mineral phases. Plutonium was added to goethite and quartz suspensions either as “fresh” (un-aged) Pu nano-colloids or as aqueous Pu(IV). Plutonium nano-colloids (2–5-nm) that formed on goethite from aqueous monomers underwent a lattice distortion relative to the ideal fluorite-type structure, fcc, PuO_2 , resulting in the formation of a bcc, Pu_4O_7 . This structural distortion resulted from an epitaxial growth of the plutonium colloid on goethite, leading to stronger binding of plutonium compared with other minerals such as quartz where the distortion was not observed. Importantly, intrinsic PuO_2 nano-colloids appeared to have a weak affinity for both goethite and quartz.



The results of Powell et al. (2011) and earlier studies suggest that the morphology, structure, and stability of Pu can vary dramatically and affect the sorptivity and mobility of Pu in the environment. An understanding of the stability of Pu nano-clusters and colloids and sorption/desorption kinetics of monomeric and colloidal Pu on common minerals is critical to predicting long-term colloid-facilitated transport behavior of Pu (Cvetkovic, 2000; Cvetkovic et al., 2004; Missana et al., 2004; Saiers and Hornberger, 1996; Steefel, 2008).

In this chapter, we examine the sorption behavior of Pu at elevated temperatures in the presence of one relevant mineral, goethite ($\alpha\text{-FeOOH}$), over a range of concentrations that span solubility-controlled to adsorption-controlled concentrations. We focus on the sorptive behavior of two common forms of Pu: aqueous Pu(IV) and intrinsic Pu(IV) nano-colloids at 25 and 80°C in a dilute pH 8 $\text{NaCl}/\text{NaHCO}_3$ solution. The morphology of Pu sorbed to goethite was characterized using TEM. We examined the relative stability of PuO_2 precipitates, PuO_2 nano-colloids, Pu_4O_7 surface precipitates, and monomeric sorbed Pu as a function of temperature and over a time scale of months.

2.2 Materials and Methods

Two series of batch sorption experiments were conducted. In the first series, aqueous Pu(IV) was reacted with goethite at 25 and 80°C. The experiment was intended to test whether the affinity or morphology of sorbed Pu was temperature-dependent. The experiment was performed under identical solution conditions used in an earlier 25°C sorption isotherm experiment (0.1g/L goethite, pH 8, 5 mM $\text{NaCl}/0.7$ mM NaHCO_3) (Zhao et al., 2010). However, in the present case, samples were equilibrated for three months rather than two weeks. Comparison of the present data to earlier isotherm data was used to evaluate the sorption kinetics and determine the stability of surface precipitates.

In the second set of experiments, intrinsic Pu(IV) nano-colloids were reacted with goethite at 25 and 80°C. The intrinsic Pu(IV) nano-colloid sorption experiments were intended to test whether the initial form of Pu affects its long-term sorption behavior and evaluate the stability of Pu(IV) nano-colloids as a function of temperature.

At the end of the three-month batch sorption experiments, Pu concentrations in the liquid phase were measured and compared to published “amorphous” PuO₂ (PuO₂(am, hyd)) solubility measurements (Neck et al., 2007) and sorption affinities (Zhao et al., 2010). In addition, a detailed characterization of the Pu associated with the goethite mineral surface was conducted using TEM. The combination of liquid phase and surface characterization was used to evaluate the effect of temperature and the comparative behavior of aqueous Pu(IV) versus intrinsic nanocolloid Pu(IV) on Pu sorption characteristics.

2.2.1 Pu stock solution

Alpha-emitting ²⁴²Pu (> 99.8% by mass) was used in the experiments. The major isotopes contributing to alpha activities are ²³⁸Pu, ^{239,240}Pu, and ²⁴²Pu with activity percentages of 15.9%, 5.2% and 78.9%, respectively. The Pu stock solution (7.6 × 10⁻⁴ M Pu(IV) in 2.06 M HCl) was purified using AG1x8 100–200 mesh anion exchange resin and filtered through a 3kD molecular weight cut-off (MWCO) filter. The oxidation state of Pu was confirmed using both UV/VIS and solvent extraction. The aqueous Pu(IV) working solution was prepared by diluting the stock solution to 1.9 × 10⁻⁴ M Pu(IV) in 1N HCl. The intrinsic Pu(IV) nano-colloid working solution was prepared by adding 1 mL 1N NaOH and 0.39 mL pH 8 buffer (5 mM NaCl/0.7 mM NaHCO₃) to 0.53 mL of the Pu(IV) stock. Another 0.06 mL of 1N NaOH was added gradually to adjust the pH to ~8.5. The intrinsic Pu colloids were washed 3 times and re-suspended in pH 8 buffer solution. The final Pu(IV) nano-colloid concentration was 1.5 × 10⁻⁴. We estimate that the intrinsic nano-colloid size was generally >1 nm. Based on TEM, the fundamental particle size of intrinsic Pu nano-colloids prepared in this manner is 2–5 nm (Figure 2-5), somewhat larger than precipitate preparations by Haire et al. (1971) and nano-clusters of Soderhom et al. (2008). Aggregation of these intrinsic nano-colloids is commonly observed such that the aggregate size is larger (Powell et al., 2011).

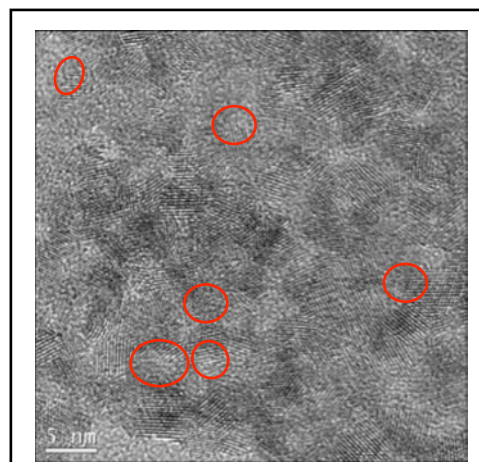


Figure 2-5. HRTEM of Pu(IV) nano-colloids produced upon precipitation of a Pu(IV) from solution at pH 8.5 and ~1N NaCl. Nano-colloids were washed in MQ water prior to deposition on TEM grid. Red outlines point to several colloids, for emphasis.

2.2.2 Goethite

Goethite was synthesized from Fe(NO₃)₃•9H₂O as described by Schwertmann and Cornell (1991). Goethite was washed with a 5 mM NaCl/0.7 mM NaHCO₃ buffer solution, sonicated for 5 minutes, and centrifuged for 60 minutes at 3500 rpm three times until constant pH was reached. Based on a spherical particle sedimentation estimate (Gee and Bauder, 1986), the goethite particle size retained was >100 nm. X-ray diffraction confirmed goethite as the major phase, the point of zero salt effect was 8.5 ± 0.1, and the BET surface area was 16 m²/g. The predominant morphology of the goethite particles was “star-shaped.” Additional characterization details can be found in Tinnacher et al. (2011).

2.2.3 Batch Experiments

All batch experiments were conducted in 10 mL Nalgene* Oak Ridge polycarbonate centrifuge tubes with sealing caps. Either aqueous Pu(IV) or intrinsic Pu(IV) nano-colloids were spiked into 9 mL of 5 mM NaCl/0.7 mM NaHCO₃ in which goethite (solid to liquid ratio of 0.1 g/L) had previously been added. Goethite-free Pu solutions were prepared in parallel. For the aqueous Pu(IV) experiments, an equivalent

amount of NaOH was added before adding the Pu spike to ensure a final solution pH of 8. The 10-mL tubes were submerged in 50-mL polypropylene conical centrifuge tubes filled with Milli-Q water to minimize evaporative losses and provide secondary containment to the radioactive samples. Over the course of the experiment, the 25°C sample tubes were stored vertically in a hood. The 80°C sample tubes were submerged in a heated water bath. Samples were periodically shaken and weighed to check for fluid evaporative losses; no significant loss of fluid was observed over the course of the experiment.

Three initial Pu concentrations were used (Table 2-1) such that the resulting equilibrium Pu concentration would be below, above, and near the PuO₂(am, hyd) solubility ($\sim 5 \times 10^{-9}$ M) (Neck et al., 2007). Two goethite-free solutions (spiked blanks) with initial Pu concentrations below and above PuO₂(am, hyd) solubility were used for comparison with sorption experiments. All solutions were allowed to react for 103 days.

At the conclusion of each experiment, two samples were taken from each tube. The first supernatant sample was taken after the goethite was allowed to settle out for 60 hrs. Based on sedimentation rates, we estimate that the supernatant included particles $< \sim 250$ nm on average (Table 2-2). The second supernatant sample was collected after centrifugation at 5000 rpm for 90 minutes *at room temperature*. In this case, the supernatant included particles $< \sim 25$ nm on average. Centrifugation was expected to effectively remove goethite particles. Sedimentation was also expected to remove the majority of goethite from solution. To test this, Fe in solution was monitored by ICP-MS. In all cases, Fe concentrations were low enough that the contribution of goethite to the measured Pu solution concentration was predicted to be negligible ($< 0.2\%$ of Pu in solution). Neither sedimentation nor centrifugation was expected to quantitatively remove dispersed Pu(IV) nano-colloids from solution. However, centrifugation would likely remove most aggregated nano-colloids. A comparison of the sedimentation and centrifugation supernatants provides information on the presence of intermediate-sized Pu colloid aggregates in solution (25–250 nm) (Table 2-2).

2.2.4 Pu analysis

Both liquid scintillation counting (LSC) and ICP-MS were used to determine Pu concentration. The LSC was used for

Table 2-1. Experimental conditions for Pu(IV) samples at 25 and 80°C.

Pu form	Initial Pu	Goethite conc.
	mol/L	g/L
Aqueous	7.3×10^{-11}	0
Aqueous	8.0×10^{-7}	0
Colloidal	9.6×10^{-11}	0
Colloidal	7.3×10^{-7}	0
Aqueous	3.8×10^{-9}	0.1
Aqueous	7.8×10^{-7}	0.1
Aqueous	3.8×10^{-6}	0.1
Colloidal	3.1×10^{-8}	0.1
Colloidal	7.3×10^{-7}	0.1
Colloidal	3.7×10^{-6}	0.1

Table 2-2. Particle segregation methods and associated particle size cut-offs.

Particle segregation method	Particle	Temp.	Particle size cut-off ¹
		°C	nm
Sedimentation	Goethite	25	375
Sedimentation	PuO ₂ (am, hyd)	25	225
Sedimentation	Goethite	80	250
Sedimentation	PuO ₂ (am, hyd)	80	125
Centrifugation	Goethite	25	35
Centrifugation	PuO ₂ (am, hyd)	25	19

¹ Sedimentation rates were calculated using goethite and PuO₂ densities of 4.27 and 11.5 g/cm³. Fluid viscosity used at 25 and 80°C were 8.90×10^{-4} and 3.55×10^{-4} , respectively. The fluid density used at 25 and 80°C was 0.997 and 0.972 g/cm³,

samples with high Pu and ICP-MS for samples in which Pu concentrations were below the LSC method's detection limit ($\sim 3 \times 10^{-10}$ M). It is important to consider the fact that sedimentation and centrifugation only segregate particles greater than the associated particle size cut off. Thus, the measured Pu concentration in solution represents both aqueous Pu and Pu nano-colloids (or aggregates) smaller than the cutoff size for sedimentation or centrifugation (i.e., Table 2-2).

2.2.5 TEM sample preparation and analysis

At the conclusion of each experiment, the solid phases were washed in MQ (>18 M Ω) water three times by sequentially centrifuging at 5000 rpm for 90 minutes, decanting the supernatant, and replacing it with fresh MQ water. The washing was performed to remove salts from solution. The solids were resuspended in MQ water by sonicating for 5 minutes and diluting $10\times$ to produce a 0.01g/L suspension. A volume of 2 to 5 μ L of each suspension was deposited on TEM carbon-coated copper grids and dried in a glass desiccator. All analyses were performed on a Philips CM 300 FEG TEM operating at 300kV and equipped with a Gatan Imaging Filter (GIF) with a $2k \times 2k$ CCD camera and an EDX detector.

2.3 Results and Discussion

2.3.1 Pu behavior in the absence of goethite

Spiked blanks (i.e., goethite-free solutions) were run to examine homogeneous precipitation of $\text{PuO}_2(\text{am, hyd})$ and potential loss of Pu to container walls. Both aqueous Pu(IV) and intrinsic Pu(IV) nano-colloid solutions were equilibrated for 103 days at 25 and 80°C; initial Pu concentrations were either oversaturated ($\sim 10^{-6}$ M) or undersaturated ($\sim 10^{-10}$ M) with respect to $\text{PuO}_2(\text{am, hyd})$. The solution concentration data, superimposed on the $\text{PuO}_2(\text{am, hyd})$ solubility data presented in Neck et al. (2007), are presented in Figure 2-6.

For all undersaturated samples, concentrations of Pu in solution were similar (sedimentation and centrifugation produced equivalent concentrations) after 103 days ($\sim 10^{-11}$ M). The initial form of Pu(IV) and temperature do not appear to have an appreciable effect on Pu concentrations in solution. However, whether Pu(IV) nano-colloids dissolved or remained dispersed in solution cannot be distinguished. Significant losses of Pu from solution did occur (70–90%). We attribute these losses to sorption to container walls, as is commonly observed. Loss of Pu as a result of precipitation and/or aggregation of Pu nano-colloids is not thermodynamically favored at these concentrations.

In all high-concentration ($\sim 10^{-6}$ M) samples, the Pu concentration remaining in solution is consistent with the range of $\text{PuO}_2(\text{am, hyd})$ solubility at 25°C as reported in Neck et al. (2007). Neck et al. (2007) found that a mixture of colloidal PuO_2 and aqueous Pu(V) are the predominant forms of Pu in solution under these conditions. However, the concentration of colloidal PuO_2 is conditional, depending on the choice of particle

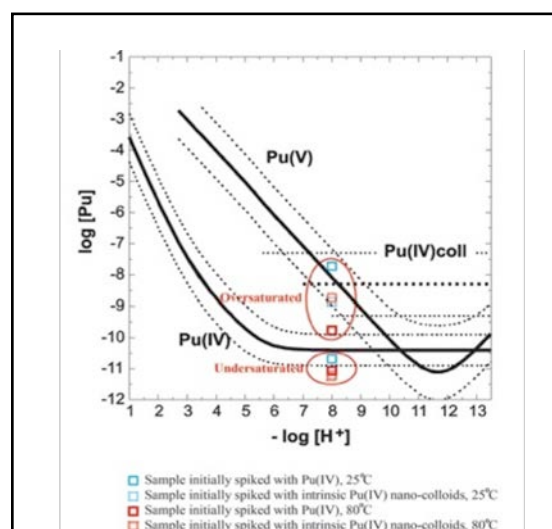


Figure 2-6. Pu concentrations in eight goethite-free spiked blanks oversaturated (initially $\sim 10^{-6}$ M) and undersaturated (initially 10^{-10} M) with respect to $\text{PuO}_2(\text{am, hyd})$. Data are superimposed over $\text{PuO}_2(\text{am, hyd})$ solubility data reported in Figure 2-5 from Neck et al. (2007). Pu concentrations in supernatants from sedimentation and centrifugation samples yielded similar results.

size range that is considered “colloidal.” In the case of Neck et al. (2007), the colloidal fraction was defined as the fraction collected by a 10 kD (~1.5-nm pore size) filter from a “clear supernatant.” Thus, the upper limit of the particle size considered “colloidal” is not strictly defined. In our case, the sedimentation results in a particle size upper limit estimate of ~250 nm for the solution phase. A higher upper limit would tend to increase the apparent Pu concentration in solution.

Intrinsic Pu(IV) nano-colloids “precipitated” from solution (~99.7%) in equal amounts at both temperatures. The “precipitation” is, in reality, an aging and aggregation process (Figure 2-5) in which PuO₂ nano-colloids retain their original crystallite size (2–5 nm). Importantly, these crystalline nano-colloids are larger than the nano-clusters identified by Soderholm et al. (2008) and may reflect the growth of nano-clusters to larger crystalline nano-colloids at low ionic strengths and high pH over time. The formation of Pu-Cl ionic bonding, for Pu(IV) monomers, is predicted to occur only at very low pHs (<1), where formation of hydrolysis species is not favored (Guillaumont et al., 2003). Thus, the stability of Cl⁻-containing nano-clusters (Soderholm et al., 2008) or high-NO₃⁻ sols (Haire et al., 1971) is likely to be electrolyte-concentration and pH-dependent.

The behavior of aqueous Pu(IV) is temperature-dependent. At 103 days, the Pu concentration at 80°C was two orders of magnitude lower than at 25°C (Figure 2-6). Precipitation at high temperatures leads to lower apparent solubilities, which reflect greater aggregation of colloidal precipitates. In contrast, aggregation of preformed PuO₂ nano-colloids at high temperatures is not as effective. This implies that colloid formation and aggregation processes are irreversible when solubilities are high. This is likely the reason why Pu(IV) colloid solubility measurements reported in Neck et al. (2007) are uncertain (logK = 8.3±1.0).

2.3.2 Pu behavior in the presence of goethite

Figure 2-7 presents the sorption of aqueous Pu(IV) and intrinsic Pu(IV) nano-colloids to goethite at 25°C. For each form of Pu, data at three concentrations are presented. For simplicity, we designate these as low-, intermediate-, and high-concentration samples. For comparison, Figure 2-7 also includes earlier aqueous Pu(IV) isotherm data at 7 and 14 days from an experiment performed over a much wider Pu(IV) concentration range while using the identical mineral and solution conditions (Zhao et al., 2010). Solution concentration data (and associated solid concentrations) are presented based on measured Pu supernatant concentrations after sedimentation (approximately <250 nm) and centrifugation (approximately <25 nm) procedures (Table 2-2). Based on ICP-MS measurements of Fe in solution, goethite was effectively removed. Thus, differences between measured Pu supernatant concentrations from these two procedures are an indication that Pu is present in substantial quantities associated with

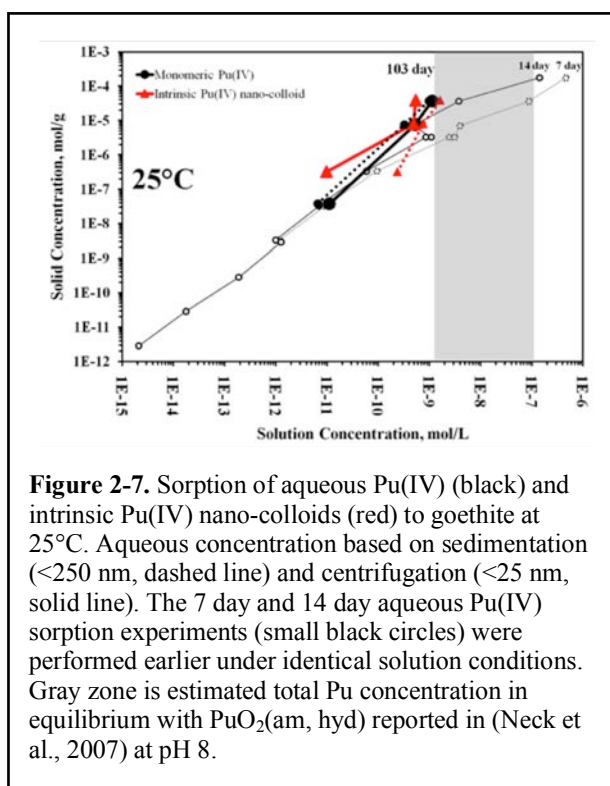


Figure 2-7. Sorption of aqueous Pu(IV) (black) and intrinsic Pu(IV) nano-colloids (red) to goethite at 25°C. Aqueous concentration based on sedimentation (<250 nm, dashed line) and centrifugation (<25 nm, solid line). The 7 day and 14 day aqueous Pu(IV) sorption experiments (small black circles) were performed earlier under identical solution conditions. Gray zone is estimated total Pu concentration in equilibrium with PuO₂(am, hyd) reported in (Neck et al., 2007) at pH 8.

aggregated PuO₂ nano-colloids in the 25–250-nm range.

The present aqueous Pu(IV) sorption data at 25°C are in excellent agreement with the earlier isotherm data. The low-concentration aqueous Pu(IV) sample matches previous data (small black symbols), indicating that equilibrium sorption was reached within 7 days. The low-concentration sorption represents monomeric adsorption of Pu(IV) to the goethite surface. The intermediate-concentration aqueous Pu(IV) sample matches the previous data at 14 days, indicating that sorption/surface precipitation reached equilibrium within 14 days. The highest-concentration aqueous Pu(IV) sample (1.1×10^{-9} M) resulted in a solution concentration lower than the earlier 14 day sample (3.8×10^{-9} M), indicating that equilibrium had not been reached within 14 days. For the intermediate and high aqueous Pu(IV) concentration samples, solubility considerations suggest that precipitation of PuO₂(am, hyd) will occur (initial Pu concentrations were 8×10^{-7} and 4×10^{-6} M, respectively, Table 2-1). Equilibrium solution concentrations are slightly lower than expected based on thermodynamic estimates alone (see Figure 2-6). However, the Pu concentration in solution may be lower simply because the particle size range to which the “colloidal” fraction was attributed (<250 nm) is smaller than that used by Neck et al. (2007).

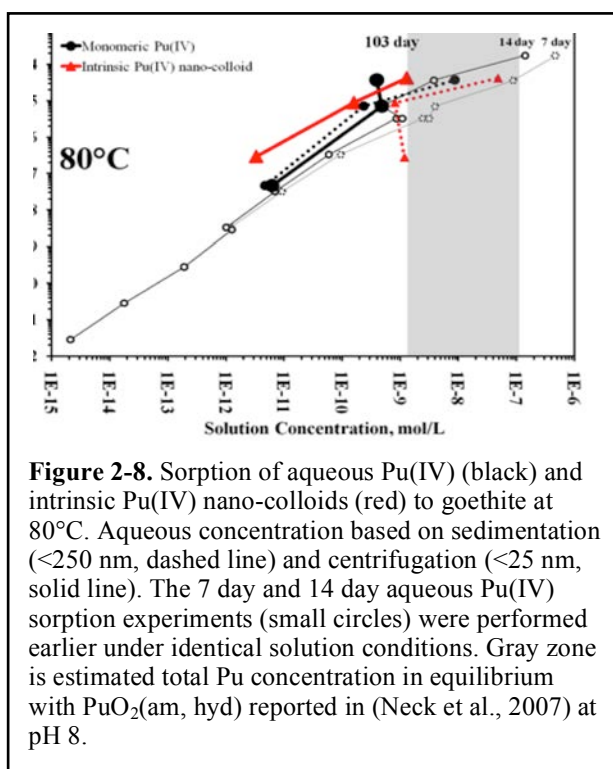
The behavior of intrinsic Pu(IV) nano-colloids differs significantly from that of aqueous Pu(IV) only in the low-concentration sample. A substantial difference between Pu concentration in solution after sedimentation (2.4×10^{-10} M) versus centrifugation (9.8×10^{-12} M) indicates that large (25–250-nm) aggregated intrinsic Pu(IV) nano-colloids are present and do not have a strong affinity for the goethite surface. It suggests that intrinsic Pu(IV) nano-colloids at low concentrations may not be subject to sorption processes that would retard their migration. However, the intermediate- and high-concentration samples do not exhibit this same behavior. The intermediate- and high-concentration intrinsic Pu(IV) nano-colloid sorption samples result in solution concentrations similar to aqueous Pu(IV) sorption samples, driven by aggregation processes that can be categorized as precipitation.

Figure 2-8 presents the 80°C sorption data for aqueous Pu(IV) and intrinsic Pu(IV) nano-colloids. The 80°C aqueous Pu(IV) sorption data are similar to the 25°C data. However, greater differences in solution Pu concentrations between sedimentation and centrifugation suggest that large 25–250-nm aggregated intrinsic Pu(IV) nano-colloids may be more stable and prevalent at higher temperatures. Haire et al. (1971) also found that temperature will increase the stability of colloidal PuO₂ in solution.

2.3.3 TEM observation of Pu morphology

2.3.3.1 Aqueous Pu on goethite, 25°C

In the presence of goethite and at 25°C, aqueous Pu(IV) has been shown to grow epitaxially, forming bcc Pu₄O₇ nano-colloids in the 2–5-nm particle size range (Powell et al., 2011). While previous observations were made on samples reacted for short durations, the Pu₄O₇ nano-



colloids appear to be stable over the longer experiment time-frame examined here (103 days). Importantly, this indicates that the Pu_4O_7 is stable on the goethite surface and will not alter to a PuO_2 phase over a time-frame of months.

Identification of PuO_2 versus Pu_4O_7 on the goethite surface was accomplished by high-resolution TEM imaging (HRTEM) combined with fast Fourier transform (FFT) analysis (HRTEM FFT) (Figure 2-9). However, we have also found that the two forms exhibit distinct morphological characteristics at the nano-scale. In general, PuO_2 nano-particles form aggregates that range in size from tens to hundreds of nanometers while Pu_4O_7 nano-colloids are uniquely associated with the goethite surface and distributed as dispersed 2–5-nm nano-particles. These morphologies are illustrated in the following discussion.

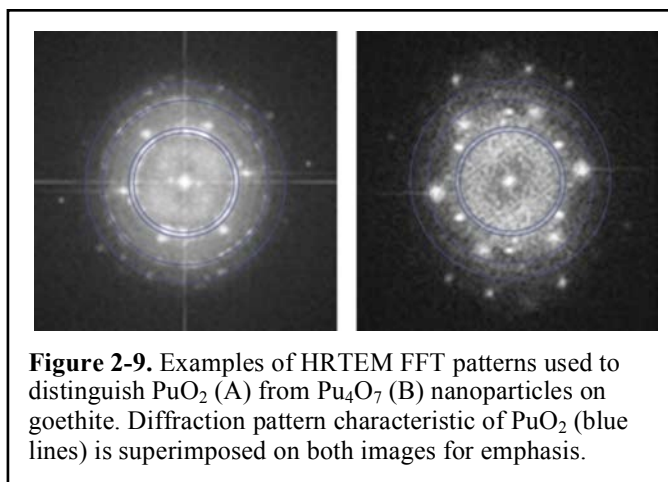


Figure 2-9. Examples of HRTEM FFT patterns used to distinguish PuO_2 (A) from Pu_4O_7 (B) nanoparticles on goethite. Diffraction pattern characteristic of PuO_2 (blue lines) is superimposed on both images for emphasis.

In the intermediate concentration sample, Pu_4O_7 nano-colloids are widely distributed over the goethite surface and dominated by isolated (dispersed) 2–5-nm nano-colloids (Figure 2-10). In the high-concentration sample, both dispersed Pu_4O_7 nano-colloids and aggregated fcc PuO_2 nano-colloids exist (Figure 2-11). Importantly, the fundamental crystalline size remains in the 2–5-nm size range for both forms of Pu nano-colloid and in all samples. In the high-concentration sample, nano-colloid aggregation is more pronounced. It cannot be ascertained whether this aggregation is purely a physical/electrostatic interaction or a chemical one. However, that difference may have a pronounced effect on the transport behavior of intrinsic Pu nano-colloids as well as the transport behavior facilitated by iron oxide colloids.

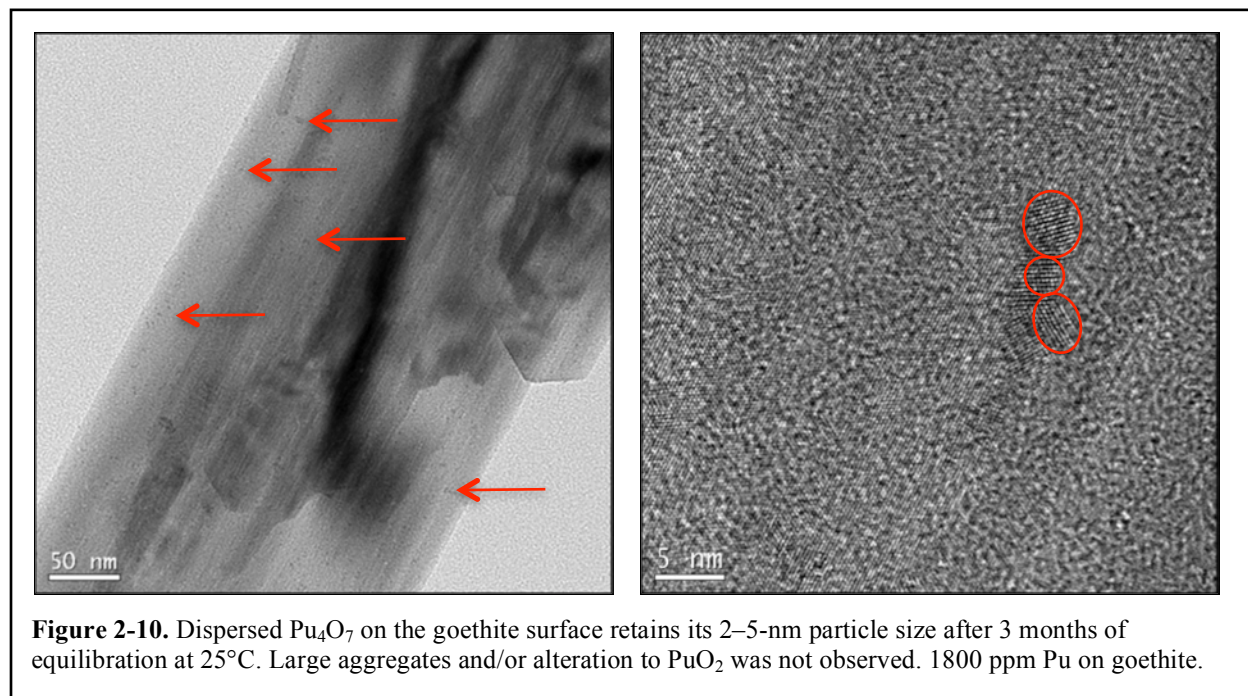


Figure 2-10. Dispersed Pu_4O_7 on the goethite surface retains its 2–5-nm particle size after 3 months of equilibration at 25°C. Large aggregates and/or alteration to PuO_2 was not observed. 1800 ppm Pu on goethite.

Importantly, aggregated nano-colloids appear to be dominated by PuO_2 nano-colloids precipitated directly from solution and weakly associated with the goethite surface. From a bulk solution standpoint, this would be characterized as precipitation of $\text{PuO}_2(\text{am, hyd})$. At the nanoscale, it is characterized as aggregation of PuO_2 nano-colloids.

2.3.3.2 Intrinsic Pu nano-colloids on goethite, 25°C

Unlike aqueous Pu(IV) sorption, intrinsic Pu(IV) nano-colloid sorption to goethite is dominated by aggregated mats of PuO_2 nano-colloids. These mats were observed in both the intermediate- and high-concentration samples (Figure 2-12). The Pu_4O_7 colloids that were observed in the aqueous Pu-experiments were not observed in any of the intrinsic Pu colloid experiments. Importantly, this indicates that the PuO_2 colloids, once formed, will not alter to Pu_4O_7 over a timeframe of months. In addition, however, the ordered PuO_2 does not appear to grow beyond its initial 2–5-nm crystalline size, consistent with previous work (Haire et al., 1971).

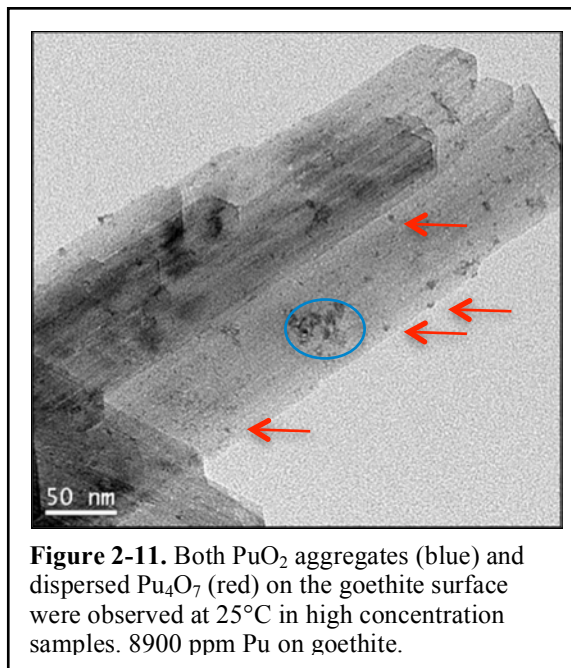
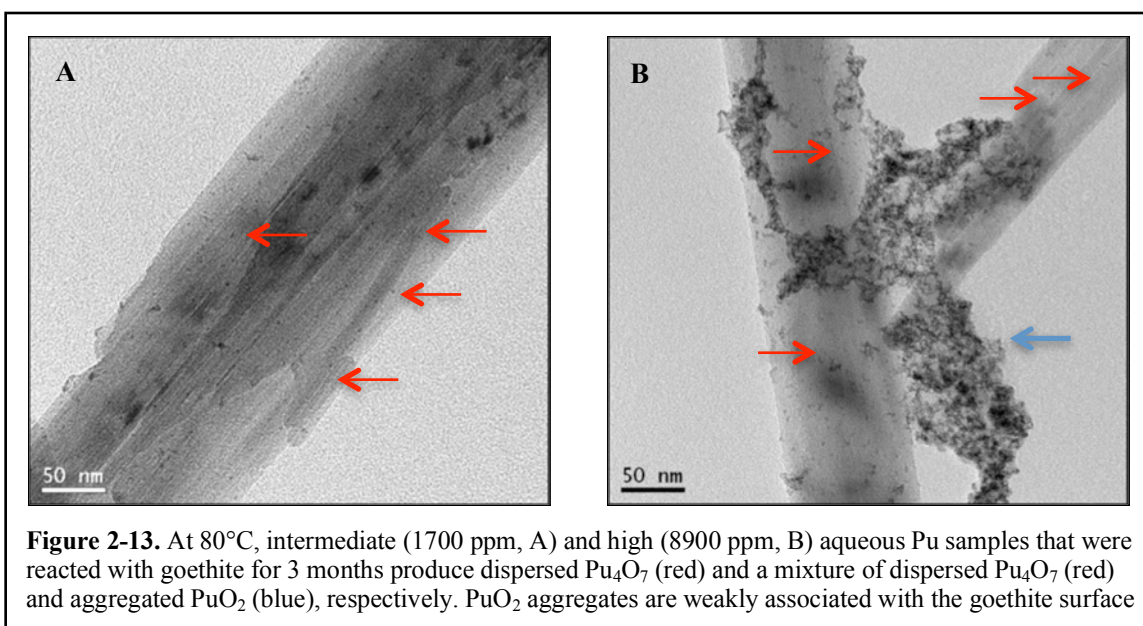
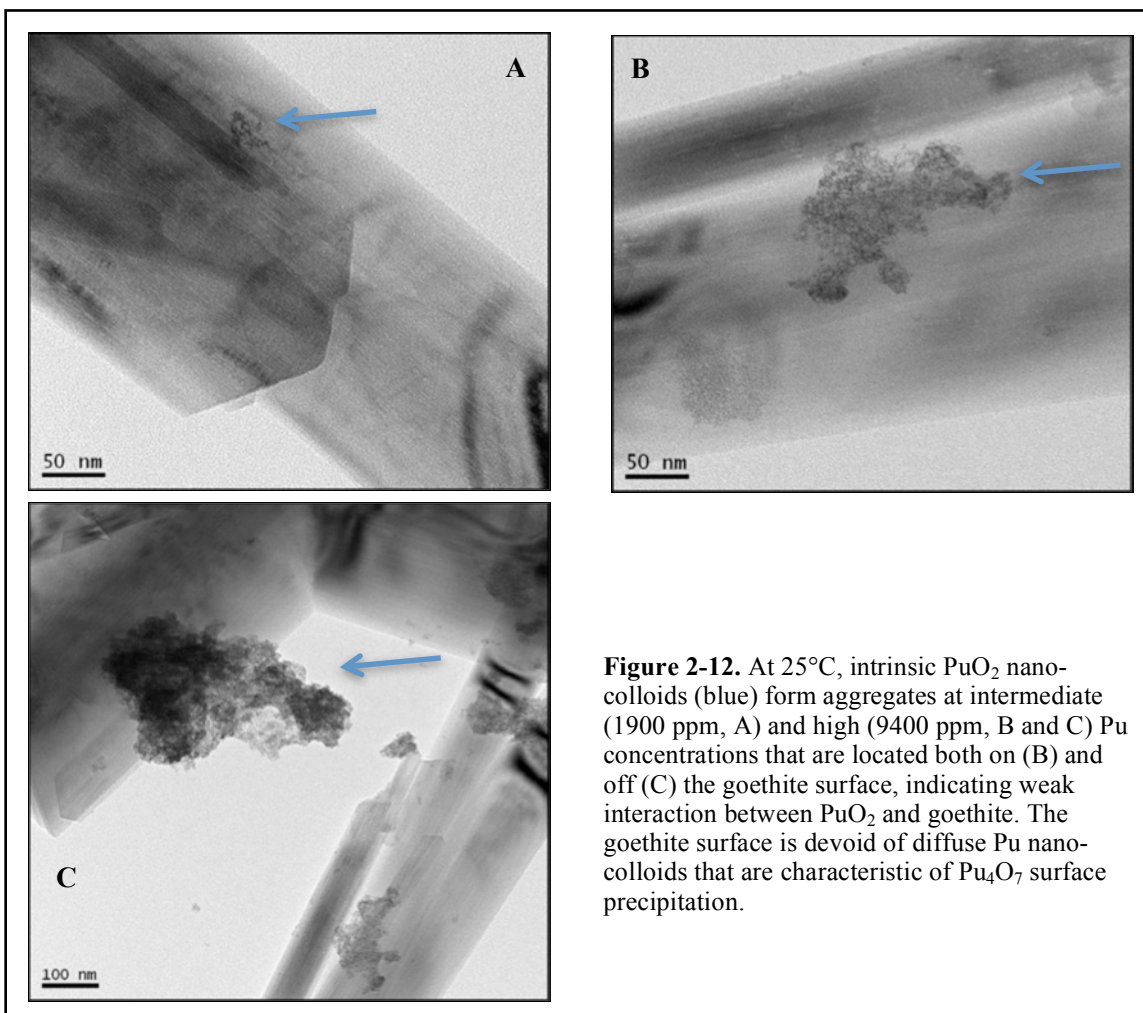


Figure 2-11. Both PuO_2 aggregates (blue) and dispersed Pu_4O_7 (red) on the goethite surface were observed at 25°C in high concentration samples. 8900 ppm Pu on goethite.

Because these mats are located both on and off goethite (Figure 12B and C), it is clear that the interaction between intrinsic PuO_2 nano-colloids and the goethite surface is much weaker than in the case of aqueous Pu(IV) sorption. The bulk solution chemistry data (Figure 2-3) suggest that the same weak interaction between PuO_2 nano-colloids and goethite exist at the low Pu concentration. However, identification of PuO_2 colloids by TEM at low surface loading is exceedingly difficult (the needle in the haystack problem). It was not attempted for the low-concentration sample.

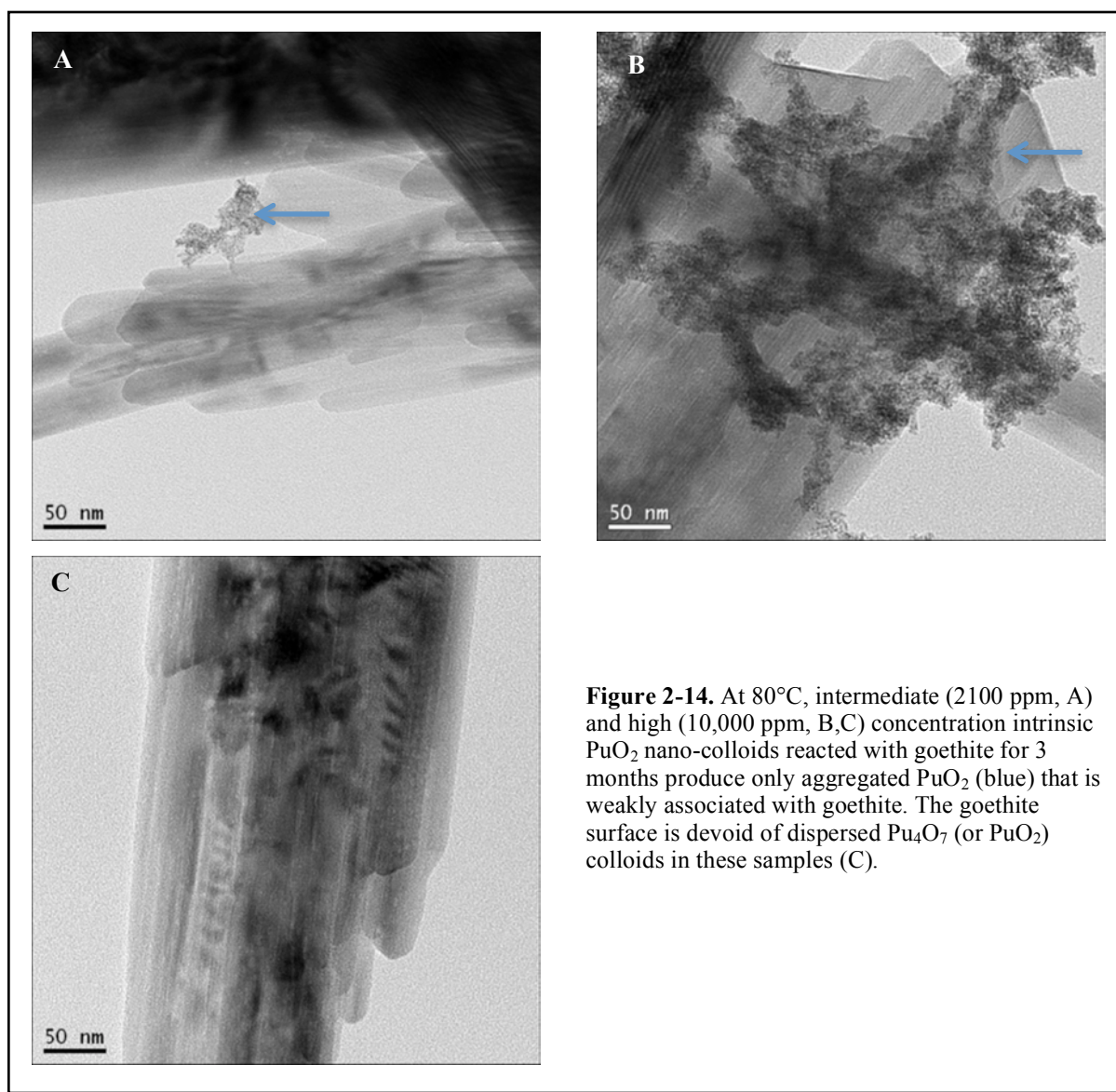
2.3.3.3 Aqueous Pu on goethite, 80°C

The characteristics of Pu associated with goethite at 80°C are not substantially different from those at 25°C. The intermediate-concentration aqueous Pu(IV) sample is dominated by dispersed Pu_4O_7 nano-colloids that are in the 2–5-nm size range (Figure 2-13). In the high-concentration sample, both aggregated PuO_2 nano-colloids and dispersed Pu_4O_7 nano-colloids are present. The aggregated PuO_2 nano-colloids are located both on and off the goethite surface while the Pu_4O_7 nano-colloids are strictly associated with the goethite surface. These observations show that Pu_4O_7 nano-colloids are formed from interactions between aqueous Pu species and goethite. In contrast, PuO_2 nano-crystals are more likely formed from aqueous Pu in solution with minimum interaction to goethite. At 80°C, the size of the aggregated PuO_2 nano-colloids appears to be larger. This is consistent with Pu concentrations measured in solution (Figure 2-5), which suggests that a significant fraction of intrinsic Pu(IV) nano-colloids are aggregated and in the 25–250-nm particle size range.



2.3.3.4 Intrinsic Pu nano-colloids on goethite, 80°C

The behavior of intrinsic Pu(IV) nano-colloids at 80°C is dominated in both intermediate- and high-concentration samples by the formation of large aggregated PuO₂ nano-colloids and little if any association with the goethite surface (Figures 2-14). In terms of bulk solution chemistry, these would be considered precipitates of PuO₂(am, hyd). HRTEM images and electron diffraction analysis indicate that the mats are composed of 2–5-nm nano-colloids with an fcc PuO₂ structure. Importantly, the results suggest that the relationship between colloidal and precipitated forms of PuO₂(am, hyd) is controlled by degree of aggregation of 2–5-nm nano-colloids. Aggregation of nano-colloids is controlled primarily by the solution conditions in which they are present—Pu concentration, solution composition (e.g., ionic strength, pH) and temperature. Thus, the concentration of dispersed intrinsic PuO₂ nano-colloids in solution will most likely be controlled by the physical aggregation behavior of PuO₂ nano-colloids.



2.4 Conclusions

The strong affinity of aqueous Pu(IV) for the goethite surface is explained by the epitaxial growth of bcc Pu₄O₇ nano-colloids on goethite. The behavior is affected minimally by temperature. However, the dispersed 2–5-nm Pu₄O₇ on the goethite surface appears to be stable over the timescale of months at both 25 and 80°C under our experimental conditions. There is no indication that the Pu₄O₇ alters to PuO₂ nano-colloid over time. When intrinsic PuO₂ nano-colloids are reacted with goethite over 103 days, both solution phase characterization in low-concentration samples and TEM of high-concentration samples indicate that the PuO₂ nano-colloids have a very weak affinity for the goethite surface. Importantly, there is no indication that the PuO₂ will alter to Pu₄O₇ nano-colloid on the goethite surface over time. Thus it appears that the association of Pu to goethite is dependent on the initial state of Pu in solution.

The crystallite size of PuO₂ nano-colloids is in the 2–5-nm range and appears to increase only slightly at higher temperatures and over time, consistent with earlier characterization of plutonium sols performed by Haire et al. (1971). Aggregation of PuO₂ nano-colloids is favored over sorption to goethite. From a bulk solution perspective, this would be characterized as precipitation and is in agreement with solubility measurements of Neck et al. (2007) for PuO₂(am, hyd). Importantly, a truly amorphous precipitate does not form. The nano-clusters identified in Soderholm et al. (2007) represent the lower limit of colloid sizes observed here by TEM. However, the exact relationship and relative stability of nano-clusters to the larger nano-colloids observed here requires further study. In addition, the relationship between these TEM observations and the bulk characterization of Pu precipitates with apparent mixed valence (i.e., PuO_{2+x}) remains an open question.

The fate of Pu in the environment is dependent on its initial form and its subsequent stability under changing geochemical conditions. Epitaxial growth of Pu₄O₇ on the goethite surface will produce a strong association between Pu and goethite, which could lead to its immobilization. The formation of Pu₄O₇ on goethite has the potential to facilitate the transport of Pu in solution facilitated by colloids.

The focus of ongoing research is on the dissolution kinetics of Pu nanoparticles and sorbed species from the iron hydroxide. Pu nanoparticle dissolution and Pu desorption kinetics must be quantified as these rates are likely to control the colloid-facilitated transport of Pu in the near-field and far-field repository environments. Experimental data summarized in this chapter illustrate the complex reaction chemistry that will control kinetics and the need for a comprehensive conceptual understanding of the underlying mechanisms controlling Pu reactive transport.

2.5 References

- Bertetti, F.P., Pabalan, R.T., Almendarez, M.G., 1998. Studies on neptunium(V) sorption on quartz, clinoptilolite, montmorillonite, and α -alumina, in: Jenne, E.A. (Ed.), *Adsorption of Metals by Geomedia*. Academic Press, San Diego, pp. 131–148.
- Conradson, S.D., Begg, B.D., Clark, D.L., den Auwer, C., Ding, M., Dorhout, P.K., Espinosa-Faller, F.J., Gordon, P.M., Haire, R.G., Hess, N.J., Hess, R.J., Keogh, D.W., Morales, L.A., Neu, M.P., Paviet-Hartmann, P., Runde, W., Tait, C.D., Veris, D.K., Vilella, P.M., 2004. Local and nanoscale structure and precipitation in the PuO_{2+x-y}(OH)_{2y}*zH₂O system. *J. Amer. Chem. Soc.* **126**, pp. 13443–13458.
- Cvetkovic, V., 2000. Colloid-facilitated tracer transport by steady random ground-water flow. *Physics of Fluids* **12**, pp. 2279–2294.
- Cvetkovic, V., Painter, S., Turner, D., Pickett, D., Bertetti, P., 2004. Parameter and model sensitivities for colloid-facilitated radionuclide transport on the field scale. *Water Resources Research* **40**.

- Gee, G.W., Bauder, J.W., 1986. Particle-size Analysis, in: Klute, A. (Ed.), *Methods of Soil Analysis: Part I - Physical and Mineralogical Methods*. American Society of Agronomy, Inc, Madison, WI, pp. 383–411.
- Guillaumont, R., Fanghanel, T., Neck, V., Fuger, J., Palmer, D.A., Grenthe, I., Rand, M.H., 2003. Update on the Chemical Thermodynamics of Uranium, Neptunium, Plutonium, Americium, and Technetium, in: Agency, O.N.E. (Ed.), *Chemical Thermodynamics*. Elsevier, Amsterdam.
- Haire, R.G., Lloyd, M.H., Beasley, M.L., Milligan, W.O., 1971. Aging of hydrous plutonium dioxide. *Journal of Electron Microscopy* **20**, pp. 8–16.
- Haschke, J.M., Allen, T.H., Morales, L.A., 2000. Reaction of plutonium dioxide with water: Formation and properties of PuO_{2+x} . *Science* **287**, pp. 285–287.
- Kaszuba, J.P., Runde, W.H., 1999. The aqueous geochemistry of neptunium: Dynamic control of soluble concentrations with applications to nuclear waste disposal. *Environmental Science & Technology* **33**, pp. 4427–4433.
- Keeney-Kennicutt, W.L., Morse, J.W., 1985. The redox chemistry of Pu(V)O_2^+ interaction with common mineral surfaces in dilute solutions and seawater. *Geochimica et Cosmochimica Acta* **49**, pp. 2577–2588.
- Kersting, A.B., Efurud, D.W., Finnegan, D.L., Rokop, D.J., Smith, D.K., Thompson, J.L., 1999. Migration of plutonium in ground water at the Nevada Test Site. *Nature* **397**, pp. 56–59.
- Kozai, N., Ohnuko, T., Matsumoto, J., Banba, T., Ito, Y., 1996. A study of the specific sorption of neptunium(V) on smectite in low pH solution. *Radiochim. Acta* **75**, pp. 149–158.
- Kozai, N., Ohnuky, T., Muraoka, S., 1993. Sorption characteristics of neptunium by sodium-smectite. *J. Nuclear Sci. Tech.* **30**, pp. 1153–1159.
- Lloyd, M.H., Haire, R.G., 1968. A sol-gel process for preparing dense forms of PuO_2 . *Nuclear Applications* **5**, pp. 114–122.
- Lujanienė, G., Motiejunas, S., Sapolaite, J., 2007. Sorption of Cs, Pu and Am on clay minerals. *Journal of Radioanalytical and Nuclear Chemistry* **274**, pp. 345–353.
- Missana, T., Garcia-Gutierrez, M., Alonso, U., 2004. Kinetics and irreversibility of cesium and uranium sorption onto bentonite colloids in a deep granitic environment. *Applied Clay Science* **26**, pp. 137–150.
- Neck, V., Altmaier, M., Seibert, A., Yun, J.I., Marquardt, C.M., Fanghanel, T., 2007. Solubility and redox reactions of Pu(IV) hydrous oxide: Evidence for the formation of $\text{PuO}_{2+x}(\text{s, hyd})$. *Radiochimica Acta* **95**, pp. 193–207.
- Office of Civilian Radioactive Waste Management, 2002. *Yucca Mountain Science and Engineering Report: Technical Information Supporting Site Recommendation Consideration*. U.S. Department of Energy, pp. 4-466.
- Penneman, R.A., Paffett, M.T., 2005. An alternative structure of Pu_4O_9 (“ $\text{PuO}_{2.25}$ ”) incorporating interstitial hydroxyl rather than oxide. *J. Solid State Chem.* **178**, pp. 563–566.
- Petit, L., Svane, A., Szotek, Z., Temmerman, W.M., 2003. First-principles calculations of PuO_{2+x} . *Science* **301**, pp. 498–501.
- Powell, B.A., Dai, Z., Zavarin, M., Zhao, P., Kersting, A.B., 2011. Stabilization of Plutonium Nano-Colloids by Epitaxial Distortion on Mineral Surfaces. *Environmental Science & Technology* **45**, pp. 2698–2703.
- Powell, B.A., Fjeld, R.A., Kaplan, D.I., Coates, J.T., Serkiz, S.M., 2004. Pu(V)O_2^+ adsorption and reduction by synthetic magnetite (Fe_3O_4). *Environmental Science & Technology* **38**, pp. 6016–6024.
- Powell, B.A., Fjeld, R.A., Kaplan, D.I., Coates, J.T., Serkiz, S.M., 2005. Pu(V)O_2^+ adsorption and reduction by synthetic hematite and goethite. *Environmental Science & Technology* **39**, pp. 2107–2114.
- Powell, B.A., Kersting, A.B., Zavarin, M., 2008. Sorption and Desorption Rates of Neptunium and Plutonium on Goethite, in: Zavarin, M., Kersting, A.B., Lindvall, R.E., Rose, T.P. (Eds.),

- Hydrologic Resources Management Program and Underground Test Area Project, FY 2006 Progress Report*. Lawrence Livermore National Laboratory, Livermore, CA, p. 90, UCRL-TR-404620.
- Sabodina, M.N., Kalmykov, S.N., Sapozhnikov, Y.A., Zkharova, E.V., 2006. Neptunium, plutonium and ¹³⁷Cs sorption by bentonite clays and their speciation in pore waters. *J. Radioanal. Nucl. Chem.* **270**, pp. 349–355.
- Saiers, J.E., Hornberger, G.M., 1996. The role of colloidal kaolinite in the transport of cesium through laboratory sand columns. *Water Resources Research* **32**, pp. 33–41.
- Sanchez, A.L., Murray, J.W., Sibley, T.H., 1985. The adsorption of plutonium IV and V on goethite. *Geochimica et Cosmochimica Acta* **49**, pp. 2297–2307.
- Schwertmann, U., Cornell, R., M., 1991. *Iron oxides in the laboratory: preparation and characterization*. VCH Verlagsgesellschaft mbH, Weinheim.
- Soderholm, L., Almond, P.M., Skanthakumar, S., Wilson, R.E., Burns, P.C., 2008. The structure of the plutonium oxide nanocluster [Pu₃₈O₅₆C₁₅₄(H₂O)₍₈₎](14-). *Angewandte Chemie-International Edition* **47**, pp. 298–302.
- Steeffel, C.I., 2008. Geochemical kinetics and transport, in: Brantley, S.L., Kubicki, J.D., White, A.F. (Eds.), *Kinetics of Water-Rock Interaction*. Springer, New York, pp. 545–585.
- Tinnacher, R.M., Zavarin, M., Powell, B.A., Kersting, A.B., 2011. Kinetics of neptunium(V) sorption and desorption on goethite: An experimental and modeling study. *Geochimica et Cosmochimica Acta* **75**, pp. 6584–6599.
- Turner, D.R., Pabalan, R.T., Bertetti, F.P., 1998. Neptunium(V) sorption on montmorillonite: An experimental and surface complexation modeling study. *Clays and Clay Minerals* **46**, pp. 256–269.
- Zhao, P., Zavarin, M., Tumey, S., Williams, R., Dai, Z., Kips, R., Kersting, A.B., 2010. *Isotherm of Pu/Goethite System: Linearity and Sorbent Surface Characterization*, AGU Fall Meeting, San Francisco.

Chapter 3. Stability of Plutonium(IV) Intrinsic Colloids in the Presence of Montmorillonite at 25 and 80 °C

3.1 Introduction

The large volumes of plutonium (Pu) designed for storage in high-level nuclear waste repositories are predicted to be a dominant long-term dose contributor under certain scenarios (Kaszuba and Runde, 1999; Office of Civilian Radioactive Waste Management, 2002). Once it is deposited in the environment, Pu has been shown to migrate in the subsurface associated the colloidal fraction of the groundwater (e.g., Kersting et al., 1999). Colloid-facilitated transport of Pu in both groundwater and surface water has been documented at several DOE sites (Kersting et al., 1999; Santschi et al., 2002). Pu sorbed to iron oxide colloids has also been detected over 4 km from its original source in Mayak, Russia (Novikov et al., 2006). These studies indicate that the Pu associated with mobile colloids has moved on the scale of kilometers. Despite the recognized importance of colloid-facilitated transport of Pu, little is known about the geochemical and biochemical mechanisms controlling its formation and stability over the range in concentrations expected in the environment. For example, how is Pu transported along flow paths that span high Pu concentrations at the source to extremely low concentrations encountered at significant distances down gradient? Without a conceptual understanding of the dominant processes and a quantitative understanding of the relevant reaction chemistry, current transport models cannot effectively predict Pu migration rates.

Pu can be associated with the colloidal fraction of groundwater in two different forms. Pu can migrate as either an ‘intrinsic’ colloid or sorbed to a naturally occurring inorganic, organic or microbial species. At high concentrations where actinide ions in solution exceed the solubility product, Pu can hydrolyze to form intrinsic Pu(IV) colloids (or sometimes, eigen-colloids) (Kim, 1991; Neck et al., 2007). As an intrinsic colloid, Pu transport will be controlled by the stability (both physical and chemical) of the Pu(IV) intrinsic colloid. At low concentrations Pu tends to sorb to inorganic or organic colloids, resulting in the formation of a pseudocolloid, and transport is determined by the Pu sorption/desorption rates on that colloidal material. Both forms of Pu colloids may exist simultaneously under some subsurface conditions. We currently do not know whether intrinsic colloids, initially formed under high Pu concentrations, will remain stable and migrate down-gradient away from their near-field environment, or if they will dissolve and the aqueous Pu will sorb to organic or inorganic or microbial colloids. Efforts to model the transport of Pu from a near-field environment to lower concentrations in the far-field are currently limited due to the lack of understanding of whether intrinsic Pu colloids will persist along the flow path.

At low Pu concentrations (below solubility), colloid-facilitated transport is likely to be controlled by pseudocolloids. However, the biogeochemical processes controlling Pu transport under these conditions, and the sorption/desorption kinetics in particular, have not been adequately quantified. The identity of naturally occurring inorganic colloids will be a function of the host rock mineralogy. Among the most ubiquitous inorganic colloids are aluminosilicate clays that are commonly observed as mobile colloids due to their inherently small particle size and prevalence as alteration minerals from original host rock material (Kersting et al., 1999). Clays are known to sorb Pu (Bertetti et al., 1998; Keeney-Kennicutt and Morse, 1985; Kozai et al., 1996; Kozai et al., 1993; Lujanienė et al., 2007; Powell et al., 2004, 2005; Powell et al., 2008; Sabodina et al., 2006; Sanchez et al., 1985; Turner et al., 1998). In addition, the proposed use of bentonite within some engineered barrier systems scenarios for high-level nuclear waste repositories provides additional importance to understanding Pu interaction with smectite aluminosilicate clays (Sabodina et al., 2006). Smectite clay may represent a key phase that will control transport of Pu in repository near and far fields.

In Chapter 2, we examined the sorption behavior of Pu in the presence of a common Fe-oxide mineral, goethite at 25 and 80°C at concentrations both above and below solubility. In this chapter, we examine the behavior of Pu in the presence of a common smectite clay mineral, montmorillonite at 25 and 80°C at concentrations both above and below the solubility of PuO₂ (am,hyd) intrinsic colloids. We designed our experiments to evaluate the stability of intrinsic Pu colloids in the presence of montmorillonite as concentrations decrease, similar to transport along a flow path.

We employed dialysis membranes in an effort to completely segregate intrinsic Pu nano-colloids (2–5 nm) from montmorillonite colloids (>100 nm) and allow aqueous Pu to establish equilibrium between both colloidal phases. Using the dialysis membrane approach, we were able to separate the dissolution of Pu intrinsic nano-colloids from the formation of Pu/clay pseudo-colloids and examine each step individually. The kinetics of dissolution of intrinsic Pu colloids in the presence and absence of clay colloids were observed and compared. The results of these efforts provide a clearer understanding of how Pu can migrate over significant temporal and spatial scales.

3.2 Experimental Approach

Batch sorption has been the most common method used to measure the affinity of a contaminant for a mineral surface. Traditionally, a known amount of adsorbate is added to a liquid suspension containing a sorbent, and the aqueous concentration of adsorbate is measured after equilibrium is reached. The resulting affinity of the adsorbate for the sorbent is reported using equation 3-1:

$$K_d = (C_{\text{init}} - C_{\text{final}}) / C_{\text{final}} * V / m \quad (3-1)$$

where C_{init} and C_{final} are initial and final aqueous concentration of adsorbate (mol/L), respectively, V is the volume of liquid (mL), and m is the mass of adsorbent (g). However, if the adsorbate is involved in other processes that also form solid phases (i.e., colloid formation or precipitation), the apparent K_d cannot address the fundamental sorption processes and may lead to a misinterpretation of experimental observations. In order to distinguish between precipitated, colloidal, and sorbed states of Pu, we employed dialysis membranes to segregate pseudocolloids from intrinsic colloids.

Dialysis membranes are commonly used to separate suspended solutes or particles of different dimensions in a liquid mixture. Desirable size separation by dialysis can be achieved by selecting the membrane pore-size molecular weight cutoff (MWCO). For example, membrane pore sizes ranging of 0.5 to 0.6 kilo Daltons (kD) are approximately equivalent to 1 to 2-nm pore sizes. In the case of Pu, dialysis membranes provide a unique function to segregate aquo (<1 nm), intrinsic nano-colloids (2–5 nm), and sorbed pseudocolloids or precipitates (>100-nm mineral phases).

Intrinsic Pu(IV) colloid stability was evaluated using the experimental design shown in Figure 3-1. Briefly, PuO₂ intrinsic colloids are placed inside the dialysis bag. The clay colloids are placed outside the dialysis bag. Thus, the colloidal montmorillonite is isolated from the intrinsic Pu(IV) colloids while exchange of truly aqueous (non-colloidal) ions is permitted. Pu detected outside the dialysis membrane over time represents dissolution of the initial Pu(IV) intrinsic colloids and diffusion across the dialysis membrane. In the presence of montmorillonite, the dissolved Pu can either remain in solution or sorb. The dissolution rate of Pu(IV) intrinsic colloids is expected to be a function of solution pH, temperature, and composition/crystallinity of the colloids. The sorption rate of Pu to montmorillonite is affected by the Pu speciation, solution Eh/pH, ionic strength, and temperature.

This novel experimental design enables us to test the stability of intrinsic colloids relative to adsorbed species on any minerals and over a range of solution conditions. By monitoring solution conditions as a function of time, we are also able to quantify the reaction kinetics as the solution approaches equilibrium. Quantifying the stability of intrinsic colloids is critical to accurately predicting the down-gradient transport behavior of Pu at near-field conditions.

3.3 Materials and Methods

3.3.1 Pu stock solution

Pu stock solutions with two different Pu isotopic ratios were used. A relatively pure alpha-emitting ^{238}Pu stock solution was used in low- and intermediate-Pu-concentration samples. The isotopic ratios in mass percentage for ^{238}Pu , ^{239}Pu , ^{240}Pu , and ^{241}Pu were 76.83%, 21.03%, 2.01%, and 0.142%, respectively. The major isotope contributing to alpha activity in this stock was ^{238}Pu (~99.87% by activity). The second Pu stock solution, used in the high-Pu-concentration experiments, was a ^{242}Pu solution spiked with ~1% of the ^{238}Pu . The mass percentages of the resulting ^{242}Pu stock for ^{238}Pu , ^{239}Pu , ^{240}Pu , ^{241}Pu , and ^{242}Pu were 0.75%, 0.21%, 0.13%, 0.04%, and 98.87%, respectively. The major isotopes contributing to alpha activity in this stock were ^{238}Pu (96.75%) and ^{242}Pu (2.93%). Pu stock solutions were purified using AG1x8 100-200 mesh anion exchange resin and filtered through a 3kD MWCO filter. The oxidation state of Pu was confirmed using both UV/VIS and solvent extraction. The aqueous Pu(IV) starting solution was prepared by diluting the stock solution into a pH 8 buffer solution and gradually adding microliters of NaOH (1N or 6N) to adjust pH to ~pH 8.

The intrinsic PuO_2 nano-colloids were prepared by neutralizing Pu(IV) stocks using NaOH solution and adjusting the pH to between 9–10. This is the same method used to prepare amorphous PuO_2 for the solubility studies used by Neck et al. (2007). After aging for more than a week, the Pu colloids were centrifuged at an RCF of 9168 for 1 hour, and the supernatant was removed. The Pu colloid particle size cut-off based on centrifugation was 14 nm. However, the fundamental particle size of intrinsic Pu nano-

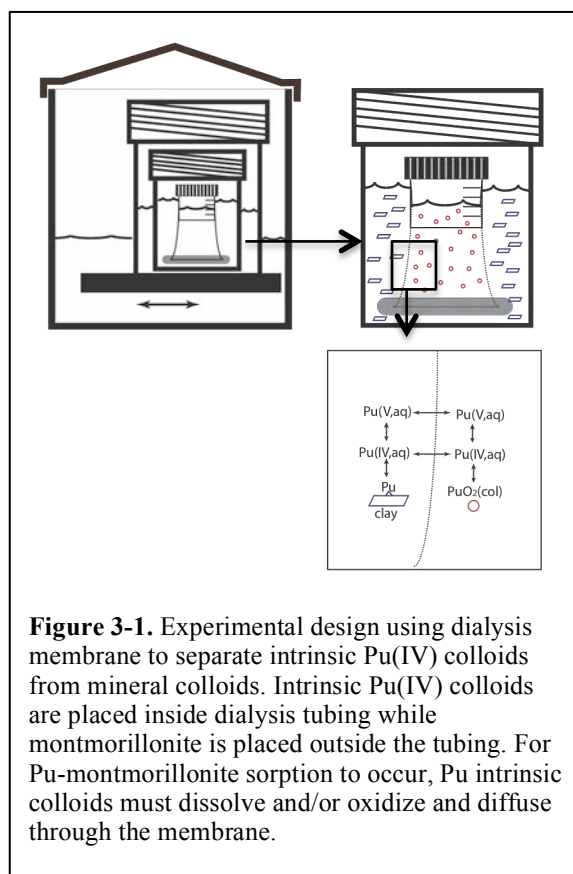


Figure 3-1. Experimental design using dialysis membrane to separate intrinsic Pu(IV) colloids from mineral colloids. Intrinsic Pu(IV) colloids are placed inside dialysis tubing while montmorillonite is placed outside the tubing. For Pu-montmorillonite sorption to occur, Pu intrinsic colloids must dissolve and/or oxidize and diffuse through the membrane.

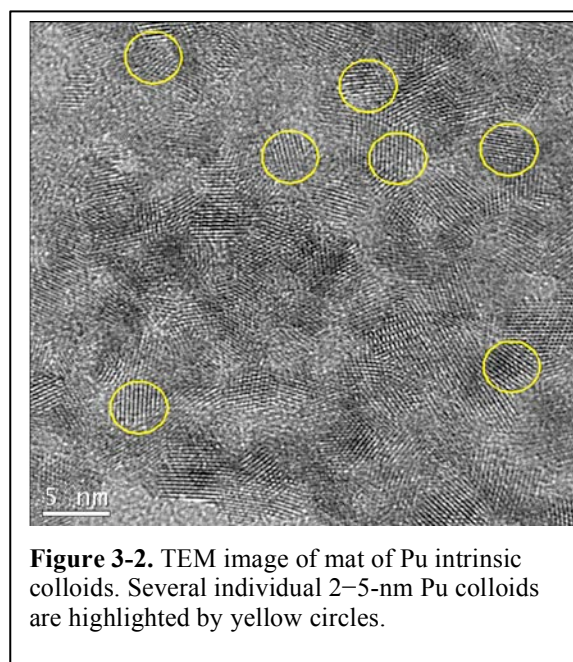


Figure 3-2. TEM image of mat of Pu intrinsic colloids. Several individual 2–5-nm Pu colloids are highlighted by yellow circles.

colloids prepared in this study is much smaller, on the order of 2–5 nm (Figure 3-2). The Pu colloids were re-suspended in Milli-Q water. The Pu colloid starting solutions were prepared by adding a spike of Pu colloids into the pH 8 buffer solution without further pH adjustment. The concentration of soluble Pu in the Pu colloid starting solutions, measured in 3kD MWCO filtrate by LSC, were 1~3% of the total colloid concentration.

3.3.2 Montmorillonite

SWy-1 montmorillonite (Clay Minerals Society) was pre-treated using 1 mM HCl (to dissolve any carbonate minerals) followed by addition of 0.1% of H₂O₂ (to oxidize organic contaminants and reduced metals (e.g., Fe²⁺)). The treated montmorillonite was centrifuged to remove excess liquid, and the wet paste was transferred to a 6–8-kD MWCO dialysis tube suspended in 0.01 M NaCl solution to produce a homoionic Na-montmorillonite. The clay minerals were dialyzed for seven days, and the NaCl solution was changed at least once per day. The clay minerals were then suspended in Milli-Q water and centrifuged to obtain the fraction of particle sizes from 50 nm to 2 microns. The wet solids were dried at 40°C until a constant weight was obtained. A stock montmorillonite suspension was made by mixing 4 g of dried montmorillonite in 400 mL of pH 8 buffer solution (10 g/L). The surface area of montmorillonite measured by N₂(g)-BET was 31.45 ± 0.17 m²/g, which is comparable to the reported value of 31.8 m²/g (Clay Minerals Repository).

3.3.3 Batch dialysis experiments

A total of 14 dialysis experiments were performed to test the experimental design and quantify the stability of intrinsic Pu(IV) colloids in the presence of montmorillonite (Table 3-1). The experiments were performed at two temperatures, 25°C (7 experiments) and 80°C (7 experiments), to evaluate the effect of temperature on intrinsic colloid stability. At each temperature, Pu was initially added either as an aqueous phase (to test simple diffusion and sorption of Pu) or as an intrinsic colloid (to test intrinsic colloid dissolution, diffusion and sorption of Pu). The initial Pu concentrations bracketed the PuO₂(am, hyd) solubility (~5 × 10⁻⁹ M) (Neck et al., 2007). In addition, montmorillonite-free solutions (spiked blanks) with initial Pu concentrations below and near PuO₂(am, hyd) solubility were used for comparison with sorption experiments and evaluation of Pu loss to container walls and the dialysis membrane.

All batch experiments were conducted in 450-mL Teflon jars with air-tight closures. 225 mL of pH 8 buffer solution (pH 8, 5 mM NaCl/0.7 mM NaHCO₃) was mixed with 25 mL of montmorillonite stock suspension to yield a 250-mL montmorillonite suspension at a solid to liquid ratio of 1g/L. A sealed dialysis tube containing 30 mL of either aqueous Pu(IV) or intrinsic PuO₂ nano-colloids was then placed in the 250 mL pH buffer solution with or without (spiked blanks) montmorillonite. The 450-mL Teflon jars were submerged in 1-L Teflon containers filled with Milli-Q water to minimize evaporative losses and provide secondary containment to the radioactive samples. Over the course of the experiment, the 25°C samples were placed on a top-loading orbital shaker, and the 80°C samples were submerged in a heated water bath (Innova 3100) and shaken at an orbital speed of 100 rpm.

Each experiment was sampled as a function of time over a three-month period. At each sampling interval, aliquots of the montmorillonite suspension were collected, centrifuged and analyzed for total Pu, Pu in the supernatant, and pH. The montmorillonite concentration in the suspension was also measured based on light scattering at a wavelength range of 300–500 nm using UV-VIS spectrometry (Cary 500, Varian).

Table 3-1. Experimental conditions for Pu(IV) samples at 25 and 80 °C.

	Expt	Pu colloids mol/L	Swy-1 Montmorillonite g/L	Expt	Pu(IV, aq) mol/L	Swy-1 Montmorillonite g/L
25 °C	1	1.13E-11	1	9	5.93E-12	1
	2	9.09E-10	1	10	6.20E-10	1
	3	2.01E-7	1	11	6.52E-12	0
	4	9.13E-10	0			
80 °C	5	1.14E-11	1	12	5.93E-12	1
	6	8.31E-10	1	13	6.20E-10	1
	7	2.01E-7	1	14	6.52E-12	0
	8	9.13E-10	0			

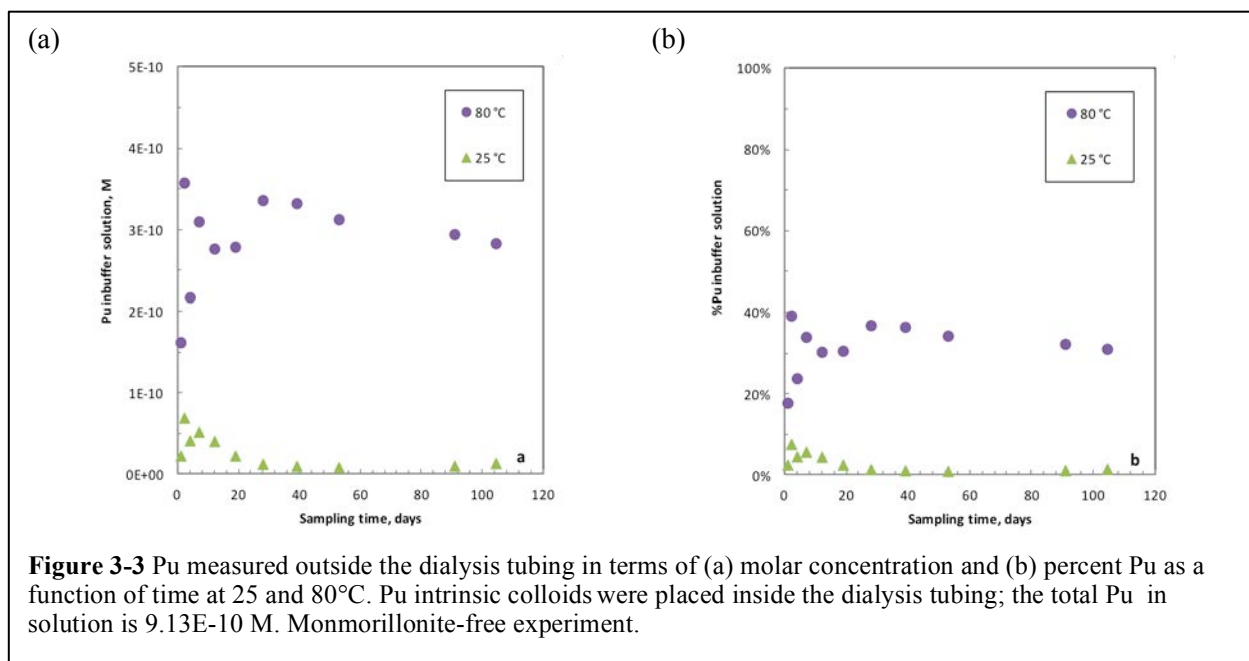
Pu concentrations listed above were calculated respect to total volume of 280 mL. The initial Pu concentrations inside the dialysis membranes were ~9 times higher than listed values.

3.4 Results and Discussion

3.4.1 Stability of Pu intrinsic colloids in the absence of clay at 25 and 80°C

Prior to performing the dialysis experiments outlined in Table 3-1, spiked blanks containing ^3H and aqueous Pu(V) were used to test the experimental design and determine diffusion rates of ^3H and Pu(V) through the dialysis membranes at 25 and 80°C (data not shown). Pu(V) was used instead of Pu(IV) to reduce the likelihood of Pu sorption to container walls. The diffusion of both ^3H and Pu(V) was rapid, and steady state was achieved within five hours at both temperatures. The diffusion rate across the membrane of both the ^3H and aqueous Pu(V) appeared to be slightly slower at 80°C than that at 25°C. This was most likely a function of mixing rates at the two temperatures and temperature-dependent behavior of the dialysis membrane material (regenerated cellulose). However, at both temperatures, diffusion was determined to be fast enough that it would not be rate limiting when evaluating colloid stability on the scale of days.

PuO₂ intrinsic colloid stability in the absence of montmorillonite (i.e., montmorillonite-free spiked blanks) is presented in Figure 3-3. The initial Pu concentration in the dialysis bag was 7.8E-9 M, which is at the solubility limit of colloidal Pu. However, the concentration of the Pu colloids with respect to total solution volume (255 mL) is 9.13E-10 M (Table 3-1). This is below the solubility of Pu colloids (Neck et al., 2007), suggesting that the intrinsic colloids should dissolve over time. However, the results presented in Figure 3-3 are inconclusive. Figure 3-3a indicates that Pu concentrations outside of the dialysis membrane increase at early time (days), but then decreases at later times (weeks–months) at both 25 and 80 °C. Sorption to container walls and membrane material appear to be affecting the long-term behavior of Pu. Figure 3-3b indicates that approximately 6% and 37% (25 and 80°C, respectively) of the total PuO₂ resides in solution outside the dialysis membrane at early time. Base on this early time data, it appears that the dissolution rate of Pu colloids is much higher at 80°C than that at 25°C. It suggests that Pu intrinsic colloids tested in this study will not be stable at Pu concentrations below their solubility and intrinsic colloid formation appears to be reversible. However, the stability of PuO₂ intrinsic colloids is a function of its morphology, crystallinity, and aging, and further investigations on Pu colloids stability are continuing by evaluating different formations of the Pu oxide. We are also conducting additional experiments to quantify the sorption of aqueous Pu onto the dialysis membranes and container walls.



3.4.2 Dissolution of Pu intrinsic colloids in the presence of clay at 25°C and 80 °C.

The dissolution of PuO₂ intrinsic colloids and sorption of Pu to montmorillonite were examined using three different initial colloidal Pu concentrations (10⁻¹¹, 10⁻⁹ and 10⁻⁷M) (Table 3-1) that bracket the range of stability identified in Neck et al. (2007). The Pu concentration in the clay suspension is plotted as a function of time and temperature in Figure 3-4. This measurement includes both the aqueous and sorbed Pu. Depending on the initial temperature and Pu concentration, aqueous Pu concentrations were between 1 and 15% of the total Pu in the suspensions. Figure 3-4 shows the total concentration of Pu outside the dialysis bag as both a concentration and a percentage. For all three initial Pu concentrations and both temperatures, the Pu concentrations initially increase rapidly and then gradually reach a plateau. Although the intrinsic colloids dissolved at both temperatures, the intrinsic colloids dissolved at a faster rate at 80°C than at 25°C. Figure 3-4b shows that the dissolution at 80°C reached a plateau within ~80 days. However, intrinsic Pu colloids continue to dissolve during the period (90–104 days) at 25°C, but at a slower rate than in the first few weeks (Figure 3-4a). After 100 days, the total concentration of Pu dissolved at 25°C is less than at 80°C for a given Pu concentration. This demonstrates that the rate of Pu colloids dissolution increases with increasing temperature. When the concentration of PuO₂ colloids is below its solubility (10⁻¹¹ M), we would expect that the intrinsic colloids dissolve than when the total Pu concentration exceeds the solubility (10⁻⁷ M) of Pu colloids. This is what we observed at elevated temperature. At room temperature, the dissolution rate is may be too slow to observe the total dissolution within our 100 day time frame. When the initial concentrations of Pu approached or exceeded solubility (10⁻⁹ and 10⁻⁷ M), a much smaller fraction of intrinsic colloids dissolved. (Figure 3-4).

By comparing the behavior of intrinsic Pu colloids in the presence versus the absence of clay colloids (Figure 3-5), it is clear that the dissolution of the intrinsic colloids is facilitated by the presence of clay. Montmorillonite provides a “sink” for aqueous Pu which creates a strong gradient for the dissolution of colloidal Pu. Pu sorption onto montmorillonite results in the formation of Pu-montmorillonite pseudocolloids. Thus, the results indicate that Pu-montmorillonite pseudocolloids may be more stable

than Pu intrinsic colloids when concentrations drop below Pu solubility. At higher temperatures, the rate of dissolution is increased.

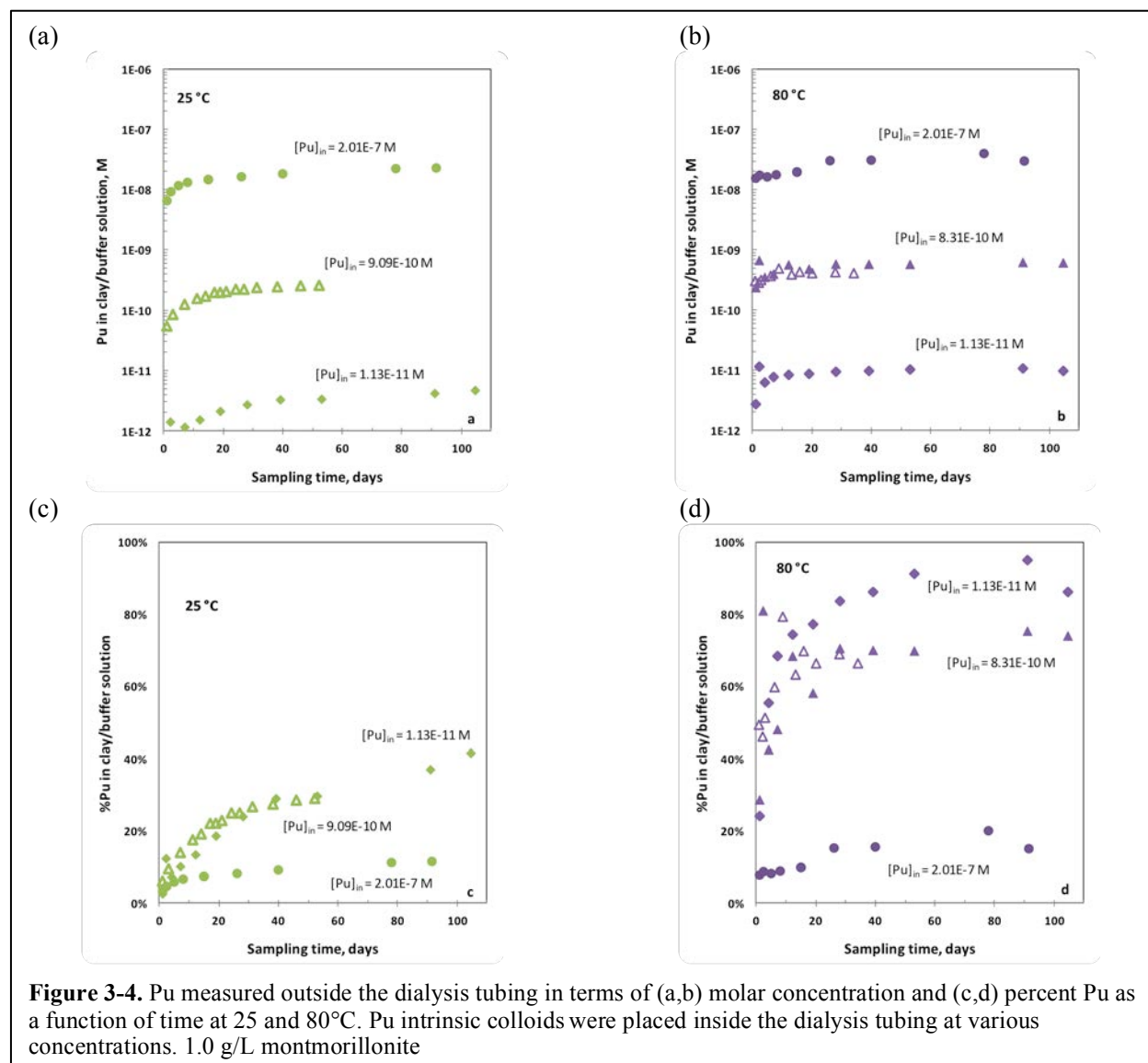


Figure 3-4. Pu measured outside the dialysis tubing in terms of (a,b) molar concentration and (c,d) percent Pu as a function of time at 25 and 80°C. Pu intrinsic colloids were placed inside the dialysis tubing at various concentrations. 1.0 g/L montmorillonite

3.4.3 Aqueous Pu(IV) sorption onto montmorillonite at 25 °C and 80 °C

To test our experimental design and evaluate how the initial state of Pu (colloidal versus aqueous) affects sorption kinetics on montmorillonite, dialysis experiments were performed using aqueous Pu(IV). In this case, the kinetics of Pu sorption to montmorillonite may be controlled by Pu(IV) diffusion across the membrane and/or Pu(IV) sorption onto the clay. However, based on the 3H and Pu(V) spiked blank experiments, diffusion rates for our experimental design are very fast (hours).

At the Pu(IV) concentrations substantially below solubility of $PuO_2(am, hyd.)$ (i.e. $5.93E-12 M$, Table 3-1), potential precipitation of $PuO_2(am, hyd.)$ or formation of colloidal PuO_2 is essentially eliminated. Therefore, quantitative diffusion of Pu(IV) and sorption to montmorillonite is expected. This is

experimentally in the 80°C data (Figure 3.6b). At 25°C, only 60% of the Pu(IV) is associated with montmorillonite at 100 days (Figure 3-6a). Nearly complete loss of Pu from the aqueous phase in the absence of clay at 25°C spiked blank solutions suggests that sorption to container walls and dialysis membrane effectively competes with montmorillonite for the sorption of Pu.

At Pu(IV) concentrations that approach $\text{PuO}_2(\text{am, hyd.})$ solubility, formation of colloidal PuO_2 cannot be ruled out. Indeed, after termination of sorption experiments, the Pu(IV) solution inside the dialysis tubes was analyzed for both aqueous and colloidal Pu species and Pu colloids were detected. A more detailed understanding of conditions under which colloidal Pu may form is warranted.

The kinetics of aqueous Pu(IV) sorption to montmorillonite at 25°C are faster than that in the colloidal PuO_2 experiments (Fig. 3-4c). Therefore, we conclude that PuO_2 dissolution is the rate limiting step in our

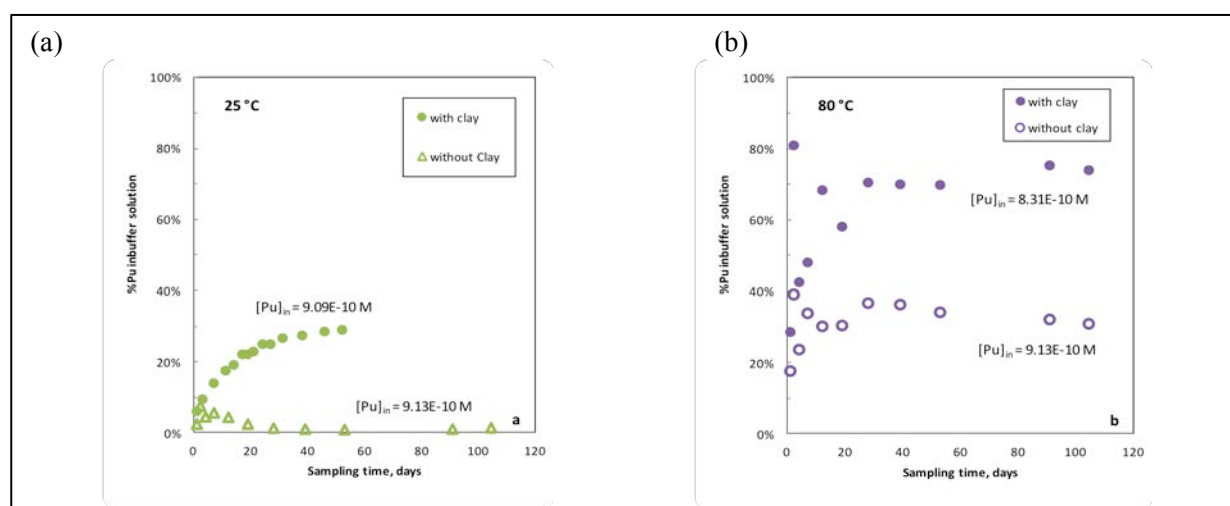


Figure 3-5. Pu measured outside the dialysis tubing at (a) 25°C and (b) 80°C as a function of time. Pu intrinsic colloids were placed inside the dialysis tubing. Comparison of montmorillonite-free (open circles) and 1.0 g/L montmorillonite (filled circles) experiments.

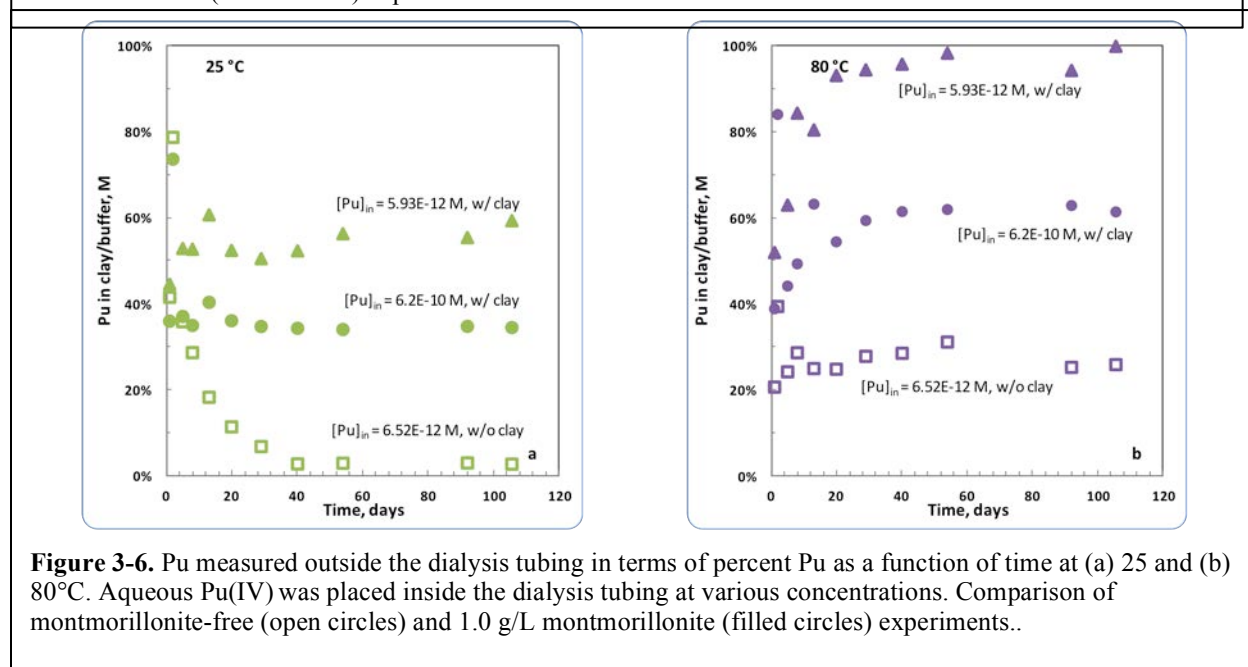


Figure 3-6. Pu measured outside the dialysis tubing in terms of percent Pu as a function of time at (a) 25 and (b) 80°C. Aqueous Pu(IV) was placed inside the dialysis tubing at various concentrations. Comparison of montmorillonite-free (open circles) and 1.0 g/L montmorillonite (filled circles) experiments..

dialysis system at room temperature.

The kinetics of aqueous Pu(IV) sorption to montmorillonite at 80°C, however, are very similar to what we observed in the colloidal PuO₂ experiments. On the timescale examined here, it appears that dissolution of colloidal PuO₂ at 80°C is fast.

3.4.4 Temperature effects on the sorption K_d

In all Pu-montmorillonite sorption experiments, both aqueous and total Pu was measured in the clay suspensions. These data are used to evaluate the sorption of Pu on montmorillonite (Figure 3-7) as a function of temperature. The results indicate that the affinity of Pu for montmorillonite increases with temperature. As a result, the K_d increases with temperature.

This result suggests that sorption of Pu on montmorillonite clay minerals is endothermic. In fact, we also observed this endothermic character in our previous Pu-goethite sorption experiments (see Chapter 2 of this report). Investigations that evaluate the temperature effects on actinides sorption onto minerals are scarce. However, this type of thermodynamic data is important to help us understand behavior of actinides interactions with minerals at near-field conditions near radiological waste repositories.

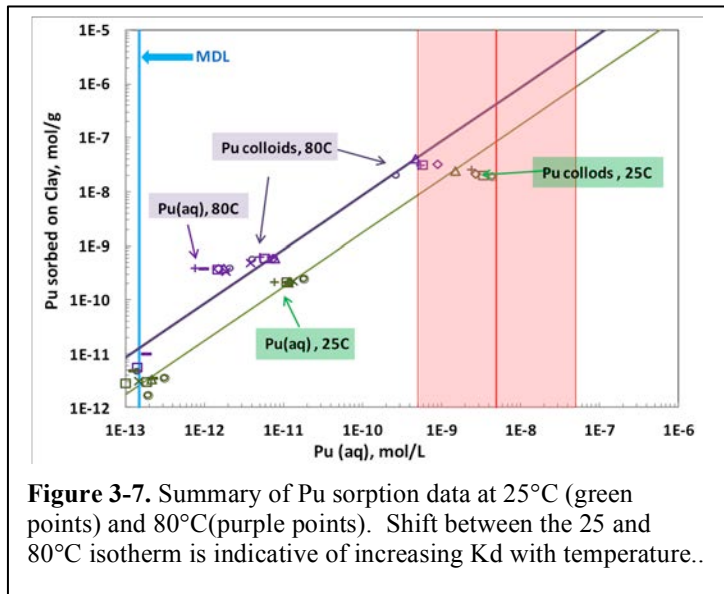


Figure 3-7. Summary of Pu sorption data at 25°C (green points) and 80°C (purple points). Shift between the 25 and 80°C isotherm is indicative of increasing K_d with temperature..

3.5 Conclusions

In this study, we have examined the stability of Pu intrinsic colloids in the presence of montmorillonite at 25 and 80 °C under atmospheric conditions. Dialysis membranes were used to segregate Pu intrinsic nano-colloids (2–5 nm) from montmorillonite colloids (>100 nm) and allow Pu aquo (<1 nm) species to establish equilibrium between both colloidal phases. Intrinsic Pu colloids were found to dissolve quickly, particularly when a strong thermodynamic gradient is provided (i.e., Pu sorption to montmorillonite). At 25°C, the dissolution of colloidal Pu is the rate limiting step in the dissolution-sorption process. Nevertheless, formation and dissolution of intrinsic PuO₂ colloids appears to be reversible. Pu colloid dissolution rates and the affinity for montmorillonite increase with temperature. The formation of Pu-montmorillonite pseudocolloids is favored over Pu intrinsic colloids at both temperatures. The reversible nature and relatively fast dissolution rates suggest that migration of Pu intrinsic colloids may be limited. However, the nature and form of Pu colloids and its associated stability can vary depending on the conditions under which they were formed. As a result, while these data suggest that migration of Pu intrinsic colloids may be limited, a broad survey of Pu colloid stability as a function of aging and crystallinity is warranted.

3.6 References

- Bertetti, F. P., Pabalan, R. T., and Almendarez, M. G., 1998. Studies on neptunium(V) sorption on quartz, clinoptilolite, montmorillonite, and α -alumina. In: Jenne, E. A. (Ed.), *Adsorption of Metals by Geomedia*. Academic Press, San Diego.
- Kaszuba, J. P. and Runde, W. H., 1999. The aqueous geochemistry of neptunium: Dynamic control of soluble concentrations with applications to nuclear waste disposal. *Environ Sci Technol* **33**, pp. 4427–4433.
- Keeney-Kennicutt, W. L. and Morse, J. W., 1985. The redox chemistry of Pu(V)O_2^+ interaction with common mineral surfaces in dilute solutions and seawater. *Geochim. Cosmochim. Acta* **49**, pp. 2577–2588.
- Kersting, A. B., Efurud, D. W., Finnegan, D. L., Rokop, D. J., Smith, D. K., and Thompson, J. L., 1999. Migration of plutonium in ground water at the Nevada Test Site. *Nature* **397**, pp. 56–59.
- Kim, J.I., 1991. Actinide colloid generation in groundwater. *Radiochimica Acta*, 52/53: pp. 71–81.
- Kozai, N., Ohnuko, T., Matsumoto, J., Banba, T., and Ito, Y., 1996. A study of the specific sorption of neptunium(V) on smectite in low pH solution. *Radiochim. Acta* **75**, pp. 149–158.
- Kozai, N., Ohnuky, T., and Muraoka, S., 1993. Sorption characteristics of neptunium by sodium-smectite. *J. Nuclear Sci. Tech.* **30**, pp. 1153–1159.
- Lujanienė, G., Motiejunas, S., and Sapolaite, J., 2007. Sorption of Cs, Pu and Am on clay minerals. *Journal of Radioanalytical and Nuclear Chemistry* **274**, pp. 345–353.
- Management, O. o. C. R. W., 2002. Yucca Mountain Science and Engineering Report: Technical Information Supporting Site Recommendation Consideration. U.S. Department of Energy.
- Neck, V., Altmair, M., Seibert, A., Yun, J. I., Marquardt, C. M., and Fanghanel, T., 2007. Solubility and redox reactions of Pu(IV) hydrous oxide: Evidence for the formation of $\text{PuO}_2 \cdot x(\text{s, hyd})$. *Radiochimica Acta* **95**, pp. 193–207.
- Novikov, A. P., Kalmykov, S. N., Utsunomiya, S., Ewing, R. C., Horreard, F., Merkulov, A., Clark, S. B., Tkachev, V. V., and Myasoedov, B. F., 2006. Colloid transport of plutonium in the far-field of the Mayak Production Association, Russia. *Science* **314**, pp. 638–641.
- Powell, B. A., Fjeld, R. A., Kaplan, D. I., Coates, J. T., and Serkiz, S. M., 2004. Pu(V)O_2^+ adsorption and reduction by synthetic magnetite (Fe_3O_4). *Environmental Science & Technology* **38**, pp. 6016–6024.
- Powell, B. A., Fjeld, R. A., Kaplan, D. I., Coates, J. T., and Serkiz, S. M., 2005. Pu(V)O_2^+ adsorption and reduction by synthetic hematite and goethite. *Environmental Science & Technology* **39**, pp. 2107–2114.
- Powell, B. A., Kersting, A. B., and Zavarin, M., 2008. Sorption and Desorption Rates of Neptunium and Plutonium on Goethite. In: Zavarin, M., Kersting, A. B., Lindvall, R. E., and Rose, T. P. Eds.), *Hydrologic Resources Management Program and Underground Test Area Project, FY 2006 Progress Report*. Lawrence Livermore National Laboratory, Livermore, CA.
- Sabodina, M. N., Kalmykov, S. N., Sapozhnikov, Y. A., and Zkharova, E. V., 2006. Neptunium, plutonium and ^{137}Cs sorption by bentonite clays and their speciation in pore waters. *J. Radioanal. Nucl. Chem.* **270**, pp. 349–355.
- Sanchez, A. L., Murray, J. W., and Sibley, T. H., 1985. The adsorption of plutonium IV and V on goethite. *Geochim. Cosmochim. Acta* **49**, pp. 2297–2307.
- Schwertmann, U. and Cornell, R., M., 1991. *Iron oxides in the laboratory: preparation and characterization*. VCH Verlagsgesellschaft mbH, Weinheim.
- Turner, D. R., Pabalan, R. T., and Bertetti, F. P., 1998. Neptunium(V) sorption on montmorillonite: An experimental and surface complexation modeling study. *Clays and Clay Minerals* **46**, pp. 256–269.

- Xu, C., Santschi, P. H., Zhong, J. Y., Hatcher, P. G., Francis, A. J., Dodge, C. J., A., R. K., Hung, C. C., and Honeyman, B. D., 2006. Colloidal Cutin-Like Substances Cross-Linked to Siderophore Decomposition Products Mobilizing Plutonium from Contaminated Soils. *Env. Sci. & Tech* **42**, pp. 211–216.
- Zavarin, M., Powell, B. A., Bourbin, M., Zhao, P., and Kersting, A. B., submitted. Np(V) and Pu(V) Sorption to Montmorillonite as a Function of Ionic Strength, pH, and Time. *Environ. Sci. Tech.*

Chapter 4. Quantifying Weak Interactions between Iodide and Clay Minerals

4.1 Introduction

Clays will play an important role in nuclear waste isolation. Besides being ubiquitous in natural systems, clay minerals may also be used as backfill or sealant material and may be the host rock surrounding the engineered disposal gallery. The major advantages of clays are their low permeability and high sorption capacities. Much of the sorption capacity stems from the fixed negative charge present on the basal surface of clay minerals. This negatively charged surface presents a large number of sorption sites for cations but repels anions. The repellent behavior has led to treating anions as non-reactive and thus highly mobile in the performance assessment of nuclear waste repositories. This assumption translates into anions being the largest dose contributors at times >10,000 years for clay-based repositories. However, literature data shows that many anions, including iodine, are retarded in clays relative to tritiated water. Tritiated water is assumed to act similarly to pore water and is the ultimate non-reactive tracer. It is assumed that the anion retardation occurs due to sorption, which is often quantified with a K_D value. These values are small; iodide K_D values have been reported from ~0.001 to 2.9 mL/g (Miller and Wang, 2012). While small, the assumption that the iodide will behave conservatively overestimates iodine dose in performance assessment analysis. Furthermore, constraining the mechanism of iodine uptake to clays may allow for material development with much larger retardation of iodine. Currently, little headway has been made with respect to understanding how a negatively charged ion interacts with a negatively charged surface.

Understanding iodine interactions with clays is hampered by two main complicating factors. First, since the total amount of interaction is relatively low, it is hard to reliably detect. To circumvent this issue, high solid:solution ratios are typically used in batch experiments and radiotracers are used to improve detection limits. The use of radiotracers is the second complicating factor, as the oxidation state of iodine in radiotracers is not always known. Recent experimentation has shown that the oxidation state in radioiodine stocks can be mixed (typically iodide (-1) and iodate (+5) are present), and that the observed iodine interactions with clays depends strongly on the redox state of iodine (Glaus et al., 2008). Gamma detection for radioiodine cannot distinguish oxidation state. Because of these two experimental issues, literature interpretations of iodine interactions with clays are often contradictory (Claret et al., 2010). In diffusive columns, iodide, when purposefully separated from iodate, has been shown to act similarly to chloride. In other diffusive systems, unpurified radioiodine appears to be retarded relative to chloride (Tournassat et al., 2007). Iodine oxidation state has also been shown to change upon contact with clay minerals (Glaus et al., 2008). Because of the conflicting information and experimental artifacts, delineating uptake mechanisms from available data is difficult.

A final issue with available data is that iodine uptake studies, batch or diffusive columns, most often use a single clay mineral. Because they are the target minerals for backfill or host rock for certain international waste programs, most nuclear-waste-related experiments to date include only illite and montmorillonite. A few also include kaolinite as a 'simpler' analogue. From an experimental perspective, this is advantageous as it simplifies the amount of clay purifications that are necessary. It also follows the traditional aspect of sorption studies used to examine ion exchange and surface complexation reactions. However, the use of a single clay forces interpretation of uptake within the confines of classical clay surface chemistry. It removes the ability to compare uptake as a function of other known clay characteristics, including fixed charge, distinguishing contributions of fixed from amphoteric charge contributions, structural characteristics of clay minerals, and variable pore scale chemistry caused by constrained space within the clay mineral.

In this study, iodide uptake experiments to seven different clay minerals are completed. Each of these minerals is characterized using BET surface area. Edge protonation state distributions are studied on all seven clay minerals through surface titrations, and fixed charge is characterized by cation exchange capacity (CEC) determinations. Iodide uptake was determined through batch experimentation using a wide range of swamping symmetric electrolyte identity and concentrations. Iodide uptake is clearly linked to cation exchange capacity. It appears that the iodide is concentrating in the interlayer spaces of the clays, which is specifically contraindicated from classical clay surface chemistry. Contrary to literature discussion, the data collected here is pointing to an uptake mechanism that is not based on a traditional surface interaction (i.e., ion exchange and surface complexation). Instead, iodide uptake appears to be related to the amount of fixed surface charge and to the physical structure of the clay. Uptake is inferred to occur due to the unique nano-environments formed from the combination of fixed charge and structurally constrained space.

4.2 Experimental Methods

4.2.1 Clay minerals and purification

The clays used all originate from the Clay Mineral Society source clays project at Purdue University. Seven total clays were used: kaolinite, ripidolite, illite, montmorillonite, palygorskite, sepiolite, and a 70/30 illite/smectite mixed layer (ID numbers KGa-1b, CCa-2, IMt-1, SWy-2, PFI-1, SepNev-1, and ISCz-1, respectively). The clays used were relatively pure; however, for several of the clays, purification steps were required to remove certain impurities. The main purification step used for all of the clays was mechanical separation at 75 microns. The <75-micron size fraction was used in all the experiments presented here. Each clay was examined by XRD for impurities. The kaolinite, sepiolite, and ripidolite did not have any measurable impurity minerals. All of the other clays had measurable amounts of quartz. There were no other clearly identifiable oxides or carbonates. The best match to the illite spectra was muscovite, although due to the small degree of crystallinity, the spectra peaks were small. The XRD spectra for the illite/smectite mixed layer clay most closely resembled pure illite, although the match was not exact.

In initial titration experiments, described below, the illite and montmorillonite samples showed significant buffer capacity around pH 8.3. It was assumed that this was a calcite impurity, as the initial titration curves were significantly different from other published sources. To remove the calcite, these two clays were washed and converted to the sodium form with ion exchange and centrifugation. Both clays were mixed with a 0.1M NaCl solution overnight. For illite, a single centrifugation for 60 minutes at 4400g was sufficient to pelletize the clay. The montmorillonite often required several centrifuge cycles (6–7 hours). Once a pellet was formed, the solution was decanted and discarded, and fresh NaCl solution was added. The mixing and centrifugation processes were repeated. The entire process was repeated two more times with DI water. Once the clays were washed, they were dried in a 100°C oven for several days. This exchange method was also used to convert the clays for CEC determinations described below.

4.2.2 Titration experiments

The surface titration of the clays was completed with a Mettler Toledo DL55. For each analysis, 1 g of clay mineral was added to 50 mls of the swamping electrolyte. Electrolytes used were 0.01, 0.1, and 0.5M NaCl solutions. The solution was constantly sparged with nitrogen to exclude atmospheric carbon dioxide. Upon addition of the clay, the solution was stirred and sparged until the pH stabilized. This generally took 10–30 minutes. Titrations were separated at the natural pH of the clay in the electrolyte. For each ionic strength, one clay sample was titrated up to pH 10.5 (base leg), while a separate sample was titrated down to pH 2.5 (acid leg). The titrants were 0.1M HCl or 0.1M NaOH. The NaOH solution

was always made immediately before use to minimize CO₂ dissolution. The titrants were added in 0.1-mL increments. Between additions, the rate of pH change was < 0.02 pH unit/second for seven seconds. The results from the two legs were combined to create the entire titration curve. Blank titrations and titrations of a commercial AIO powder were also completed. Because of the smaller surface area of the AIO powder, 5 g of material had to be used instead of 1 g. The longest titrations required about 20 hours to complete, while the shortest required only 10 to 20 minutes. The titrations were completed in triplicate, and the averaged response is shown below.

4.2.3 CEC determination

The method used follows that of (Kahr and Madsen, 1995). This method requires that the clays be in the sodium exchanged form. This was completed for all of the clays through ion exchange and centrifugation, described above. To determine CEC, an increasing ratio of methylene blue to clay was added. For all of the clays except montmorillonite, this was completed by adding a fixed mass of clay (0.2 g) and variable concentrations of methylene blue (up to 1E-2 M). For montmorillonite, the large CEC value required smaller masses of clay (down to 0.02 g) to increase the ratio of methylene blue to clay. Initial experimentation showed minimal methylene blue wall sorption in the 15-mL centrifuge tubes used for the reaction. The clay/methylene blue mixture was mixed for 4 hours. At the end of four hours, the suspension was centrifuged at 2600g until a sample could be removed from the supernatant. This required between 1 and 4 hours depending on the clay. Methylene blue was quantified using a spectrophotometer at 670 nm. Sorption isotherms were created plotting the amount of methylene blue sorbed vs. the amount added. Deviation from a 1:1 line demarcated the endpoint, and the CEC was interpolated from the plot. An example figure is shown for ripidolite in Figure 4-1.

4.2.4 Iodide sorption experiments

Batch iodide-sorption experiments were completed in triplicate for all of the clay minerals. The only purification step performed on the clays was dry-sieving at 75 microns. The < 75-micron fraction was used. A constant iodide concentration of 3.94E-4 M (50mg/L) was used for all of the batch reactors. For each set of experiments, the ionic composition and concentration of the swamping electrolyte was held constant. The electrolytes and concentrations used are shown in Table 4-1. A constant solid:solution ratio of 100g/L was used in all of the experiments.

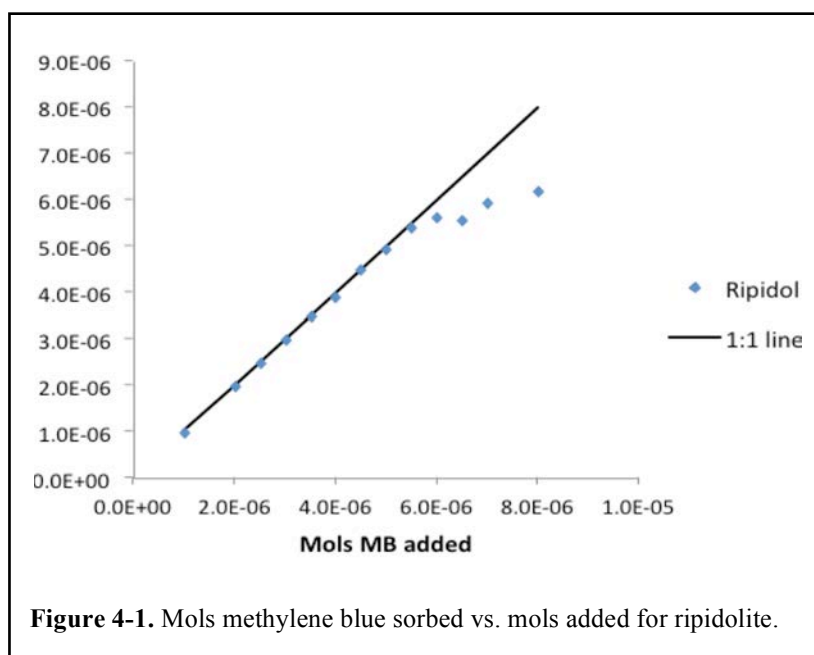


Figure 4-1. Mols methylene blue sorbed vs. mols added for ripidolite.

Table 4-1. Experimental summary of electrolytes and concentrations. An X denotes which were used in these experiments.

Concentration (M)	NaCl	NaBr	KCl
1.0	X		
0.1	X	X	X
0.01	X		

The batch reactors were 50-mL centrifuge tubes. Blanks confirmed the absence of wall sorption or iodide loss to volatilization. To each tube, the clay and electrolyte solution was added, and the suspensions were equilibrated overnight. An iodide spike was added after equilibration. The spike was an ion chromatography iodide standard with no detectable iodate. The batch reactors were mixed in the dark at room temperature for seven days in a horizontal position on a shaker table. After seven days, the samples were centrifuged for 1 hour at 4400g. The supernatant was removed with a pipette and refrigerated for analysis. The pH was measured immediately before the iodide spike was added, and again at the end of the seven-day mixing period both before and after centrifuging. No attempt was made to keep the pH constant or at a specific level. The pH reported is the equilibrium pH for the given clay minerals in the specified electrolyte. After the uptake sample had been removed, an equal amount of DI water was added to the vial. The slurry was mixed for four days. At the end of four days the sample was centrifuged as above, and a sample was removed for analysis. This sample represents a reversal of the uptake process, and gives information regarding the oxidation state of the iodine species after uptake.

The samples were analyzed using a Dionex 1100 ion chromatograph (IC) with an AS23 guard and analytical column, and a bicarbonate/carbonate eluent. Methods were developed to simultaneously measure iodide and iodate.

4.3 Results

4.3.1 pKa distributions

Surface charge of clay minerals (σ_0) can be calculated from the titration curves using equation 4-1 (Wang et al., 2007),

$$\sigma_0 = \frac{(C_A - C_B + [\text{OH}^-] - [\text{H}^+])F}{S_a} \quad (4-1)$$

where C_A and C_B are the concentrations of acid and base needed to attain a specific pH on the titration curve, $[\text{OH}^-]$ and $[\text{H}^+]$ are the OH^- and H^+ concentrations, F is the Faraday constant (96,490 C/mol), and S_a is the surface area of the clay mineral. In performing these calculations, the measured BET surface area was used. In the case of clays, this method does not give total surface charge as it does not take into account the fixed charge of the clay surfaces. More accurately, this method quantifies the total amount of proton sorption to the clay, and converts this to sorbed proton charge. Assuming that the protons exhibit Langmuirian behavior, the protonation state of clays (Q) can be calculated and related to the binding site distribution ($f(\text{pK})$), and the acidity constants (pK) by equation 4-2,

$$Q = \int_{\text{pK}_{min}}^{\text{pK}_{max}} \frac{f(\text{pK})}{1 + 10^{-\text{pK} + \text{pH}}} d(\text{pK}) \quad (4-2)$$

Q is calculated from the titration curves, and the distribution of acidity constants is calculated from deconvolution of equation 4-2 with the condensation approximation (equation 4-3),

$$f(pK) \approx \frac{dQ}{dpH} \quad (4-3)$$

The calculated distribution of sites is presented using a five-point smoothing window. The individual distributions are shown in Figures 4-2 and 4-3 (following pages).

For many of the clays and for the AIO material, the behavior of the pK distributions was erratic at pH<4 and >10. It is suspected that dissolution of the minerals was occurring, which interferes with the titration process. The results and discussion here are restricted to pH values between 4 and 10. The pK values are read directly from the plots; pK values correspond to the peaks in the curves. For example, the AIO plot has two distinct peaks at pH 4.7 and 7.5 for both 0.01M and 0.1M NaCl concentrations. When the ionic strength is at 0.5M, other peaks may be present. A major point from these curves, which is elaborated below, is that for changing ionic strengths, the AIO peaks are largely invariant. For nearly all of the clay minerals, there are significant changes as a function of ionic strength. For some clays it appears that the increase in ionic strength diminishes surface proton activity by suppressing the peaks (e.g., ripidolite). In others it appears that more peaks are present with increasing ionic strength (e.g., palygorskite). And in others the number of peaks is similar, but the pK value is shifted (e.g., illite/smectite mixed layer).

4.3.2 CEC and surface area

Table 4-2 shows the results of the methylene blue experiments. Besides direct determination of CEC, methylene blue also allows for the calculation of surface area assuming monolayer sorption and a molecular area of 130 Å². Generally methylene blue surface areas are higher than BET surface area determinations. Also, the discrepancy increases as the CEC increases. The classical interpretation is that the BET surface area represents only the ‘external’ surface area of a clay; the interlayer space is inaccessible to the nitrogen molecules. Because the methylene blue determinations take place in aqueous suspension, it is assumed that the clays can delaminate, and the methylene blue surface area is more representative of the ‘total’ surface area of a clay. The difference between them is the interlayer area. All of these surface areas are reported in Table 4-2. Sepiolite is the one exception to the general behavior. The BET surface area was larger than the methylene blue surface area. This leads to the physically meaningless negative internal surface area shown in Table 4-2.

Table 4-2. CEC and surface area values for the clays used. Surface-area determination methods are explained in the text.

	CEC (meq/100g)	BET S.A. (m ² /g)	Total S.A. (m ² /g)	Internal S.A. (m ² /g)
Kaolinite	1.50	11.31	11.76	0.45
Ripidolite	3.00	8.02	23.49	15.47
Illite	14.98	31.46	117.21	85.76
Illite/Smectite	24.69	29.82	193.23	163.41
Montmorillonite	109.53	28.29	857.17	828.88
Sepiolite	17.41	201.43	136.27	-65.16
Palygorskite	39.96	141.52	625.45	483.93

4.3.3 Iodide batch uptake experiments

Tables 4-3 and 4-4 show the pH values at the different points in the experiments. Table 4-3 shows the pH values for equimolar electrolyte concentrations but varying electrolyte identities. Table 4-4 shows the pH values for varying concentrations of NaCl electrolytes. In general the values are somewhat bimodal, being centered around pH 4 or pH 8. During the course of mixing, the pH changed only slightly, typically decreasing within ~0.2 pH units. Centrifuging caused larger shifts in pH, the largest being 0.98 pH units for the KCl electrolyte experiments with ripidolite. Differences between equimolar electrolytes are fairly small suggesting similar Na^+/H^+ and K^+/H^+ exchange constants. With increasing sodium concentration, the pH decreases consistent with Na^+ exchange for H^+ on the basal surfaces of the clays.

Because solid:solution ratio and added iodide were consistent across the experiments, the removals are shown as a percent in Tables 4-5 and 4-6. Table 4-5 shows the percent removal as a function of electrolyte, and Table 4-6 shows the percent removal as a function of NaCl concentration. Negative values are most likely caused by anion exclusion due to the fixed negative charge of the clay interface. Generally removals decrease as a function of increasing CEC. However, palygorskite and sepiolite act significantly different than the other clays, which is discussed in detail below. For equimolar concentrations, NaCl has the highest removals, followed by NaBr and then KCl. The relative standard deviations were generally quite good. IC instrumental variation alone has been estimated at about 2%. For several of the more egregious RSD values, more replicates are currently being performed.

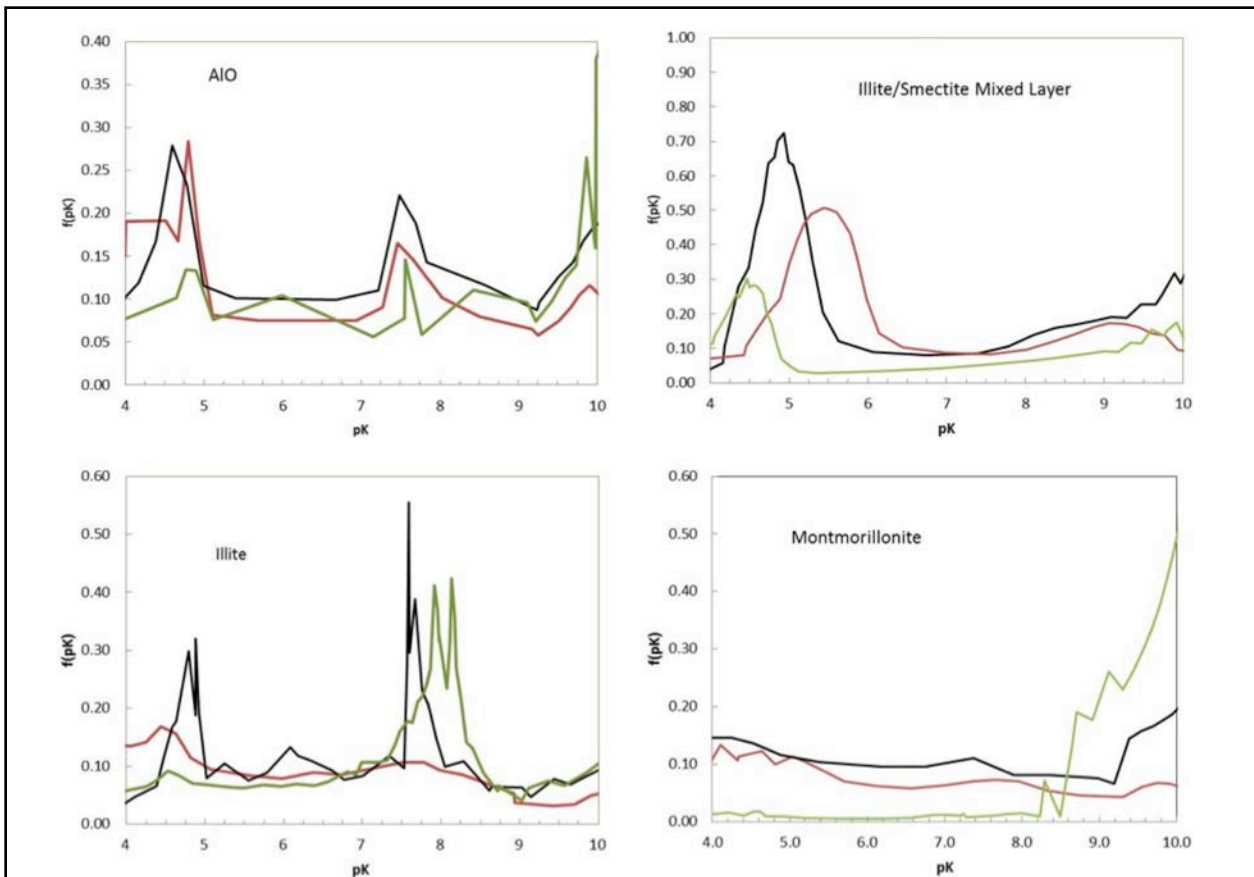


Figure 4-2. pK_a distributions for AIO, illite, illite/smectite mixed layer, and montmorillonite. The red, black, and green lines represent 0.01M, 0.1M, and 0.5M NaCl, respectively.

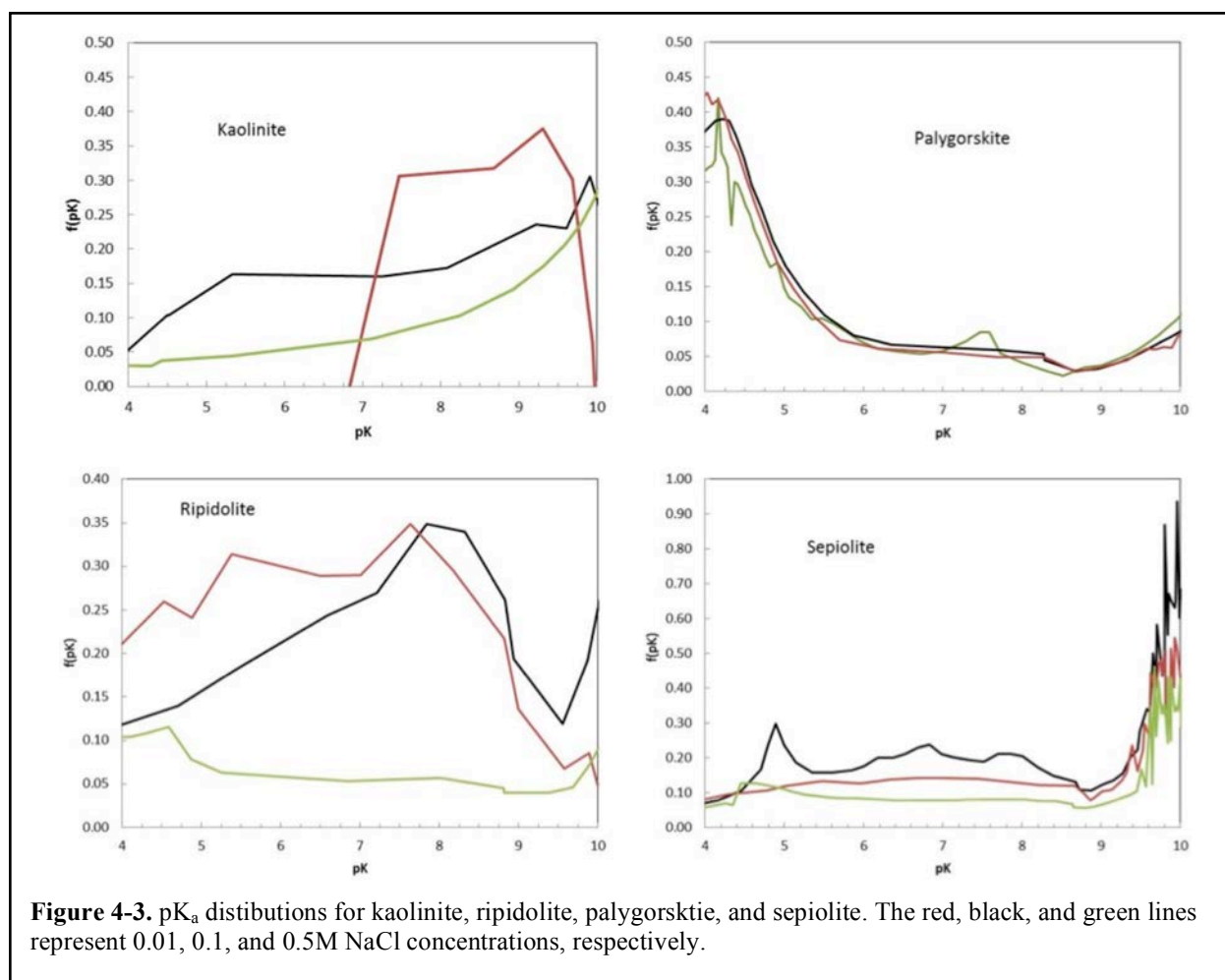


Figure 4-3. pK_a distributions for kaolinite, ripidolite, palygorskite, and sepiolite. The red, black, and green lines represent 0.01, 0.1, and 0.5M NaCl concentrations, respectively.

For experiments where the electrolyte identity was held constant and the concentration was variable, the iodide uptake behavior separates into two classes. Iodide uptake peaked at 0.1M NaCl concentrations for kaolinite, ripidolite, illite, illite/smectite, and sepiolite. Removals got progressively larger with increasing electrolyte concentration for montmorillonite and palygorskite.

4.4 Discussion

4.4.1 Titrations

Aluminum oxide acts as a simple model system in this series of experiments; it both confirms the methodological process and acts as a frame of reference for understanding the clay behaviors. As expected from surface complexation theory as well as other experiments and models, the pK_a values are largely invariant as a function of ionic strength. Small shifts may be attributable to changes in chemical potential as a function of ionic strength. This affect is not taken into account with the titration curve inversion method. It does appear that there may be other peaks starting to appear at the highest ionic strength studied, although there is no ready explanation for this behavior.

The clays have a much broader range of behaviors (Figures 4-2 and 4-3 above). Illite, illite/smectite mixed layer, and montmorillonite set up a continuum of minerals (smectite and montmorillonite are synonymous in this case). These three clays represent two mineral endmembers with an intermediate of

mixed composition. The major pK_a values for illite are centered at a pH of about 8 with smaller peaks at pH \sim 4.6. There also appears to be more pK_a peaks at 0.1M NaCl than at either 0.5 or 0.01M NaCl. The illite/smectite mixed layer has some of the most consistent behavior across the range of ionic strength. The major pK_a peak is ionic-strength-dependent. At low ionic strength it is centered at pH 5.5; at 0.1M ionic strength the peak is centered at pH 5; and at the highest ionic strength the peak is centered at pH 4.5. This peak shifting is far more extreme than was seen for the AIO material, so it can be surmised that the shift is caused by something other than changing EDL potential. Since the change in ionic strength corresponds with a change in the sodium concentration, this shift may be representative of the Na^+/H^+ exchange reaction. If this is the case, it is unclear why a similar reaction was not seen in the montmorillonite sample where Na^+/H^+ exchange would also be common. For montmorillonite, the pK_a distribution is not particularly remarkable. The surface appears proton neutral independent of ionic strength. At the highest ionic strength there appears to be a broad peak starting at pH 8 that does not return to 'baseline' in the experimental range; this may be attributable to the same mechanisms that cause similar noise at pH >10 . Despite the continuum of mineralogy, there is no consistency between the pK_a distributions of these three minerals. From the observable scale, the clay minerals seem to act independently; the illite/smectite behavior is not dominated by the contribution of either of the endmembers.

Table 4-3. pH values at different points in the experiment for equimolar electrolytes.

	0.1M Electrolyte								
	NaCl			NaBr			KCl		
	Before spike	Before Centrifuging	After Centrifuging	Before spike	Before Centrifuging	After Centrifuging	Before spike	Before Centrifuging	After Centrifuging
Kaolinite	4.23	4.21	4.39	4.43	4.47	4.28	4.18	4.12	4.07
Ripidolite	8.73	8.51	8.10	8.76	8.63	8.20	8.79	8.59	7.81
Illite	8.45	8.27	8.16	8.48	8.31	7.95	8.28	8.08	8.01
Illite/Smectite	4.00	4.06	4.24	4.22	4.26	4.03	3.91	3.85	3.82
Montmorillonite	8.15	8.05	8.05	8.19	8.14	8.05	8.09	8.03	7.90
Sepiolite	7.89	7.66	7.83	7.98	7.63	7.75	7.92	7.64	7.80
Palygorskite	7.98	7.76	7.90	8.05	7.84	7.82	7.84	7.63	7.87

Table 4-4. pH values at different points in the experiment for changing concentrations of NaCl electrolyte.

	NaCl Electrolyte								
	0.01M			0.1M			1.0M		
	Before spike	Before Centrifuging	After Centrifuging	Before spike	Before Centrifuging	After Centrifuging	Before spike	Before Centrifuging	After Centrifuging
Kaolinite	4.70	4.83	4.73	4.23	4.21	4.39	4.04	4.27	4.19
Ripidolite	8.79	8.57	8.15	8.73	8.51	8.10	8.74	8.59	8.37
Illite	8.68	8.46	8.30	8.45	8.27	8.16	8.37	8.22	7.87
Illite/Smectite	4.38	4.57	4.40	4.00	4.06	4.24	3.57	3.65	3.74
Montmorillonite	8.65	8.55	8.50	8.15	8.05	8.05	7.78	7.77	7.73
Sepiolite	7.92	7.64	7.83	7.89	7.66	7.83	7.78	7.50	7.71
Palygorskite	8.17	7.93	7.99	7.98	7.76	7.90	7.83	7.75	7.75

Table 4-5. Percent removal and percent relative standard deviation for iodide removal in 0.1M electrolytes.

	CEC	% removal			% RSD		
	meq/100g	NaCl	NaBr	KCl	NaCl	NaBr	KCl
Kaolinite	1.50	13.8	3.7	-0.1	2.4	6.5	2.2
Ripidolite	3.00	10.1	2.4	-3.2	3.4	7.6	1.8
Illite	14.98	4.6	1.3	-5.3	5.9	0.0	2.5
Illite.Smectite	24.69	3.6	-0.1	-5.1	0.7	1.1	1.1
Montmorillonite	109.53	-3.4	-6.1	-21.4	3.5	0.7	11.4
Sepiolite	17.41	0.1	7.3	1.0	2.8	1.3	2.9
Palygorskite	39.96	2.3	11.2	9.0	3.0	0.5	1.6

Table 4-6. Percent removals and percent relative standard deviation for iodide removal in varying concentrations of NaCl electrolyte.

	CEC	% removal			% RSD		
	meq/100g	0.01M	0.1M	1.0M	0.01M	0.1M	1.0M
Kaolinite	1.50	4.5	13.8	1.0	2.5	2.4	2.9
Ripidolite	3.00	1.3	10.1	4.2	2.1	3.4	1.6
Illite	14.98	-4.9	4.6	2.6	4.4	5.9	2.1
Illite.Smectite	24.69	-1.6	3.6	2.9	2.6	0.7	0.8
Montmorillonite	109.53	-15.9	-3.4	5.7	6.2	3.5	0.8
Sepiolite	17.41	5.6	0.1	-0.2	29.5	2.8	3.1
Palygorskite	39.96	-2.6	2.3	6.5	5.4	3.0	2.4

Kaolinite is proton neutral at both 0.5M and 0.1M NaCl values. At the 0.01M NaCl values, there is a broad peak ranging from pH 7 to 10. Ripidolite becomes progressively more proton neutral with increasing ionic strength. At the lowest ionic strength there are three potential peaks. At the intermediate ionic strength there is a single broad peak centered at pH 8.2, while at the highest ionic strength there is only a single discernible peak at pH 4.5. This type of behavior is consistent with a ‘masking’ of surface effects as a function of increasing ionic strength. The increased sodium may be dampening the effect of proton sorption.

Sepiolite and palygorskite are structurally similar minerals. Both are fibrous in nature but have differently sized pore spaces that allow for different amounts of associated water. They are also chemically distinct as palygorskite has structural aluminum, and sepiolite is a pure magnesium silicate. Unsurprisingly, their titration data are also quite distinct. Sepiolite appears proton neutral, except for a peak at pH 5 at 0.1M ionic strength. The noise at pH >9.5 continues as pH increases, which is attributed to dissolution. Palygorskite has similar behaviors independent of ionic strength. There is a large single peak at 4.2, and a smaller peak at pH 7.5 when ionic strength is 0.5M. The pK_a values of palygorskite are similar to those of the pure AlO. This was the anticipated result from all of the clays expect for sepiolite. All of the other clay minerals used have edge aluminol sites that may have similar behavior to the surface sites of AlO. The lack of pK_a peaks for the clay minerals means either that the overall differences between AlO and clay alters the acidity of the edge

aluminol sites so that they are no longer comparable (Brady et al., 1996), or that some other process besides surface protonation is dominating behavior (i.e., Na^+/H^+ exchange).

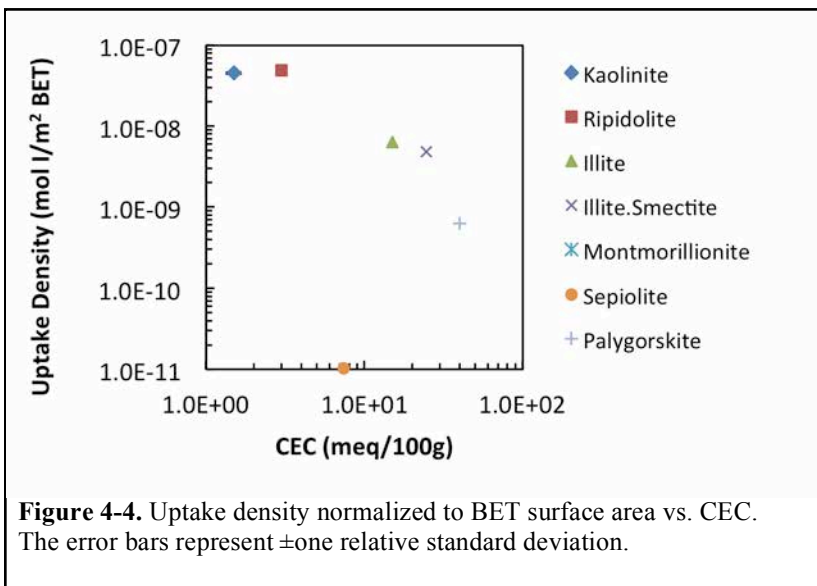
4.4.2 CEC and iodide uptake

The advantage of the experimental setup is that comparisons can be made between uptake and fundamental clay structures. Clays are layered aluminosilicates with discrete tetrahedral (Si-O) and octahedral (Al-O or Mg-O) layers. The physical layering and specific chemical identities within these layers and the smallest repeating unit of the clay layers all dictate clay mineral identity. The smallest repeating unit for kaolinite is two layers, one being tetrahedral, one being octahedral (1:1 clay). For illite, illite/smectite, and montmorillonite, the smallest repeating unit is an octahedral layer sandwiched between two tetrahedral layers (2:1 clay). Ripidolite is also a 2:1 clay, but the smallest repeating unit has an extra octahedral layer present between the 2:1 layering. All of these clays are layered clays, and can be physically represented at a larger scale by a stack of plates, where the interlayer space is the plane between the plates. Sepiolite and palygorskite are both fibrous clays. They both have a 2:1 repeating unit, but the individual plates invert in a regular pattern. Thus the interlayer space is long and columnar instead of being planar as in the layered clays. The void in palygorskite is slightly smaller than that of sepiolite. Using these physical descriptions, it is clear that the fibrous clays are behaving quite differently from the layered clays. In Table 4-5 the behaviors of the layered clays are inverted relative to the fibrous clays. When conditions allowed for large uptake in the layered clays, uptake was low in the fibrous clays. When uptake was small in the layered clays, it was larger in the fibrous clays. When NaCl was used, uptake in the fibrous clays was small independent of concentration. The differences between the clays imply an uptake mechanism dependent on the size and shape of the interlayer space.

To help develop a physical conceptual model of iodide interaction with the clay minerals, the molar uptake was normalized to the three different surface areas and plotted as a function of CEC (Figures 4-4 to 4-6). The figures shown are from the 0.1M NaCl experiments. Uptake can be expressed through equation 4-4,



where $\equiv X$ represents an exchange site on the clay surface, and $\equiv XI^-$ represents iodide that has been taken up by the clay surface. While this equation is identical in form to that typically used for cation exchange on clays, the use here is not intended to imply a mechanism. The $\equiv X$ site is more broadly representative of an unknown but surface-based interaction between iodide and the clay. Using this reaction as a guide to Figures 4-1 through 4-3, the CEC is analogous to $\equiv X$ (x-axis), and the iodine surface concentration is represented by the $\equiv XI^-$ (y-axis). Using equation 4, a linear log-log plot of surface concentration to CEC would be expected. When



normalized to BET (external) surface area, this is not the case. When normalized to the methylene blue (total) or internal surface area, the plots become more linear. Negative uptakes or surface area (internal sepiolite) do not plot in log-log space. The linear relationship implies an uptake mechanism associated with the total or interior surfaces of the clay, as opposed to the external surfaces of the clay. It also minimizes the possibility that the iodide is interacting with the edge sites through a traditional surface complexation formation mechanism. If the latter had been the case, the linear relationship would have been strongest when normalized to the BET surface area.

The interaction of iodide in the interlayer spaces is problematic if using the classical surface chemical interpretation of a clay surface. Using a classical interpretation, the data implies that negatively charged iodide is concentrating at the very surface where the fixed negative charge is located. Charge repulsion constraints dictate that this should not occur. When considering only the percent removals, the charge repulsion arguments would seem to hold.

Smaller CEC values (smaller fixed negative charge) have larger amounts of uptake. However, the surface charge characteristics should be identical for equimolar NaCl and NaBr experiments, yet the uptake is quite different. The data are pointing to a mechanism that is surface oriented, allows for negatively charged ions to approach a negatively charged surface, and changes as a function of salt concentration and identity. Model development is currently underway to mathematically interpret the observed behaviors. In general, processes being considered are the effects of constrained interlayer space on water behaviors and of the formation of ion pairs either in the interlayer or as part of a surface complex. Within the fixed-charge, nanostructured environment of clay minerals, water will orient as a function of charge. This orientation of water changes the dielectric properties, which in turn alters the effective hydration energies of ions. This change in dielectric properties favors more ion pair formation with increasing fixed

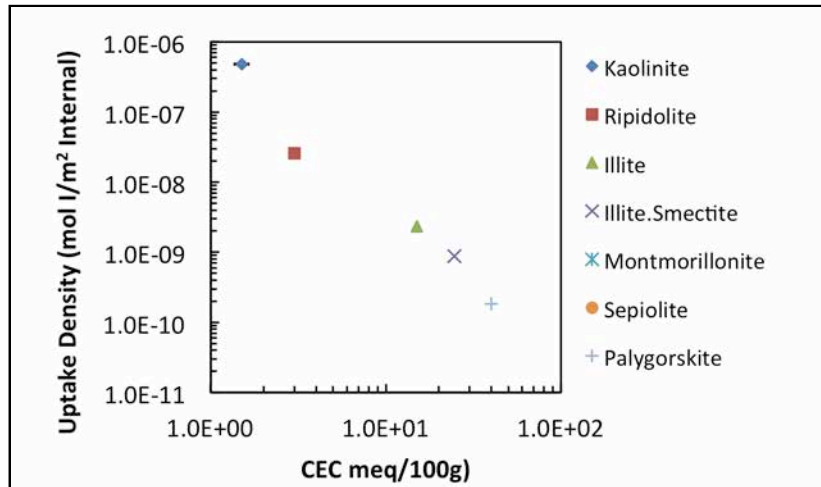


Figure 4-5. Uptake density normalized to internal surface area vs. CEC. The error bars represent plus/minus one relative standard deviation.

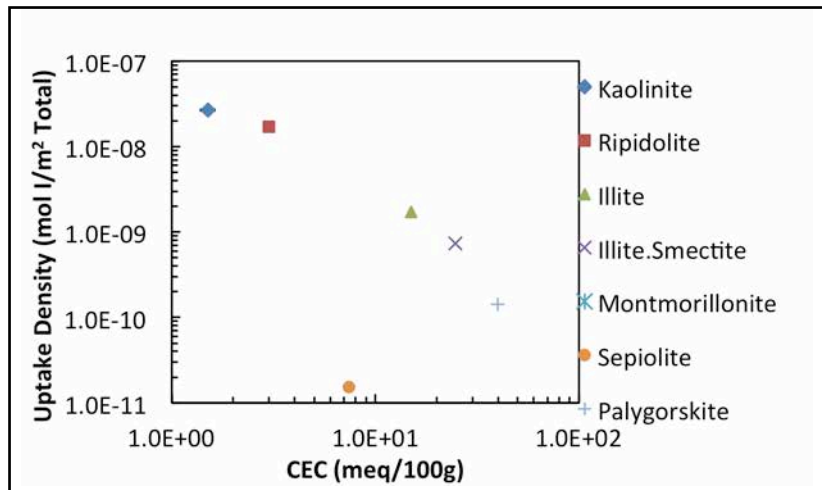


Figure 4-6. Uptake density normalized to total surface area vs. CEC. The error bars represent plus/minus one relative standard deviation.

surface charge. This conceptual model may explain the ability of iodide to concentrate in the interlayer. Instead of an anion, the iodide may be present as a neutral ion pair. Further, it may accumulate in the interlayer space as the ion pair formation is more favored in pore structures than it is in the bulk solution.

It cannot be stated with certainty, but it appears that the iodide remains as iodide and does not disproportionate to iodate for the studied conditions. IC analysis can separate these two ions. However, there is an unknown impurity in the clays that directly interferes with iodate quantitation. In desorption experiments, consisting of a four-day DI water rinse after the end of an iodide batch experiment, iodide was present in the wash water. For certain clays (e.g., kaolinite), the impurity was present in smaller amounts. In these clays we may be able to say for certain whether disproportionation occurred. In clays with larger amounts of the impurity, this may remain uncertain. Further data analysis is underway to determine what can be definitively concluded about iodate in these systems.

4.5 Conclusions and Future Work

In the literature, models describing clay protonation and sodium exchange are converging to a three-site, four-reaction model. One site and reaction is for Na^+/H^+ exchange; one site and two reactions are devoted to the amphoteric protonation of Al-O edge sites; and the third site and final reaction is the protonation of the Si-O edge sites. The inversion method used here to interpret the titration curves gives consistent information between theory and experiment for the Al-O. However for the clays, the behaviors were far more disparate than expected. Comparing the results to the theory just described, the expectation would have been four distinct peaks; three would have been independent of ionic strength, and the fourth would have shifted consistently with ionic strength. Clearly this is not what occurred. It is unclear what is causing this discrepancy between published results and those presented here.

The iodide removals as a function of ionic strength and composition merit mathematical interpretations. If successfully described through a model incorporating ion pair formation, this will represent a significant shift in discourse regarding anion interactions with clays. While the presence of ion pairing has been acknowledged in the literature (Appelo et al., 2010), it has rarely been applied to data. The implications of this ion pair formation may inform the imperfect membrane effect observed in heavily compacted clay systems (Tournassat and Appelo, 2011).

In the near future, quantitative descriptions of the observed iodide uptake will be developed. This idea will be further tested under diffusive conditions in compacted clay columns. The characteristic length of pore structures in clay systems shifts downward with increasing compaction. The increased compaction increases the proportion of nano-scale environments analogous to that of the interlayer space in the clays. It is expected that as compaction increases, so would ion-pair formation, but the amount of ion-pair formation would also still be affected by the fixed charge in the interlayer space. The diffusion experiments will include a matrix of clays and compaction stresses to directly probe this idea.

4.6 References

- Appelo, C.A.J., Van Loon, L.R., Wersin, P., 2010. Multicomponent diffusion of a suite of tracers (HTO, Cl, Br, I, Na, Sr, Cs) in a single sample of Opalinus Clay. *Geochim. Cosmochim. Acta* **74**, pp. 1201–1219.
- Brady, P.V., Cygan, R.T., Nagy, K.L., 1996. Molecular Controls on Kaolinite Surface Charge. *Journal of Colloid and Interface Science* **183**, pp. 356–364.
- Claret, F., Lerouge, C., Laurieux, T., Bizi, M., Conte, T., Ghestem, J.P., Wille, G., Sato, T., Gaucher, E.C., Giffaut, E., Tournassat, C., 2010. Natural iodine in a clay formation: Implications for iodine fate in geological disposals. *Geochim. Cosmochim. Acta* **74**, pp. 16–29.

- Glaus, M.A., Muller, W., Van Loon, L.R., 2008. Diffusion of iodide and iodate through Opalinus Clay: Monitoring of the redox state using an anion chromatographic technique. *Appl Geochem* **23**, pp. 3612–3619.
- Kahr, G., Madsen, F.T., 1995. Determination of the cation exchange capacity and the surface area of bentonite, illite and kaolinite by methylene blue adsorption. *Applied Clay Science* **9**, pp. 327–336.
- Miller, A.W., Wang, Y., 2012. Radionuclide Interaction with Clays in Dilute and Heavily Compacted Systems: A Critical Review. *Environ. Sci. Technol.* **46**, pp. 1981–1994.
- Tournassat, C., Appelo, C.A.J., 2011. Modelling approaches for anion-exclusion in compacted Na-bentonite. *Geochim. Cosmochim. Acta* **75**, pp. 3698–3710.
- Tournassat, C., Gaucher, E.C., Fattahi, M., Grambow, B., 2007. On the mobility and potential retention of iodine in the Callovian-Oxfordian formation. *Physics and Chemistry of the Earth* **32**, pp. 539–551.
- Wang, Y.F., Gao, H.Z., Yeredla, R., Xu, H.F., Abrecht, M., 2007. Control of pertechnetate sorption on activated carbon by surface functional groups. *Journal of Colloid and Interface Science* **305**, pp. 209–217.

Chapter 5. Laboratory Testing Complementing Grimsel Field Work: Conservative Tracer Screening and Preliminary Radionuclide Transport Experiments

5.1 Introduction

In FY 2012, two activities were conducted at Los Alamos National Laboratory (LANL) that complemented or supported field testing at the Grimsel Test Site in Switzerland, an underground research laboratory in fractured crystalline rock (see Chapter 6 for details of field testing conducted in 2011 and 2012). The first activity was a small tracer screening project that was conducted to evaluate sorption onto Grimsel granite and FEBEX bentonite of three different fluorescent dye tracers that could potentially be used simultaneously in field tests because of their different excitation and emission wavelengths. The goals of this project were to (1) evaluate whether any degradation or sorption of uranine (sodium fluorescein) occurred in synthetic Grimsel groundwater in the presence of the granite and bentonite, since unexplained loss of this tracer was observed in some of the 2011 field tests; (2) evaluate the sorption behavior of two fluorescent tracers that might be used simultaneously with uranine or possibly in lieu of uranine if uranine loss continued to be a problem in field experiments; and (3) evaluate the pH dependence of uranine fluorescence, and more importantly, the recovery of fluorescence after fluorescence loss at low pH, which could potentially explain the observed loss of uranine in the field tests. This activity was completed in early FY 2012, and the results are reported in their entirety here.

The second activity was just initiated in late April of 2012, and only very preliminary results are reported here. We had hoped to start this activity sooner, but it there was a delay in hiring staff to conduct this research. In this activity, Los Alamos is evaluating the sorption and desorption behavior of uranium (^{233}U) and neptunium (^{237}Np) onto/from Grimsel granite in a synthetic Grimsel groundwater. We designed a set of small-scale column experiments to interrogate uranium sorption and desorption rates in a more robust manner than has been previously done, but preliminary results indicated that there was essentially no measurable sorption of uranium onto the granite. We then conducted a small number of batch sorption experiments with neptunium and the same water and rock, and the results from these experiments indicated weak neptunium sorption that should be measurable in the small-scale column experiments. We have not yet initiated these experiments but will do so before this report is finalized.

5.2 Field Tracer Screening Experiments

The field tracer screening experiments introduced above are described in this section, including methods, results and interpretations of this completed study.

5.2.1 Materials and methods

5.2.1.1 Water, rock, and tracers

The groundwater used in all experiments was a synthetic Grimsel ground water (SGGW) with the recipe given in Table 5-1. The pH of the SGGW was prepared was 8.6, which agrees quite well with the field-measured pH at the Grimsel site (about 8.8). However, some experiments were conducted with the SGGW buffered to pH 6.8 by adding $\text{H}_2\text{PO}_4^-/\text{HPO}_4^{2-}$ as a buffer. The amount of phosphate added to achieve this buffering was not measured precisely, but it is estimated to have increased the ionic strength of the

Table 5-1. Synthetic Grimsel Groundwater Recipe.

Compound	g/L
Na_2SO_4	0.1440
KCl	0.0048
MgCO_3	0.0427
NaHCO_3	0.2733
CaCl_2	0.0130
H_4SiO_4	0.0341
pH	8.6-8.8

SGGW by a factor of 2 to 3 to overcome the buffering capacity of the carbonate/bicarbonate in the SGGW. The reason for conducting experiments at a pH of 6.8 was that it was believed that the pH in the field tracer injection loop may have dropped below 7 at times (for unknown reasons), so experiments at a pH of 6.8 would tell us whether uranine fluorescence decreases or sorption losses may have occurred in the field experiments in which the uranine mass could not be accounted for. Also, by conducting sorption experiments at a pH of 6.8, we could evaluate whether any of the other tracers screened might be susceptible to sorption at lower pHs.

The solids used for the experiments were provided by our Grimsel collaborators. These included:

- Crushed granite core from borehole CFM 11.002 at the Grimsel test site (avoiding the open fracture with the altered shear zone surfaces, since there was not enough of this material to include representatively in the tests) sieved to 75–500 μm .
- Gently crushed FEBEX bentonite sieved to less than 45 μm to exclude accessory minerals and intended to include only readily dispersible clay.

The granitic material was crushed and sieved at LANL. No characterization of the solids was conducted other than the size range provided by the sieving. However, quantitative x-ray diffraction (QXRD) analysis was conducted for the granite used in the radionuclide experiments described in Chapter 6, and the granite in the two sets of experiments should have been identical other than the batch for the fluorescent tracer experiments including one shear zone surface.

The three tracers evaluated in the laboratory tests and their initial concentrations in the sorption experiments were:

- Sodium fluorescein (uranine) - ~ 0.5 mg/L.
- Amino G acid (7-amino-1,3-naphthalenedisulfonic acid) - ~ 1 mg/L.
- Sodium 1,5-naphthalene disulfonate - ~ 1 mg/L.

The sodium fluorescein was from Fluka, Inc., the amino G acid was provided by our Grimsel collaborators (part of the stock they use for field experiments), and the 1,5 naphthalene disulfonate was provided by the University of Utah (shared through a mutual DOE geothermal tracer project).

5.2.1.2 Batch sorption experiments

All of the sorption experiments were conducted as batch experiments in 50-ml polycarbonate Oak Ridge centrifuge tubes. The experimental matrix was as follows:

- 20 reactors at pH 6.8 and 20 reactors at pH 8.6
- At each pH:
 - 5 controls with 10 ml water with all 3 tracers added, no granite or bentonite.
 - 5 reactors with 10 ml water + tracers, 25 mg bentonite, no granite.
 - 5 reactors with 16.5 ml water + tracers, 5 g granite, no bentonite.
 - 5 reactors with 16.5 ml water + tracers, 25 mg bentonite, 5 g granite.

Note that the 16.5 ml in the latter two sets of reactors included 15 ml of tracer solution + ~ 1.5 ml of residual SGGW from preconditioning the granite and bentonite for approximately one week before addition of the tracers. The bentonite in the bentonite-only reactors was also preconditioned, but in these reactors it was possible to remove essentially all the water before adding tracer solution. The solid-

solution separations were achieved using an IEC benchtop centrifuge run at ~6000 rpm for ~10 minutes, which was sufficient to obtain a good separation of both the granite and bentonite. This separation procedure was also used to separate solids and solutions to sample the solution phase during the batch sorption experiments.

After the one-week of pre-equilibration (not needed for the blanks), SGGW + tracers were added to the reactors. Samples were collected for tracer fluorescence analysis by removing ~250 μL (after centrifugation) by micropipettor after 1, 3, 7, and 14 days of contact time. Solution pH was checked each time the reactors were sampled (stable within 0.2 pH units in all cases except for controls at pH 8.6, for which variation was 0.35 pH units). The fluorescence of each tracer was measured using a Shimadzu RF 5301 scanning fluorimeter (60–75 μL was loaded into cuvettes for measurement). Tracer concentrations were based on peak fluorescence intensity from a scan of emission wavelengths while keeping the excitation wavelength constant at the peak excitation. However, for fluorescein, the excitation wavelength was set to 475 nm instead of the peak excitation at 490 nm because there was significant scatter of the incident light at 490 nm (likely due to incomplete filtering of the very strong fluorescence emission), which interfered with the emission spectrum. The fluorescence scanning parameters were as follows:

- Sodium fluorescein – 475 nm excitation, 490–540 nm emission scan, peak near 515 nm.
- Amino G acid – 355 nm excitation, 425–475 nm emission scan, peak near 450 nm.
- Sodium 1,5-naphthalene disulfonate – 220 nm excitation, 310–360 nm emission scan, peak near 334 nm.

The three tracers were verified to not interfere with each other (no overlap of spectra). Thus, all three could be used simultaneously in a tracer test without having to rely on chromatographic separations. For the measurements, the fluorimeter slits were adjusted for each tracer to obtain good signal-to-noise ratio. Fluorescein had the highest fluorescence intensity per unit concentration, followed by the 1,5-naphthalene sulfonate, with amino G acid having the lowest intensity per unit concentration.

Calibration curves were prepared for each tracer every time fluorescence was measured, but these were ultimately not needed because all the measured concentrations were within 85% of the concentrations in the control sample (which was also the concentration of the highest standard). The standards were (1) the starting solution(s), (2) a 3:1 dilution of the starting solution(s), and (3) a 10:1 dilution of the starting solution(s). None of the measured concentrations came close to the 3:1 dilutions, and the calibration curves were always linear with intercepts very close to zero, so the concentrations were simply assumed to be directly proportional to measured fluorescence.

5.2.1.3 Experiments evaluating tracer fluorescence as a function of pH

The fluorescence of all three tracers as a function of pH was measured by starting with 20 ml of the pH 8.6 tracer solution and adding small amounts of HCl to incrementally lower the pH down to ~5.7. The fluorescence was measured at each incremental pH. The pH was then increased by adding small amounts of NaOH to incrementally raise the pH up to approximately the starting value of 8.6. The initial pH changes in either direction were rather large but then proceeded in increments of about 0.3–0.4 units. Corrections were made to account for dilution resulting from the HCl and NaOH additions, although these were small because relatively concentrated solutions were used for the pH adjustments.

5.2.1.4 Fluorescence recovery of fluorescein (uranine) in pH 6.8 reactors after adjusting solutions to pH 8.6

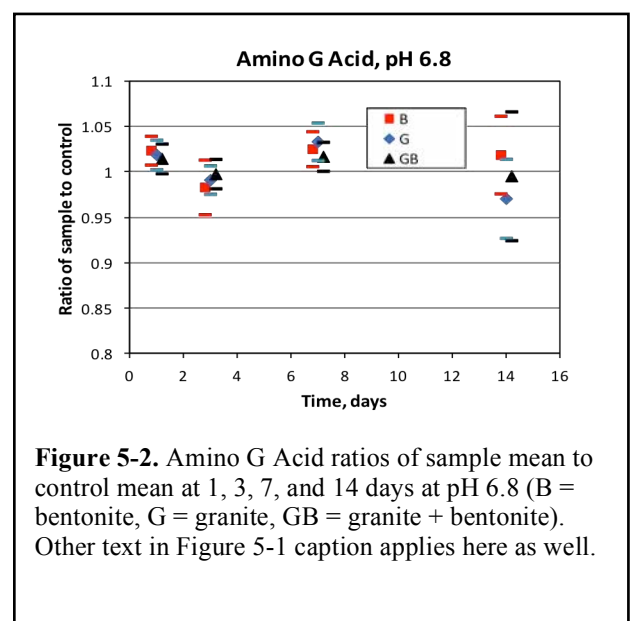
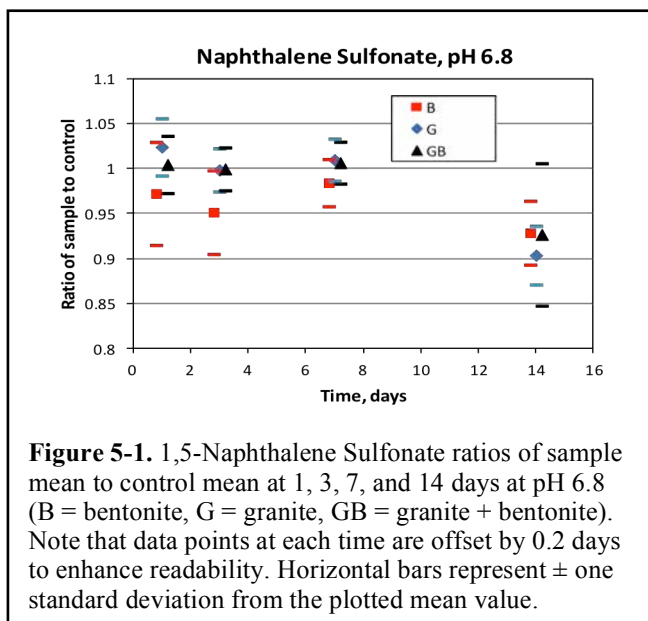
The fluorescence of the fluorescein was significantly less at pH 6.8 than pH 8.6, presumably because a significant fraction of the fluorescein at pH 6.8 was protonated ($pK_a = 6.4$) and the protonated molecule does not fluoresce as strongly as the unprotonated anion. To evaluate the recovery of fluorescence after contact with the solids, 5 ml of solution from each of the pH 6.8 reactors was sampled (after centrifugation) after 21 days of contact with the solids, and the samples were adjusted to pH 8.6 using NaOH. The fluorescence intensity of the pH-adjusted samples was then measured at the fluorescein wavelengths. If the fluorescence of the samples containing bentonite and/or granite was significantly lower than in the controls (after accounting for dilution factors), it would suggest that the solids had some effect on the ability of the fluorescein to recover its fluorescence at the higher pH. Alternatively, it could suggest that some of the protonated fluorescein at pH 6.8 adsorbed to the solids and was not recovered when the sample was taken after centrifugation; this possibility seems unlikely, as the fluorescein in solution should have re-equilibrated if any of the protonated fluorescein sorbed, and the sorption would have been evident from the pH 6.8 samples taken at 1, 3, 7, and 14 days.

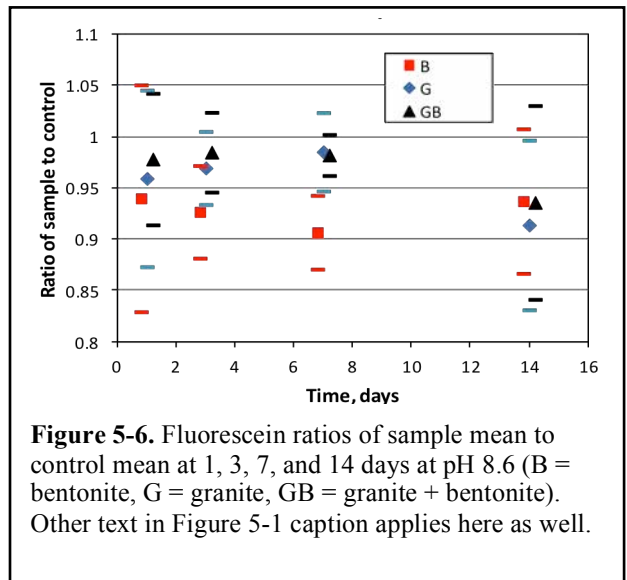
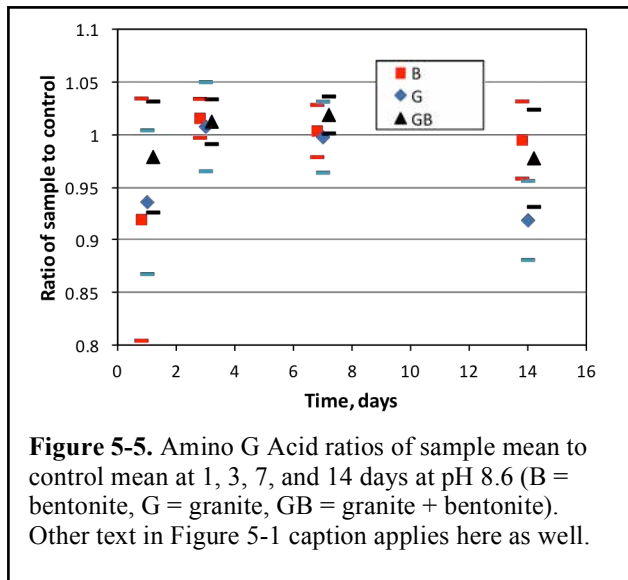
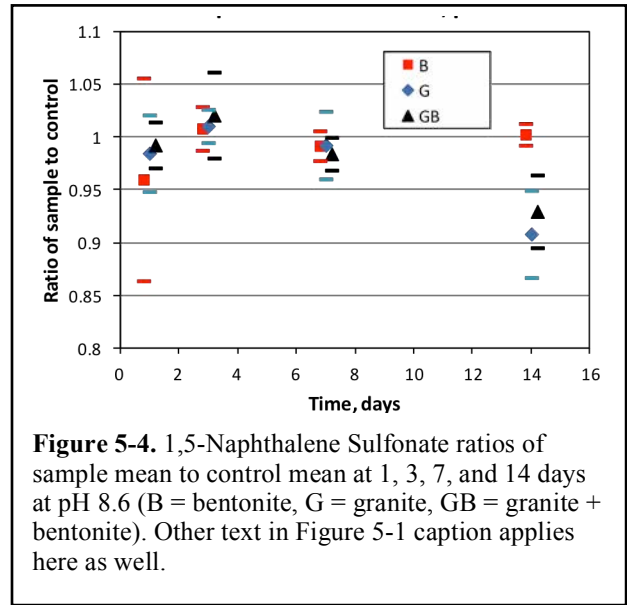
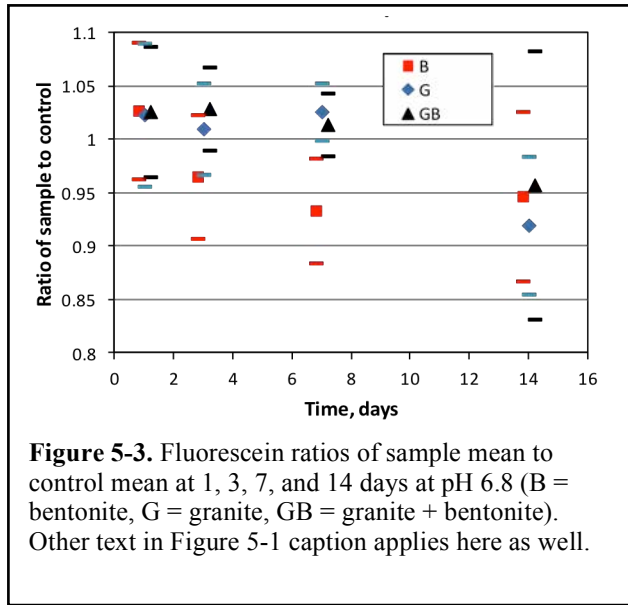
5.2.2 Results of field tracer screening experiments

5.2.2.1 Batch sorption experiments

The fractions of each tracer adsorbed as a function of time relative to the controls are shown in Figures 5-1 through 5-6 (one figure for each of the three tracers at each of the two pHs). The data points are the ratio of the mean of five measurements for each of the solids (one from each of the five reactors) to the mean of the five measurements of each control. The measured concentrations in all of the samples containing bentonite and/or granite were corrected for the dilution resulting from the residual SGW left behind in the reactors after the pre-equilibration step. The horizontal bars correspond to plus and minus one standard deviation from the mean of the ratios, with the standard deviations of the ratios calculated using

$$SD_{ratio} = \sqrt{(SD_{sample})^2 + (SD_{control})^2} \text{ (i.e., additivity of variances)}$$





Additionally, an Aspin-Welch one-sided t test was conducted for each tracer at each time (Choi, 1978). The results of these tests are provided in Tables 5-1 and 5-2, corresponding to the two pHs. The values marked with an asterisk (*) indicate t values that failed the hypothesis test that the mean of the sample measurements was equal to or greater than the mean of the controls (i.e., no sorption) at the 95% confidence level (so it is interpreted that there is 95% confidence that sorption occurred when the hypothesis test failed). It is apparent that most of the measurements passed the test, indicating no sorption. In cases where the test failed, the t values were generally quite close to the t values for rejection, and several of these tests would have passed if the confidence level were increased to 99%.

The results might suggest a small amount of sorption, but it is also possible that the slightly increased tendency for lower fluorescence in the samples relative to the controls was the result of imperfect separations of solids and liquids that resulted in fluorescent light scattering and thus slight extinction of

the fluorescence signal in the samples. The slight tendency for greater apparent sorption after 14 days relative to the earlier times is consistent with this hypothesis, as more fine materials would be expected to be suspended after longer times. However, this result might also suggest a slow sorption process. For the Grimsel field experiments, where tracer residence times in the shear zone are typically less than three days, such slow sorption processes combined with the small amount of sorption would have minimal impact on the observed transport behavior of the tracers. The pH generally did not differ by more than 0.1 unit between the samples and the controls, so this is an unlikely explanation for any apparent sorption in the experiments.

Table 5-2. *t* statistics from Aspin-Welch hypothesis test that mean of sample fluorescence was less than mean of controls at pH 6.8. Values less than approximately 2.0 (indicated by *) suggest sorption at the 95% confidence level.

Tracer, Sample	1 day	3 days	7 days	14 days
NDS, bentonite	-1.113	-2.450	-1.363	-4.847*
NDS, granite	1.644	-0.144	0.927	-7.311*
NDS, bentonite+granite	0.318	-0.033	0.624	-2.233*
Amino G, bentonite	3.302	-1.247	2.904	0.980
Amino G, granite	2.598	-1.224	3.542	-1.538
Amino G, bentonite+granite	2.015	-0.253	2.371	-0.134
Fluorescein, bentonite	0.923	-1.384	-3.245*	-1.580
Fluorescein, granite	0.759	0.524	2.125	-3.025*
Fluorescein, bentonite+granite	0.935	1.620	1.061	-0.791

Table 5-3. *t* statistics from Aspin-Welch hypothesis test that mean of sample fluorescence was less than mean of controls at pH 8.6. Values less than approximately 2.0 (indicated by *) suggest sorption at the 95% confidence level.

Tracer, Sample	1 day	3 days	7 days	14 days
NDS, bentonite	-0.972	0.881	-1.303	0.560
NDS, granite	-0.958	1.477	-0.535	-5.473*
NDS, bentonite+granite	-0.769	1.123	-2.303*	-4.911*
Amino G, bentonite	-1.688	1.941	0.380	-0.264
Amino G, granite	-2.216*	0.435	-0.110	-5.230*
Amino G, bentonite+granite	-0.884	1.361	2.439	-1.072
Fluorescein, bentonite	-1.293	-3.920*	-6.392*	-2.128*
Fluorescein, granite	-1.104	-1.979*	-0.880	-2.551*
Fluorescein, bentonite+granite	-0.780	-0.887	-2.040	-1.623

5.2.2.2 Tracer fluorescence as a function of pH

The pH dependence of tracer fluorescence intensity is shown in Figures 5-7 to 5-9, with one plot for each of the three tracers. The fluorescence of the 1,5-naphthalene sulfonate is concluded to be insensitive to pH over the range interrogated. The Amino-G acid may have exhibited a slight decrease in fluorescence as pH increased over the range from ~6 to ~9, although the decrease is relatively minor and may simply reflect measurement error. The fluorescein shows a pronounced pH dependence of fluorescence, with about a factor-of-two difference between the fluorescence at a pH of ~6 and a pH of ~9 (higher

fluorescence at 9). This result is consistent with literature data (Diehl and Markuszewski, 1989). Importantly, the fluorescence decrease observed at lower pH values was recovered in the same sample when the pH was increased. This shows that the pH dependence of fluorescein fluorescence is completely reversible. It also suggests that if the pH varies significantly during a tracer test, either the pH dependence of fluorescein fluorescence should be accounted for using a pH-dependent correction factor or samples should be adjusted to the same pH before measurement (preferably to pH greater than 8 to maximize fluorescence signal and get into a pH range where the pH dependence is weak or disappears).

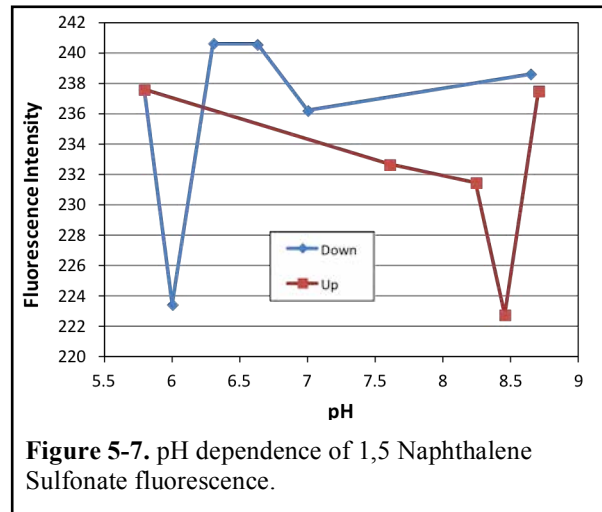


Figure 5-7. pH dependence of 1,5 Naphthalene Sulfonate fluorescence.

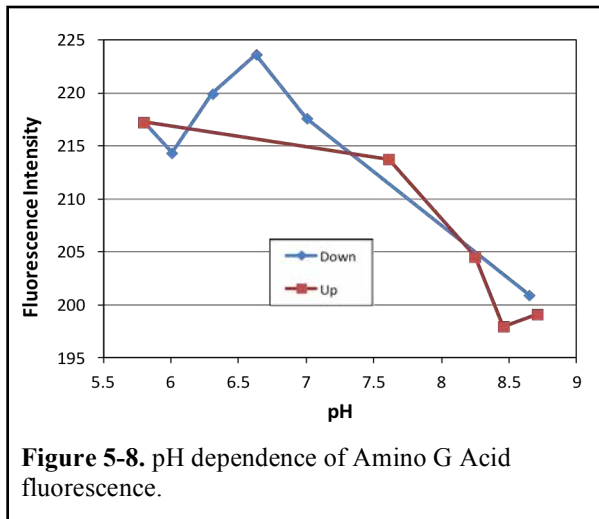


Figure 5-8. pH dependence of Amino G Acid fluorescence.

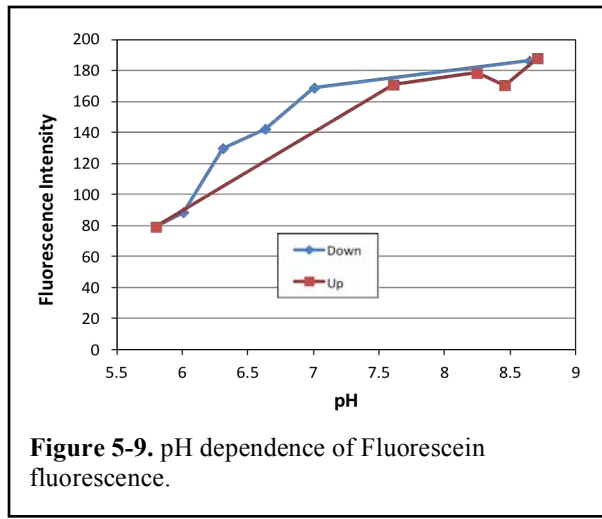


Figure 5-9. pH dependence of Fluorescein fluorescence.

5.2.2.3 Fluorescein fluorescence recovery in solutions from pH 6.8 batch sorption reactors

The fluorescence intensity of the fluorescein in the pH 6.8 samples containing bentonite and/or granite after pH adjustment to ~8.6 was approximately the same as in the pH-adjusted controls (plot not provided here). In fact, after accounting for dilution factors, the fluorescence intensity was slightly greater in the samples containing solids than in the controls, although this difference was not statistically significant. This result suggests that after three weeks of contact with the solids at pH 6.8, the fluorescein fluorescence fully recovered when the pH was adjusted to ~8.6.

5.2.3 Conclusions from field tracer screening studies

It is concluded that none of the three fluorescent tracers adsorbed significantly to either bentonite or granite in synthetic Grimsel ground water at pHs of 6.8 and 8.6. Although sorption cannot be ruled out statistically in some of the batch sorption experiments, it was relatively weak at best, and the apparent sorption may have been caused by experimental influences such as the suspension of fines that suppressed the fluorescence signal slightly in the reactors containing solids. The bentonite loading was only

~2500 mg/L (to approximate a very high colloid load), so the conclusion of no significant sorption to bentonite should be qualified with this in mind. A minor amount of sorption of any of the tracers cannot be ruled out, but if there was any sorption, it was at the lower limit of what could be detected in the batch experimental method employed here. Small amounts of sorption could be better interrogated by running a column experiment (column packed with Grimsel solids), injecting all the tracers simultaneously, and comparing their breakthrough curves to a known conservative tracer such as ^3HHO or a halide (bromide or iodide).

Of the three fluorescent tracers, only fluorescein exhibited a significant pH dependence of fluorescence. This dependence is consistent with what has been reported in the literature (decrease in fluorescence with decreasing pH starting at around 7.5) (Diehl and Markuszewski, 1989). However, it was verified that the fluorescence intensity of fluorescein will fully recover in solutions adjusted from lower pH to a pH greater than ~8 (and this is true even after extended contact with Grimsel solids). Therefore, if pH varies significantly during a Grimsel tracer test, it should be possible to obtain valid fluorescein breakthrough curves either by using a pH-dependent correction factor for fluorescence intensity or by adjusting the pH of all samples to greater than 8 before fluorescence measurement.

5.3 Preliminary Results from Uranium and Neptunium Transport Experiments in Grimsel Granite

Laboratory testing to evaluate the reactive transport of uranium and neptunium in crushed Grimsel granite was initiated in late April 2012, and at the time of this report, only very preliminary results were available. Uranium and neptunium were selected for this investigation for two reasons:

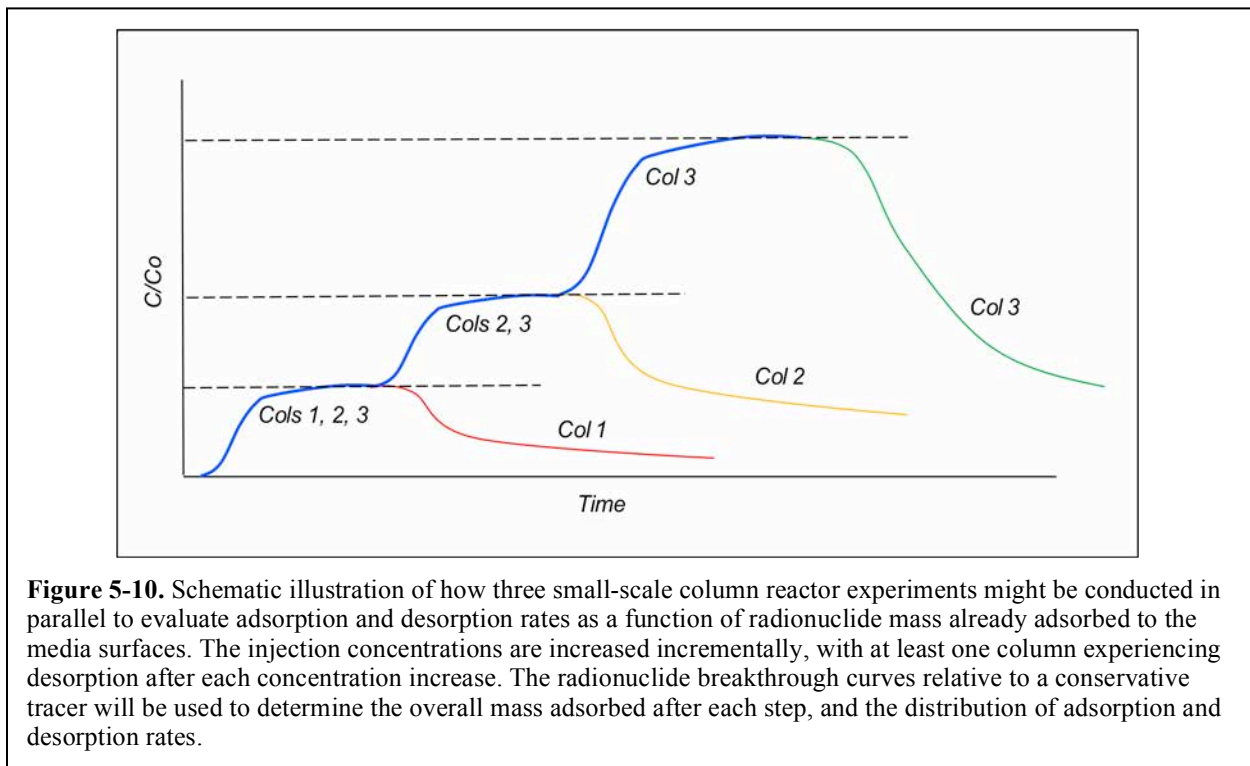
- They are both expected to be relatively weakly sorbing radionuclides in granite systems, particularly at higher pH (8–9) and in waters containing significant bicarbonate/ carbonate concentrations. They also have relatively high solubilities compared to other actinides (on the order of 10^{-5} M for U(VI)), so they could potentially contribute significantly to dose estimates in performance assessment scenarios.
- Both radionuclides will be used in field transport experiments at the Grimsel test site in 2012. Neptunium will be one of several radionuclides in a colloid-facilitated tracer transport experiment involving injection of a radionuclide cocktail in a bentonite colloid suspension. Uranium will be one of several radionuclides doped into a bentonite plug that will be emplaced in a borehole and allowed to swell and erode in a flowing shear zone.

Besides evaluating the transport of the two radionuclides in the Grimsel flow system, an overarching goal of the Los Alamos experimental effort is to develop and demonstrate a method for more robustly interrogating the adsorption and desorption behavior of any reactive radionuclide in the far field of a repository system (although the methods could apply equally well to the near-field or EBS systems). From this perspective, the Grimsel flow system is being used as a proxy or example for any far-field flow/transport system. However, the results of the work will clearly have relevance for uranium and neptunium transport in many granite environments.

5.3.1 Experimental plans for interrogating radionuclide adsorption and desorption rate distributions

The first phase of the planned reactive-transport evaluation approach is to conduct small-scale column transport experiments that are designed to interrogate adsorption and desorption rates in more detail than previously possible. These experiments will be conducted in lieu of more standard batch adsorption

experiments that would involve similar amounts of sorbent material, such as the batch experiments for the fluorescent tracers described in Section 5.2. The small-column reactor approach is schematically illustrated in Figure 5-10. In this approach, the reactive radionuclide is co-injected with a conservative tracer such as ^3HHO into a small column packed with the sorbent material of interest, and the experiment is allowed to proceed until the reactive radionuclide concentration in the column effluent reaches the injection concentration (or after a considerably long time if the sorption is strong enough to preclude the concentration from reaching the injection concentration in a reasonable time). Several such columns can be run in parallel to evaluate experimental reproducibility or the influence of changes in rock mineralogy, water chemistry, or flow rate. The rate at which the radionuclide concentration approaches the injection concentration relative to the rate at which ^3HHO approaches its injection concentration can be used to estimate adsorption rate constant(s) in the column. In principle, this approach will allow adsorption rates to be determined with greater fidelity than in a batch sorption experiment.

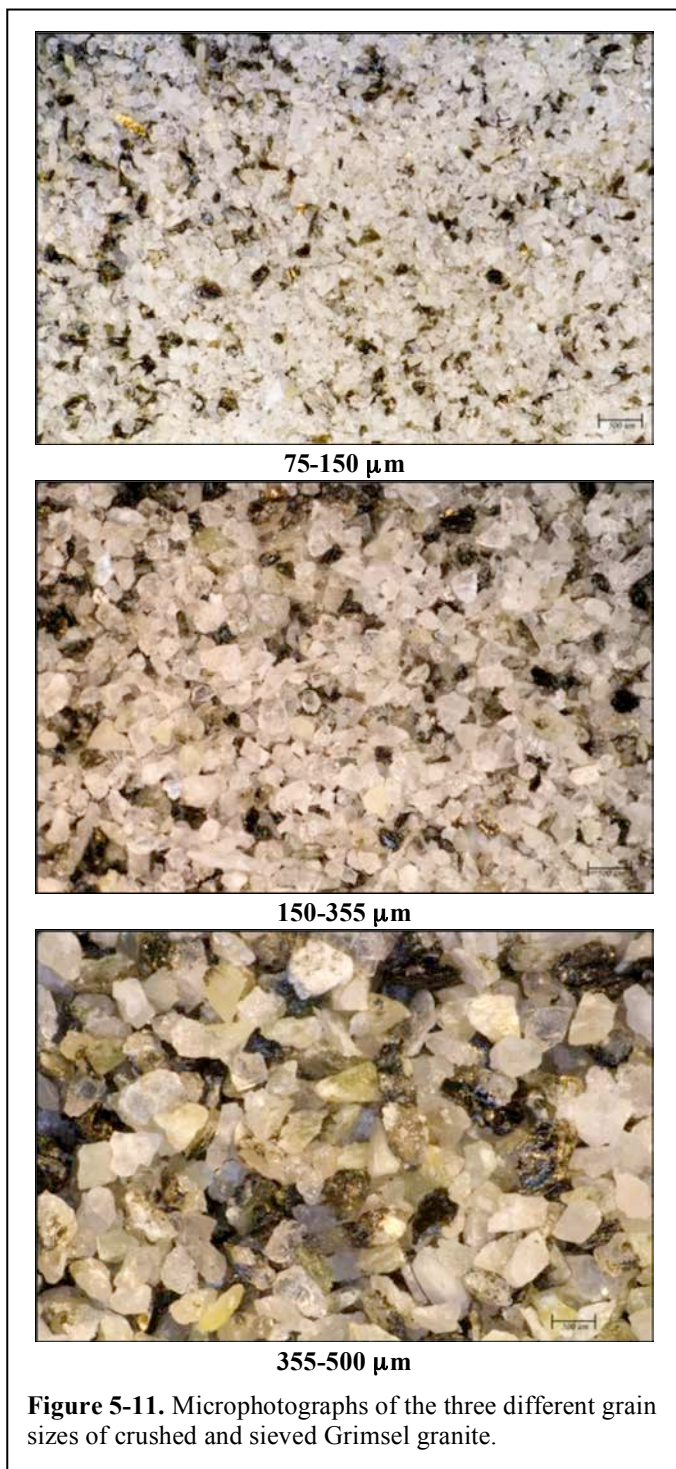


After the radionuclide concentration(s) have reached their injection concentration(s), the injection solution can either be switched to a radionuclide-free solution to observe desorption rates from the material in the column, or the injection concentration(s) can be increased further to observe how the adsorption rate depends on the amount of radionuclide already adsorbed. If columns are run in parallel, some could be run with an increase in concentration and others with a decrease. As Figure 5-10 implies, the possible combinations of increases and decreases are limited only by the number of columns that can be managed comfortably. By conducting several step increases in radionuclide concentrations, some of which are followed by concentration decreases, adsorption and desorption rates can be interrogated after different incremental amounts of adsorption or after different time periods of contact between the radionuclides and solids. The interrogation after different amounts of adsorption would allow evaluation of nonlinear adsorption effects and whether desorption occurs preferentially from initially occupied

sorption sites or from sorption sites that are occupied later in the experiment. Interrogation after different time periods of contact between the radionuclides and solids would allow evaluation of processes such as bond-aging effects (is desorption slower after radionuclides have been in contact with the solid surfaces for longer time periods?).

The goal of these experiments is to develop robust radionuclide adsorption and desorption rate *distributions* that can be used in reactive-transport process models to more accurately predict radionuclide transport over larger time and distance scales. As the work presented in Chapter 3 implies, the distribution of adsorption and desorption rates (the latter in particular) can have a significant influence on the predicted transport behavior of a reactive radionuclide such as uranium or neptunium. In the case of the work of Chapter 3, the relevant distributions were not fully interrogated experimentally, so they were approximated with a finite number of first-order adsorption and desorption reactions that had widely varying rates and finite surface-site densities for the reactions with slower desorption rates to match the available data sets. We hypothesize that by more rigorously interrogating the adsorption and desorption rate distributions, we can improve the ability to match such data sets and thus improve larger-scale predictions, although it may mean relaxing some of the assumptions that are conventionally made about adsorption and desorption reactions (i.e., linear, first-order reactions).

After developing adsorption and desorption rate distributions from small-scale column experiments, the distributions will be tested in larger-scale column experiments in which both the concentration vs. time history in the column effluent and the residual radionuclide distribution in the column after the experiment are determined. These measurements are analogous to the column transport data sets used in the inversion exercise of Chapter 8.



5.3.2 Preliminary experiments and experimental results

An initial set of small-scale column experiments was conducted to evaluate uranium adsorption and desorption onto/from crushed Grimsel granite from borehole CFM 11.002 in an SGGW (see recipe in Table 5-1). The granite used in the experiments was crushed and sieved into three different grain sizes (75–150 μm , 150–355 μm , and 355–500 μm), and each grain size was used to pack three separate columns. Microphotographs of the different grain size materials are shown in Figure 5-11. None of the size fractions included any material from the two shear zone fracture surfaces that were present in the core. Each grain size was analyzed by QXRD, and the results are shown in Table 5-4. The large percentages of mica in each fraction are believed to be an artifact of the analysis, as none of the samples visually looked like they contained any more than a few percent mica. Mica is well known to produce a very strong x-ray diffraction signal, and it also tends to strongly orient in a single direction in powdered samples. Both of these characteristics could have caused the interpreted mica weight percentages to be biased much higher than the actual weight percentages in the samples. We are re-analyzing some fresh granite samples taken from the same core, using extra care to minimize this potential bias. We are also analyzing a small amount of material taken from one of the shear zone fracture surfaces, which we are quite certain is predominantly mica. The trend in Table 5-4 of an increasing percentage of plagioclase relative to quartz as the granite grain size increases is consistent with the microphotographs of Figure 5-11, which show an apparent increase in the dark plagioclase relative to the light quartz as the grain size increases. This result is not surprising given the tendency for quartz to more easily cleave into smaller grains than plagioclase.

Table 5-4. Quantitative X-ray diffraction interpretation of Grimsel granite samples shown in Fig. 5-11.

Sample	Quartz	Plagioclase	K-Feldspar	Mica	Chlorite	Kaolinite	Epidote*	Total
75-150 μm	42.9	27.5	4.2	24.9	0.2	0.4	--	101.1
150-355 μm	24.3	43.8	7.8	23.6	0.2	0.2	--	99.9
355-500 μm	15.3	46.4	6.7	30.9	0.2	0.5	---	100.0

*There are tiny amounts (probably a few tenths of percent) of epidote.

The small-scale columns were made from 0.9-cm inner-diameter (ID) polyethylene tubing by cutting the tubing into 5-cm lengths and then threading the ends of the columns to allow plastic end fittings to be screwed into them. Figure 5-12 shows photos of the packed columns after they were set up for flow. In addition to the nine columns packed with the three different granite grain sizes (three columns for each size), one column was not packed with any material. This column served as a blank to evaluate whether there was any uranium adsorption to the polyethylene tubing or the end fittings.

The columns were saturated with the SGGW after being flushed with CO_2 to remove air and then evacuated to remove most of the CO_2 prior to the introduction of water. The columns were allowed to flow with deaerated SGGW for approximately two weeks before uranium was introduced. This procedure helped precondition the granite surfaces with the SGGW groundwater and flush any mobile fines from the columns. The uranium solution injected into the columns was approximately 10^{-6} M U, with the majority of the uranium being natural U from a 1000-mg/L ICP-MS standard and the remainder being ^{233}U



(Isotope Products, Inc.) to raise the alpha activity of the solution to 900–1000 counts per minute/mL, or CPM/mL. The addition of ^{233}U allowed high-precision analyses by alpha liquid scintillation counting (Perkin-Elmer Tri-Carb 2500). The injection solution was also spiked with ^3HHO to serve as a conservative tracer against which uranium transport could be compared.

By comparing the breakthrough curves of ^3HHO and U, it was anticipated that it would be possible to detect even very small amounts of U adsorption to the granite. Small amounts of adsorption can be difficult to quantify or even identify in batch sorption experiments because adsorption is deduced from differences in concentrations in reactors containing sorbent and in control reactors containing no sorbent. Analytical errors in both measurements can easily mask small amounts of adsorption. However, in column experiments, small amounts of adsorption can be quantified quite accurately from differences in arrival times of reactive and conservative tracers, which are much less influenced by analytical error.

We were anticipating relatively small amounts of adsorption of uranium onto the Grimsel granite because of the high pH of the SGGW (8.6 to 8.8) and the near saturation of the water with respect to calcite. Uranium adsorption is known to be low at pHs of 8 to 10 and in the presence of calcium because of the tendency for neutral and negatively charged calcium-uranyl-carbonate complexes to form in solution and be the dominant uranium aqueous species under these conditions (Dong and Brooks, 2006). The tests were originally planned to be carried out in a manner similar to that depicted in Figure 5-10, where for each grain size, one of the columns would be subjected to desorption after the first step increase in uranium concentration and the other two columns would have a further increase. Then one of those two columns would be subjected to desorption after the second increase, and the other would have a third increase before being subjected to desorption.

All the columns were run at flow rates of 0.25–0.3 mL/hour, with the exception of one column that was inadvertently run at about 0.17 mL/hour. These flow rates resulted in column residence times of 10–12 hours and 18–19 hours, respectively. The ^3HHO and uranium breakthrough curves obtained from one of the small-scale column experiments is shown in Figure 5-13. It is apparent that there was no retardation of the uranium relative to the ^3HHO , so there was no measurable adsorption of the uranium to the Grimsel granite in the SGGW. The breakthrough curves of Figure 5-13 were typical of breakthrough curves in all 10 columns, including the blank column, so it was concluded that there was no measurable uranium

adsorption to any of the different granite grain sizes. Because of this result, none of the columns were subjected to further increases in uranium concentration, and all were simply flushed out to evaluate where there was any apparent desorption (which there was not).

These results are not surprising given the lack of highly sorptive minerals in the granite (assuming the mica percentage in Table 5-4 is overestimated) and the high pH of the SGGW. Future experiments may be conducted at lower pH (~7) where greater U adsorption to almost any surface would be expected because of the shift in aqueous speciation to more sorptive uranium species at lower pH. Also, it would be worthwhile to conduct experiments using the shear zone mineralogy (e.g., predominantly mica) rather than the bulk granite mineralogy to achieve better representation of transport in the Grimsel shear zone.

Previous field tracer tests at the Grimsel test site indicated a 30–40% lower mass recovery of uranium than conservative tracers (Möri, 2004) despite the fact that tracer residence times in the shear zone were on the order of only a few hours. However, it is unlikely that enough shear zone material could be obtained to conduct many small-scale column experiments or even batch sorption experiments. Mica from another source might have to be used in such experiments.

Because of the lack of adsorption of uranium in the small-scale columns, it was decided to transition immediately to evaluating the adsorption and desorption behavior of neptunium in the same columns. Neptunium is expected to adsorb more strongly to the granite surfaces than uranium, although it would not normally be considered a strongly adsorbing radionuclide. To avoid conducting another set of relatively labor-intensive experiments without any measurable adsorption, a small set of batch sorption experiments was conducted to evaluate whether the neptunium appeared to be adsorbing significantly to the granite. Three batch reactors were run in parallel for both the 75–150- μm and 355–500- μm granite size fractions, and two control reactors were also run. Five g of crushed granite and approximately 12 mL of solution were initially loaded into each reactor (no granite and ~10 mL solution in the controls). The reactors were sampled at 6, 22, and 77 hours. The results are shown in Figure 5-14, where the y-axis is the ratio of the mean

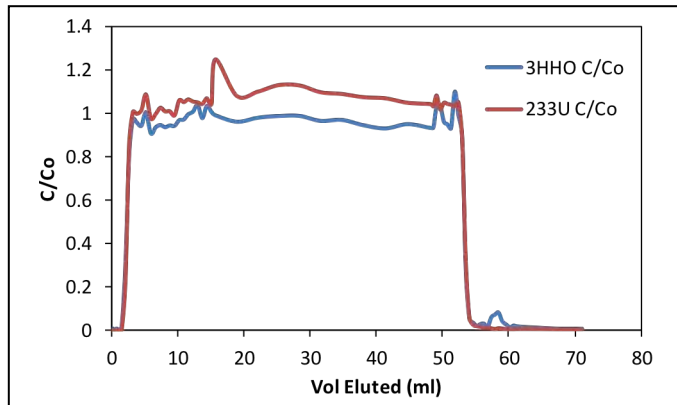


Figure 5-13. ^3HHO and uranium breakthrough curves from one of the small-scale column experiments (150–355 μm granite). The lack of any difference between the breakthrough curves (other than the slight differences in plateau concentrations) indicates that the uranium was not adsorbing appreciably to the granite surfaces.

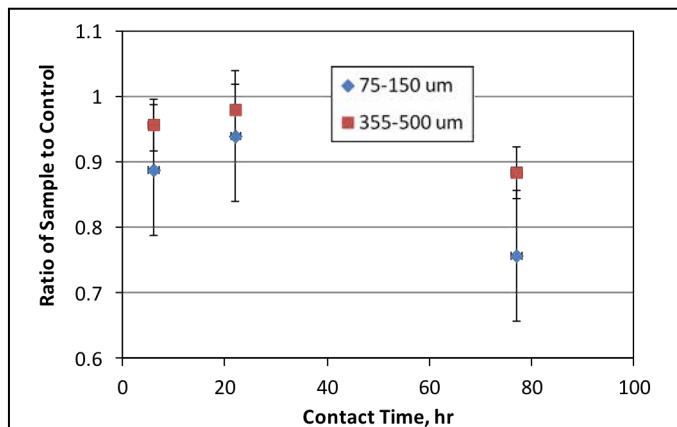


Figure 5-14. Ratio of the mean neptunium concentration in the samples to the mean concentration in the controls for batch adsorption experiments with the smallest and largest grain size fractions of the Grimsel granite.

concentration in the samples to the mean concentration in the controls after correction for dilution effects in the samples. Each data point in Figure 5-14 corresponds to the average of three samples, and the error bars correspond to approximately two standard deviations from the mean of the three samples. It is apparent that despite the relative large error bars (typical of batch experiments with small amounts of adsorption), the neptunium appears to be adsorbing significantly to the granite surfaces in these experiments. The fact that the data points for the smaller grain size are lower than for the larger size further suggests adsorption of the neptunium to the granite, as this result is to be expected because of the greater surface area per unit mass of the smaller-grained material (note that gas adsorption surface area measurements have not yet been conducted). A ratio of 0.9 in Figure 5-14 corresponds to a retardation factor of about 1.5 in the small columns, which should be quite readily measurable. Thus, we plan to inject neptunium (in SGGW) into the small columns in the near future.

5.4 Conclusions

Experiments have not progressed far enough yet to draw any firm conclusions about the ability of the new small-scale column method to interrogate radionuclide adsorption and desorption rate distributions to improve predictions of radionuclide transport in process models. The small uranium column experiments exhibited no adsorption of the uranium onto the Grimsel granite, although this was not surprising given the high pH of the synthetic Grimsel groundwater used in the experiments. The lack of adsorption obviously precludes a robust test of the new method. We are now transitioning to evaluating the adsorption and desorption behavior of neptunium in the small columns (same Grimsel granite system). Batch adsorption experiments have indicated a sufficient amount of neptunium adsorption in the Grimsel system to see a significant delay in the neptunium breakthrough in the small columns relative to a conservative tracer.

The fluorescent tracers fluorescein (uranine), amino-G acid, and 1,5 naphthalene disulfonate did not measurably adsorb to Grimsel granite and FEBEX bentonite in laboratory batch sorption experiments in synthetic Grimsel groundwater between pH 6.8 and 8.6. Based on these results, the three tracers could be used simultaneously as conservative tracers in field tracer tests because their fluorescence spectra are readily distinguishable. The test results do not explain the apparent loss or degradation of fluorescein in some of the field tracer tests at the Grimsel Test Site.

5.5 References

- Choi, S. C., 1978. *Introductory Applied Statistics in Science*. Prentice-Hall, Englewood Cliffs, New Jersey.
- Diehl, H. and Markuszewski, R., 1989. Studies on Fluorescein – VII. The Fluorescence of Fluorescein as a Function of pH, *Talanta*, **36**(3), pp. 416–418.
- Dong, W. and Brooks, S., 2006. Determination of the formation constants of ternary complexes of uranyl and carbonate with alkaline earth metals (Mg^{2+} , Ca^{2+} , Sr^{2+} , and Ba^{2+}) using anion exchange method. *Env. Sci. Tech.*, **40**(15), pp. 4689–4695.
- Möri, A. (Ed.), 2004. The CRR final project report series 1: Description of the Field Phase – Methodologies and Raw Data. *Nagra Technical Report NTB 03-01*. Nagra, Wettingen, Switzerland.

Chapter 6. Summary of Fieldwork at the Grimsel Field Site: Interpretations and Inferences from CFM Tracer Tests 10-01 through 12-02

6.1 Introduction

The Colloids Formation and Migration (CFM) project testbed at the Grimsel Test Site is schematically illustrated in Figure 6-1. CFM tracer tests 10-01 through 10-04 were conducted in 2010 with tracer injection into CFM 06.002i2 and extraction from the Pinkel surface packer approximately 6.1 m from the injection interval. These tests included two colloid-homologue tracer tests (10-01 and 10-03) that were conducted at different Pinkel extraction flow rates and therefore had significantly different tracer residence times in the MI shear zone. FEBEX bentonite colloids and the same four homologues were used in each test. An interpretation of test 10-03 is provided in this informal report, and both the colloid and homologue interpretations are compared with previously-reported interpretations from test 10-01. The interpretation of test 10-03 is complicated by the low recovery of uranine in the test, which was subsequently observed in other tests and has tentatively been attributed to some sort of first-order degradation process occurring in the tracer injection loop. A method for correcting the uranine breakthrough curve for the effects of this degradation is presented.

In 2011, three monitoring boreholes (CFM 11.001, 11.002, and 11.003) were completed in close proximity ($40 \text{ mm} \pm 5 \text{ mm}$) to CFM 06.002 (shown in Figure 6-1, with close-up layout shown Figure 6-2); tracer tests 11-01 through 11-03 were conducted to provide evaluations of the natural flow rate in the MI shear zone through injection interval CFM 06.002i2 when steady collection flow rates were established at the Pinkel surface packer. These tests were also conducted to evaluate the ability to conduct low-volume sampling of the monitoring boreholes

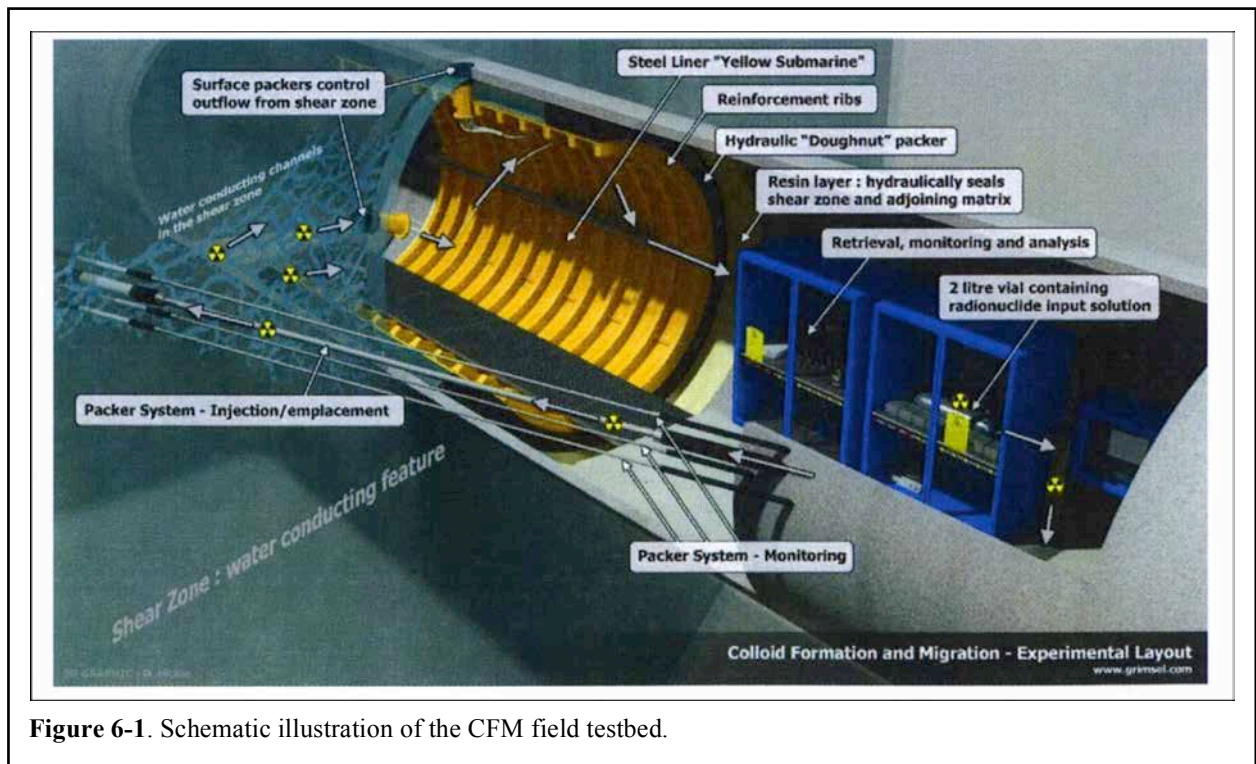
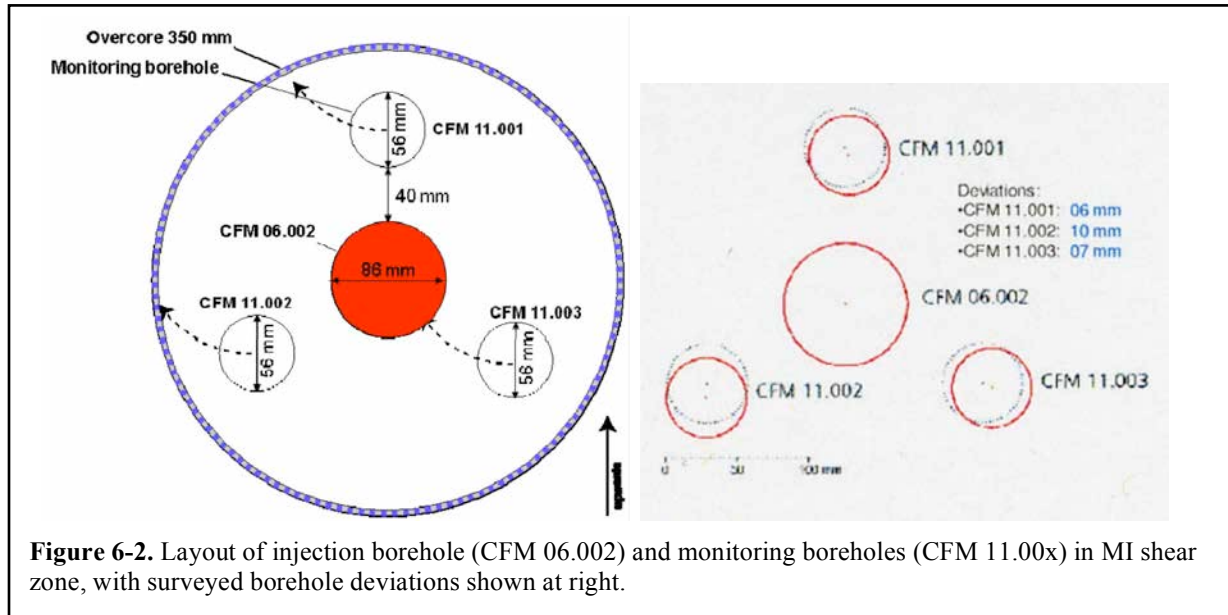


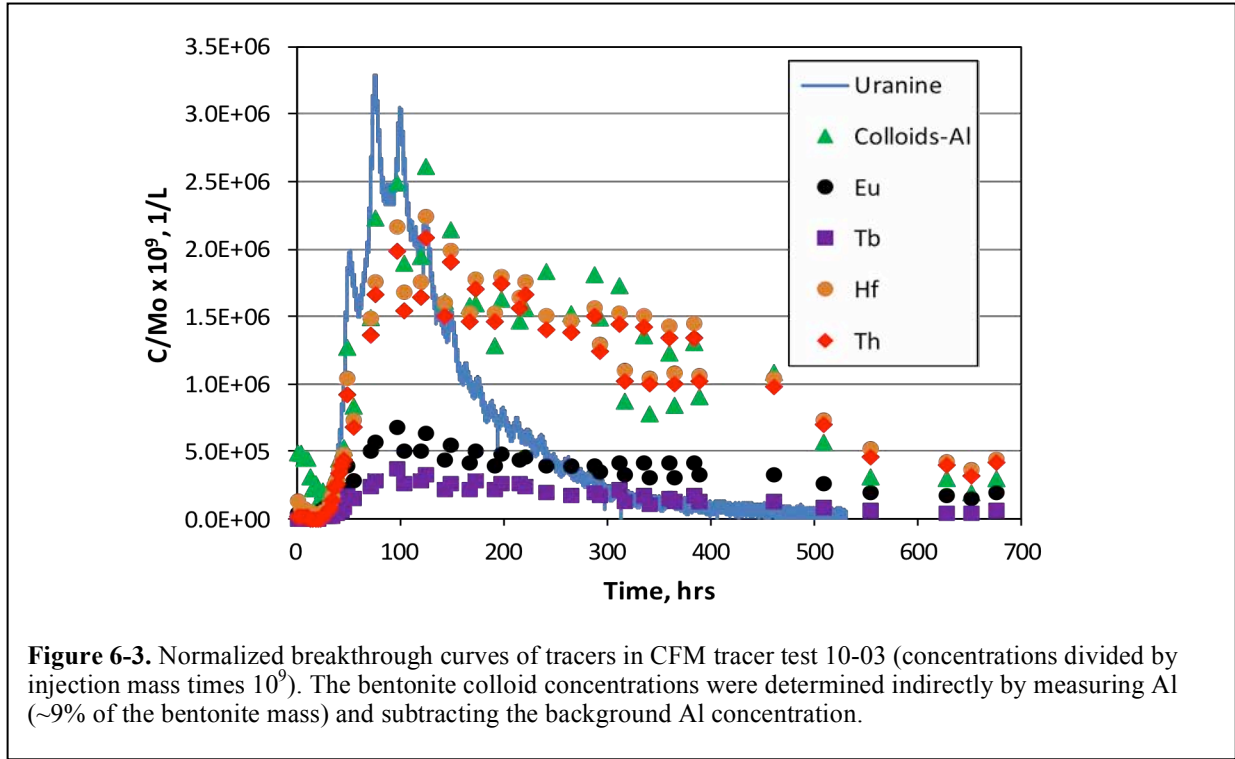
Figure 6-1. Schematic illustration of the CFM field testbed.



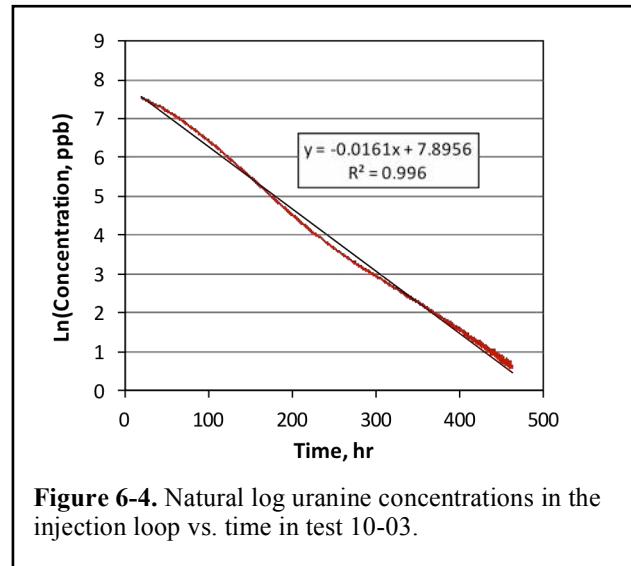
after the bentonite emplacement in CFM 06.002i2 later in 2012. Tracer test 12-01 was conducted to evaluate conservative tracer responses at the Pinkel surface packer when a small net injection rate was imposed in CFM 06.002i2 (because no tracer responses were observed at the Pinkel surface packer in the 11-0x series tests conducted without a net injection rate). Finally, tracer test 12-02 was conducted under the same injection and outflow conditions as 12-01 but with the injection of a cocktail of radionuclides and bentonite colloids instead of just conservative fluorescent dye tracers. This chapter summarizes interpretations and inferences from these tracer tests, although the interpretations of colloid and radionuclide breakthrough curves in test 12-02 are deferred to a later date when these data are fully developed and made available.

6.2 Colloid-Homologue Tracer Test 10-03, and Comparison to Tracer Test 10-01

The normalized breakthrough curves (observed concentrations divided by injection masses) of all tracers in test 10-03 are shown in Figure 6-3. In this test, the four actinide/radionuclide homologues listed in the legend of Figure 6-3 were pre-sorbed onto FEBEX bentonite colloids (95+% adsorption at time of injection), and the colloids were co-injected with uranine as a conservative tracer. A peculiar feature of the breakthrough curves is that the uranine has a lower recovery than that of the bentonite colloids (based on aluminum recovery), which is contrary to observations in previous tracer tests involving uranine and bentonite colloids. This feature makes it impossible to estimate a meaningful filtration rate constant for the bentonite colloids because a higher recovery of colloids relative to a conservative tracer implies either a negative filtration rate constant or some process that is causing loss or attenuation of the conservative tracer in the system (such as matrix diffusion, which would not significantly affect the colloids because of their small diffusion coefficients). Significant loss of uranine due to matrix diffusion was ruled out because there was little evidence of such loss in previous tracer tests, and also because matrix diffusion tends to result in long breakthrough curve tails, not the truncated uranine tail shown in Figure 6-3.



The uranine concentration as a function of time in the injection loop during test 10-03 is shown in Figure 6-4. The negative of the slope in this log-linear plot multiplied by the volume of the injection interval provides an estimate of the flow rate through the interval during the test. As Figure 6-4 shows, the slope of log-linear concentration decline in the injection interval is -0.0161 hr^{-1} , and given the injection interval volume of 3000 ml for this test (2000-ml tracer tank + 1000-ml interval volume and tubing), the flow rate through the interval is estimated to be 0.805 ml/min. However, subsequent testing in which a second conservative fluorescent dye tracer (amino-G acid, or AGA) was used in conjunction with uranine suggested that the uranine was degrading by some unknown process in the injection loop. Figure 6-5 shows the injection loop concentrations as a function of time for both AGA and uranine in tracer test 11-02. The log-linear slope analyses of these data indicated that the slope up to 289 hours (when a relatively high net injection rate was imposed) was $-0.000868 \text{ hr}^{-1}$ for the AGA and $-0.009694 \text{ hr}^{-1}$ for the uranine. If the slope for the AGA is taken as a reflection of the true flow rate through the injection interval, then the difference between the two slopes (0.00883 hr^{-1}) provides an estimate of the first-order degradation rate constant for the uranine in the injection interval. The fact that the log-linear plot of the uranine concentration is linear implicates a first-order uranine decay process (the plot would have curvature if the process were not first order). Given that the circulation flow rate through the injection interval was about the same in tests 10-03



and 11-02 (28–35 ml/min vs. 26–30 ml/min, respectively) and the same injection loop equipment was used in both tests, it is reasonable to assume that the uranine degradation rate was similar in both tests.

To correct for the uranine degradation in the injection loop in test 10-03, the uranine degradation rate constant deduced from the 11-02 test can be subtracted from the apparent flow-rate decay constant in test 10-03 to obtain an estimate of the true flow-decay constant in test 10-03: $0.0161 - 0.00883 = 0.00727 \text{ hr}^{-1}$, which for an injection interval volume of 3000 ml translates to a flow rate of 0.364 ml/min through the injection interval. However, during the first 125 hours of test 10-03, during which the peak extraction tracer concentrations were observed, the slope of the log-linear injection concentration history plot was -0.0146 hr^{-1} , which results in a lower flow-rate estimate through the injection interval of 0.289 ml/min during this important time period. This flow-rate estimate was used for the interpretations of the extraction tracer breakthrough curves.

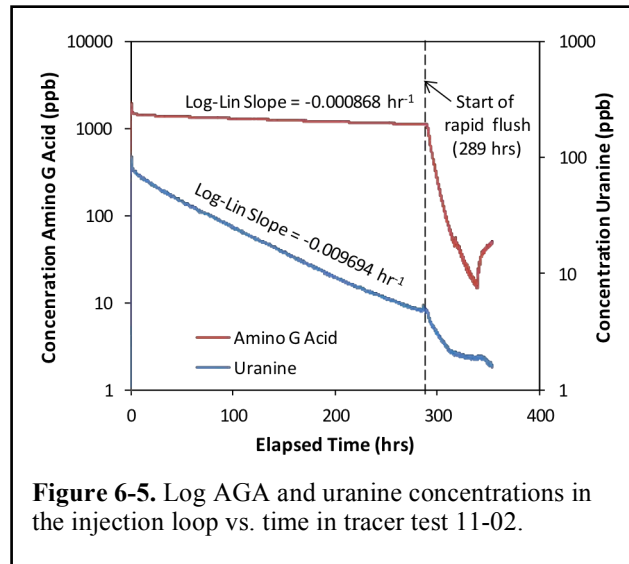


Figure 6-5. Log AGA and uranine concentrations in the injection loop vs. time in tracer test 11-02.

If it is assumed that the uranine degradation occurs only in the injection loop and not in the shear zone, then mean residence times and Peclet numbers (test length scale divided by longitudinal dispersivity) in test 10-03 can be estimated from the uranine extraction breakthrough curve by conducting a RELAP model analysis (Reimus et al., 2003) using the observed uranine injection-loop concentration history as the input function. The results of this analysis are shown in Figure 6-6, with an estimated mean residence time of 64 hr, a Peclet number of 15, and a mass fraction participating in the tracer test of 0.19 (i.e., a mass recovery of 19%, which is in good agreement with the observed mass recovery of approximately 20%). The assumption that the uranine degrades only in the injection loop is supported by two independent observations: (1) the mass recovery of uranine in test 11-02 after a relatively high net injection rate was imposed (at 289 hr) was greater than that of the AGA by more than a factor of 2 (based on the mass remaining in the injection interval at 289 hrs), and (2) batch sorption tests of uranine conducted at Los Alamos in synthetic Grimsel groundwater using Grimsel granite and FEBEX bentonite colloids as sorption substrates indicated no apparent sorption or degradation of the uranine (Section 4.3).

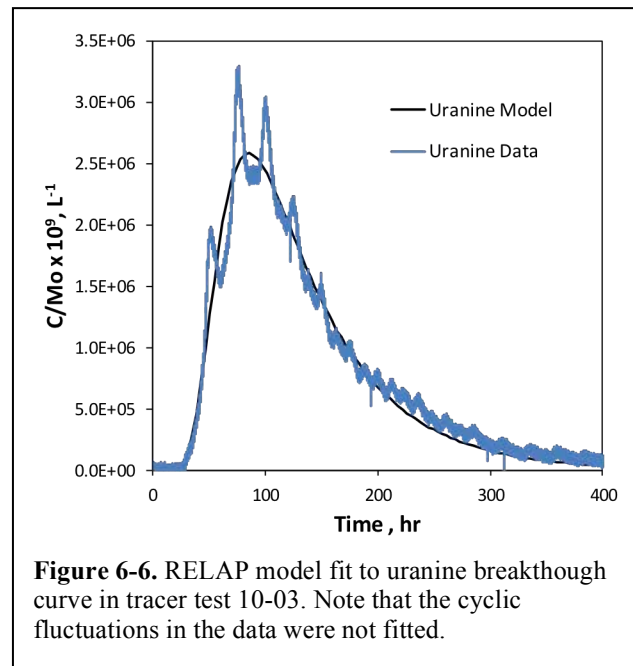


Figure 6-6. RELAP model fit to uranine breakthrough curve in tracer test 10-03. Note that the cyclic fluctuations in the data were not fitted.

To estimate transport parameters for the bentonite colloids and homologues in test 10-03, and in particular the filtration rate constant of the colloids, it is necessary to correct the uranine extraction breakthrough curve for the injection-loop degradation of the uranine (which does not apply to the colloids or homologues). Assuming an injection flow rate of 0.289 ml/min instead of 0.805 ml/min (see above) partially accomplishes this correction, but it is also necessary to make a correction for the mass recovery that would occur without the uranine degradation. By multiplying the observed uranine injection concentration history by $\exp(0.00883t)$, with t in hours, a corrected injection concentration history is obtained.

Over the first 340 hr of the test 10-03, the mass associated with this corrected injection concentration history is almost exactly double the mass associated with this observed injection concentration history. Thus, to obtain a corrected extraction concentration history, the tracer mass fraction in RELAP was increased from 0.19 to a value necessary to obtain a mass recovery ~ 2 times the observed mass recovery at about 400 hr into the test. (400 hours was used because it is approximately the sum of the 64-hr mean residence time in the shear zone and the 340 hr used for the mass correction calculation – note that the mass correction was not extended beyond 340 hr because the inverse exponential correction factor becomes very small and the concentration data becomes noisier after 350 hr, which imparts significant error to the calculations.) Because the injection flow rate observed during the first 125 hrs of the test (0.289 ml/min) was slightly lower than the average injection flow rate observed during first 340 hr (0.364 ml/min), the actual correction factor applied to obtain a factor of 2 greater mass recovery at the Pinkel surface packer after 400 hr was 2.35, so the tracer mass fraction in RELAP was increased from 0.19 to 0.452 (i.e., this analysis suggests that the mass recovery of uranine without the degradation in the injection loop would have been about 45%). The resulting corrected extraction breakthrough curve for uranine is shown in Figure 6-7 along with the uncorrected uranine breakthrough curve and the normalized colloid breakthrough curve based on aluminum concentrations. Note that the corrected uranine breakthrough curve quite closely approximates the colloid breakthrough curve, suggesting nearly conservative transport behavior of the colloids. Also shown in Figure 6-7 is a corrected uranine extraction breakthrough curve obtained from a more rigorous analysis that accounts for the changes in injection flow rate that apparently occurred during the tracer test (i.e., 0.289 ml/min from 0–125 hrs, 0.479 ml/min from 126–260 hrs, and 0.234 ml/min from 260–380 hrs). This more rigorous analysis suggested that a uranine mass fraction of 0.416 participated in the tracer test (as opposed to 0.452 for the other analysis). The two model curves shown in Figure 6-7 have the same overall extraction recovery, equal to a factor of 2 greater than the observed uranine recovery.

Because the two uranine model curves of Figure 6-7 are quite similar and neither accounts for the cyclic fluctuations in concentrations resulting from earth tides, it was decided to use the smoother curve to serve as the basis for the interpretation of the colloid and homologue breakthrough curves. A best fit to the

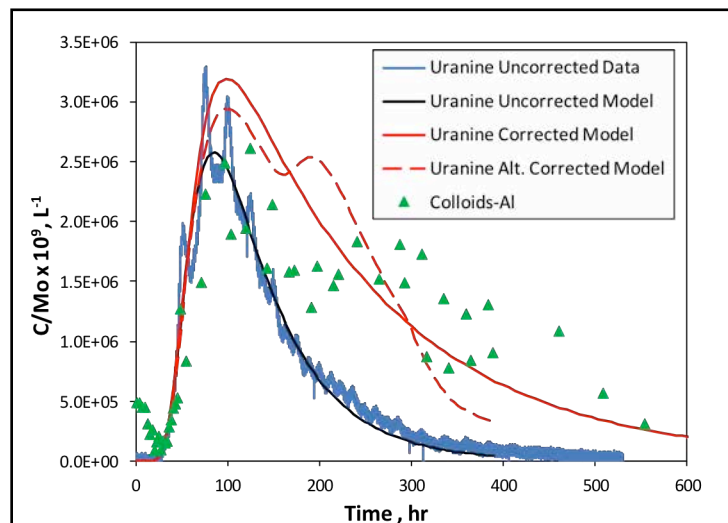
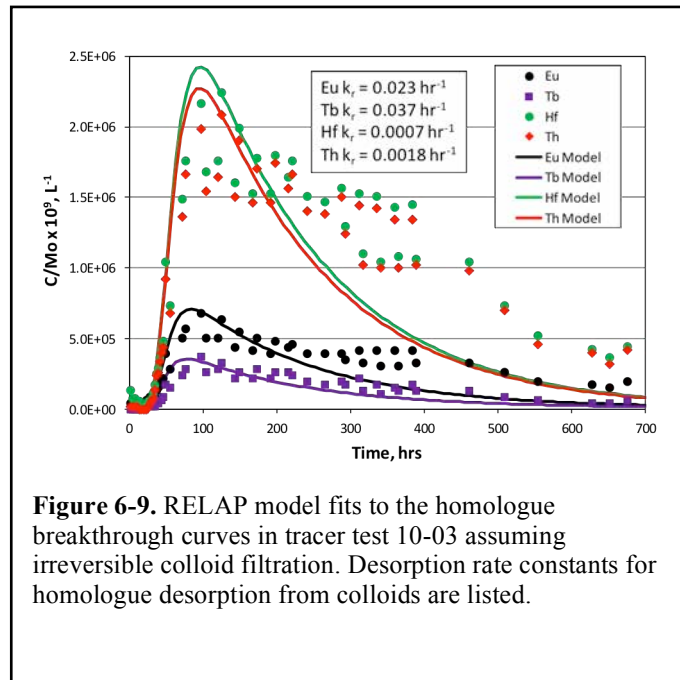
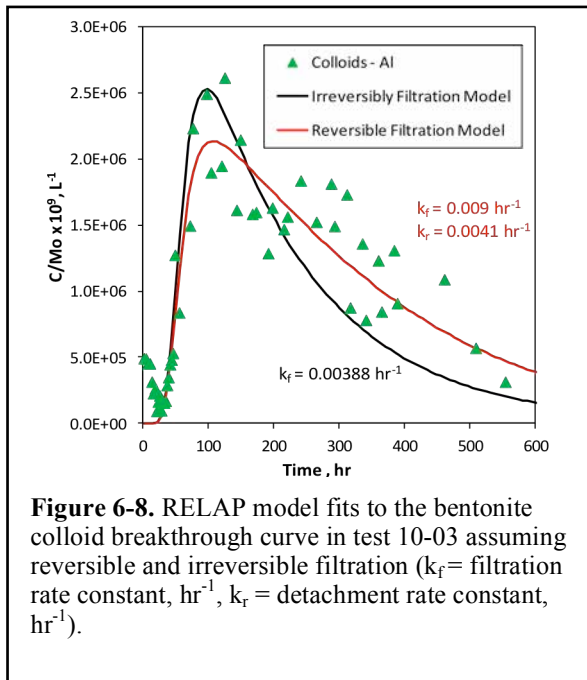


Figure 6-7. Plot showing corrected uranine breakthrough curves for tracer test 10-03 (assuming constant injection flow rate and varying injection flow rate (alt.) – red lines) relative to uncorrected uranine data and bentonite colloid data.

colloid breakthrough curve was obtained by assuming that the colloids transported identically to the uranine (smooth correction) except that they also experienced a first-order filtration rate. Figure 6-8 shows model fits in which it was assumed that the colloid filtration process was irreversible and reversible, with the filtration parameters listed on the figure. Not surprisingly, the reversible fit is better than the irreversible fit because an additional fitting parameter is included in the model.

Figure 6-9 shows fits to the homologue breakthrough curves assuming that the homologues, which were almost completely adsorbed to the bentonite colloids when they were injected, transported identically to the colloids except for a first-order desorption rate from the colloids. In this case, the irreversible filtration curve fit of Figure 6-8 was used for the colloids. Furthermore, it was assumed that once the homologues desorbed from the colloids, they were effectively removed from the tracer test by adsorbing strongly to immobile surfaces in the shear zone. The desorption rate constants estimated for each homologue are listed in Figure 6-9.



The RELAP model was not capable of conducting a similar analysis when reversible colloid filtration was assumed, so RELAP was used to obtain an unconstrained fit to the colloid breakthrough curve (i.e., no constraints on mean residence time, Peclet number, and mass fraction) to provide a basis for estimating homologue desorption rate constants in the case of reversible colloid filtration. The resulting fit to the colloid breakthrough curve is shown in Figure 6-10 along with the reversible colloid filtration fit of Figure 6-8. Figure 6-11 shows the best-fitting homologue breakthrough curves obtained assuming that the colloids followed the unconstrained fit of Figure 6-10. The homologue desorption rate constants in this case are slightly smaller than in the irreversible colloid filtration case because the peak colloid concentrations are predicted to be lower than in the irreversible filtration case, so less homologue desorption is needed to match the peak homologue concentrations. Note that the tails of the homologue breakthrough curves are fit much better in Figure 6-11 than Figure 6-9 because the tail of the colloid breakthrough curve is approximated much better when reversible colloid filtration is assumed (simulated using the unconstrained model fit of Figure 6-10).

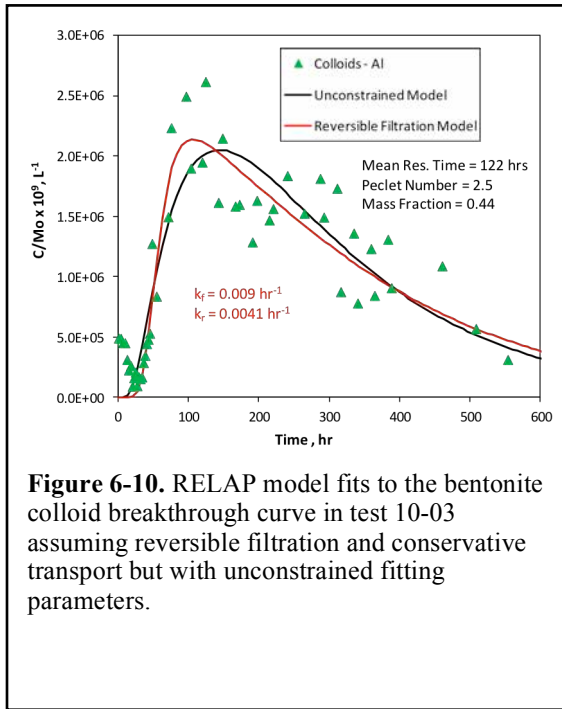


Figure 6-10. RELAP model fits to the bentonite colloid breakthrough curve in test 10-03 assuming reversible filtration and conservative transport but with unconstrained fitting parameters.

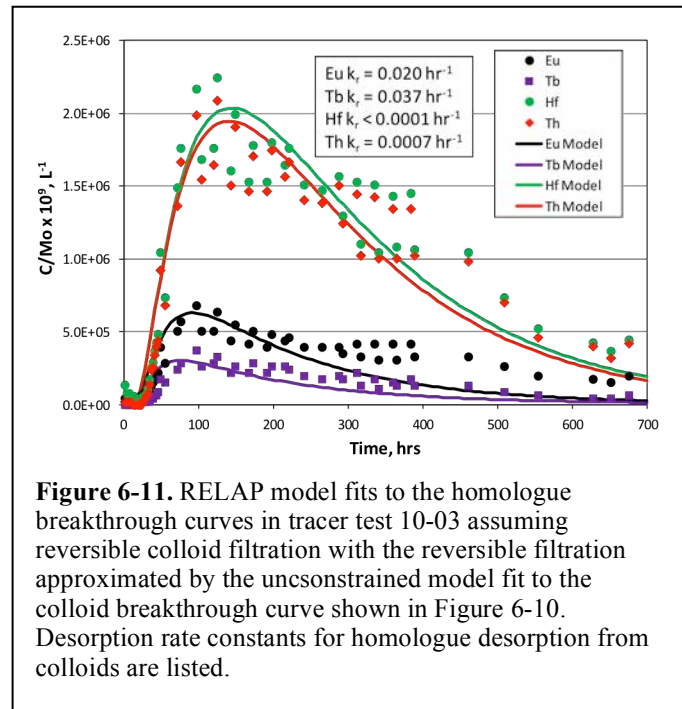


Figure 6-11. RELAP model fits to the homologue breakthrough curves in tracer test 10-03 assuming reversible colloid filtration with the reversible filtration approximated by the unconstrained model fit to the colloid breakthrough curve shown in Figure 6-10. Desorption rate constants for homologue desorption from colloids are listed.

It is informative to compare the colloid and homologue transport-parameter estimates obtained from tracer tests 10-01 and 10-03. The same process was used to estimate the transport parameters in both tests except that a correction for uranine was not needed in test 10-01 because there was no apparent degradation of the uranine in that test. Figures 6-12 and 6-13 show the resulting best-fitting colloid and homologue breakthrough curves for test 10-01, respectively. Details of the analyses were provided in last year's UFD milestone report for saturated zone transport (Arnold et al., 2011). The key test variables and best-fitting transport parameters in the two tests are listed in Table 6-1.

Table 6-1 shows that there was a greater apparent colloid filtration rate constant in test 10-01 than in test 10-03, and the desorption rate constants for the homologues were also greater in test 10-01 than in test 10-03.

However, the general trends of greater desorption of Eu and Tb from the colloids than either Hf or Th are consistent between the two tests. The reasons for the differences in the rate constants in the two tests are unknown. It would be interesting to find out if the homologues were adsorbed to the colloids for a greater amount of time before injection in test 10-03 than in test 10-01. If this were the case, it might suggest that

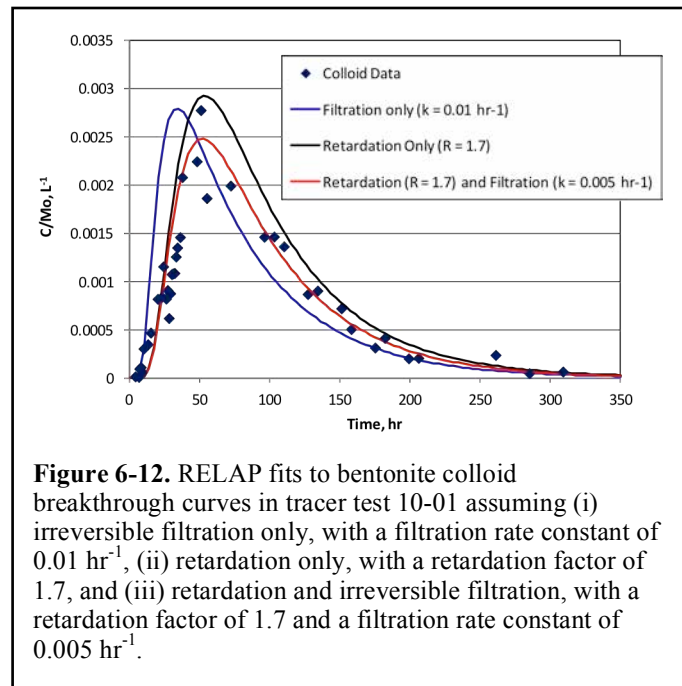


Figure 6-12. RELAP fits to bentonite colloid breakthrough curves in tracer test 10-01 assuming (i) irreversible filtration only, with a filtration rate constant of 0.01 hr^{-1} , (ii) retardation only, with a retardation factor of 1.7, and (iii) retardation and irreversible filtration, with a retardation factor of 1.7 and a filtration rate constant of 0.005 hr^{-1} .

aging of homologue-colloid bonds resulted in less homologue desorption from the colloids in test 10-03. It would also be informative to find out if there were any difference in the way that the bentonite colloids were generated for the two tests, as this might suggest a difference in the transport and adsorption properties of the colloids. Of course, it must be kept in mind that the colloid filtration rate constant estimated in test 10-03 is highly dependent on the uranine breakthrough curve, which in turn is dependent on the accuracy of the method used to convert the observed uranine breakthrough curve to the breakthrough curve used for the colloid filtration analysis. It is reasonable to assume that the flow pathways in the shear zone were similar in the two tests, although the mean residence time in test 10-03 was approximately three times longer than in test 10-01.

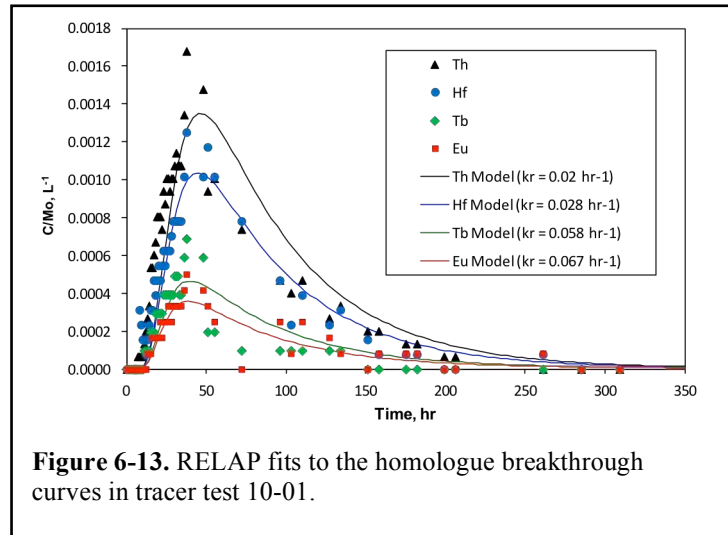


Figure 6-13. RELAP fits to the homologue breakthrough curves in tracer test 10-01.

Table 6-1. Comparison of transport parameters deduced from RELAP modeling for homologue tracer tests 10-01 and 10-03 (see Figures 6-8, 6-10 and 6-12 for details of deduced colloid filtration rate parameters in the two tests).

Parameter	Test 10-01	Test 10-03
Pinkel Extraction Flow, mL/min	48	10
Deduced Injection Interval Flow, mL/min	0.56	0.29 (first 125 hrs)
Mean Uranine Residence Time*, hr	22	64
Uranine Peclet Number*	9	15
Uranine Recovery, Observed	0.82	0.19-0.2
Uranine Recovery, Modeled	0.85	0.45 (corrected)
Colloid filtration rate constant**, hr ⁻¹	0.006-0.01	0.0039-0.009
Eu desorption rate constant, hr ⁻¹	0.067	0.020-0.023
Tb desorption rate constant, hr ⁻¹	0.058	0.037
Hf desorption rate constant, hr ⁻¹	0.028	0.0001-0.0007
Th desorption rate constant, hr ⁻¹	0.02	0.0007-0.0018

* Residence times and Peclet numbers apply to the shear zone only; they do not include the residence time and dispersion in the injection interval.

** The first value for test 10-01 is for irreversible filtration assuming there is also some reversible filtration with an effective retardation factor of 1.7; the second value assumes irreversible filtration only. The first value for test 10-03 assumes irreversible filtration, and the second value assumes slow, reversible filtration.

6.3 Inferences about Shear Zone Flow Pathways from Conservative Tracer Responses in Tracer Tests 10-01 through 12-02

The injection and extraction concentration histories of conservative tracers in CFM tracer tests 10-01 through 12-02 collectively offer some insights into residence times in flow pathways as a function of injection and extraction flow rates in the MI shear zone between injection interval CFM 06.002i2 and the

Pinkel surface packer. With the exception of test 11-01, each of the tracer tests provided an interpretable tracer breakthrough curve at the extraction point (Pinkel) as well as an injection concentration history in CFM 06.002i2. Starting with test 11-01, the three new monitoring boreholes CFM 11.001, 11.002, and 11.003 were included as part of the flow system, and it immediately became apparent that the flow through CFM 06.002i2, presumably at least partly induced by the extraction of water at the Pinkel surface packer, was dramatically reduced (by nearly an order of magnitude) compared to what it had been before the monitoring boreholes were installed. The apparent explanation for this flow reduction is that the flow pathways in the immediate vicinity of CFM 06.002i2 were altered by the drilling of the monitoring boreholes, which either caused some blockage of pre-existing pathways or perhaps removed previous blockages that helped channel flow through the injection interval. However, the imposition of even a relatively low net injection rate into CFM 06.002i2 (similar to the natural flow rates observed before the monitoring boreholes were installed) resulted in rapid tracer responses at the Pinkel surface packer, suggesting that the effects of the flow pathway modifications could be quite easily overcome with a minor “push” into the injection interval.

Each of the tracer tests was analyzed using the RELAP model in a manner similar to that of tracer test 10-03 in the previous section to obtain estimates of flow rates through the injection interval and mean residence times in the MI shear zone. The injection and extraction flow rates and the estimated mean residence times and Peclet numbers in the shear zone in each test are listed in Table 6-2. Table 6-2 also lists the tracer recoveries in each test (corrected recovery in the case of uranine in test 10-03). For all tests in which both AGA and uranine were used, the analysis was based on the AGA concentration histories because of the apparent degradation of uranine in the injection loop in most tests in which this tracer was used. Note that the apparent flow rates through the injection interval in tests 10-01 through 10-04 (prior to installation of the monitoring boreholes) do not appear to vary linearly with the extraction flow rate, suggesting that the flow rate through the injection interval was dependent on natural flow conditions in the entirety of the shear zone at the time of the tests rather than induced by the extraction flow rate.

Table 6-2. Extraction and injection flow rates, mean residence times (shear zone), Peclet numbers (shear zone), and conservative tracer mass recoveries inferred from RELAP modeling of tracer tests 10-01 through 12-02.

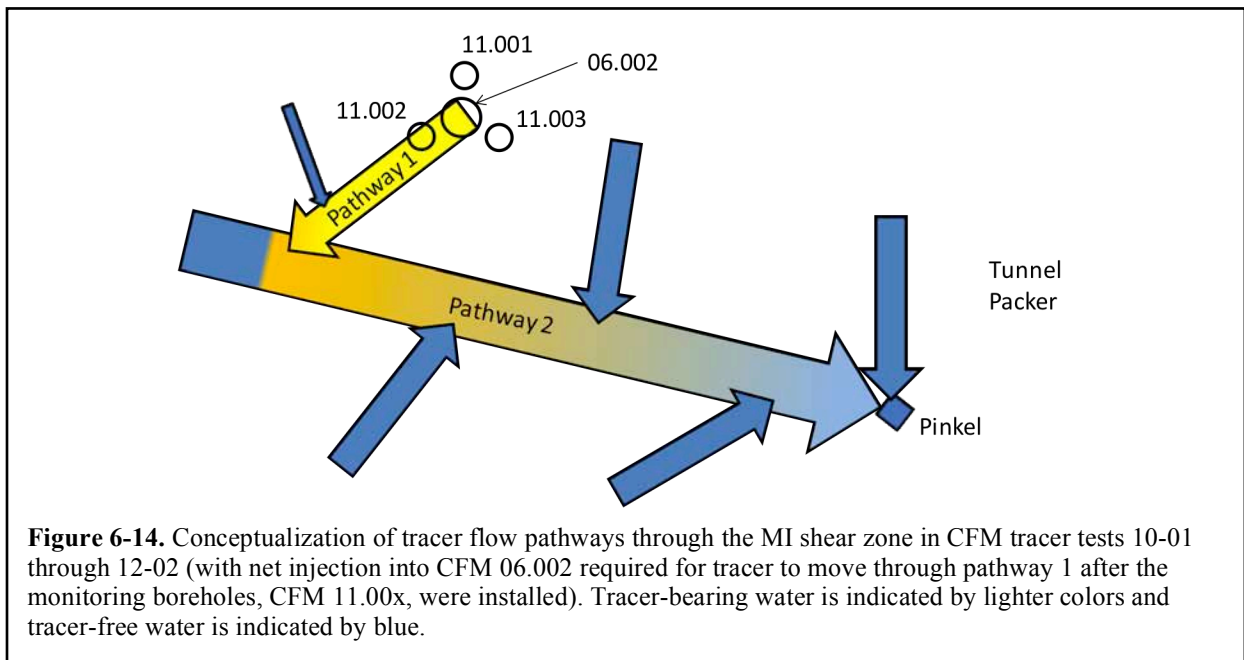
Test	Ext. Flow, mL/min	Inj. Flow*, mL/min	Res. Time, hrs	Peclet No.	Modeled Tracer Recovery**
10-01	48	0.56	22	9	0.85
10-02	10	1.51-0.42	31	31	0.74
10-03	10	0.29-0.48	64	15	0.45
10-04	25	1.01-0.645	19	6	1.0
11-02	25	6.68	9.6	10	0.92
11-03	25	0.255	34	11	0.86
12-01	25	0.395	33	16	0.64
12-02	25	0.49-0.36	35	8	0.60

*Injection flow rates are calculated from slopes of log-linear plots of injection concentration vs. time in the injection interval. The first number is the initial injection flow rate, and second number is the flow rate that occurred after the initial flow rate.

**Modeled tracer recoveries do not necessarily exactly match observed recoveries. Note that the recovery for test 10-03 is corrected for uranine degradation assumed to occur in the injection loop.

Conceptually, the travel time for tracers between CFM 06.002i2 and the Pinkel surface packer can be divided into two components: (1) a component that depends primarily on the flow rate through the injection interval and represents a flow pathway that carries tracers out of the injection interval toward a second flow pathway that ultimately reaches the Pinkel; and (2) a component representing a flow pathway that does not intersect the injection interval but flows directly to the Pinkel and therefore depends on the extraction flow rate. Dilution with tracer-free

water from the shear zone can occur along either flow pathway, although it is likely that more dilution occurs along pathway 2 or perhaps even right at the Pinkel extraction point than in pathway 1. This conceptualization is depicted schematically in Figure 6-14. Note that flow pathway 1 is depicted as moving through monitoring borehole CFM 11.002 because this borehole had by far the best communication with CFM 06.002i2 in tracer test 11-03. However, this inference cannot be proven without further testing because the interborehole communication in test 11-03 was established under natural flow conditions, not the net injection conditions required for tracer recovery at the Pinkel after installation of the monitoring boreholes.



The sum of the travel times in each pathway in a given tracer test must equal the mean residence time in the shear zone deduced from the RELAP analysis for that test. If it is assumed that the same two flow pathways are involved in each tracer test, then the *relative* times that tracers spend in each pathway in each test should be inversely proportional to either the injection or extraction flow rates, depending on which flow pathway is being considered. For example, if we consider tracer tests 10-01 and 10-02, and we assume that the travel times in pathways 1 and 2 in test 10-01 are X and Y, respectively, then the travel times in test 10-02 would have to be 0.371X and 4.8Y, respectively (given that the injection flow rate in test 10-01 was 0.371 [= 0.56/1.51] times that in test 10-02 and the extraction flow rate in 10-01 was 4.8 [= 48/10] times that in 10-02). We can then solve for X and Y for these two tests by simultaneously solving the following equations:

$$X + Y = 22 \quad (\text{Eq. 6-1})$$

$$0.371X + 4.8Y = 31 \quad (\text{Eq. 6-2})$$

The result is $X = 16.85$ hr and $Y = 5.15$ hr. That is, over 25% of the time in the shear zone in test 10-01 was spent in the first flow pathway, and less than 25% was spent in the second flow pathway. However, in test 10-02, only 6.25 hr were spent in the first flow pathway (because of the higher flow rate through the injection interval) but 24.75 hr were spent in the second flow pathway (because of the much lower extraction flow rate in 10-02 relative to 10-01). This analysis can be extended to any pair of tests, or it could be applied simultaneously to numerous tests as a minimization problem where the values of X and Y that minimize the differences between the right and left sides of the equations are solved. For this analysis, the tracer tests were paired in various combinations to solve for X and Y . The 10-0x series tests were paired together in all possible combinations, and likewise the 11-0x and 12-0x series tests were paired together in all possible combinations. The tests from the two different series were not paired together because of the potential differences in the flow pathways caused by the installation of the monitoring boreholes between the two series.

It was immediately observed that the best results appeared to be obtained from combinations in which the injection and extraction flow rates were varied in opposite directions (e.g., the example of tests 10-01 and 10-02 given above) and that poorer results were obtained when there were only small differences in the flow rates between the two tests (e.g., tests 11-03, 12-01 and 12-02) or when the flow rates varied in the same direction (tests 10-03 and 10-04). Mathematically, it is understandable that these latter situations would lead to more poorly constrained estimates of X and Y .

Results from the paired analyses are listed in Table 6-3. Note that the pairing of 10-03 and 10-04 leads to unrealistic residence times in the second flow pathway for these two tests, which is a consequence of the flow rates in each pathway increasing by almost the same fraction from test 10-03 to 10-04 (meaning that the decrease in overall residence time in 10-04 could be attributed to the flow rate increases in either or both flow pathways). Results are not shown for the pairings between tests 11-03, 12-01, and 12-02 because all of these tests had the same extraction flow rate and nearly the same overall mean residence time and injection flow rate (Table 6-2), so the resulting estimates of X and Y were very poorly constrained. However, the pairings of each of these tests with test 11-02 (i.e., the AGA breakthrough curve after 289 hr, when a high net injection rate was imposed) yielded good results. Note that for all of the analyses, the injection flow rate deduced from the injection concentration history (slope of log-linear plot multiplied by injection interval volume) was used instead of the flow rate nominally reported from flowmeter measurements. The former was considered to be a more accurate measure of the flow rate through the interval, which in principle could be different from the net injection flow rate if there were an additive or subtractive component of the natural flow through the interval.

From a practical standpoint, the results of Table 6-3 are perhaps best summarized by multiplying each of the residence times in pathways 1 and 2 by the injection or extraction flow rate, respectively, and then averaging the results to obtain constants that, when divided by the specific flow rates in a given test, will yield an estimate of the travel times in each pathway in the test. When this is done for all combinations of the results from tests 10-01 through 10-04, with the exception of the 03-04 pairing, the result is that the travel time in pathway 1 (flowing out of the injection interval) is given by $9.9/A$ hrs, where A is the injection flow rate in ml/min, and the travel time in pathway 2 is given by $274/B$ hrs, where B is the extraction flow rate in ml/min. For tests 11-02 through 12-01 (using only the pairings of 11-02 with all other tests), the results are $9.9/A$ and $203/B$ hr, respectively.

Table 6-3. Tracer residence times in pathways 1 and 2 (Figure 6-14) as deduced from paired analyses of overall residence times in tracer tests.

Test Predicted	Test Paired With	Pathway 1 Res. Time, hrs	Pathway 2 Res. Time, hrs
10-01	10-02	16.85	5.15
10-02	10-01	6.25	24.75
10-01	10-03	13.6	8.4
10-03	10-01	23.8	40.2
10-01	10-04	17	5
10-04	10-01	9.4	9.6
10-02	10-03	7.85	23.15
10-03	10-02	40.86	23.15
10-02	10-04	6.1	24.9
10-04	10-02	9.0	10.0
10-03	10-04	57.4	6.6
10-04	10-03	16.25	2.65
11-02	11-03	0.97	8.63
11-03	11-02	25.37	8.63
11-02	12-01	1.5	8.1
12-01	11-02	24.9	8.1
11-02	12-02	2.0	7.6
12-02	11-02	27.4	7.6

The excellent agreement between the two sets of tests for pathway 1 suggests that the local flow pathway modifications caused by the installation of the monitoring boreholes prior to the 11-0x series of tests did not substantially alter the larger-scale flow pathways or residence times of this pathway, provided the injection flow rate is above some critical value. Below some critical value (estimated to be somewhere between 0.14 ml/min and 0.25 ml/min based on results from 11-01 and 11-03), it is likely that the natural flow through the shear zone in the vicinity of CFM 06.002i2 carries most tracer out of the injection interval into pathways that do not intersect pathway 2. Very small extraction responses of uranine in test 11-01 under natural flow conditions suggest that there is a small amount of communication between the injection interval and pathway 2 at injection interval flow rates of 0.10–0.14 ml/min, but this communication could not be quantified because of the lack of a uranine injection concentration history in this test due to saturation of the injection fluorimeter signal for uranine.

The differences in the pathway 2 residence times as a function of extraction flow rate determined from the two sets of tracer tests, i.e., 272/B vs. 203/B hrs, is not easily explained, although for an extraction flow rate of 25 ml/min, this difference is only ~11 hr vs. ~8 hr. Modifications of local flow pathways around CFM 06.002i2 would not be expected to significantly influence pathway 2 residence times, although this possibility cannot be ruled out. Perhaps the best plausible explanation for the differences is that the larger pathway 2 residence times deduced from the 10-0x series of tests are a consequence of two of the four tests being conducted at the very low extraction flow rate of 10 ml/min, whereas all of the tests from 11-02 through 12-02 were conducted at an extraction flow rate of 25 ml/min. Tests conducted at lower extraction flow rates are more likely to be influenced by the natural flow conditions in the shear zone, which may have had a superimposing effect of increasing residence times in pathway 2, with the increase being less pronounced for higher extraction flow rates. The low conservative tracer recovery deduced for test 10-03, which had an extraction flow rate of 10 ml/min and a much longer shear zone residence time

than any other test, supports this hypothesis (although there is some uncertainty in the recovery because of the uranine degradation). Given this line of reasoning, residence times of 203/B hr for pathway 2 are considered more likely than 273/B hr when Pinkel extraction flow rates are 25 ml/min or greater.

Future directions to better understand how residence times in flow pathways between CFM 06.002i2 and the Pinkel surface packer depend on injection and extraction flow rates should include additional consideration of the influence of the natural flow system, which in turn is likely influenced by variables such as lake levels and far-field shear zone heads. An analysis incorporating these natural system effects could be conducted for tests 10-01 through 12-02 if lake levels and shear zone head data were available for all these tests.

6.4 Conclusions

The interpretation of CFM homologue tracer test 10-03, including corrections for uranine degradation in the injection loop deduced from tracer test 11-02, suggests that the FEBEX bentonite colloids in this test experienced approximately the same filtration parameters as the bentonite colloids in tracer test 10-01. The two tests were conducted in the same flow configuration, but test 10-03 had a shear-zone residence time approximately three times longer than test 10-01. The primary difference in the colloid transport in the two tests was that the first arrival of the bentonite was delayed somewhat relative to the conservative tracer uranine in test 10-01, whereas there was little or no delay in the first arrival but greater tailing of the bentonite relative to uranine in test 10-03. Some reversible colloid filtration was inferred from both tests, with the delayed colloid arrival suggesting reversibility in test 10-01, and the extended colloid tailing suggesting reversibility in test 10-03. The homologues had slightly smaller apparent desorption-rate constants from the bentonite colloids in test 10-03, resulting in slightly greater colloid-facilitated transport of the homologues in this test relative to test 10-01. The reasons for the greater colloid-facilitated transport of the homologues in test 10-03 are unclear at this time. It is suggested that the details of colloid preparation and the procedure for adsorption of homologues to the colloids be evaluated for both tests 10-01 and 10-03 to look for any differences that might help explain the observed differences in the transport behavior of either the colloids or the homologues in the two tests.

The combined analysis of shear-zone residence times as a function of injection and extraction flow rates in tests 10-01 through 12-02 suggests a two-pathway conceptual model for flow in the shear zone between CFM 06.002i2 and the Pinkel surface packer, with the residence time in the first pathway being dependent primarily on the injection flow rate and the residence time in the second pathway being dependent primarily on the extraction flow rate. The first flow pathway was apparently disrupted locally around CFM 06.002i2 after the three monitoring boreholes (CFM 11.001, .002, and .003) were installed in 2011, resulting in less communication between CFM 06.002i2 and the Pinkel under natural dilution conditions in CFM 06.002i2. However, the communication between CFM 06.002i2 and the Pinkel was almost the same before and after installation of the monitoring holes when a net injection flow of at least 0.25 ml/min was introduced to CFM 06.002i2. It is suggested that the conceptual model of flow through the shear zone could be improved by incorporating the influence of natural system variables such as lake levels and far-field heads in tests 10-01 through 12-02. A better conceptual model of flow through the shear zone is important for both the planning and interpretation of the in-situ radionuclide-doped bentonite emplacement test scheduled for later in 2012.

6.5 References

- Arnold, B. A., Reimus, P. W., and James, S. C., 2011. Flow and Transport in Saturated Media: FY2011 Status Report. Prepared for U.S. Department of Energy Used Fuel Disposition Campaign, *FCRD-USED-2011-000311*, Sandia National Laboratories and Los Alamos National Laboratory.
- Reimus, P. W., Pohll, G., Mihevc, T., Chapman, J., Papelis, L., Lyles, B., Kosinski, S., Niswonger, R., and Sanders, P., 2003. Testing and parameterizing a conceptual model for radionuclide transport in a fractured granite using multiple tracers in a forced-gradient test, *Water Resour. Res.*, **39**(12), p. 1350, doi:10.1029/2002WR001597.

Chapter 7. Modeling Radionuclide Transport in Clays

7.1 Introduction

Clay/shale has been considered as potential host rock for geological disposal of high-level nuclear waste throughout the world, because of its low permeability, low diffusion coefficient, high retention capacity for radionuclides, and capability to self-seal fractures induced by tunnel excavation. For example, Callovo-Oxfordian argillites at the Bure site, France (Fouche et al., 2004), Toarcian argillites at the Tournemire site, France (Patriarche et al., 2004), Opalinus Clay at the Mont Terri site, Switzerland (Meier et al., 2000), and Boom clay at the Mol site, Belgium (Barnichon and Volckaert, 2003) have all been under intensive scientific investigation (at both field and laboratory scales) for understanding a variety of rock properties and their relationships to flow and transport processes associated with geological disposal of nuclear waste. Clay/shale formations may be generally classified as indurated or plastic clays (Tsang and Hudson, 2010). The latter (including Boom clay) is a softer material without high cohesion; its deformation is dominantly plastic.

During the lifespan of a clay repository, the repository performance is affected by complex thermal, hydrogeological, mechanical, and chemical (THMC) processes, such as heat release due to radionuclide decay, multiphase flow, formation of damage zones, radionuclide transport, waste dissolution, and chemical reactions. All these processes are interrelated. An in-depth understanding of these coupled processes is critical for the performance assessment (PA) of the repository. These coupled processes may affect radionuclide transport by changing transport paths, e.g., formation and evolution of excavation damaged zone (EDZ), and by altering flow, mineral, and mechanical properties that are related to radionuclide transport. While radionuclide transport in clay formation has been studied using laboratory tests (e.g., Appelo et al. 2010, Garcia-Gutierrez et al., 2008, Maes et al., 2008), short-term field tests (e.g., Garcia-Gutierrez et al. 2006, Soler et al. 2008, van Loon et al. 2004, Wu et al. 2009) and numerical modeling (de Windt et al. 2003; 2006), the effects of THMC processes on radionuclide transport are not fully investigated.

The objectives of the research activity documented in this chapter are to improve a modeling capability for coupled THMC processes and to use it to evaluate the THMC impacts on radionuclide transport. This research activity addresses several key Features, Events, and Processes (FEPs), including FEP 2.2.08, Hydrologic Processes, FEP 2.2.07, Mechanical Processes, and FEP 2.2.09, Chemical Process—Transport, by studying near-field coupled THMC processes in clay/shale repositories and their impacts on radionuclide transport.

This chapter documents the progress that has been made in FY12. Section 7.2 discusses the development of THMC modeling capability. Section 7.3 reports modeling results of THMC impacts on radionuclide transport. Planned work for the remaining months of FY12 and proposed work for FY13 are presented in Section 7.4.

7.2 Technical Approaches

This section presents technical approaches used to model THMC processes and their impacts on the migration of U(VI), a common radionuclide.

7.2.1 Simulator

The numerical simulations are conducted with TOUGHREACT-FLAC3D, which integrates TOUGH-FLAC (Rutqvist et al., 2011) and TOUGHREACT Version 2 (Xu et al., 2011). TOUGH-FLAC3D

sequentially couples the finite-difference geomechanical code FLAC3D with the finite-volume, multiphase fluid flow code, TOUGH2 (Pruess et al., 1999).

TOUGHREACT is a numerical simulator for chemically reactive nonisothermal flows of multiphase fluids in porous and fractured media (Xu and Pruess, 2001; Spycher et al., 2003; Sonnenthal et al., 2005; Xu et al., 2006; Xu, 2008; Zhang et al., 2008; Zheng et al., 2009). The code was written in Fortran 77 and developed by introducing reactive chemistry into the multiphase fluid and heat flow simulator TOUGH2 (Pruess, 2004). The code can be applied to one-, two-, or three-dimensional porous and fractured media with physical and chemical heterogeneity, and can accommodate any number of chemical species present in liquid, gas, and solid phases. A variety of subsurface thermal, physical, chemical, and biological processes are considered in TOUGHREACT code under a wide range of conditions of pressure, temperature, water saturation, ionic strength, and pH and Eh. TOUGHREACT Version 2 (Xu et al., 2011) is the latest version of TOUGHREACT. The major chemical reactions that can be considered in TOUGHREACT include aqueous complexation, acid-base, redox, gas dissolution/exsolution, cation exchange mineral dissolution/precipitation, and surface complexation.

TOUGHREACT-FLAC3D was linked in Zheng et al. (2011) to provide the necessary numerical framework for modeling the fully coupled THMC processes. The usefulness of this modeling capability has been demonstrated for modeling of bentonite swelling as a result of changes in saturation and pore-water composition using a simple linear elastic swelling model. In this study, TOUGHREACT-FLAC3D is further enhanced by incorporating a new sorption model for U(VI), to be discussed later.

7.2.2 An elastic model for chemical-mechanical coupling

A detailed discussion of TOUGH-FLAC and its capability to simulate THM deformation is presented in Rutqvist et al. (2011). TOUGHREACT-FLAC3D has the same capability for modeling THM processes. In addition, it has the capability to handle coupling between chemical and mechanical processes. While incorporation of more advanced approaches for handling this coupling into TOUGHREACT-FLAC3D is under consideration, this study employs the relatively simple approach of Laredj et al. (2010).

Laredj et al. (2010) extended the nonlinear elastic model for mechanical deformation (Thomas and He, 1995) by adding a chemical concentration term. It is assumed that the increment of total strain is the sum of the strain increments due to the changes in net mean stress, suction, and chemical solute concentration:

$$d\epsilon = d\epsilon_p + d\epsilon_s + d\epsilon_n \quad (7-1)$$

where the subscripts p , s , and n refer to net mean stress, suction, and chemical solute concentrations, respectively. The stress-strain relationship can be expressed as:

$$\begin{aligned} d\sigma &= D(d\epsilon - d\epsilon_s - d\epsilon_n) \\ &= D(d\epsilon - A_s ds - A_n dn) \end{aligned} \quad (7-2)$$

with

$$d\epsilon_s = A_s ds \quad (7-3)$$

$$d\epsilon_n = A_n dn \quad (7-4)$$

where D is the elastic matrix, σ is the effective stress, and A_s and A_n are constants. Laredj et al. (2010) derived the relation between chemical concentration variation and the corresponding strain and proposed the following expression for A_n :

$$A_n = -\frac{(5.312 \ln c - 23.569)}{\sqrt{n}} - \frac{7.252 \times 10^{-4}}{n^2} \quad (7-5)$$

Rutqvist et al. (2011) included a linear elastic swelling model using a swelling stress, σ_s , that is linearly proportional to the saturation:

$$d\sigma_s = 3K\beta_{sw}ds_l \quad (7-6)$$

where K is the bulk modulus and β_{sw} is a moisture swelling coefficient.

To consider the swelling due to both moisture and chemical concentration change, we include the stress due to a chemical concentration change in equation 7:

$$d\sigma_s = 3K\beta_{sw}ds_l + A_n dn \quad (7-7)$$

7.2.3 Chemical model

As previously indicated, TOUGHREACT-FLAC3D considers a number of chemical reactions that are relevant to radionuclide transport, including aqueous complexation, mineral dissolution/precipitation, cation exchange, and surface complexation. In this section, we present the reactions that are directly related to U(VI) only.

7.2.3.1 Aqueous complexation of U(VI)

Aqueous complexes considered in this study are listed in Table 7-1. Reaction constants are taken from Spycher et al. (2011); most of them are largely consistent with those used in Davis et al. (2004). Among these aqueous species, $\text{Ca}_2\text{UO}_2(\text{CO}_3)_3^0$ and $\text{CaUO}_2(\text{CO}_3)_3^{-2}$ tend to dominate uranium chemistry under typical porewater compositions. A chemical-reaction model that neglects these two species could significantly underestimate the aqueous concentration of U(VI).

7.2.3.2 Sorption reactions

Adsorption/desorption is another important reaction controlling the migration of U(VI) in clay formations. The adsorption/desorption of uranium onto different types of sediments has been widely studied. Although there are still some reactive transport models utilizing the distribution-coefficient (constant-Kd) modeling approach to describe the retardation of uranium in aquifers caused by adsorption reactions (Bethke and Brady, 2000), surface complexation models are currently the most popular ones for calculating the adsorption/desorption of uranium. Typically, surface complexation reactions (including the relevant surface species, the binding constants, and the stoichiometry of the mass action equations) are derived by fitting the macroscopic dependence of adsorption as a function of pH (Davis et al., 1998). Surface reactions can be coupled with aqueous complexation reactions to simulate macroscopic sorption as a function of aqueous chemical conditions.

Table 7-1. Aqueous complexes for U(VI).

Aqueous complexes	Reactions								Logk (25 °C)
	Stoi.	Species	Stoi.	Species	Stoi.	Species	Stoi.	Species	
$(\text{UO}_2)_{11}(\text{CO}_3)_6(\text{OH})_{12}^{-2}$	-18	H ⁺	6	HCO ₃ ⁻	11	UO ₂ ⁺²	12	H ₂ O	25.855
$(\text{UO}_2)_2(\text{OH})_2^{+2}$	-2	H ⁺	2	H ₂ O	2	UO ₂ ⁺²			5.659
$(\text{UO}_2)_2\text{CO}_3(\text{OH})_3^-$	-4	H ⁺	1	HCO ₃ ⁻	2	UO ₂ ⁺²	3	H ₂ O	11.245
$(\text{UO}_2)_2\text{OH}^{+3}$	-1	H ⁺	1	H ₂ O	2	UO ₂ ⁺²			2.729
$(\text{UO}_2)_3(\text{CO}_3)_6^{-6}$	-6	H ⁺	3	UO ₂ ⁺²	6	HCO ₃ ⁻			8.099
$(\text{UO}_2)_3(\text{OH})_4^{+2}$	-4	H ⁺	3	UO ₂ ⁺²	4	H ₂ O			11.962
$(\text{UO}_2)_3(\text{OH})_5^+$	-5	H ⁺	3	UO ₂ ⁺²	5	H ₂ O			15.624
$(\text{UO}_2)_3(\text{OH})_7^-$	-7	H ⁺	3	UO ₂ ⁺²	7	H ₂ O			32.2
$(\text{UO}_2)_3\text{O}(\text{OH})_2(\text{HCO}_3)^+$	-4	H ⁺	1	HCO ₃ ⁻	3	H ₂ O	3	UO ₂ ⁺²	9.746
$(\text{UO}_2)_4(\text{OH})_7^+$	-7	H ⁺	4	UO ₂ ⁺²	7	H ₂ O			21.995
$\text{UO}_2(\text{SO}_4)_2^{-2}$	1	UO ₂ ⁺²	2	SO ₄ ⁻⁻					-3.962
UO_2Cl^+	1	Cl ⁻	1	UO ₂ ⁺²					-0.141
$\text{UO}_2\text{Cl}_2(\text{aq})$	1	UO ₂ ⁺²	2	Cl ⁻					1.146
UO_2F^+	1	F ⁻	1	UO ₂ ⁺²					-5.034
$\text{UO}_2\text{F}_2(\text{aq})$	1	UO ₂ ⁺²	2	F ⁻					-8.519
UO_2F_3^-	1	UO ₂ ⁺²	3	F ⁻					-10.762
$\text{UO}_2\text{F}_4^{-2}$	1	UO ₂ ⁺²	4	F ⁻					-11.521
$\text{UO}_2\text{OSi}(\text{OH})_3^+$	-1	H ⁺	1	SiO ₂ (aq)	1	UO ₂ ⁺²	2	H ₂ O	2.481
$\text{UO}_2\text{SO}_4(\text{aq})$	1	SO ₄ ⁻²	1	UO ₂ ⁺²					-3.049
UO_2OH^+	-1	H ⁺	1	H ₂ O	1	UO ₂ ⁺²			5.218
$\text{UO}_2(\text{OH})_2(\text{aq})$	-2	H ⁺	2	H ₂ O	1	UO ₂ ⁺²			12.152
$\text{UO}_2(\text{OH})_4^{-2}$	-4	H ⁺	1	UO ₂ ⁺²	4	H ₂ O			32.393
$\text{UO}_2\text{CO}_3(\text{aq})$	-1	H ⁺	1	HCO ₃ ⁻	1	UO ₂ ⁺²			0.396
$\text{UO}_2(\text{CO}_3)_2^{-2}$	-2	H ⁺	2	HCO ₃ ⁻	1	UO ₂ ⁺²			4.048
$\text{UO}_2(\text{CO}_3)_3^{-4}$	-3	H ⁺	3	HCO ₃ ⁻	1	UO ₂ ⁺²			9.141
$\text{CaUO}_2(\text{CO}_3)_3^{-2}$	-3	H ⁺	1	Ca ⁺²	3	HCO ₃ ⁻	1	UO ₂ ⁺²	3.806
$\text{Ca}_2\text{UO}_2(\text{CO}_3)_3$	-3	H ⁺	2	Ca ⁺²	3	HCO ₃ ⁻	1	UO ₂ ⁺²	0.286

Although numerous surface complexation models have been developed to describe the sorption of uranium on clay minerals, these models differ in many details and generally lack consistency.

First, models differ in the types of sites. Clay minerals, such as illite, kaolinite, and smectite, usually have two types of surface sites: (1) permanent negatively charged sites whose charges are structural, also called basal face sites, and (2) variably charged sites that usually reside at the edge of a mineral, also called edge sites—Gu et al. (2010). These edge sites were also further divided into aluminol and silanol (McKinley et al. 1995) or even Fe(III)-hydroxyls groups (Tournassat et al. 2004). Also, in studying the sorption of U(IV) on montmorillonite, illite, and Opalinus clay formations, Bradbury and Baeyens (2005), Bradbury and Baeyens (2009b), and Bradbury and Baeyens (2011) use two types of sites—one “strong” site and two “weak” sites: the strong sites are analogous to basal face sites, and the weak sites are similar in definition to the edge sites.

Second, these models also differ in the way they account for the electrostatic term— using a triple-layer model (McKinley et al. 1995), a double-layer model (Arda et al. 2006; Arai et al. 2006), or a constant-capacity model, or ignoring the electrostatic term (Bradbury and Baeyens 2005; Bradbury and Baeyens 2009b; Bradbury and Baeyens 2011).

Third, the surface species, i.e., surface complexation binding of U(VI), used in the models described above are very different. Sometimes the differentiation of surface species are supported by microscopic experimental results (Catalano and Brown Jr., 2005), but more frequently researchers do so only because more than one reaction is needed to fit the measured data (McKinley et al., 1995). Moreover, the aqueous chemical environment in which the sorption tests were conducted also affects the surface species that forms. For example, the model in Korichi and Bensmali (2009) was developed in the absence of Ca^{+2} and the model of Gao et al. (2010) did not consider Ca and CO_3^{-2} .

In this study, we use the so called two-site protolysis nonelectrostatic surface complexation and cation exchange sorption model (2 SPNE SC/CE) (Bradbury and Baeyens, 2011). In this model, surface protonation reactions that involve a strong site (ill_sOH or mon_sOH) and two weak sites (ill_w1OH, ill_w2OH or mon_w1OH, mon_w2OH) are used to describe acid-base titration measurements, whereas surface complexation reactions with the one strong site and two weak sites are needed to describe the sorption edge and isotherm measurements for the sorption of U(VI) on montmorillonite and illite. A detailed discussion of the 2 SPNE SC/CE model for montmorillonite was given in Bradbury and Baeyens (2005); a similar discussion for illite was given in Bradbury and Baeyens (2009a) and Bradbury and Baeyens (2009b). The first twelve reactions listed in Table 7-2 are the surface protonation reactions on montmorillonite and illite (Bradbury and Baeyens, 2009b), the next six reactions are the surface complexation reactions for the sorption of U(VI) on illite, and the last six reactions are the surface complexation reactions for the sorption of U(VI) on montmorillonite.

Table 7-2. The surface protonation reactions on montmorillonite and illite and surface complexation reactions for the sorption of U(VI) on montmorillonite and illite (Bradbury and Baeyens, 2009b)

Surface complexation	logK
$\text{ill_sOH}_2^+ = \text{ill_sOH} + \text{H}^+$	-4
$\text{ill_sO}^- + \text{H}^+ = \text{ill_sOH}$	6.2
$\text{ill_w1OH}_2^+ = \text{ill_w1OH} + \text{H}^+$	-4
$\text{ill_w1O}^- + \text{H}^+ = \text{ill_w1OH}$	6.2
$\text{ill_w2OH}_2^+ = \text{ill_w2OH} + \text{H}^+$	-8.5
$\text{ill_w2O}^- + \text{H}^+ = \text{ill_w2OH}$	10.5
$\text{mon_sOH}_2^+ = \text{mon_sOH} + \text{H}^+$	-4.5
$\text{mon_sO}^- + \text{H}^+ = \text{mon_sOH}$	7.9
$\text{mon_w1OH}_2^+ = \text{mon_w1OH} + \text{H}^+$	-4.5
$\text{mon_w1O}^- + \text{H}^+ = \text{mon_w1OH}$	7.9
$\text{mon_w2OH}_2^+ = \text{mon_w2OH} + \text{H}^+$	-6
$\text{mon_w2O}^- + \text{H}^+ = \text{mon_w2OH}$	10.5
$\text{ill_sOUO}_2^+ + \text{H}^+ = \text{ill_sOH} + \text{UO}_2^{+2}$	-2
$\text{ill_sOUO}_2\text{OH} + 2\text{H}^+ = \text{ill_sOH} + \text{UO}_2^{+2} + \text{H}_2\text{O}$	3.5
$\text{ill_sOUO}_2(\text{OH})_2^- + 3\text{H}^+ = \text{ill_sOH} + \text{UO}_2^{+2} + 2\text{H}_2\text{O}$	10.6

Surface complexation	logK
$\text{ill_sOUO}_2(\text{OH})_3^{-2} + 4\text{H}^+ = \text{ill_sOH} + \text{UO}_2^{+2} + 3\text{H}_2\text{O}$	19
$\text{ill_w1OUO}_2^+ + \text{H}^+ = \text{ill_w1OH} + \text{UO}_2^{+2}$	-0.1
$\text{ill_w1OUO}_2\text{OH} + 2\text{H}^+ = \text{ill_w1OH} + \text{UO}_2^{+2} + \text{H}_2\text{O}$	5.3
$\text{mon_sOUO}_2^+ + \text{H}^+ = \text{mon_sOH} + \text{UO}_2^{+2}$	-3.1
$\text{mon_sOUO}_2\text{OH} + 2\text{H}^+ = \text{mon_sOH} + \text{UO}_2^{+2} + \text{H}_2\text{O}$	3.4
$\text{mon_sOUO}_2(\text{OH})_2^- + 3\text{H}^+ = \text{mon_sOH} + \text{UO}_2^{+2} + 2\text{H}_2\text{O}$	11
$\text{mon_sOUO}_2(\text{OH})_3^{-2} + 4\text{H}^+ = \text{mon_sOH} + \text{UO}_2^{+2} + 3\text{H}_2\text{O}$	20.5
$\text{mon_w1OUO}_2^+ + \text{H}^+ = \text{mon_w1OH} + \text{UO}_2^{+2}$	-0.7
$\text{mon_w1OUO}_2\text{OH} + 2\text{H}^+ = \text{mon_w1OH} + \text{UO}_2^{+2} + \text{H}_2\text{O}$	5.7

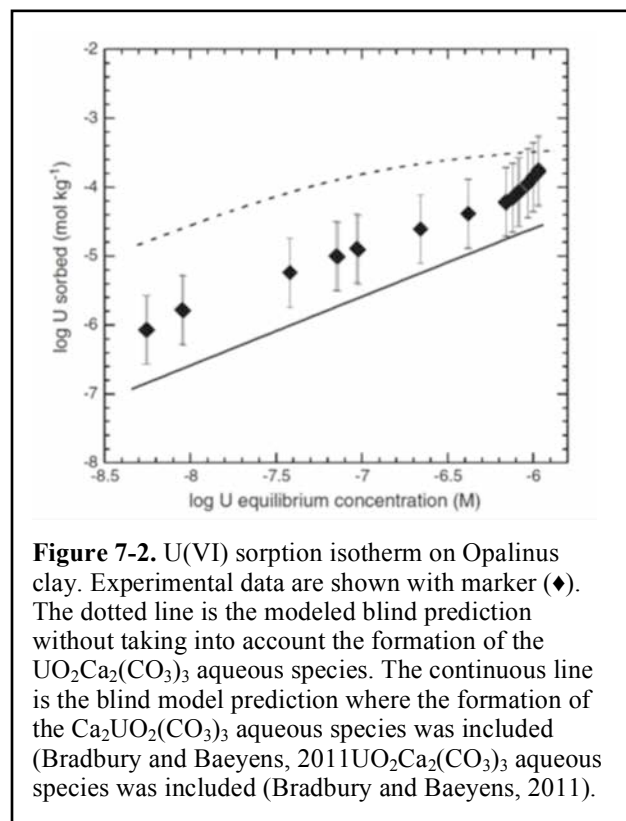
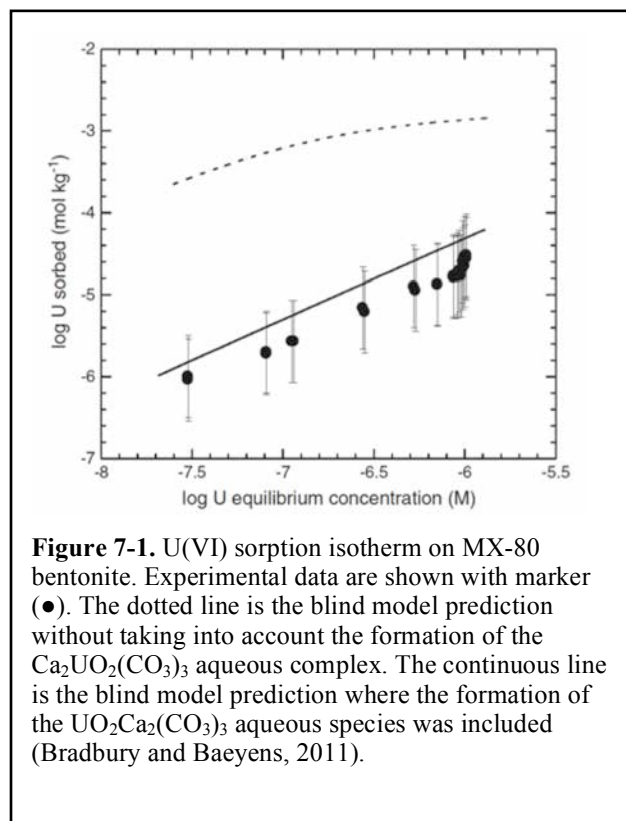
In addition to the surface complexation reactions listed in Table 7-2, cation exchange reactions are also required to describe the pH sorption edge and isotherm measurement, listed in Table 7-3.

Table 7-3. Cation exchange reactions on montmorillonite and illite (Bradbury and Baeyens, 2009b)

Cation exchange reaction	$K_{\text{Na/M}}$
$\text{Na}^+ + \text{ill-H} = \text{ill-Na} + \text{H}^+$	1
$\text{Na}^+ + \text{ill -K} = \text{ill -Na} + \text{K}^+$	0.0775
$\text{Na}^+ + 0.5 \text{ ill -Ca} = \text{ill -Na} + 0.5\text{Ca}^{+2}$	0.302
$\text{Na}^+ + 0.5 \text{ ill -Mg} = \text{ill -Na} + 0.5\text{Mg}^{+2}$	0.302
$\text{Na}^+ + 0.5 \text{ ill-UO}^{+2} = \text{ill-Na} + 0.5\text{UO}^{+2}$	0.473
$\text{Na}^+ + \text{mon-H} = \text{mon -Na} + \text{H}^+$	1
$\text{Na}^+ + \text{mon -K} = \text{mon -Na} + \text{K}^+$	0.0775
$\text{Na}^+ + 0.5 \text{ mon -Ca} = \text{mon -Na} + 0.5\text{Ca}^{+2}$	0.302
$\text{Na}^+ + 0.5 \text{ mon -Mg} = \text{mon -Na} + 0.5\text{Mg}^{+2}$	0.302
$\text{Na}^+ + 0.5 \text{ mon -UO}^{+2} = \text{mon -Na} + 0.5\text{UO}^{+2}$	0.84

7.2.3.3 Verification of the sorption model with published data

Bradbury and Baeyens (2011) applied the above-mentioned reactions to sorption isotherms of U(VI) on MX-80 bentonite and Opalinus clay. However, some discrepancies were observed between the data and their model results, as illustrated in Figures 7-1 and 7-2. Although they mentioned that a Ca-U-carbonate aqueous complex, i.e., $\text{Ca}_2\text{UO}_2(\text{CO}_3)_3$, was included in their model, it is not clear whether they included other aqueous complexes, which also might have a substantial effect on the data fitting.



In order to test our model and improve the match between data and model, reactions in Table 7-1, 7-2 and 7-3 were incorporated into a batch model, and simulations were conducted with TOUGHREACT. The model results are compared with the data reported in Bradbury and Baeyens (2011). MX-80 bentonite contains 75 wt% of montmorillonite (Muller-Vonmoos and Kahr, 1983), and Bradbury and Baeyens (2011) assumed that montmorillonite is the only adsorbent for U(VI). Here, we make the same assumption. Figure 7-3 shows the calculated U(VI) sorption isotherm for MX-80 bentonite. Model results from TOUGHREACT match closely with the model results of Bradbury and Baeyens (2011).

As revealed in Bradbury and Baeyens (2011), consideration of a $\text{Ca}_2\text{UO}_2(\text{CO}_3)_3$, makes a significant difference to the sorption isotherm of U(VI). As more aqueous complexes of U(VI) have been reported (e.g., Bernhard et al., 2001; Spycher et al., 2011), they should be included in the geochemical models. For example, in addition to $\text{Ca}_2\text{UO}_2(\text{CO}_3)_3$, $\text{CaUO}_2(\text{CO}_3)_3^{-2}$ could be another Ca-U-carbonate aqueous complex that could affect the sorption of U(VI). In the TOUGHREACT model shown in Figure 7-3, all the aqueous complexes listed in Table 7-1 are included. In order to evaluate how the inclusion of aqueous complexes affect the calculation of the U(VI) sorption isotherm, we test three scenarios as illustrated in Figure 7-4: without $\text{Ca}_2\text{UO}_2(\text{CO}_3)_3$, without $\text{Ca}_2\text{UO}_2(\text{CO}_3)_3$ and $\text{CaUO}_2(\text{CO}_3)_3^{-2}$, and without all the aqueous complexes that contains carbonate. Without including the important aqueous complexes, models tend to overestimate the sorption of U(VI).

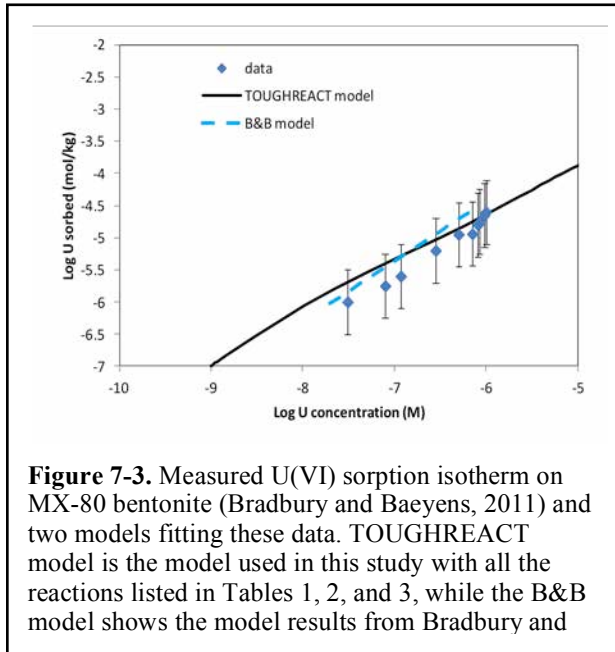


Figure 7-3. Measured U(VI) sorption isotherm on MX-80 bentonite (Bradbury and Baeyens, 2011) and two models fitting these data. TOUGHREACT model is the model used in this study with all the reactions listed in Tables 1, 2, and 3, while the B&B model shows the model results from Bradbury and

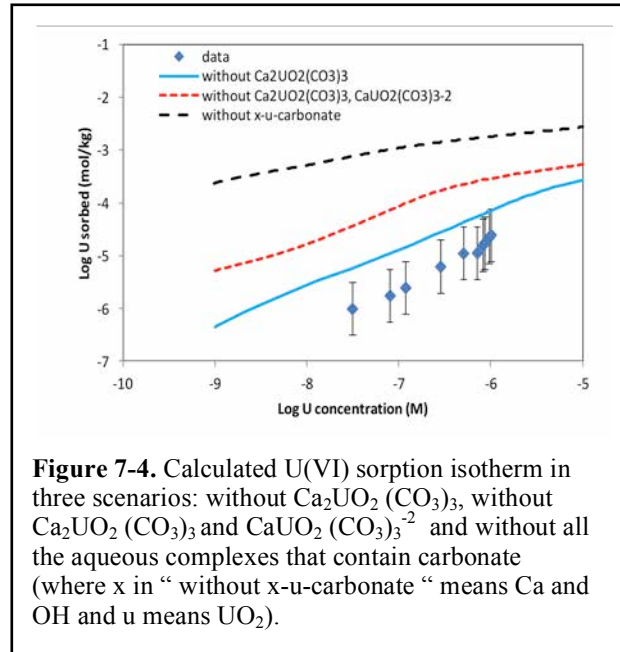


Figure 7-4. Calculated U(VI) sorption isotherm in three scenarios: without $\text{Ca}_2\text{UO}_2(\text{CO}_3)_3$, without $\text{Ca}_2\text{UO}_2(\text{CO}_3)_3$ and $\text{CaUO}_2(\text{CO}_3)_3^{-2}$ and without all the aqueous complexes that contain carbonate (where x in “without x-u-carbonate” means Ca and OH and u means UO_2).

Although the amount of illite and illite/smectite mixed layers reported in Lauber et al. (2000) are slightly different from those reported in Thury (2002) (which might be attributed to the different sampling locations), it is clear that Opalinus clay contains around 22% illite and 10–18 wt% of illite/smectite mixed layers. In Bradbury and Baeyens’ (2011) model for the sorption of U(VI) on Opalinus clay, they assumed that sorption occurred exclusively on illite with mass fraction of 40%. In an effort to reproduce their model with “TOUGHREACT model A” in Figure 7-5, we make the same assumption. Our model deviates from the model of Bradbury and Baeyens (2011) at lower U(VI)

concentrations, but matches well at higher U(VI) concentrations. This might be caused by the difference in the aqueous complexes and the thermodynamic data. Considering that Opalinus clay also contains some montmorillonite, “TOUGHREACT model B” assumes 22% illite and 14% montmorillonite (see Table 7-5), which, as Figure 7-5 shows, fits better to the measured U(VI) sorption isotherm.

7.2.3.4 Uranium minerals

In the geological repository environment, radionuclides originate from used-fuel waste packages. The degradation of these waste packages is an extremely complex issue. Used fuel pellets are largely composed of

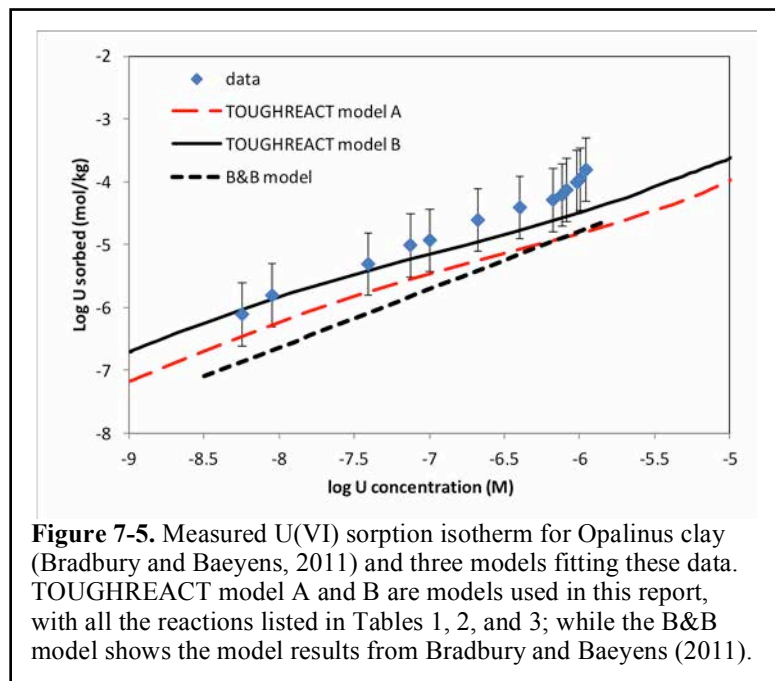
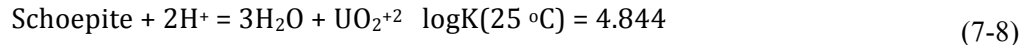


Figure 7-5. Measured U(VI) sorption isotherm for Opalinus clay (Bradbury and Baeyens, 2011) and three models fitting these data. TOUGHREACT model A and B are models used in this report, with all the reactions listed in Tables 1, 2, and 3; while the B&B model shows the model results from Bradbury and Baeyens (2011).

solid UO_2 . Usually, UO_2 would undergo oxidative dissolution with oxidants (typically H_2O_2) produced by α -radiolysis (De Windt et al., 2006): $\text{UO}_2(\text{s}) + \text{H}_2\text{O}_2 = \text{UO}_2^{+2} + 2\text{OH}^-$, U(VI) (UO_2^{+2}) is produced and would precipitate as a secondary U(VI) phase. For example, in a 10-year degradation of $\text{UO}_2(\text{s})$ by dripping water (Bernot, 2005), 11 phases were identified, including schoepite, soddyite, boltwoodite or na-boltwoodite, and uranophane. The formation of these phases depends on possible environmental conditions, such as the aqueous and mineralogical composition of the media in contact with the waste package, as well as the pH, Eh, and CO_2 partial pressure. The oxidation of $\text{UO}_2(\text{s})$ and the formation of secondary U(VI) phases are slow and usually simulated as kinetics processes (De Windt et al., 2003). However, as the waste packages degrade, the U concentration is controlled by the least soluble uranium phase that is stable under the given geochemical conditions. To be conservative, and for reasons of simplicity, the source concentration of uranium is usually determined by the solubility of the U(VI) phase that is possibly present in the given performance assessment environment. After an evaluation of the possible U(VI) minerals, Bernot (2005) selected schoepite as the controlling phase, because laboratory studies of Wronkiewicz et al. (1996) showed it to be the dominant early-formed phase in $\text{UO}_2(\text{s})$ degradation. In this report, we take the same strategy and assume that the waste package is composed only of schoepite; the concentration of U(VI) is then controlled by the following reaction:



The logK value of the reaction is taken from the EQ3/6 database data0.ymp.R5, and the variation in logK as a function of temperature is given as:

$$\log K(T) = 14.6 \ln(T) - 92.016 - 1.644 \times 10^{-2}T + 5.5357 \times 10^{-3}/T \quad (7-9)$$

where T is temperature (K).

7.3 Model Setup

7.3.1 Model domain

The THMC simulations were conducted for a hypothetical bentonite-back-filled nuclear waste repository in clay rock. The repository example is taken from the DECOVALEX IV project involving a horizontal nuclear waste emplacement tunnel at 500 m depth (Figure 7-6) (Rutqvist et al., 2009). The problem has been simulated by a number of teams in the DECOVALEX project using simplified models of bentonite behavior.

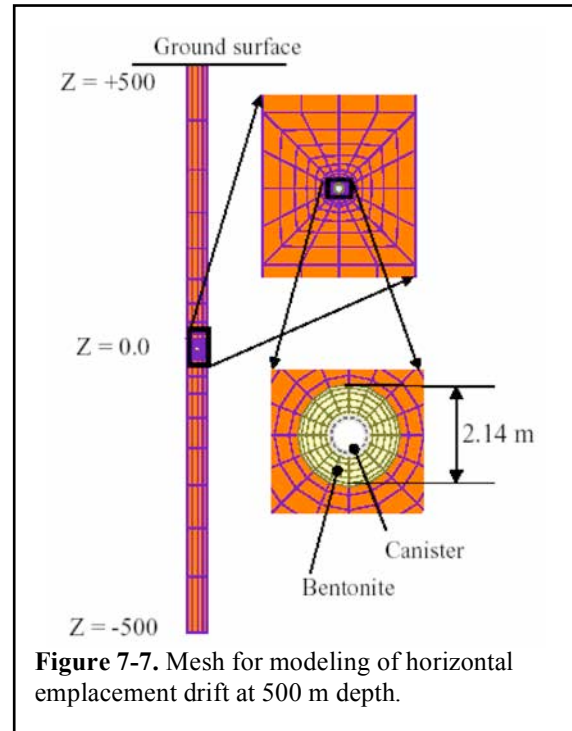
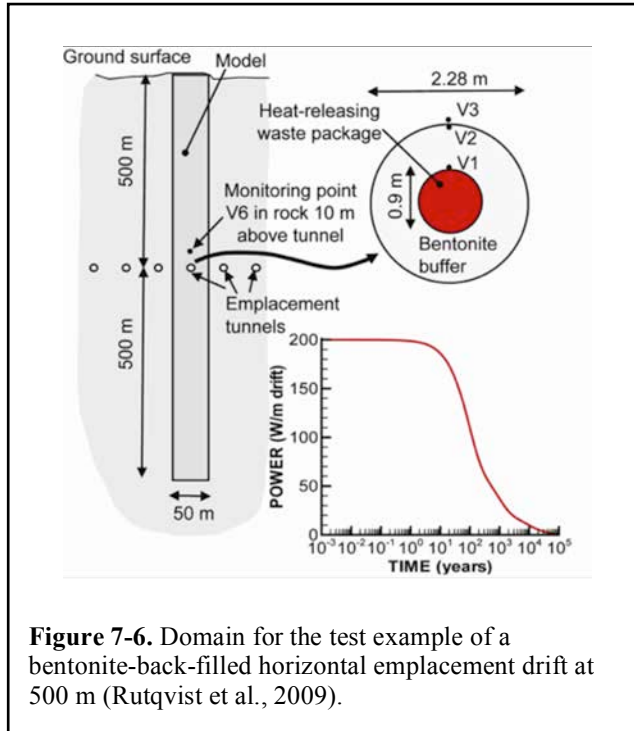
In this study, a calculation using the improved TOUGHREACT-FLAC3D was carried out with an elastic approach for mechanical deformation, assuming that the rock matrix is isotropic. We constructed a numerical model with a geometry containing one circular tunnel and consisting of 368 grid blocks. The configuration of the model is shown in Figure 7-7. The Z-axis is set as vertical in the model, while the horizontal Y- and X-axes are aligned parallel and perpendicular to the emplacement tunnel, respectively.

7.3.2 Initial and boundary conditions

7.3.2.1 THM model

The emplacement tunnel is located at 500 m depth underground, with an initial stress field subjected to the self-weight of the rock mass. Zero normal displacements are prescribed on the lateral boundaries of the model. Vertical displacements are prevented at the bottom. The model simulation was conducted in a

non-isothermal mode with a time-dependent heat power input (Rutqvist et al., 2009), adopted from the heat load developed for the Generic Disposal System Environment (GDSE) within the UFD for Pressurized Water Reactor (PWR) used nuclear fuel.



7.3.2.2 Chemical model

In this hypothetical case, it is assumed that the EBS is composed of Kunigel-V1 bentonite (Ochs et al., 2004), and the mineral composition of the bentonite is listed in Table 7-4. It is also assumed that the host rock is Opalinus clay (Thury, 2002) with the mineral composition listed in Table 7-5.

The pore-water composition of the bentonite (Ochs et al., 2004) and clay formation (Fernandez et al., 2007) are listed in Table 7-7. Fernandez et al. (2007) conducted five onsite water sampling campaigns from the borehole BDI-B1 (see Table 7-6). Here, we use the average concentrations of these five campaigns. Note that laboratory-measured pH is used in order to be consistent with concentrations of other chemical species. Although redox potential (Eh) was measured in the field, because it is known (e.g., Appelo and Postma, 1994) that field-measured Eh is hardly reliable, we take the Eh calculated from the redox couple $\text{Fe}^{+2}/\text{Fe}^{+3}$, which is 268 mV. Given that the pore water is under mild oxidizing conditions, uranium is likely present in its U(VI) form (UO_2^{+2}).

The initial water for EBS bentonite was taken from Sonnenthal et al. (2008) and used in the benchmark for the DECOVALEX-THMC project (Sonnenthal et al., 2008). For F^- , Br^- , and $\text{O}_2(\text{aq})$, which were not reported in Sonnenthal et al. (2008), we simply assumed that they have the same concentration as that in Opalinus clay. F^- and Br^- , though they are not of great interest in current simulations, are included to account for their aqueous complexing with U(VI). In TOUGHREACT, redox potential is represented by $\text{O}_2(\text{aq})$ concentration.

Table 7-4. Mineral composition of the bentonite used in the model, taken from the Kunigel-VI bentonite (Ochs et al., 2004).

Mineral	Abundance (volume fraction)
Schoepite	0
Calcite	0.023
Illite	0
Kaolinite	0
chlorite	0
montmorillonite-na	0.475
Quartz	0.335
K-Feldspar	0.041
Siderite	0
Dolomite	0.029
Ankerite	0

Table 7-5. Mineral composition of the clay formation used in the model, taken from the Opalinus clay (Thury, 2002).

Mineral	Abundance (volume fraction)
Schoepite	0
Calcite	0.1
Illite	0.223
Kaolinite	0.174
Chlorite	0.1445
montmorillonite -na	0.1426
Quartz	0.1845
K-Feldspar	0
Siderite	0.01256
Dolomite	0
Ankerite	0.00798

Table 7-6. Chemical characteristics of the water samples collected in the different water sampling campaigns from borehole BDI-B1 (Fernandez et al., 2007).

Date	Unit	22/04/2003	25/06/2003	28/10/2003	12/07/2004	01/03/2005	average
EC	(mS/cm)	29.8	26.8	28.1	24.3	26.2	27.04
pH	field	–	6.8	6.9	7	7.6	7.075
pH	lab	7.3	7.5	7.4	7.6	7.6	7.48
Eh	(mV)	n.d.	83	77	-7	-24.2	32.2
Eh	calc.(mV)	316	339	339	228	118	268
F	(mg/L)	0.3	0.3	0.3	0.19	0.51	0.32
I	(mg/L)	2.2	2.2	1.8	2	2.6	2.16
NH ₄	(mg/L)	14.2	12.7	14	13	13	13.38
Br	(mg/L)	31	28	28	19	22	25.6
Cl	(mg/L)	11000	12000	11000	13000	11800	11760
SO ₄	(mg/L)	2100	1833	1700	1700	1600	1786.6
Alk.cHCO	(mg/L)	344	347	313	303	280	317.4
Fe total	(mg/L)	2.2	4.3	4.1	3.3	1.31	3.042
Fe(II)	(mg/L)	1.3	1.6	1	3.1	1.26	1.652
SiO ₂	(mg/L)	7.4	9.2	4.2	5.8	8.3	6.98
K	(mg/L)	88	89	93	73	80	84.6
Al	(mg/L)	0.1	0.1	0.1	0.12	<0.05	0.105
Li	(mg/L)	0.8	0.8	n.d.	n.d.	n.d.	0.8
B	(mg/L)	0.1	3.5	3.1	3	2.5	2.44
Ca	(mg/L)	922	1033	886	880	806	905.4
Mg	(mg/L)	611	574	456	505	395	508.2
Na	(mg/L)	6480	6300	6650	6300	6000	6346
Sr	(mg/L)	43	40	41	36	37	39.4
Mn	(mg/L)	0.4	0.3	0.3	0.22	0.12	0.268
Ni	(mg/L)	0.1	<0.03	0.07	<0.03	0.07	0.08
Zn	(mg/L)	33	2.3	0.05	<0.05	<0.05	11.78

Table 7-7. Pore-water composition of EBS bentonite and host clay rock.

	EBS Bentonite: Kunigel-V1 (<i>Sonnenthal et al., 2008</i>)	Opalinus Clay (<i>Fernandez et al., 2007</i>)
pH	8.40	7.40
Eh	0.268	0.268
Cl	1.50E-05	3.32E-01
SO ₄ ⁻²	1.10E-04	1.86E-02
HCO ₃ ⁻	3.49E-03	5.18E-03
Ca ⁺²	1.37E-04	2.26E-02
Mg ⁺²	1.77E-05	2.09E-02
Na ⁺	3.60E-03	2.76E-01
K ⁺	6.14E-05	2.16E-03
Fe ⁺²	2.06E-08	3.46E-06
SiO ₂ (aq)	3.38E-04	1.10E-04
AlO ₂ ⁻	1.91E-09	3.89E-08
F-	1.68E-05	1.68E-05
Br-	3.2E-04	3.2E-04
O ₂ (aq)	1.07E-41	1.07E-41
UO ₂ ⁺²	1E-10	1E-10

Table 7-8 lists the thermal and hydrodynamic parameters used in the model. Those for bentonite are taken from Sonnenthal (2008), while those for clay formations are mostly taken from Thury (2002).

Table 7-8. Thermal and hydrodynamic parameters.

Parameter	Clay formation	Bentonite
Grain density [kg/m ³]	2700	2700
Porosity ϕ	0.15	0.41
Saturated permeability [m ²]	5.0×10^{-20}	2.0×10^{-21}
Relative permeability, k_{rl}	$m = 0.6, S_{rl} = 0.01$	$K_{rl} = S^3$
Van Genuchten α [1/Pa]	6.8×10^{-7}	3.3×10^{-8}
Van Genuchten m	0.6	0.3
Compressibility, β [1/Pa]	3.2×10^{-9}	5.0×10^{-8}
Thermal expansion coeff., [1/°C]	0.0	1.0×10^{-4}
Dry specific heat, [J/kg °C]	800	8000
Thermal conductivity [W/m °C] dry/wet	2.2/2.2	0.5/1.3
Tortuosity for vapor phase	$\phi^{1/3} S_g^{10/3}$	$\phi^{1/3} S_g^{10/3}$

Mineral dissolution/precipitation is kinetically controlled, except that schoepite is assumed in equilibrium. The kinetic law for mineral dissolution/precipitation is given in Xu et al. (2006). The kinetic rate for the mineral considered in the current model is given in Table 7-9. Note that the surface areas listed in Table 7-9 are calculated for tuff (Sonnenthal et al., 2005). Their applicability to the clay formation considered is questionable. Further refinement of the surface-area calculation is needed in the future when the THMC model is applied to a realistic scenario.

Table 7-9. Kinetic properties for minerals considered in the model (Xu et al., 2006)

Mineral	A (cm ² /g)	Parameters for Kinetic Rate Law							
		Neutral Mechanism		Acid Mechanism			Base Mechanism		
		k ₂₅ (mol/m ² /s)	E _a (KJ/mol)	k ₂₅	E _a	n(H ⁺)	k ₂₅	E _a	n(H ⁺)
Primary:									
Schoepite	Assumed at equilibrium								
Quartz	9.8	1.023×10 ⁻¹⁴	87.7						
K-feldspar	9.8	3.89×10 ⁻¹³	38	8.71×10 ⁻¹¹	51.7	0.5	6.31×10 ⁻¹²	94.1	-0.823
Kaolinite	151.6	6.91×10 ⁻¹⁴	22.2	4.89×10 ⁻¹²	65.9	0.777	8.91×10 ⁻¹⁸	17.9	-0.472
Illite	151.6	1.66×10 ⁻¹³	35	1.05×10 ⁻¹¹	23.6	0.34	3.02×10 ⁻¹⁷	58.9	-0.4
Chlorite	9.8	3.02×10 ⁻¹³	88	7.76×10 ⁻¹²	88	0.5			
Calcite	3.5	1.6×10 ⁻⁷	23.5						
Dolomite	12.9	2.52×10 ⁻¹²	62.76	2.34×10 ⁻⁷	43.54	1			
Ankerite	9.8	1.26×10 ⁻⁹	62.76	6.46×10 ⁻⁴	36.1	0.5			
Smectite-Na	151.6	1.66×10 ⁻¹³	35	1.05×10 ⁻¹¹	23.6	0.34	3.02×10 ⁻¹⁷	58.9	-0.4
Na-montmorillonite	151.6	1.66×10 ⁻¹³	35	1.05×10 ⁻¹¹	23.6	0.34	3.02×10 ⁻¹⁷	58.9	-0.4

7.4 Modeling Results

The model considers a canister, an EBS bentonite, and a host clay formation. Initially, the EBS bentonite is under an unsaturated condition, and temperature is 25°C everywhere. The model was run for 10,000 years. It is assumed that the canister is broken and U(VI) is released by the dissolution of schoepite after 1000 years. Note that assuming that canister failure would occur in 1000 years is very conservative in comparison with other THMC simulations on radionuclide migration. For example, De Windt et al. (2006) assumed that canister failure occurs after 10,000 years. However, after 1000 years, the EBS becomes fully saturated, and water-rock interactions are close to equilibrium conditions, THMC processes evolve very slowly thereafter, unless there were some incidents such as earthquakes. In other words, the THMC environment in which radionuclides migrate would not change substantially from 1000 years to 10,000 years. Therefore, it is expected that the starting time of U(VI) release, whether it be 1000 years or 10,000 years, would not affect U(VI) migration significantly.

7.4.1 THM Evolutions

To investigate the THM behavior around the emplacement tunnel, we first present the response induced by heating and hydration processes, based on elastic analysis. THM behavior is described by the temperature, pore pressure, and saturation variations around the repository, as well as the stress distribution at monitoring points A, B, C, and D as marked in Figure 7-8.

Two simulations are presented here that differ in the elastic model: the first one adopted a linear elastic swelling model as in equation 7-6, called THMC1 here; the second one used an elastic swelling model that accounts for both moisture and chemical concentration change as illustrated by equation 7-7, called THMC2 here. A comparison of the calculated stress fields from THMC1 and -2 allows us to evaluate the contribution of chemically induced swelling.

Figure 7-9 shows the temperature evolution at locations A, B, C, and D, and Figure 7-10 shows the temperature field at three different elapsed times (at 10, 100, and 10,000 years). It is shown that a maximum temperature of about 90°C is reached at the surface of the waste canister after about 20–30 years. Then, the temperature begins to decline steadily. At 10,000 years, the temperature has declined to about 40°C, which is higher than its initial value. The temperature fields from THMC1 and -2 show no difference, since these two models differ only in chemical-mechanical coupling.

Figure 7-11 shows the pore-pressure evolutions at A, B, C, and D; and the contours of the pore pressure at 10, 100, and 10,000 years are displayed in Figure 7-12. At 10 years, there is an evident increase in pore pressure. A maximum pore pressure of about 3.0 MPa is reached in the host clay formation adjacent to the EBS bentonite after about 100 years. Then, the pore-pressure evolution shows a tendency to stabilize at a constant value from 100 to 2000 years. After 2000 years, the pore pressure begins to decline steadily.

Again THMC1 and -2 show no difference in pore-pressure evolution, since these two models differ only in chemical-mechanical coupling.

Figure 7-13 shows the saturation evolution at A, B, C, and D; and the contours of the liquid saturation at 10, 100, and 10,000 years are displayed in Figure 7-14. In the area close to the heater (point A in Figure 7-13), EBS bentonite undergoes a de-saturation in the first two years caused by the heating from the canister, and then gradually becomes fully saturated after 20 years. The near-field clay formation in the vicinity of the buffer (point C in Figure 7-13) desaturates initially because of the relative low permeability of the clay formation. The clay formation is very close to full saturation after 30 years, with a saturation degree larger than 99%, lasting for 10,000 years (Figure 7-14).

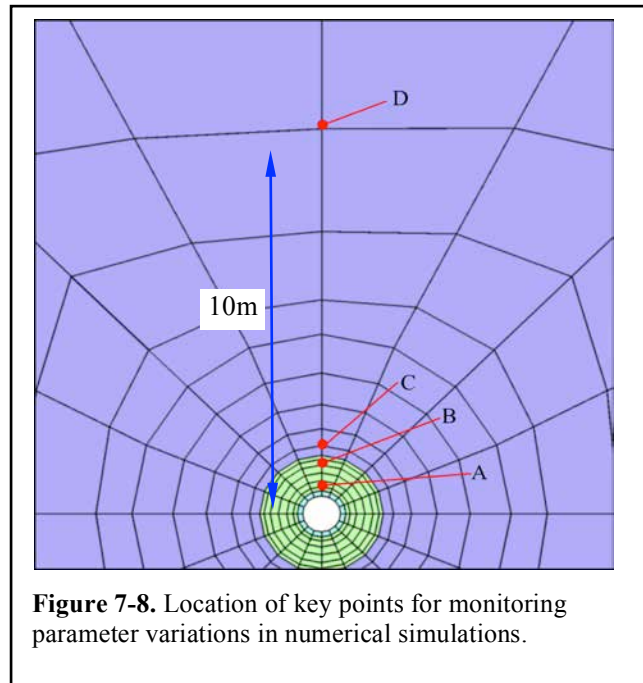


Figure 7-8. Location of key points for monitoring parameter variations in numerical simulations.

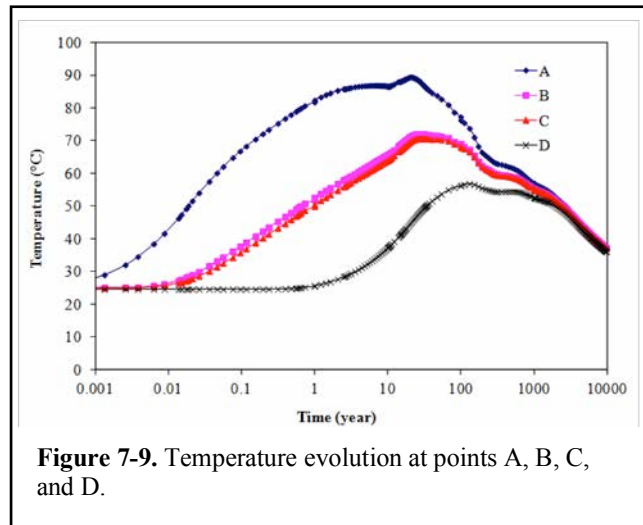
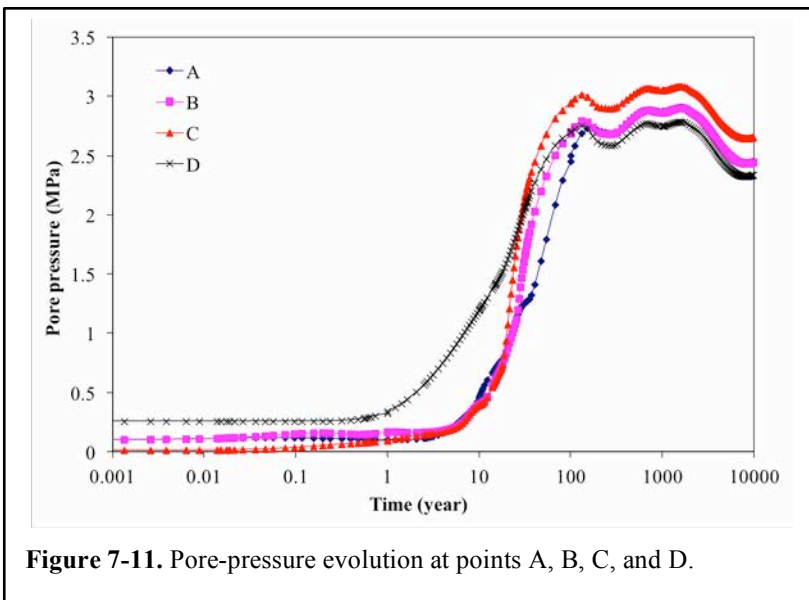
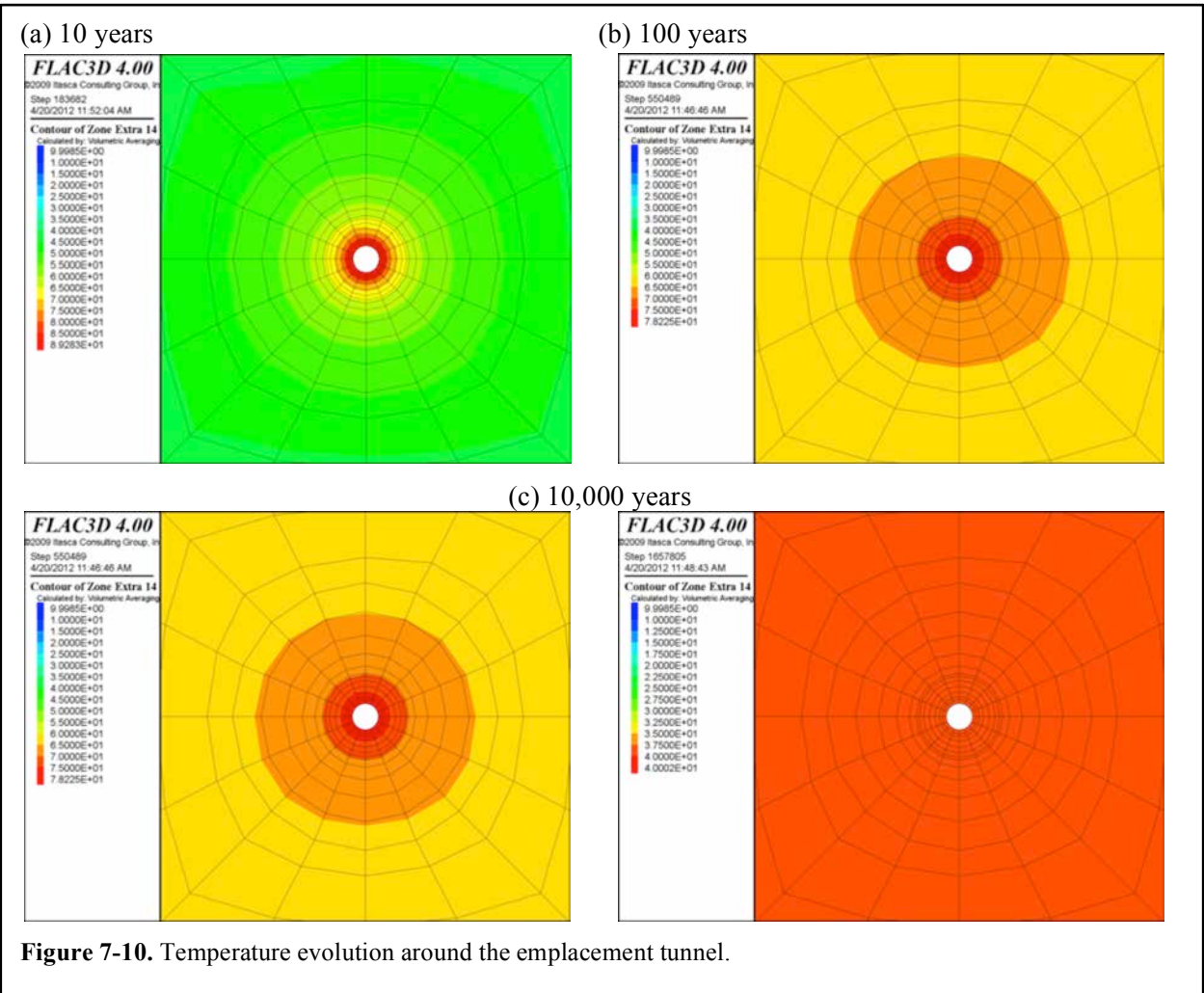


Figure 7-9. Temperature evolution at points A, B, C, and D.



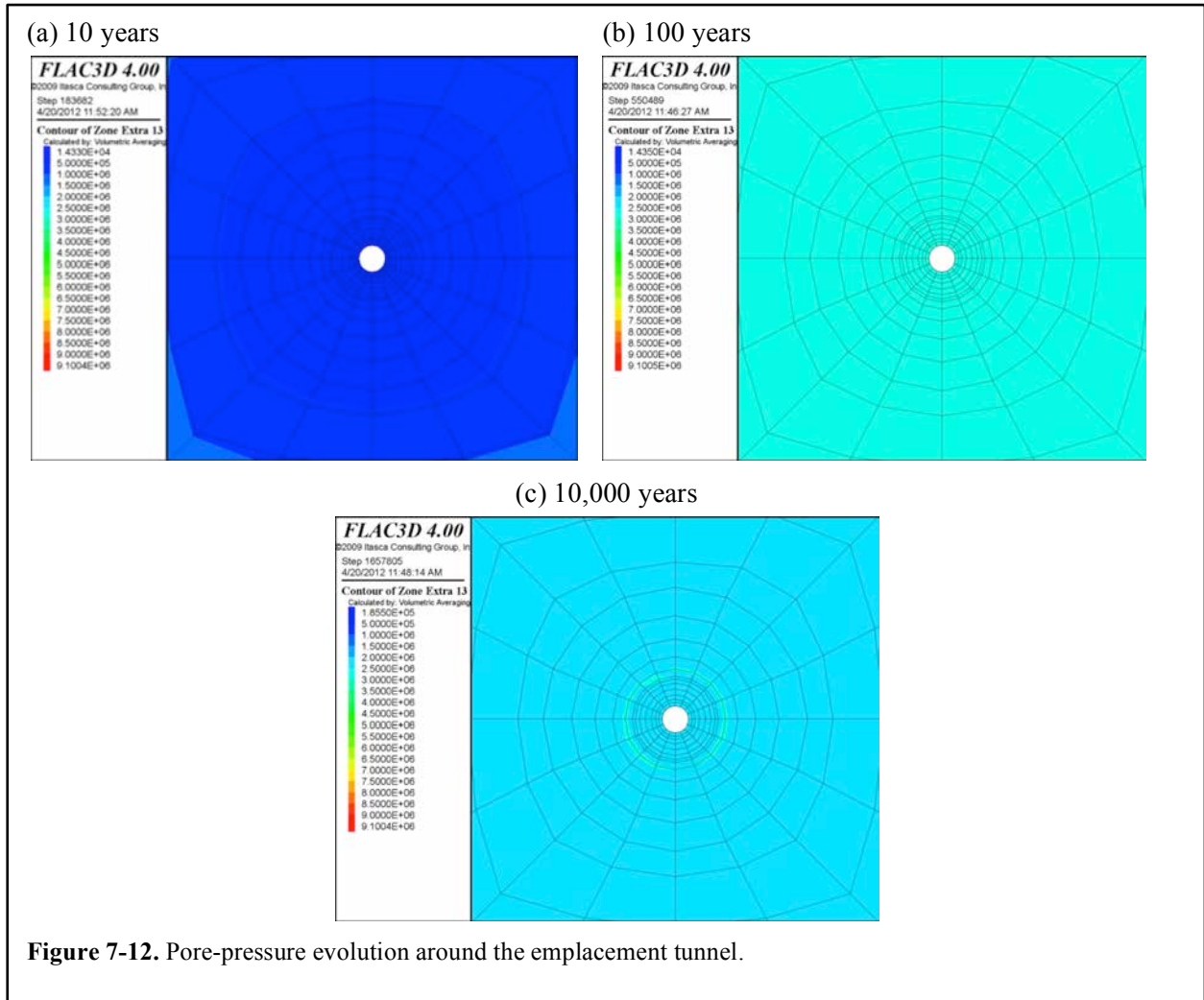


Figure 7-12. Pore-pressure evolution around the emplacement tunnel.

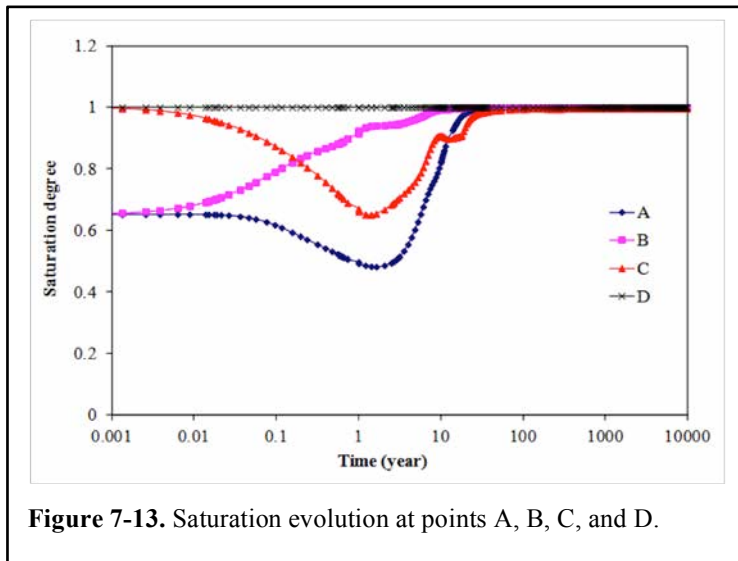
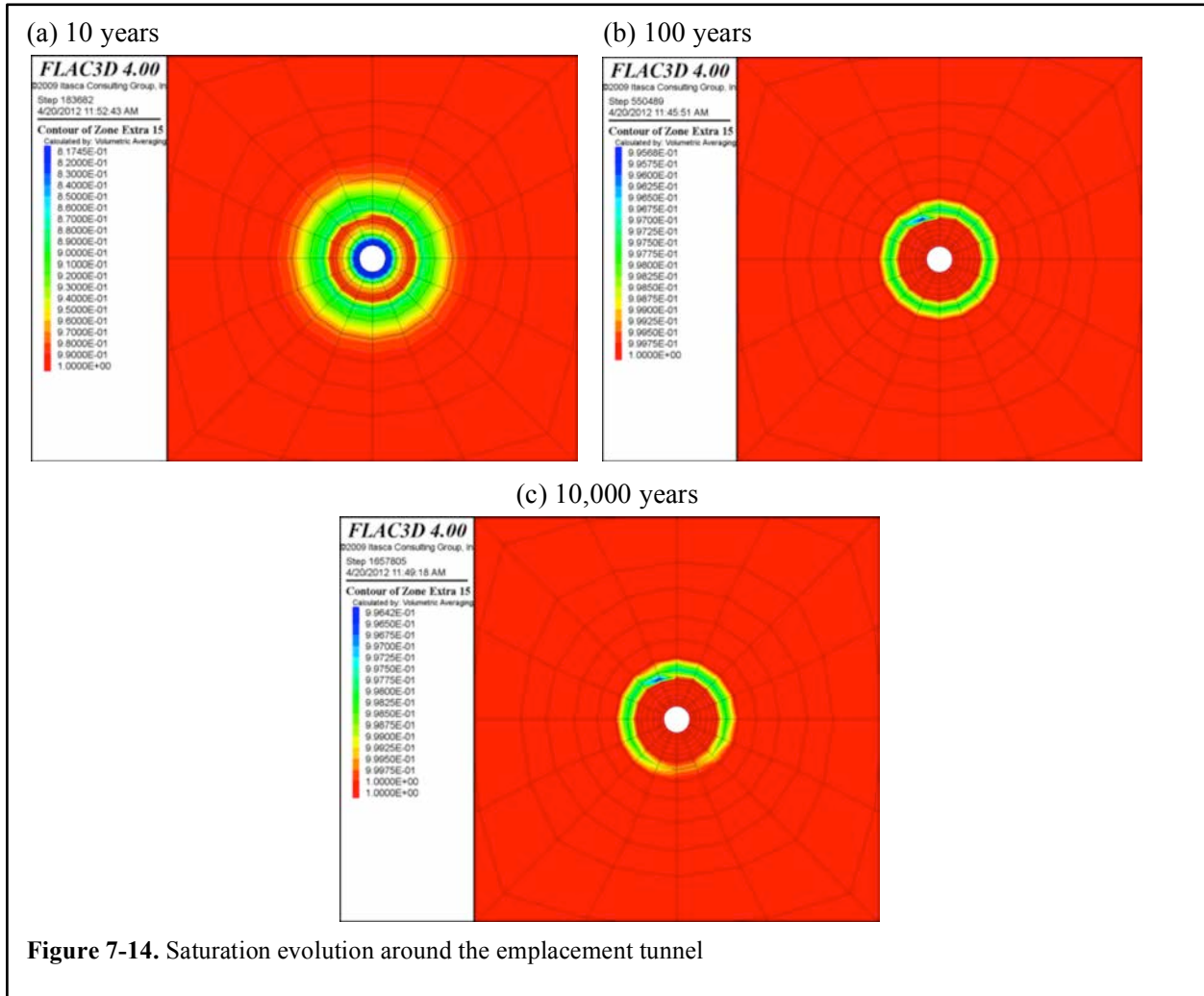


Figure 7-13. Saturation evolution at points A, B, C, and D.



The evolution of maximum and minimum compressive principal stresses is the most important factor in determining the state of failure for the rock mass surrounding the deposition hole. Figures 7-15–7-18 present the numerical results of THMC1 and -2 for the evolution of stress at points A, B, C, and D as part of the evaluation of repository stability. Generally, the compressive stress increases with heating before 100 years. At about 10 years, there is an increment of stress, particularly at points A and B. The maximum compressive principal effective stress, σ_1 , about 9 MPa, is reached at point C (i.e., the location in the rock mass adjacent to the EBS bentonite). The maximum σ_1 of about 108 MPa is reached at point C after about 100 years, while the minimum compressive principal effective stress, σ_3 , is relatively small. The risk for rock failure is the highest at about 100 years. It can thus be concluded that the first 100 years is a key phase for the safety of the repository, when the heat-induced stress plays an important role in the stability of the rock mass surrounding the emplacement tunnel.

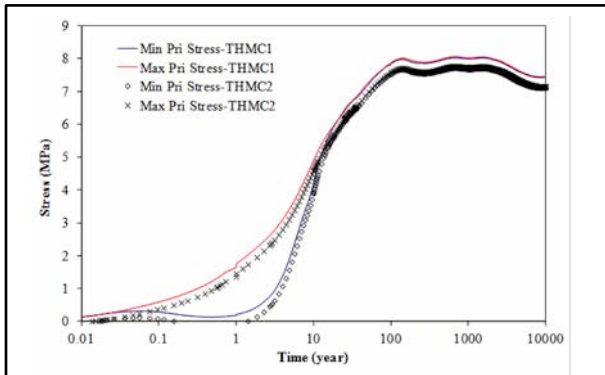


Figure 7-15. Simulation results of maximum and minimum principal compressive effective stresses (σ_1 and σ_3) at point A.

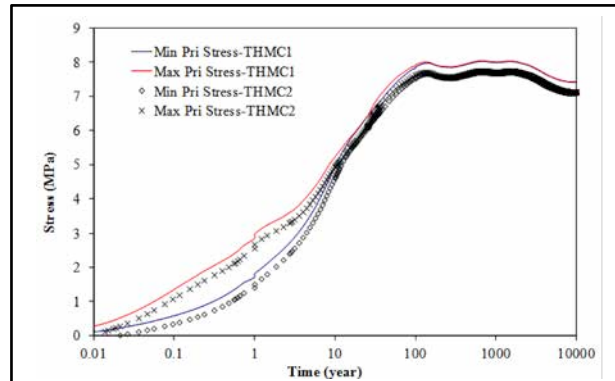


Figure 7-16. Simulation results of maximum and minimum principal compressive effective stresses (σ_1 and σ_3) at point B.

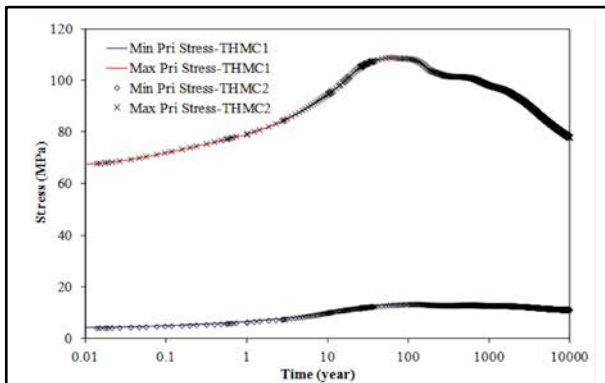


Figure 7-17. Simulation results of maximum and minimum principal compressive effective stresses (σ_1 and σ_3) at point C.

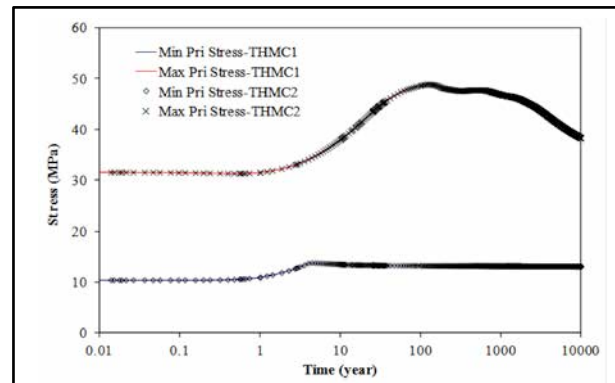


Figure 7-18. Simulation results of maximum and minimum principal compressive effective stresses (σ_1 and σ_3) at point D.

Comparisons between the numerical results of THMC1 and -2 show that the stresses (both maximum principal stress and minimum principal stress) within the EBS bentonite are higher in THMC1. The chemically induced swelling accounts for about 5% of the total effective stress. However, the stresses in the surrounding clay rock (presented by point C and D in Figure 7-17 and 7-18) are not evidently different, because the total solute concentration changes within these zones are rather minimal, as shown in the next section.

7.4.2 Reactive transport simulation results

7.4.2.1 Chemical evolution

Initially, the pore water in EBS bentonite has low concentrations of most species, because diluted water was used to fabricate the bentonite blocks. Chemical reactions could be triggered by several processes, including dispersion (molecular diffusion and hydrodynamic dispersion), mixing caused by the influent of host-clay-formation water, heating from the canister, or the self-adjustment of water composition towards a water-rock equilibrium (given that initial water is usually not under equilibrium with the minerals in the bentonite). The evolution of Cl (Figure 7-19a and b) mainly reflects dispersion and mixing. A quick rise

in Cl concentration (Figure 7-19b) indicates that such processes are fairly fast. One reason could be an overestimated dispersion effect. THMC simulations are computationally expensive. Thus, in order to minimize the number of grid blocks in the model, a relative coarse mesh is used for EBS. An EBS with a radial distance of about 0.8 m is discretized to six ring layers, which leads to a gridding distance of 0.15 m and a numerical dispersion coefficient of 0.075 m. Such a high dispersion coefficient results in the fast equilibrium of EBS pore water with host clay formation water. Na, while experiencing cation exchange and mineral precipitation/dissolution, seems also largely controlled by mixing between the bentonite pore water and clay-formation water, and dispersion processes; its evolution is similar to that of Cl (Figure 7-19 a, b).

K, Al and SiO₂(aq) are chemical species whose evolutions are typically controlled by Si-Al minerals. The diluteness of the initial bentonite pore water suggests that the water composition listed in Table 7-2 is probably just the recipe of the water that was used to make the bentonite block. Unsurprisingly, bentonite pore water undergoes a quick adjustment of Al and SiO₂(aq) as is determined by the interaction of montmorillonite, illite, chlorite, quartz and k-feldspar. After that, montmorillonite keeps dissolving (Figure 7-20), which raises the concentration of Al and SiO₂(aq). However, the precipitation of chlorite and K-feldspar overcome this increase, and consequently the Al concentration keeps dropping, with the lowest point coincidental with the maximum precipitation of K-feldspar at 200–400 years. Afterwards, the K-feldspar starts to dissolve (Figure 7-20), which leads to a rebounding of Al concentration (Figure 7-19) to a relatively steady level after 600 years. This steady level is maintained as the dissolution of montmorillonite and the precipitation of chlorite and illite is maintained at a relatively constant rate, until 1400 to 1500 years. After that, the Al concentration increases slightly because chlorite precipitation slows down due to the limited availability of Fe.

Potassium (K) concentrations undergo a rapid increase (Figure 7-19), caused by the influent of clay-formation water that contains higher K concentration (see Table 7-2). This increase induces the precipitation of illite and K-feldspar, and consequently the concentration of K drops quickly until 600 years, when the precipitation of K-feldspar stops. After that, the K concentration keeps dropping at a relatively slow pace, corresponding to the precipitation of illite, until 1400 to 1500 years. At that time, the precipitation of chlorite slows down significantly, and more Al is available for the illite precipitation, so that illite precipitation increases and causes a further sharp drop in K concentration. Later on, illitization processes, i.e., the transformation of montmorillonite to illite, continues, and K concentration decreases at a slow, steady pace.

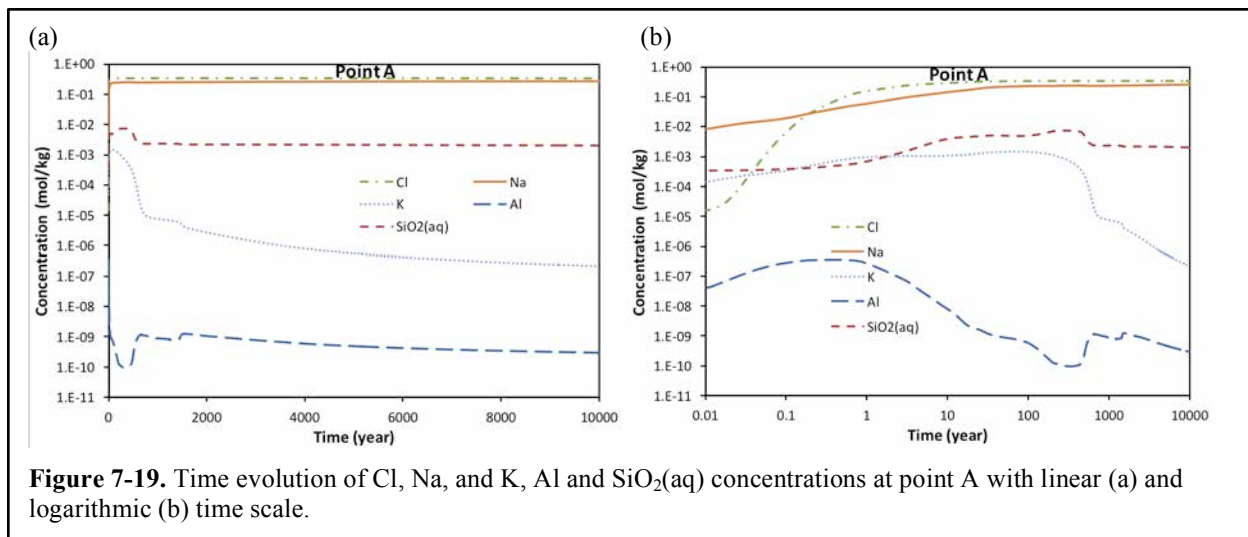
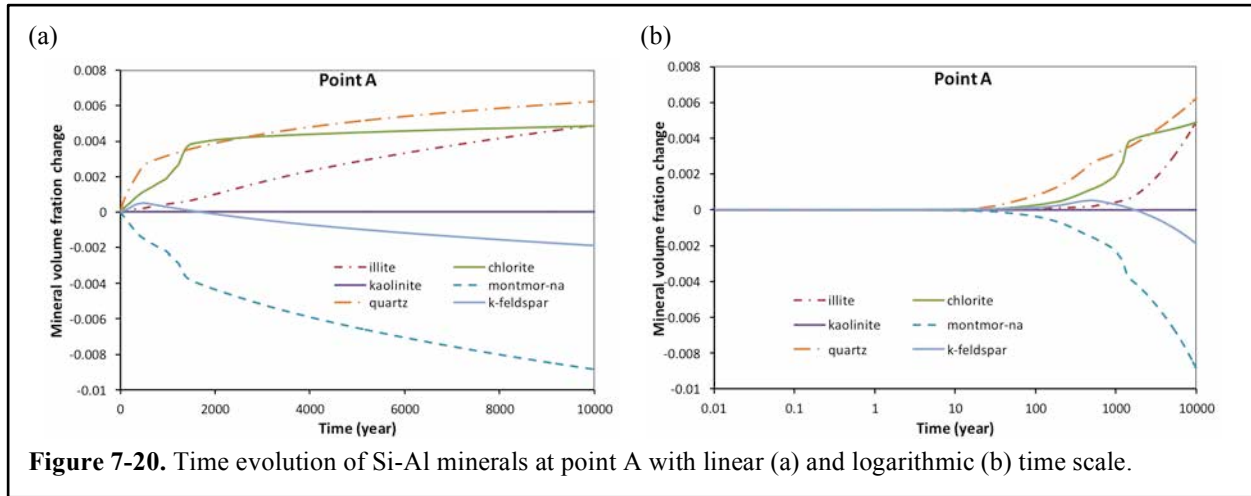
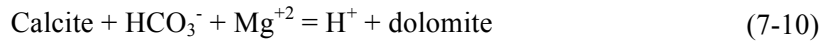


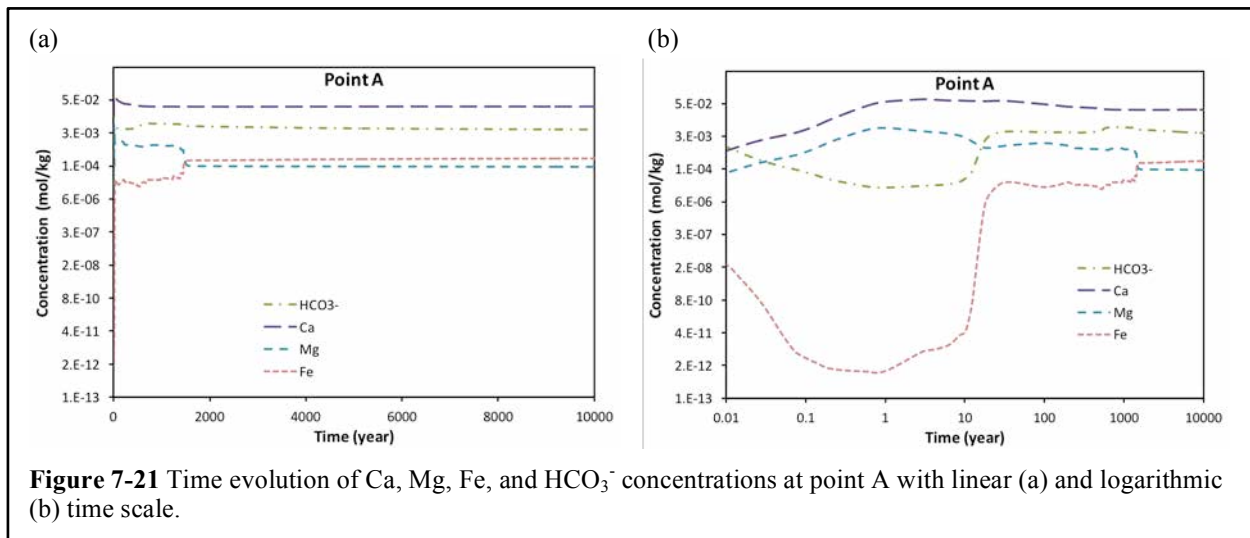
Figure 7-19. Time evolution of Cl, Na, and K, Al and SiO₂(aq) concentrations at point A with linear (a) and logarithmic (b) time scale.



The initial concentrations of bivalence cations and carbonate are totally out of equilibrium with carbonate minerals. In the short term, i.e., the first 10 years, the transport (dispersion and mixing) and dynamic equilibrium determine the evolution of Ca, Mg, and HCO_3^- . The fast dispersion of solutes leads to an increase in Ca and Mg (Figure 7-21b), which triggers the dissolution of calcite and precipitation of dolomite (Figure 7-22), with the reaction as follows:



As this reaction keeps moving to the right-hand side, HCO_3^- concentration is dragged down (Figure 7-21b). Mg concentration increases due to the transport process cannot be overcome at the very beginning (less than one year) by the precipitation of dolomite, but Mg starts to go down after 1 year. At around 10 years, as Mg concentration is low enough, reaction (10) reverses and moves toward the left-hand direction, i.e., dolomite dissolves and calcite precipitates, which continues until 1500 years. As a result, the HCO_3^- concentration stays at a relatively high level for this time period. But Mg concentration is disrupted by the precipitation of chlorite and maintained at a relatively low level. At around 1500 years, a turning point is reached — the dolomite precipitation stops, which leads to a sharp drop in Mg concentration.



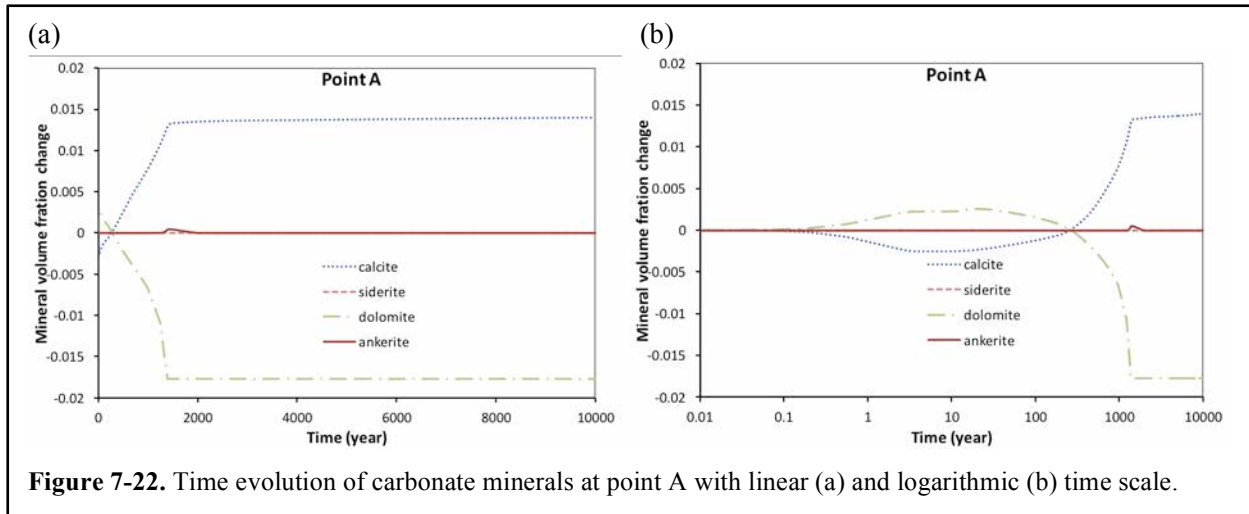


Figure 7-22. Time evolution of carbonate minerals at point A with linear (a) and logarithmic (b) time scale.

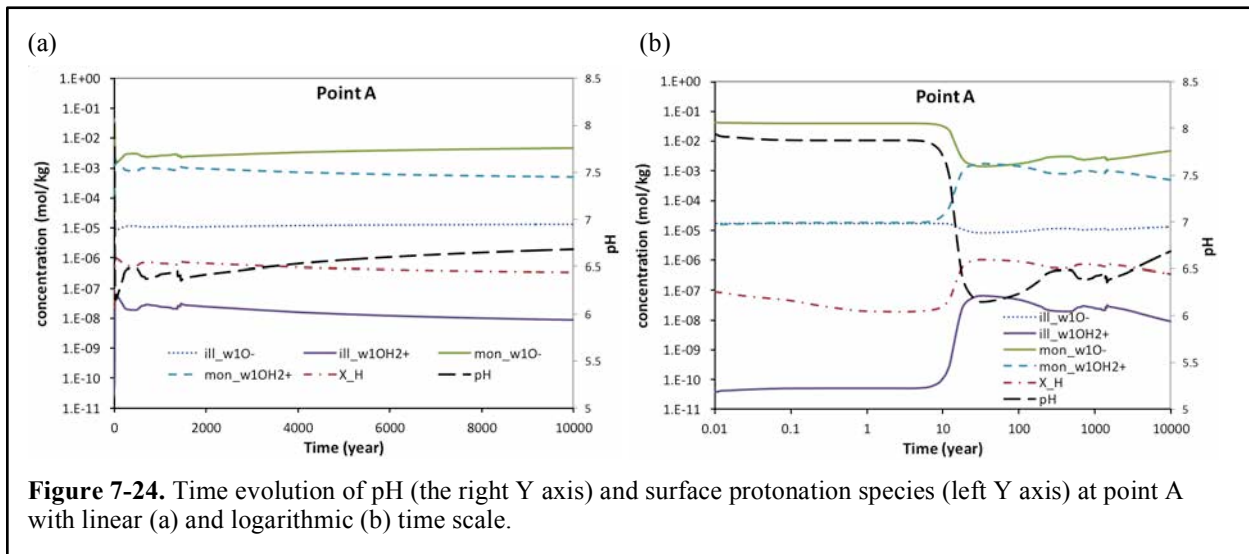
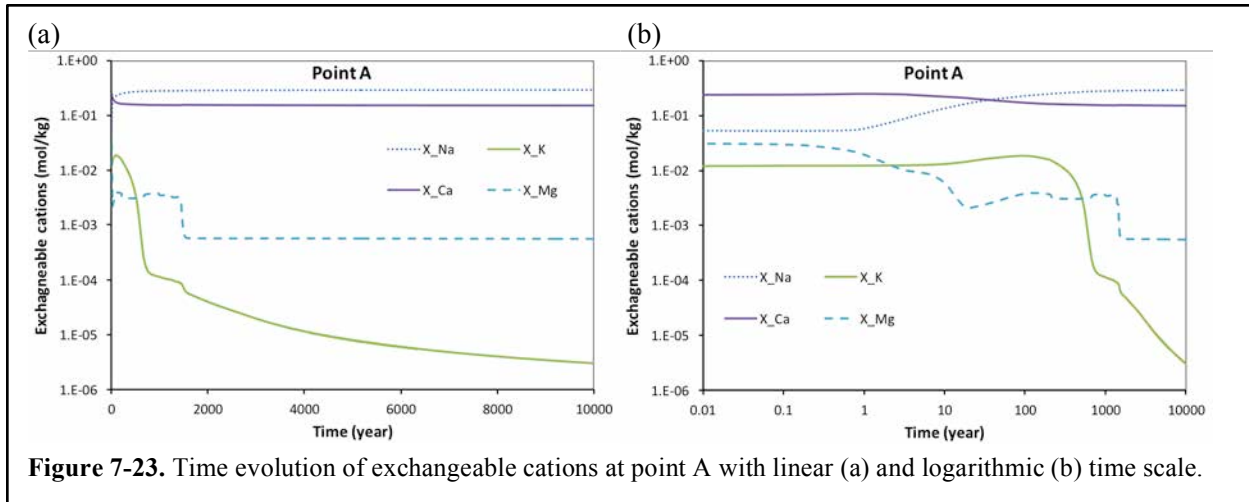
The evolution of the Fe concentration at point A (Figure 7-21a, b) is mainly the consequence of two competitive processes: (1) dispersion and mixing, which tends to raise the Fe concentration, and (2) the precipitation of chlorite, which tends to decrease Fe concentration. The competition between these two processes varies over time. Initially (in less than one year), the precipitation of chlorite wins the competition, and Fe concentration decreases (Figure 7-21b). Later, however, the influent of water with high Fe content raises the Fe concentration at point A and eventually reaches a level very similar to the Fe concentration in the pore water of the clay formation. Around 1500 years, a sharp increase in Fe concentration occurs (Figure 7-21a, b) due to a significant slowdown in chlorite precipitation. After that, the concentration of Fe remains stable until 10,000 years (Figure 7-21a, b). Note that canister corrosion is not considered in the model. If this process is included, the behavior of Fe would be different.

Cation exchange reactions interact with other types of reactions, and the changes in exchangeable cations could affect the swelling properties of EBS buffer and probably the migration of radionuclides. Figures 7-23a and b show the time evolution of four major exchangeable cations from the montmorillonite sites. Although illite forms due to illitization and provides some additional exchange capability, exchangeable sites from illite make a very minimal contribution, because the amount of illite that forms is rather small, a volume fraction of about 0.4% after 10,000 years (Figure 7-20), and illite also has lower exchangeable capacity. In line with the changes in aqueous concentration of Na, K (Figure 7-19), Ca, and Mg (Figure 7-21), exchangeable cations undergo a similar time evolution. As aqueous concentration of Na increases, exchangeable Na increases as well, and eventually becomes the dominant exchangeable cations. Exchangeable Ca initially occupies most exchangeable sites, but starts to decrease after about 10 years, mainly because the precipitation of calcite takes the aqueous Ca, so that Ca is released from exchangeable sites to replenish. The exchangeable sites occupied by Mg also have some fluctuations following the change in aqueous Mg, for the reasons discussed above, but at later stages, decrease in exchangeable Mg is dominant, acting to replenish the aqueous Mg consumed by the precipitation of chlorite (Figure 7-20). K is also released from the exchangeable sites, mostly to meet the need of K for illitization. Eventually, this K is reduced to a very low level (Figure 7-23).

Protons are involved in many reactions, with the most important ones being the dissolution/precipitation of minerals like montmorillonite, chlorite, illite, dolomite and calcite—and the protonation reaction with surface sorption sites and exchangeable sites. Figures 7-24a and b, show the evolution of pH and some important surface protonation species. Around 10 years, when the temperature peaks, montmorillonite

dissolves and chlorite precipitates rapidly, which leads to significant drops in pH. As a result, more surface sites are protonated, which is demonstrated by an increase in the concentration of mon-w1OH₂⁺ (the protonated species of the weak site type 1 on montmorillonite surface) and ill-w1OH₂⁺ (the protonated species of the weak site type 1 on the illite surface) and a corresponding decrease in deprotonated species mon-w1O⁻ and ill-w1O⁻. The rest of the surface proton species is also similarly affected, but their concentrations are orders of magnitude lower and not shown in Figure 7-24. Also shown in Figure 7-24 are the protons that go to the exchangeable sites; they show a trend similar to the surface protonated species, but the concentration is much lower.

Point B is located in the EBS bentonite adjacent to the bentonite-clay formation interface. The chemical evolution at point B is very similar to that at point A, except at an early stage. The faster hydration at point B leads to a quicker rise in concentrations for all species, for example, Cl, K, and Ca, as shown in Figure 7-25. After 10 years, the concentration profiles at points A and B almost overlap, although slight differences are observed for K, because K is controlled by illitization, which is affected by temperature, and temperatures at point A and B are different.



Point C is located in the clay formation, close to the bentonite/clay formation interface. Initially, the concentration of Cl decreases, and then recovers (Figure 7-26 a, b), which represents the effect of dispersion into bentonite and water inflow from the far field of the clay formation. Na behaves similarly to Cl (Figure 7-26a, b), although it is affected by chemical reactions. Al concentration drops in the first year (Figure 7-26a, b) due to the precipitation of chlorite. Since the Al concentration is very low, very little chlorite precipitation is enough to change the Al concentration significantly. Note that the changes in chlorite in the first year are too small to be seen in Figure Figure27a and b. After that, Al concentrations gradually recover as montmorillonite starts to dissolve. Around 670 years, there is a significant

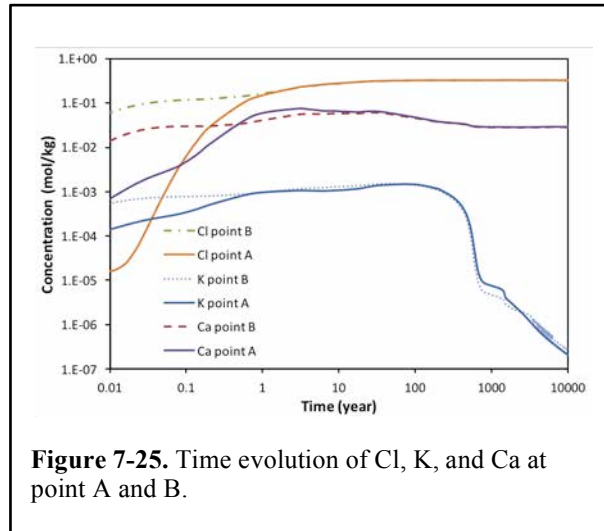


Figure 7-25. Time evolution of Cl, K, and Ca at point A and B.

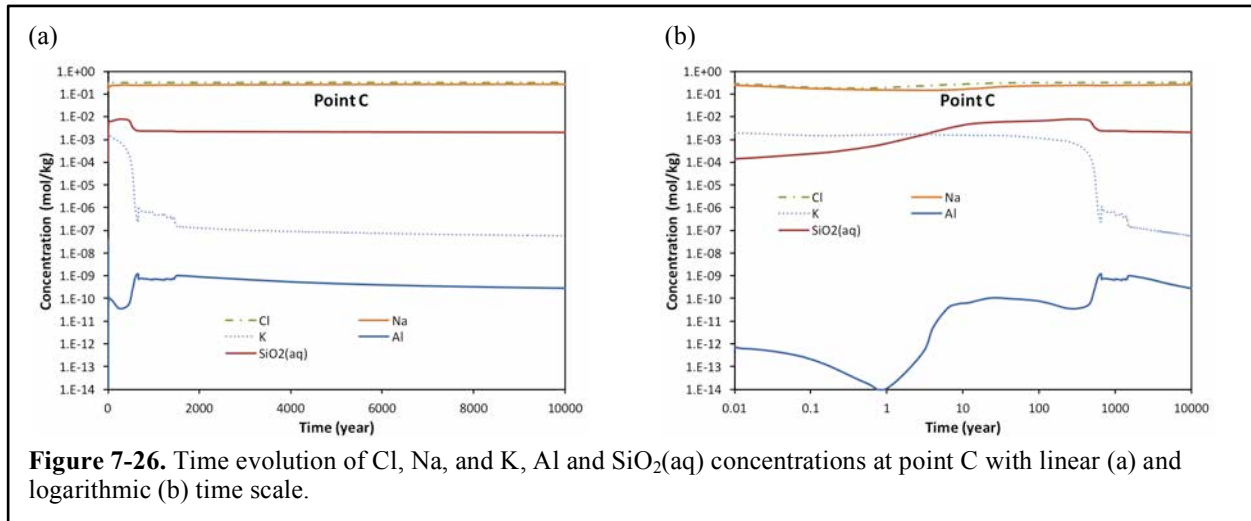


Figure 7-26. Time evolution of Cl, Na, and K, Al and SiO₂(aq) concentrations at point C with linear (a) and logarithmic (b) time scale.

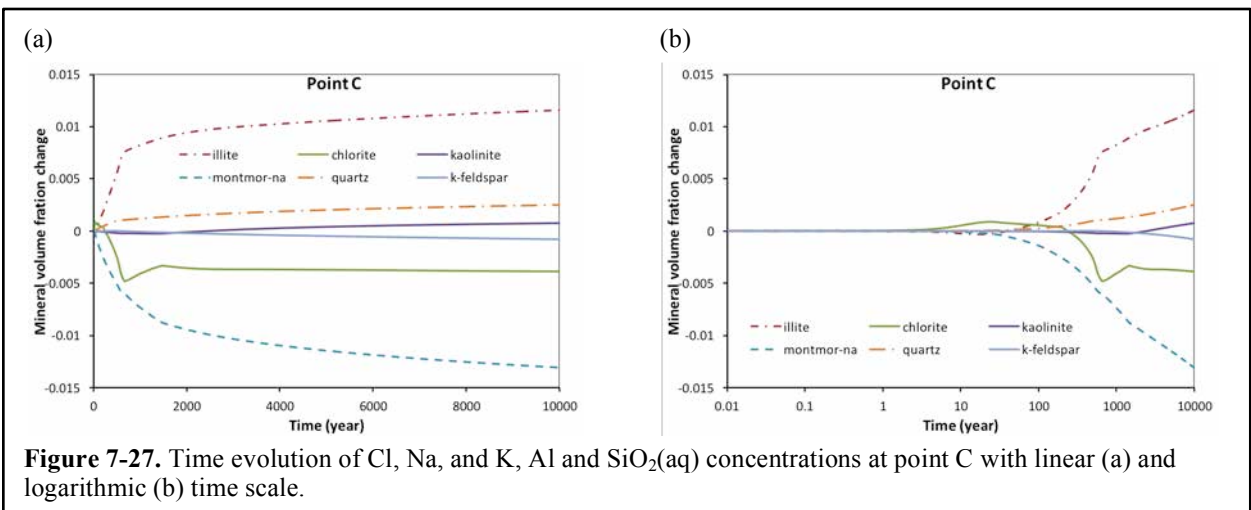


Figure 7-27. Time evolution of Cl, Na, and K, Al and SiO₂(aq) concentrations at point C with linear (a) and logarithmic (b) time scale.

change in the chemical system. Before that, K concentration decreased steadily due to the precipitation of illite; SiO₂(aq) concentrations increased steadily due to the dissolution of montmorillonite and chlorite, despite the precipitation of quartz and illite consuming some SiO₂(aq). The turning point at 670 years is triggered by the completion of the transformation from calcite and siderite to ankerite (Figure 7-29). As the ankerite stops precipitating, chlorite dissolution loses its driving force, and chlorite starts to precipitates, which significantly hinders the precipitation of illite. As a result, the decrease in K concentrations becomes very slow. At 1500 years, chlorite precipitation stops; consequently, illite precipitation accelerates and K concentrations undergo a sharp drop. After 1500 years, the K concentration slowly decreases as the dissolution of montmorillonite and the precipitation of illite continue.

At an early stage (less than a couple years), bivalence cations undergo some changes (Figure 7-28a, b) to accommodate the hydrodynamic and chemical interactions between EBS bentonite and the clay formation. After that, the transformation of calcite and siderite to ankerite (Figure 7-29a, b) leads to an increase in bicarbonate and a decrease in Fe and Mg. After 670 years, however, such transformation stops, triggering a series of sudden changes in K, Al, and some Al-Si minerals, as described above.

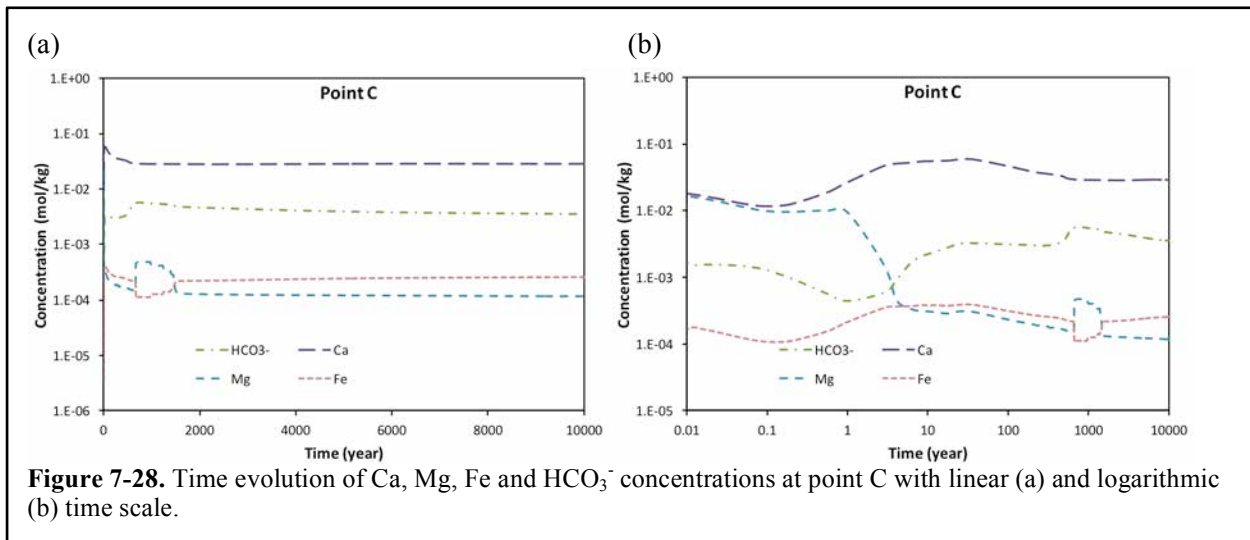


Figure 7-28. Time evolution of Ca, Mg, Fe and HCO₃⁻ concentrations at point C with linear (a) and logarithmic (b) time scale.

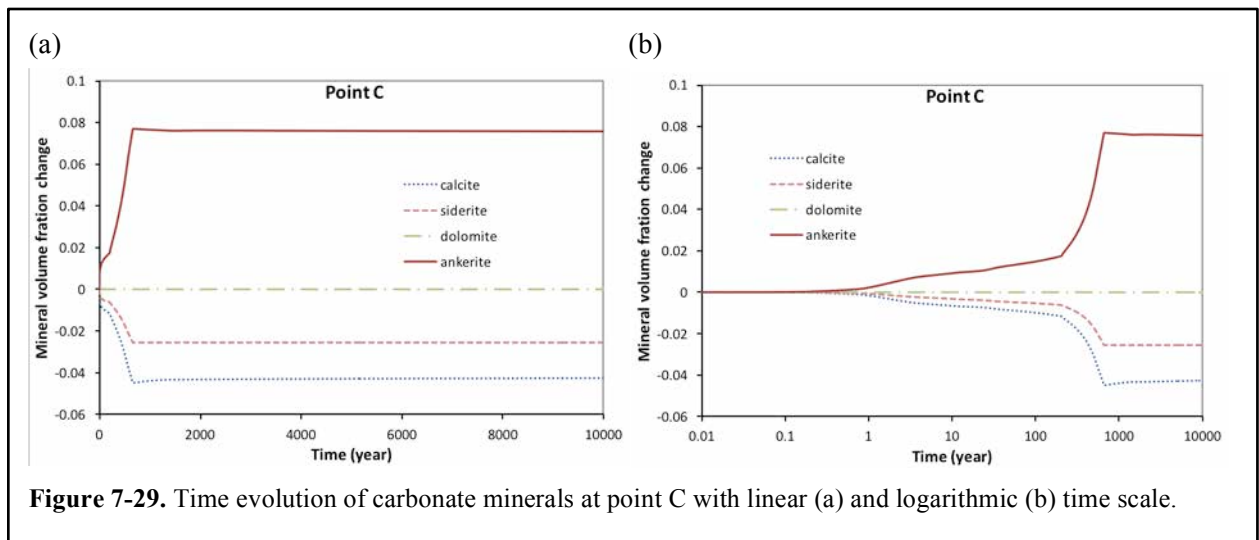


Figure 7-29. Time evolution of carbonate minerals at point C with linear (a) and logarithmic (b) time scale.

Exchangeable cations closely follow the changes in their aqueous counterparts. Initially, most sites are occupied by Ca, but later, sites occupied by Na exceed the Ca sites (Figure 7-30a, b), which causes a decrease in the weighted average of exchangeable cations. According to Zheng et al. (2011), such changes may lead to a decrease in the swelling capability of the clay formation.

Point D is located in the clay formation about 10 m away from the bentonite-clay formation interface. As shown by the concentration of Cl (Figure 7-31), the chemical system is not affected by hydrodynamic processes, but it is known that such formations usually undergo diagenesis processes. One of these processes is illitization, which eventually uses most of the available K in the groundwater, with K concentration becoming very low (Figure 7-31).

7.4.2.2 U(VI) migration

In our current model, it is assumed that canisters have collapsed after 1000 years. Figure 7-32 shows the concentration of U(VI) at the canister assumed to be composed of pure schoepite. The concentration of U(VI) is mainly controlled by the dissolution of schoepite, but also affected by the concentration of calcium and carbonate, since the Ca-U-carbonate aqueous complexes is the dominant U(VI) aqueous species. A maximum concentration of about 1 mM could be reached.

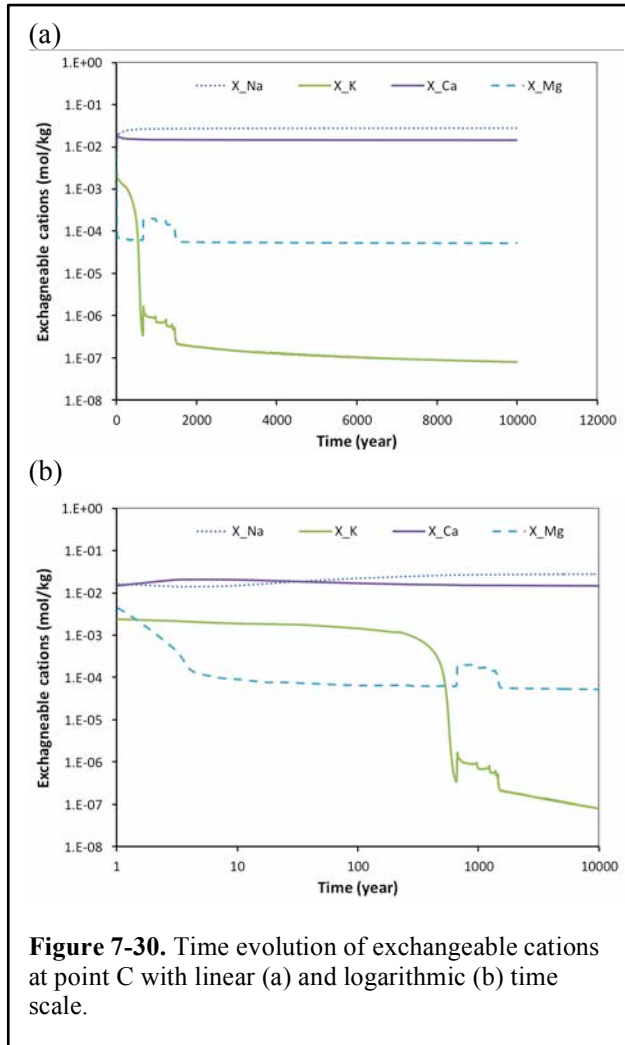


Figure 7-30. Time evolution of exchangeable cations at point C with linear (a) and logarithmic (b) time scale.

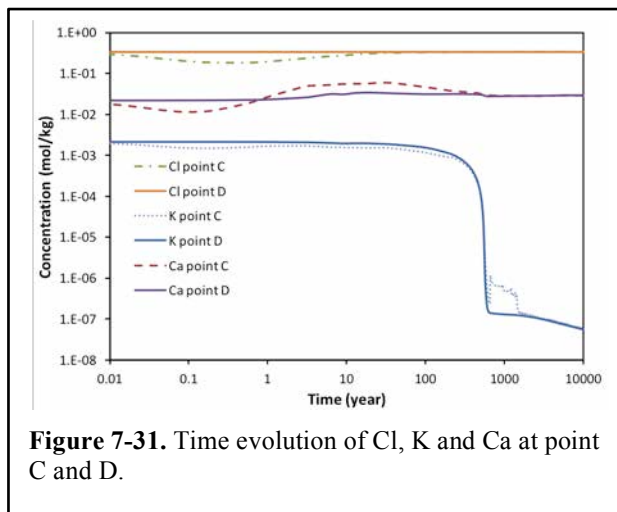


Figure 7-31. Time evolution of Cl, K and Ca at point C and D.

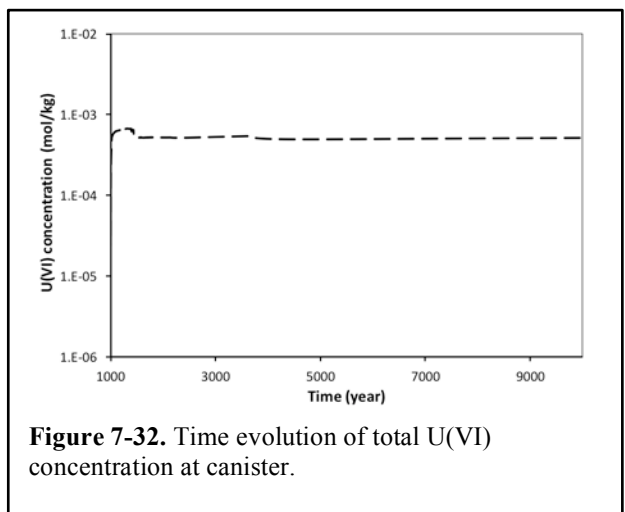


Figure 7-32. Time evolution of total U(VI) concentration at canister.

U(VI) leaches out of the canister and move into the EBS bentonite by diffusion and dispersion. Concentrations of U(VI) at point A, the closest point in the bentonite adjacent to the canister, increase quickly, and the temporal delay is hardly noticeable. However, bentonite possesses very strong sorption capability and adsorbs most of the U(VI). As shown in Figure 7-33, the concentration of sorbed U(VI) increases significantly. As a result, the concentration of aqueous U(VI) increases only to about $1e-4$ M, about one order of magnitude lower than that at the canister. Cation exchange does not contribute substantially enough to retard the migration of U(VI) in current simulations. Figure 7-33 shows the U(VI) on exchangeable sites ($X_{UO_2^{+2}}$) is about six orders of magnitude lower than that at sorption sites.

Figure 7-34 shows the temporal breakthrough of U(VI) at six monitoring locations. Point A is near the canister and Point B is close to the bentonite-host rock interface, but located in the bentonite. Point C is the first node in the host clay formation beyond the bentonite-host rock interface. Points D, E, and F are well inside the clay formation, at distances to the bentonite-host rock interface of about 10, 20, and 450 m, respectively. Model results show that U(VI) quickly breaks through the EBS bentonite. It takes about 100 years for U(VI) to appear at Point D and then about 200 years to reach Point E. Slight increases in U(VI) concentration are also observed at Point E 500 years after the release of U(VI) from the canister. But the concentration remains very low after 10,000 years.

Figures 7-35 and 7-36 show the spatial distribution of aqueous U(VI) concentration at 1000 and 10,000 years, respectively. Symmetry is observed in both X and Z directions, indicating the model domain could be one quarter of the current domain, which would save substantial computation time.

Figure 7-37 shows temporal profiles of sorbed U(VI) concentration at points A, B, C, D, E, and F. Sorbed U(VI) concentration is the sum of each

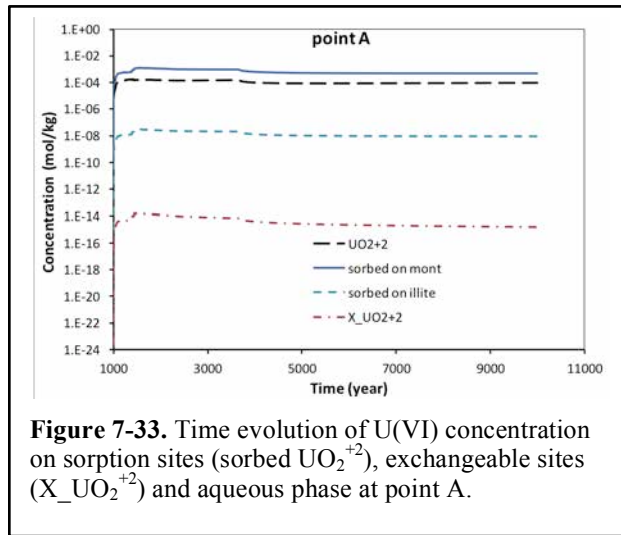


Figure 7-33. Time evolution of U(VI) concentration on sorption sites (sorbed UO_2^{+2}), exchangeable sites ($X_{UO_2^{+2}}$) and aqueous phase at point A.

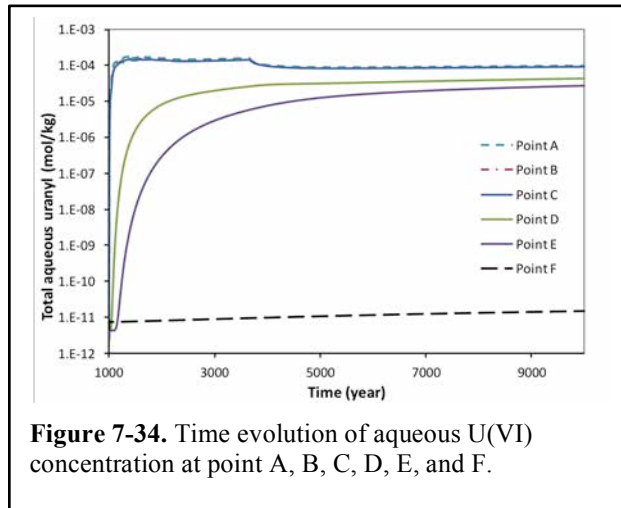


Figure 7-34. Time evolution of aqueous U(VI) concentration at point A, B, C, D, E, and F.

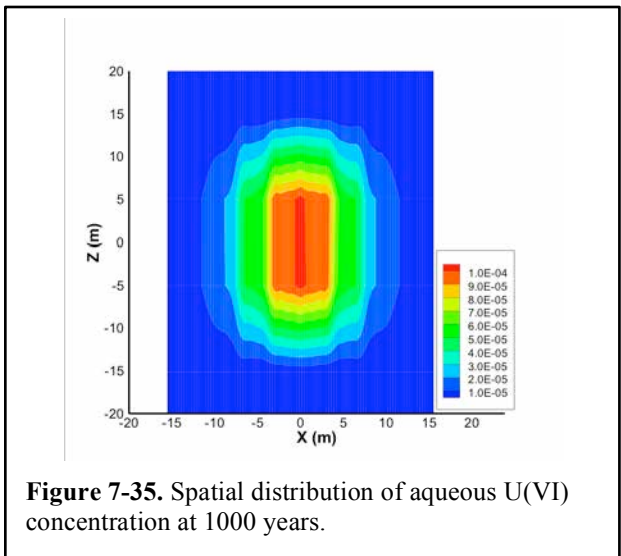


Figure 7-35. Spatial distribution of aqueous U(VI) concentration at 1000 years.

individual surface species listed in Table 7-2. The current model considers the adsorption of U(VI) on illite and smectite. In EBS bentonite, smectite is initially the only adsorbent. As illitization continues, illite forms and adsorbs U(VI) as well, but with a rather minimal contribution to total sorbed U(VI) in EBS. In the host clay formation, both illite and smectite can adsorb U(VI). At points B and C, although the aqueous U(VI) concentrations are very similar (see Figure 7-27), the total sorbed U(VI) concentrations are quite different.

Since the EDZ is not considered yet in this study and diffusion is the dominant transport process for U(VI) migration, mechanical changes affect the migration of U(VI) rather indirectly—swelling changes porosity and subsequently the tortuosity via the model of Millington and Quirk (1961) (see Table 7-6 for the relation between porosity and tortuosity). Both mineral precipitation/dissolution and stress changes can change the porosity. However, in clay formations, the porosity changes due to mineral precipitation/dissolution that overshadow the porosity changes (Fig. 7-38). Note that the discontinuity of curves is caused by the truncation of numbers. Therefore, the THC model, which does not consider mechanical processes, shows a U(VI) migration very similar to the THMC model; for example, the breakthrough curve at Point D as shown in Figure 7-39. Also shown in Figure 7-39 is a model that does not consider sorption (or surface complexation) reactions. Consideration of sorption makes significant difference in model results.

7.5 Conclusions and Future Work

For clay formations, coupled thermal, hydrological, mechanical, and chemical (THMC) processes are expected to have a significant impact on the long-term safety of a clay repository. These coupled processes may affect radionuclide transport specifically by changing transport paths (e.g., formation and evolution of EDZ) and altering flow, mineral, and mechanical properties that are related to radionuclide transport. The objectives of this research activity

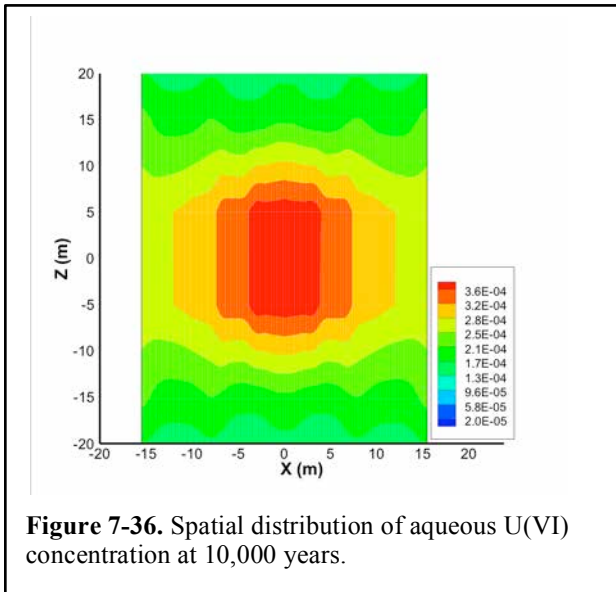


Figure 7-36. Spatial distribution of aqueous U(VI) concentration at 10,000 years.

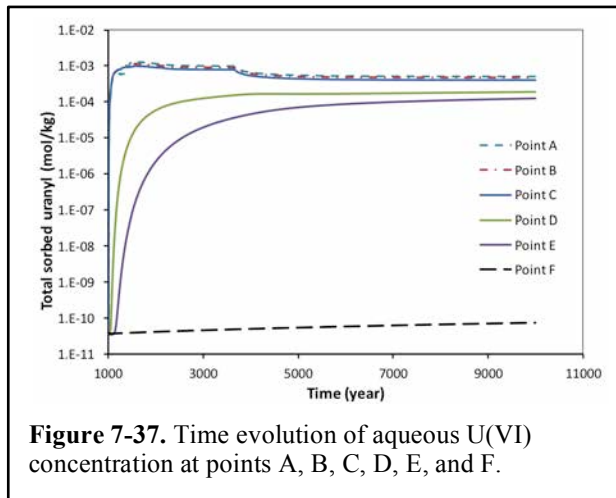


Figure 7-37. Time evolution of aqueous U(VI) concentration at points A, B, C, D, E, and F.

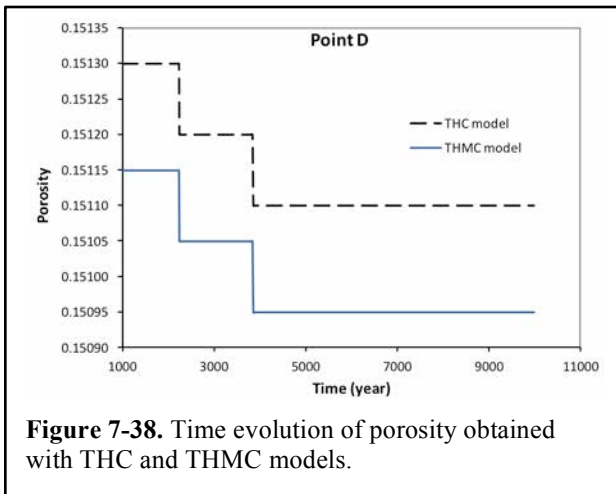
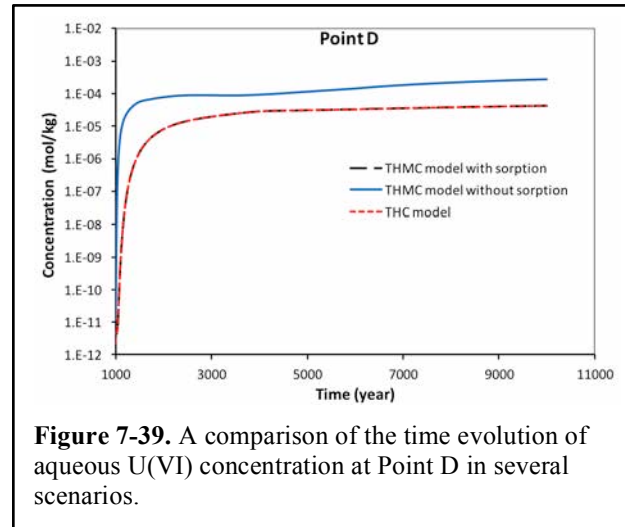


Figure 7-38. Time evolution of porosity obtained with THC and THMC models.

are to improve the modeling capability for coupled THMC processes and to use that improved capability to evaluate the THMC impacts on radionuclide transport. Our FY12 accomplishments include the following:

- The TOUGHREACT-FLAC3D simulator developed in Zheng et al. (2011) was further enhanced by incorporation of the two-site protolysis non-electrostatic surface complexation and cation exchange sorption model (2 SPNE SC/CE) (Bradbury and Baeyens, 2011) for U(VI).
- Coupled THMC simulations have been conducted to demonstrate the usefulness of the TOUGHREACT-FLAC3D simulator and to evaluate the THMC impacts on U(VI) transport.



The major findings from the THMC simulations include the following:

- The chemical-mechanical coupling based on linear elastic swelling model leads to 5% difference in effective stress compared with the model that ignores such coupling effect before the EBS bentonite becomes fully saturated.
- Ca and bicarbonate concentrations have a significant effect on U(VI) transport by aqueous complexation. A reactive transport model that neglects such an effect may underestimate the U(VI) concentration and migration rate.
- Montmorillonite is the most important adsorbent for U(VI) in clay formations, although its content in these formations is less than that of illite. Surface complexation plays a major role in adsorbing U(VI), whereas cation exchange does not make a significant contribution toward retarding the migration of U(VI).
- The effect of mechanical processes on the migration of U(VI) seems not be significant for an undamaged clay repository according to the current modeling results.

For the remaining months of FY12, we will

- Perform sensitivity analyses by varying major THMC parameters to further evaluate the impact of coupled THMC processes on the migration of U(VI) in clay formations.

For FY13, we propose the following tasks:

- Refine the chemical model (such as including redox reactions). In the current model, it is assumed that the system is under oxidizing conditions and that such conditions persist for 10,000 years. Changes in redox conditions may significantly change the behavior of uranium.
- Include EDZ in the current model.
- Develop and test other chemical-mechanical coupling constitutive relationships.

7.6 References

- Appelo, C. J. A. and D. Postma, 1994. *Geochemistry, groundwater and pollution*. Rotterdam, Netherlands, A.A.Balkema.
- Appelo, C. A. J., L. R. Van Loon and P. Wersin, 2010. Multicomponent diffusion of a suite of tracers (HTO, Cl, Br, I, Na, Sr, Cs) in a single sample of Opalinus Clay. *Geochimica et Cosmochimica Acta* **74**(4), pp. 1201–1219.
- Arai, Y., M. McBeath, J. R. Bargar, J. Joye and J. A. Davis, 2006. Uranyl adsorption and surface speciation at the imogolite–water interface: Self-consistent spectroscopic and surface complexation models. *Geochimica et Cosmochimica Acta* **70**(10): pp. 2492–2509.
- Arda, D., J. Hizal and R. Apak, 2006. Surface complexation modelling of uranyl adsorption onto kaolinite based clay minerals using FITEQL 3.2. *Radiochimica Acta* **94**(12), pp. 835–844.
- Barnichon J.D. and G. Volckaert, 2003. Observations and Predictions of Hydromechanical Coupling Effects in the Boom Clay, Mol Underground Research Laboratory, Belgium, *Hydrogeology Journal* **11**(1), pp. 193–202.
- Bernot, P., 2005. *Dissolved concentration limits of radioactive elements*, ANL-WIS-Md-000010 REV 05.
- Bernhard, G., G. Geipel, T. Reich, V. Brendler, S. Amayri and H. Nitsche, 2001. Uranyl(VI) carbonate complex formation: Validation of the $\text{Ca}_2\text{UO}_2(\text{CO}_3)_3(\text{aq})$ species. *Radiochimica Acta* **89**(8_2001), p. 511.
- Bethke C. M. and P. V. Brady, 2000. How the Kd Approach Undermines Group Water Cleanup. *Ground Water* **38**, pp. 435–443.
- Bradbury, M. H. and B. Baeyens, 2005. Modelling the sorption of Mn(II), Co(II), Ni(II), Zn(II), Cd(II), Eu(III), Am(III), Sn(IV), Th(IV), Np(V) and U(VI) on montmorillonite: Linear free energy relationships and estimates of surface binding constants for some selected heavy metals and actinides. *Geochimica et Cosmochimica Acta* **69**(4), pp. 875–892.
- Bradbury, M. H. and B. Baeyens, 2009a. Sorption modelling on illite Part I: Titration measurements and the sorption of Ni, Co, Eu and Sn. *Geochimica et Cosmochimica Acta* **73**(4), pp. 990–1003.
- Bradbury, M. H. and B. Baeyens, 2009b. Sorption modelling on illite. Part II: Actinide sorption and linear free energy relationships. *Geochimica et Cosmochimica Acta* **73**(4), pp. 1004–1013.
- Bradbury, M. H. and B. Baeyens, 2011. Predictive sorption modelling of Ni(II), Co(II), Eu(III), Th(IV) and U(VI) on MX-80 bentonite and Opalinus Clay: A “bottom-up” approach. *Applied Clay Science* **52**(1–2), pp. 27–33.
- Catalano, J. G. and G. E. Brown Jr., 2005. Uranyl adsorption onto montmorillonite: Evaluation of binding sites and carbonate complexation. *Geochimica et Cosmochimica Acta* **69**(12), pp. 2995–3005.
- Davis, J. A., J. A. Coston, D. B. Kent and C. C. Fuller, 1998. Application of the Surface Complexation Concept to Complex Mineral Assemblages. *Environmental Science & Technology* **32**(19), pp. 2820–2828.
- Davis, J. A., D. E. Meece, M. Kohler and G. P. Curtis, 2004. Approaches to surface complexation modeling of Uranium(VI) adsorption on aquifer sediments. *Geochimica et Cosmochimica Acta* **68**(18), pp. 3621–3641.
- De Windt, L., A. Burnol, P. Montarnal and J. van der Lee, 2003. Intercomparison of reactive transport models applied to UO₂ oxidative dissolution and uranium migration. *Journal of Contaminant Hydrology* **61**(1-4), pp. 303–312.
- De Windt, L., H. Schneider, C. Ferry, H. Catalette, V. Lagneau, C. Poinssot, A. Poulesquen and C. Jegou, 2006. Modeling spent nuclear fuel alteration and radionuclide migration in disposal conditions. *Radiochim. Acta* **94**, pp. 787–794.
- Fernández, A. M., M. J. Turrero, D. M. Sánchez, A. Yllera, A. M. Melón, M. Sánchez, J. Peña, A. Garralón, P. Rivas, P. Bossart and P. Hernán, 2007. On site measurements of the redox and carbonate system parameters in the low-permeability Opalinus Clay formation at the Mont Terri Rock Laboratory. *Physics and Chemistry of the Earth, Parts A/B/C* **32**(1-7), pp. 181–195.

- Fouche O., Wright H., Cleach J. L., and Pellenard P., 2004. Fabric Control on Strain and Rupture of Heterogeneous Shale Samples by Using a Non-Conventional Mechanical Test, *Applied Clay Science* **26**, pp. 367–387.
- Garcia-Gutierrez, M., J. L. Cormenzana, T. Missana, M. Mingarro, U. Alonso, J. Samper, Q. Yang and S. Yi, 2008. Diffusion experiments in Callovo-Oxfordian clay from the Meuse/Haute-Marne URL, France. Experimental setup and data analyses. *Physics and Chemistry of the Earth* **33**, S125–S130.
- Garcia-Gutierrez, M., J. L. Cormenzana, T. Missana, M. Mingarro and P. L. Martin, 2006. Large-scale laboratory diffusion experiments in clay rocks. *Physics and Chemistry of the Earth* **31**(10-14), pp. 523–530.
- Gao, L., Z. Yang, K. Shi, X. Wang, Z. Guo and W. Wu, 2010. U(VI) sorption on kaolinite: effects of pH, U(VI) concentration and oxyanions. *Journal of Radioanalytical and Nuclear Chemistry* **284**(3), pp. 519–526.
- Gu, X., L. J. Evans and S. J. Barabash, 2010. Modeling the adsorption of Cd (II), Cu (II), Ni (II), Pb (II) and Zn (II) onto montmorillonite. *Geochimica et Cosmochimica Acta* **74**(20), pp. 5718–5728.
- Korichi, S. and A. Bensmaili, 2009. Sorption of uranium (VI) on homoionic sodium smectite experimental study and surface complexation modeling. *Journal of Hazardous Materials* **169**(1-3), pp. 780–793.
- Laredj, N., H. Missoum and K. Bendani, 2010. Modeling the effect of osmotic potential changes on deformation behavior of swelling clays. *Journal of Porous Media* **13**(8), pp. 743–748.
- Lauber, M., Baeyens, B., Bradbury, M.H., 2000. *Sorption of Cs, Sr, Ni, Eu, Th, Sn and Se on Mont Terri Opalinus Clay: physico-chemical characterisation and sorption measurements*. PSI Bericht Nr. 00-10 Paul Scherrer Institut, Villigen, Switzerland and Nagra NTB 00-11, Nagra, Wettingen, Switzerland.
- Maes, N., S. Salah, D. Jacques, M. Aertsens, M. Van Gompel, P. De Cannière and N. Velitchkova, 2008. Retention of Cs in Boom Clay: Comparison of data from batch sorption tests and diffusion experiments on intact clay cores. *Physics and Chemistry of the Earth, Parts A/B/C* **33**(Supplement 1): pp. S149–S155.
- McKinley, J. P., J. M. Zachara, S. C. Smith and G. D. Turner, 1995. The influence of uranyl hydrolysis and multiple site-binding reactions on adsorption of U(VI) to montmorillonite. *Clays and Clay Minerals* **43**(5), 586–598.
- Müller-Vonmoos, M., Kahr, G., 1983. Mineralogische untersuchungen von wyoming bentonite MX-80 und montigel. NTB 83-13, Nagra, Wettingen, Switzerland.
- Ochs, M., B. Lothenbach, M. Shibata and M. Yui, 2004. Thermodynamic modeling and sensitivity analysis of porewater chemistry in compacted bentonite. *Physics and Chemistry of the Earth, Parts A/B/C* **29**(1): pp. 129–136.
- Patriarche D., Ledoux E., Simon-Coincon R., Michelot J., and Cabrera J, 2004. Characterization and Modeling of Diffusive Process for Mass Transport through the Tournemire Argillites Aveyron, France, *Applied Clay Science* **26**, pp. 109–122.
- Pruess, K., C. Oldenburg and G. Moridis, 1999. TOUGH2 User's Guide, Version 2.0, Lawrence Berkeley National Laboratory, Berkeley, CA.
- Pruess, K., 2004. The TOUGH Codes— a family of simulation tools for multiphase flow and transport processes in permeable media. *Vadose Zone Journal* **3**, pp. 738–746.
- Rutqvist, J., Barr, D., Birkholzer, J.T., Fujisaki, K., Kolditz, O., Liu, Q.-S., Fujita, T., Wang, W., Zhang, C.-Y., 2009. A comparative simulation study of coupled THM processes and their effect on fractured rock permeability around nuclear waste repositories. *Environmental Geology* **57**, pp. 1347–1360.
- Rutqvist, J., 2011. Status of the TOUGH-FLAC simulator and recent applications related to coupled fluid flow and crustal deformations. *Computers & Geosciences* **37**(6), pp. 739–750.
- Sonnenthal, E., A. Ito, N. Spycher, M. Yui, J. Apps, Y. Sugita, M. Conrad and S. Kawakami, 2005. Approaches to modeling coupled thermal, hydrological, and chemical processes in the Drift Scale Heater Test at Yucca Mountain. *Int. J. Rock Mech. Min. Sci.* **42**, pp. 6987–6719.

- Sonnenthal, E., 2008. Chapter 5 in: Birkholzer, J. Rutqvist, E. Sonnenthal, and D. Barr, Long-Term Permeability/Porosity Changes in the EDZ and Near Field due to THM and THC Processes in Volcanic and Crystalline-Bentonite Systems, *DECOVALEX-THMC Project Task D Final Report*.
- Soler, J. M., J. Samper, A. Yllera, A. Hernández, A. Quejido, M. Fernández, C. Yang, A. Naves, P. Hernán and P. Wersin, 2008. The DI-B in situ diffusion experiment at Mont Terri: Results and modeling. *Physics and Chemistry of the Earth, Parts A/B/C* 33(Supplement 1), pp. S196–S207.
- Spycher, N., K. Pruess and J. Ennis-King, 2003. CO₂-H₂O mixtures in the geological sequestration of CO₂. I. Assessment and calculation of mutual solubilities from 12 to 100°C and up to 600 bar. *Geochimica et Cosmochimica Acta* 67(16), pp. 3015–3031.
- Spycher, N. F., M. Issarangkun, B. D. Stewart, S. Sevinç Şengör, E. Belding, T. R. Ginn, B. M. Peyton and R. K. Sani, 2011. Biogenic uraninite precipitation and its reoxidation by iron(III) (hydr)oxides: A reaction modeling approach. *Geochimica et Cosmochimica Acta* 75(16), pp. 4426–4440.
- Tang C. A. and Hudson J.A., 2010. *Rock Failure Mechanisms*, Taylor & Francis, London, UK.
- Tournassat, C., E. Ferrage, C. Poinssignon and L. Charlet, 2004. The titration of clay minerals: II. Structure-based model and implications for clay reactivity. *Journal of Colloid and Interface Science* 273(1): pp. 234–246.
- Thury, M., 2002. The characteristics of the Opalinus Clay investigated in the Mont Terri underground rock laboratory in Switzerland. *Comptes Rendus Physique* 3(7-8): pp. 923–933.
- Van Loon, L. R., P. Wersin, J. M. Soler, J. Eikenberg, T. Gimmi, P. Hernan, S. Dewonck and S. Savoye, 2004. In-situ diffusion of HTO, ²²Na⁺, Cs⁺ and I⁻ in Opalinus clay at the Mont Terri underground rock laboratory. *Radiochim. Acta* 92, pp. 757–763.
- Wronkiewicz, D.J.; Bates, J.K.; Wolf, S.F.; and Buck, E.C., 1996. Ten-year results from unsaturated drip tests with UO₂ at 90°C: implications for the corrosion of spent nuclear fuel. *Journal of Nuclear Materials* 238(1), pp. 78–95.
- Wu, T., S. Amayri, J. Drebert, L. R. Van Loon and T. Reich, 2009. Neptunium(V) Sorption and Diffusion in Opalinus Clay. *Environmental Science & Technology* 43(17): pp. 6567–6571.
- Xu, T., N. Spycher, E. Sonnenthal, G. Zhang, L. Zheng and K. Pruess, 2011. TOUGHREACT Version 2.0: A simulator for subsurface reactive transport under non-isothermal multiphase flow conditions. *Computers & Geosciences* 37(6): pp. 763–774.
- Xu, T. and K. Pruess, 2001. Modeling multiphase non-isothermal fluid flow and reactive geochemical transport in variably saturated fractured rocks: *1 Methodology*. *Am. J. Sci.* 301: pp. 16–33.
- Xu, T. and K. Pruess, 2008. Numerical studies on enhanced CO₂ dissolution and mineral trapping due to formation of aqueous complexes. *Computational Methods in Water Resources*. San Francisco, California.
- Xu, T., E. Sonnenthal, N. Spycher and K. Pruess, 2006. TOUGHREACT: A simulation program for non-isothermal multiphase reactive geochemical transport in variably saturated geologic media. *Computers and Geosciences* 32, pp. 145–165.
- Zhang G., Spycher N., Sonnenthal E., Steefel C., and Xu T., 2008, Modeling reactive multiphase flow and transport of concentrated aqueous solutions. *Nuclear Technology* 164, pp. 180–195.
- Zheng, L., J. A. Apps, Y. Zhang, T. Xu and J. T. Birkholzer, 2009. On mobilization of lead and arsenic in groundwater in response to CO₂ leakage from deep geological storage. *Chemical geology* 268(3-4), pp. 281–297.
- Zheng, L., J. Rutqvist, J. Houseworth, J. Davis, R. Tinnacher, L. Li and H-H Liu, 2011. Investigation of near-field thmc coupled processes, milestone report in FUD, Work Package number 1.02.08.03.

Chapter 8. Advanced Parameter Uncertainty Quantification Using Null Space Latin Hypercube Sampling: Application to Uranium and Neptunium Transport Experiments

8.1 Introduction

With the ever-increasing computational power available to modelers, no longer are simulations of complex systems relegated to a single deterministic prediction. Such an approach is particularly ill-suited for environmental systems that typically contain vast aleatory and epistemic uncertainties. Moreover, it is understood that models make imperfect predictions, especially when applied to complex, heterogeneous, reactive groundwater systems. However, given advances in both parameter estimation including uncertainty analysis methodologies and computational horsepower, models can be used to both quantify their predictive uncertainty through optimal processing of all available site data and human expertise, and to reduce that uncertainty to its theoretical minimum. Such models can and should be used in decision analyses contexts to ensure optimum and safe management decisions.

Models provide effective decision support when they are designed to explore and quantify uncertainty or to test hypotheses pertaining to future environmental behavior under proposed management plans. A hypothesis can be rejected if it has a low likelihood of occurrence, which is defined as when such an event is incompatible with available system hard and soft data (Doherty et al., 2011, Table 3-4). Hard data are composed of empirical point measurements of a system's properties as well as historical measurements of system state; soft data comprise inferred knowledge and expertise based on multi-year site studies or data from other sites.

The approach demonstrated here involves a complimentary set of experiments and an interpretive modeling strategy that couples a simplified geochemical description of the system with transport calculations. The modeling strategy recognizes that it may never be possible to fully account for all the mineralogical heterogeneities in real systems, so it represents these heterogeneities as an ensemble of sorption sites with characteristic adsorption and desorption rate constants that have widely varying values. It is hypothesized that for any given heterogeneous system, appropriate adsorption and desorption rate constants can be estimated from a set of carefully planned laboratory experiments, and that the resulting description of the system will be robust enough to provide reliable upscaled predictions of reactive transport in field settings. The key to the approach is to conduct a variety of different experiments that interrogate the adsorption and desorption rates in different but complementary ways to effectively capture the ensemble behavior of the system. It is also important that these experiments interrogate an appropriate representation of the system mineralogy and geochemistry. The approach is simplified when the groundwater chemistry of the system is relatively constant spatially and temporally with respect to key parameters such as pH, Eh, and major ion concentrations, as is often the case over relatively large scales in natural systems that have not been altered by engineered barriers. However, the approach can in principle be extended to situations where these parameters are not constant. In this work, experimental data on sorption and desorption of uranium (U) and neptunium (Np) on fractured volcanic tuff (Dean, 2010) are re-examined using the Parameter ESTimation code, PEST (Doherty, 2009, 2010). Moreover, PEST's null-space Monte Carlo (NSMC) (Tonkin and Doherty, 2009) tool is upgraded to incorporate Latin Hypercube Sampling (LHS) (Iman and Shortencarier, 1983) to reduce the computation requirements to effectively quantify parameter uncertainty.

8.2 Experimental Background

While details of the experiment can be found in the work of Dean (2010) and Arnold et al. (2011), a short description is provided. Between 2008 and 2010, a series of adsorption, desorption, and column transport experiments were conducted to evaluate the transport of U and Np through saturated volcanic tuffs. It is expected that for most geologic disposal systems involving used fuel as a waste form, these two radionuclides will be potential contributors to dose. They fall in the general category of weakly sorbing radionuclides that are not expected to be strongly influenced by colloid-facilitated transport.

In the experiments interpreted here, the medium was a clay-rich, ash-flow tuff from borehole UE-25c#2 near on the Nevada Test Site, and the ground water was from well J-13 at the Nevada Test Site (details of the tuff and groundwater are provided in Tables 3-1 and 3-2 of Arnold et al. (2011). Dean (2010) conducted batch sorption experiments with these materials using both ^{233}U and ^{237}Np and then followed these with desorption experiments performed in the same vessels as the adsorption experiments. The desorption experiments involved flowing radionuclide-free water through the vessels containing the crushed radionuclide-bearing rock and measuring the concentrations of desorbed radionuclides in the effluent as a function of time. Larger-scale column experiments were also conducted by injecting either ^{233}U or ^{237}Np along with ^3HHO and evaluating the adsorption/desorption behavior of the actinides by comparing their breakthrough curves in the column effluent to that of the ^3HHO . Finally, these columns were frozen and sectioned after the experiments were completed so that the disposition of the radionuclides that had not eluted from the columns could be determined, serving as an additional measure of transport of the actinides. Arnold et al. (2011) provide additional details of the experiments.

8.3 Numerical Modeling

In an attempt to interpret her experiments, Dean (2010) used a single-species modeling approach that involved assuming first-order adsorption and desorption kinetics with different surface site densities and different rate constants for several different types of sites (varying from weak to very strong). The assumption of weak and strong sites on the surface is consistent with what others have assumed (Davis and Curtis, 2003; Liu et al., 2009; Liu et al., 2008; Qafoku et al., 2005), and it is also consistent with the qualitative observations from the $\mu\text{-EXAFS}$ measurements (Arnold et al., 2011, p. 29). The system of equations assumed for the single-component model for the sorption/desorption experiments is given by (note that four sites are assumed here):

$$\frac{dC}{dt} = \frac{1}{V_T} \left\{ Q(C_{in} - C) - \left[\sum_{i=1}^4 k_{f_i} \left(1 - \frac{s_i}{s_{i_{\max}}} \right) \right] C + \sum_{i=1}^4 k_{r_i} s_i \right\}, \quad (\text{Eq. 8-1})$$

$$\frac{ds_i}{dt} = \frac{1}{M} \left[k_{f_i} \left(1 - \frac{s_i}{s_{i_{\max}}} \right) C - k_{r_i} s_i \right], \quad (\text{Eq. 8-2})$$

where, C = concentration out of reaction vessel, CPM/mL or mol/mL,
 C_{in} = concentration in solution flowing into reaction vessel, CPM/mL or mol/mL,
 s_i = concentration sorbed to site i , CPM/g or mol/mL,
 $s_{i_{\max}}$ = maximum concentration that can be sorbed to site i , CPM/g or mol/mL,
 V_T = volume of solution in reaction vessel, mL,
 Q = flow rate through reaction vessel (zero during sorption phase), mL/hr,

M = mass of solid, g,
 k_{f_i} = forward (adsorption) rate constant for site i , mL/g-hr,
 k_{r_i} = reverse (desorption) rate constant for site i , 1/hr,
 t = time, hr.

Four different sites were assumed ($i = 4$). The rate constants and site densities (maximum concentrations that can be sorbed to a site) were adjusted to obtain a least-squares fit to the sorption/desorption data, and then the best-fitting parameters were used in a column transport model that implemented the reactions of equations 8-1 and 8-2 in the 1-D advection-dispersion equation to describe column transport:

$$\frac{\partial C}{\partial t} = D \frac{\partial^2 C}{\partial x^2} - v \frac{\partial C}{\partial x} - \frac{\rho}{\theta} \left\{ \left[\sum_{i=1}^4 k_{f_i} \left(1 - \frac{S_i}{S_{i_{\max}}} \right) \right] C + \sum_{i=1}^4 k_{r_i} S_i \right\}, \quad (\text{Eq. 8-3})$$

where, D = solute dispersion coefficient in column, cm²/hr,
 v = mean pore velocity in column, cm/hr,
 x = distance along column, cm,
 ρ = bulk density of tuff in column, g/cm³,
 θ = column porosity.

Equations 8-2 and 8-3 were used to describe the solid- and solution-phase concentrations, respectively, as a function of time and distance in the columns. Breakthrough curves of ³HHO, which was always injected simultaneously with U or Np in the column experiments, provided estimates of hydrodynamic parameters (flow velocity and dispersivity) to use in equation 8-3 for modeling the column experiments. The ³HHO data also indicated that diffusion between flowing and stagnant water in the columns was negligible (i.e., the lack of any ³HHO tailing indicated there was no need for a dual-porosity model to describe the experiments).

Dean (2010) found that when the reaction parameters deduced from the sorption/desorption experiments were used in the column transport model, they significantly over predicted the U or Np breakthrough curves in the column experiments. This was true despite the fact that some of the sorption sites were deduced to have very slow desorption kinetics in the sorption/desorption experiments. Furthermore, when the sorption and desorption rate constants and site densities were adjusted to provide a reasonable match to the column breakthrough data, the distributions of radionuclides remaining in the columns at the end of the experiments were poorly approximated (the radionuclides were predicted to have moved further through the columns than they actually did). Likewise, adjustment of the rate parameters to achieve a good match to the post-mortem radionuclide profiles resulted in a significant under prediction of the column breakthrough curves.

In Arnold et al. (2011), the modeling approach of Dean (2010) (equations 8-1 to 8-3) was modified to account for up to three aqueous species that react with each other and with the surface sorption sites of equations 8-1 to 8-3. Thus, equations 8-1 to 8-3 effectively became nine equations; three equations for each of the three separate aqueous species, with solution-phase reaction terms included in equations 8-1 and 8-3. It was assumed that there was only a single predominant sorbed species (all three aqueous species reacted with the surfaces to form the same sorbed species). With these assumptions, the reactions associated with each sorption site are depicted in Figure 8-1.

The multicomponent reaction scheme of Figure 8-1, as employed by Arnold et al. (2011), provided significantly improved simultaneous model fits to the data sets of Dean (2010). However, the fits were accomplished by a manual process that was by no means optimal, and the resulting fits were not entirely satisfactory. The combination of the multicomponent modeling approach and the multiple transport data sets provides an appropriately challenging inverse problem for the facilities of PEST. In the remainder of this chapter, the automated calibration of the model to achieve a match to the data sets is described, and then both linear and nonlinear uncertainty analyses using PEST routines are described.

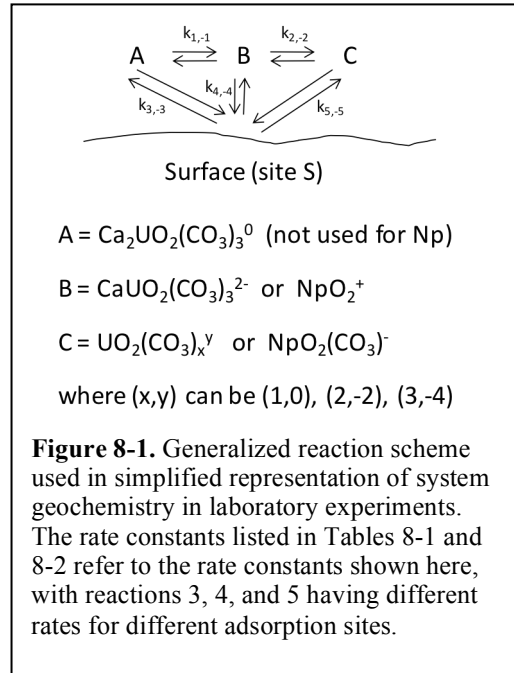
8.4 Model Calibration

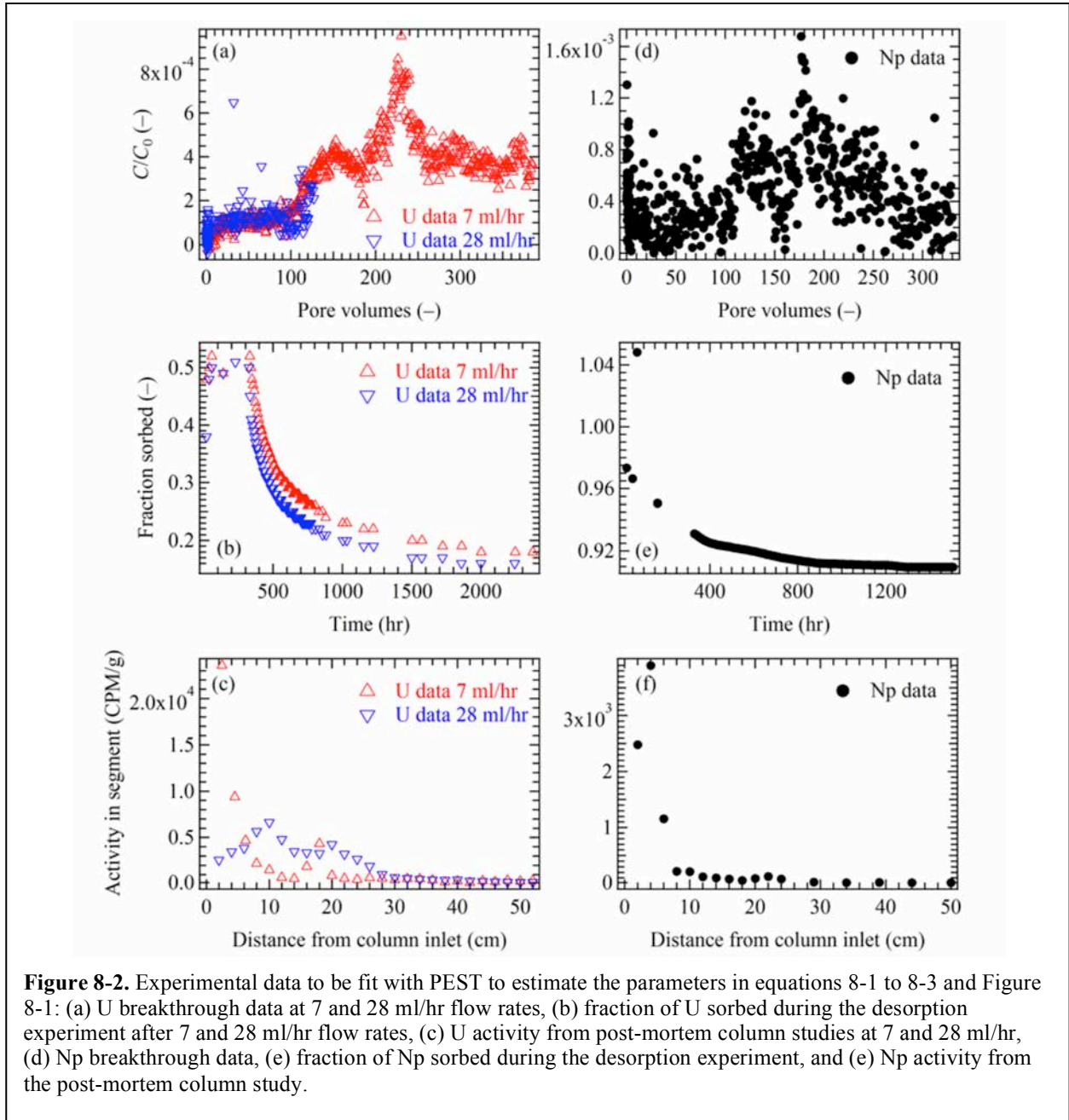
Model calibration can be as much art as science because it is often up to best scientific judgment to include salient features and exclude those considered less important.

Moreover, data weights can be assigned according to any number of justifiable schemes. For example, for each radionuclide, fits are simultaneously sought to three different experiments (for U, two different flow rates were also used resulting in five experimental data sets to be fit simultaneously with the same set of parameters). This means that the classical approach of using the inverse of the uncertainty of each data point as its weight may not be optimum.

All experimental data fit with the conceptual model described by equations 8-1 to 8-3, with the multicomponent modifications of Figure 8-1, are shown in Figure 8-2. U data are in the left column; Np data on the right. U was studied under two different flow rates; 7 and 28 ml/hr. The top row shows normalized concentrations of U and Np eluted from columns in the column experiments (breakthrough curves). The middle row shows the fraction of U and Np adsorbed to volcanic tuff material in adsorption/desorption experiments, with the transition from adsorption to desorption (achieved by flowing radionuclide-free water through the adsorption reactors) occurring approximately 330 hours into the experiments. The bottom row shows the activity in segments of the columns (top row) after the breakthrough experiments were completed (post-mortem studied showing residual, perhaps irreversibly sorbed, U and Np in the columns).

PEST was first run in parameter estimation mode with initial parameter guesses specified according to the hand-calibrated values reported by Arnold et al. (2011, Tables 3-4 and 3-5). These initial guesses with corresponding parameter ranges that PEST could interrogate are listed in Table 8-1. Parameter limits were assigned fairly broadly, but took into account expert judgment. The classical way to weight a calibration effort is to specify the weight of each datum equal to the inverse of its uncertainty. Upon discussions with the experimentalist (Reimus, 2012, personal communication), weights were assigned as the inverse of the standard deviation in measurement noise of each data point. The fits returned from this PEST iteration were not particularly satisfying; clearly the process was complicated by the fact that both the magnitudes of the data and the number of data points per experiment vary by orders of magnitude. Toward this end, a hierarchical weighting scheme was adopted whereby the intra-experimental observational uncertainties





were honored, but these were scaled such that each experiment contributed roughly equally to the overall objective function (inter-experimental weights were adjusted to yield a contribution to the overall objective function of near unity). For the breakthrough experiments in Figure 8-2a and d, for the intra-experimental weights, a moving standard deviation across 10 data points was used as the uncertainty with weights as the inverse of these. Each Np weight was multiplied by 0.03, each 7-ml/hr U weight was multiplied by 0.01, and each 28-ml/hr U weight was multiplied by 0.015 to yield an intra-experimental objective function of near 1; final weights are shown in Figure 8-3. The standard deviation for each of the

Table 8-1. Parameter initial guesses with upper and lower limits allowed during the estimation process listed parenthetically (see Figure 8-1 for definition of rate constants).

Neptunium					
Parameter	Solution	Site 1	Site 2	Site 3	Site 4
$k_{1,-1}$ A to B; B to A (1/hr) ^a	10; 0.001				
$k_{2,-2}$ B to C; C to B (1/hr) ^b	2; 2 (10^{-3} – 10^3)				
k_3 A to S (ml/g-hr) ^c		10^{-3}	10^{-3}	10^{-3}	10^{-3}
k_{-3} S to A (1/hr) ^d		0	0	0	0
k_4 B to S (ml/g-hr)		30 (10^{-3} – 10^3)	8 (1 – 10^3)	7 (0.1 – 10^3)	7 (0.1 – 10^3)
k_{-4} S to B (1/hr) ^d		0	0	0	0
k_5 S to C (1/hr)		5 (0.1 – 10^3)	7 (10^{-3} – 100)	0.02 (10^{-3} – 10^3)	10^{-3} (10^{-3} – 10^3)
k_{-5} , S to C (1/hr)		27 (10^{-3} – 5×10^3)	0.02 (10^{-3} – 10^3)	4×10^{-4} (10^{-3} – 10^3)	9.1×10^{-3} (10^{-8} – 10^3)
$S_{i_{max}}$ ($\mu\text{mol/g}$)		3.7×10^5 (1 – 10^6)	200 (1 – 10^6)	481 (1 – 10^6)	3.5×10^3 (1 – 10^6)
Uranium					
$k_{1,-1}$ A to B; B to A (1/hr) ^e	10; 5 (0.1 – 10^3)				
$k_{2,-2}$ B to C; C to B (1/hr) ^f	0.01; 20 (10^{-3} – 10^3)				
k_3 A to S (ml/g-hr)		30 (10^{-3} – 10^3)	30 (0.1 – 100)	0.5 (5×10^{-3} – 50)	0.08 (5×10^{-3} – 1)
k_{-3} S to A (1/hr) ^d		0	0	0	0
k_4 B to S (ml/g-hr)		30 (0.01 – 100)	30 (1 – 10^4)	0.5 (0.01 – 10)	0.08 (0.1 – 100)
k_{-4} S to B (1/hr) ^d		0	0	0	0
k_5 S to C (1/hr)		30 (1 – 500)	35 (0.1 – 500)	1.8 (0.1 – 10)	0.4 (10^{-3} – 2)
k_{-5} , S to C (1/hr)		27 (1 – 5×10^3)	1 (0.05 – 10)	0.0052 (10^{-4} – 0.1)	10^{-3} (10^{-6} – 10^{-3})
$S_{i_{max}}$ ($\mu\text{mol/g}$)		2.0×10^3 (5×10^4 – 10^6)	1.4×10^4 (10 – 10^3)	2.2×10^4 (10^3 – 10^6)	1.5×10^4 (10^3 – 10^5)

^aNot estimated because the A species was considered absent from the Np chemistry (Arnold et al., 2011, Figure 3-10).

^bForward and reverse rates were assumed equal because this reaction is assumed in equilibrium.

^cAssigned negligible values because there is no A species present.

^dIrreversible sorption assumed.

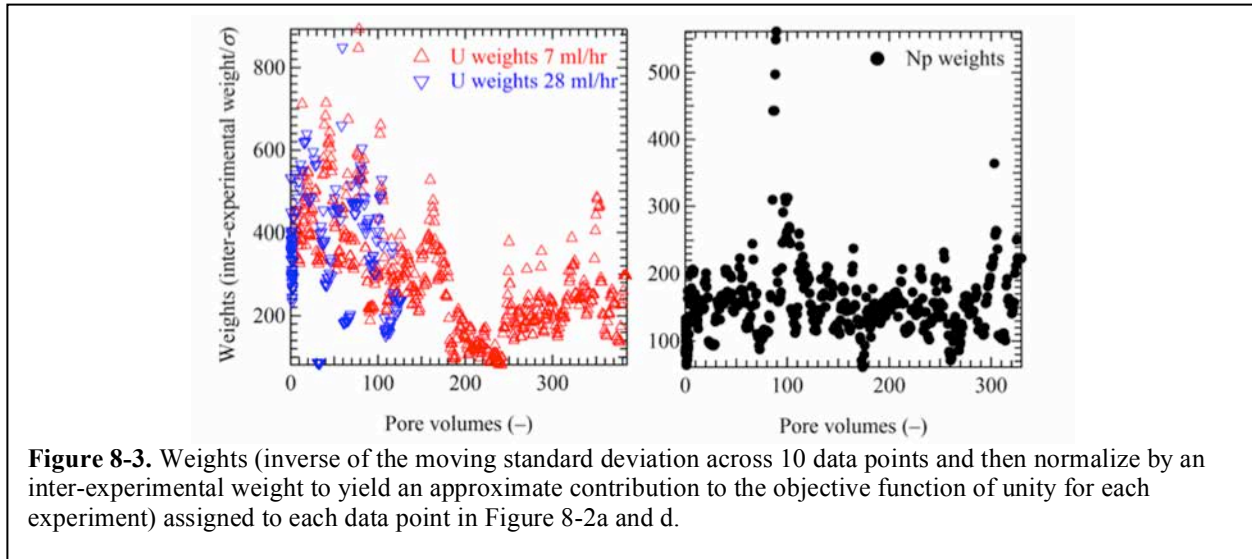
^eForward to reverse ratio fixed to 2:1 (only forward rate, k_1 , estimated).

^fForward to reverse ratio fixed to 1:200 (only forward rate, k_2 , estimated).

Note: Mean water residence time in the 7-ml/hr column was determined to be 7.8 hr and in the 28-ml/hr column it was 1.8 hr from ³HHO breakthrough curves. Injection pulses were approximately 1 pore volume (~50 ml). The U injection concentration was 10^{-6} M.

data points in Figure 8-2b and e is equal to the difference in data across the two U desorption experiments, 0.043. This yields a weight of 23. These were multiplied by 0.31 (to obtain a weight of 7.2) to yield an intra-experimental contribution to the objective function of near 1. For the post-mortem activity data in Figure 8-2c, when the flow rate was 7 ml/hr, the standard deviation was ~300 (weight of 0.00333), and when the flow rate was 28 ml/hr, the standard deviation was ~1000 (weight 0.001) for the first 13 data points and ~200 (weight 0.005) for the remaining. For the Np data in Figure 8-2f, the standard deviation was ~100 (weight 0.01). Each of these weights was multiplied by 0.015, 0.055, 0.055, and 0.09, respectively, to yield nearly equal inter-experimental contributions to the objective function (final weights are 5.5×10^{-5} , 2.8×10^{-4} , 5.0×10^{-5} , and 9.2×10^{-4} , respectively).

As noted above, the initial PEST iteration did not yield particularly satisfying fits to the data. Acknowledging the difficulty noted by Arnold et al. (2011) of fitting all experiments simultaneously (particularly for the U experiments) as well as the fact that models are imperfect vessels of knowledge for our system, we allow a different set of parameters to fit the simulation of each experiment. However, regularization data were added to the objective function whereby the differences between the same parameters were to be kept as close to zero as possible. Using the results from the first PEST iteration as initial guesses (same parameter ranges) and the new weighting scheme that respects intra-experimental



weighting yet yields inter-experimental contributions to the objective function of near unity, PEST was run in parameter estimation mode with regularization and truncated singular value decomposition (Doherty, 2009, Sections 7 and 8.4).

To be more specific, for the Np experiments, 34 parameters were estimated, two for each of the parameters with ranges listed in Table 8-1. Note that k_1 , k_{-1} , and k_3 were not estimated for Np because there is no species A present (see Arnold et al., 2011, Figure 3-10). The first set of 17 parameters was used to solve equation 8-3, which yields simulations corresponding to output data in Figure 8-2d and f. The second set of 17 was used to solve equations 8-1 and 8-2 and corresponds to the data in Figure 8-2e. Nominally, these two sets of parameters should be the same; regularization data were provided to the parameter estimation process to help ensure this. For the U experiments, 66 parameters were estimated; 22 each for the 7- and 28-ml/hr data in Figure 8-2a and c and 22 for the data in Figure 8-2b. Again, each of the three sets of parameters should be equal, but an inability of the models to capture all of the nuances in the experiments (and to then yield a single parameter set that calibrates all experiments equally well) led us to expand the calibration effort to include multiple values for a single parameter. Uncertainty across all equivalent parameters will be investigated.

The results from the two-step PEST calibration (once with a single set of parameters where the weights of each datum were the inverse of its uncertainty and again allowing inter-experimental parameter differences where the intra-experimental uncertainties are honored, but inter-experimental weights were adjusted to yield near unit contributions to the objective function from each experiment) are shown in Figure 8-4. Each set of best-fit parameters is listed in Table 8-2 (two sets for the Np data and three sets for the U data).

8.5 Linear Uncertainty Analysis

The PEST utility GENLINPRED performs generalized linear predictive uncertainty analyses. These analyses include estimates of parameter identifiability and uncertainty reduction (Doherty and Hunt, 2009). Also, it can determine how much a parameter's uncertainty is reduced as a function of each group of data in Figure 8-2. Identifiability is an indicator of our ability to determine a parameter's value based on the available data set. Uncertainty reduction is the fraction of the parameter range specified in Table 8-1 that can be reduced through the calibration process based on the available data sets. Figure 8-5 shows the identifiabilities and relative uncertainty reduction for all parameters. Two bars are listed for each

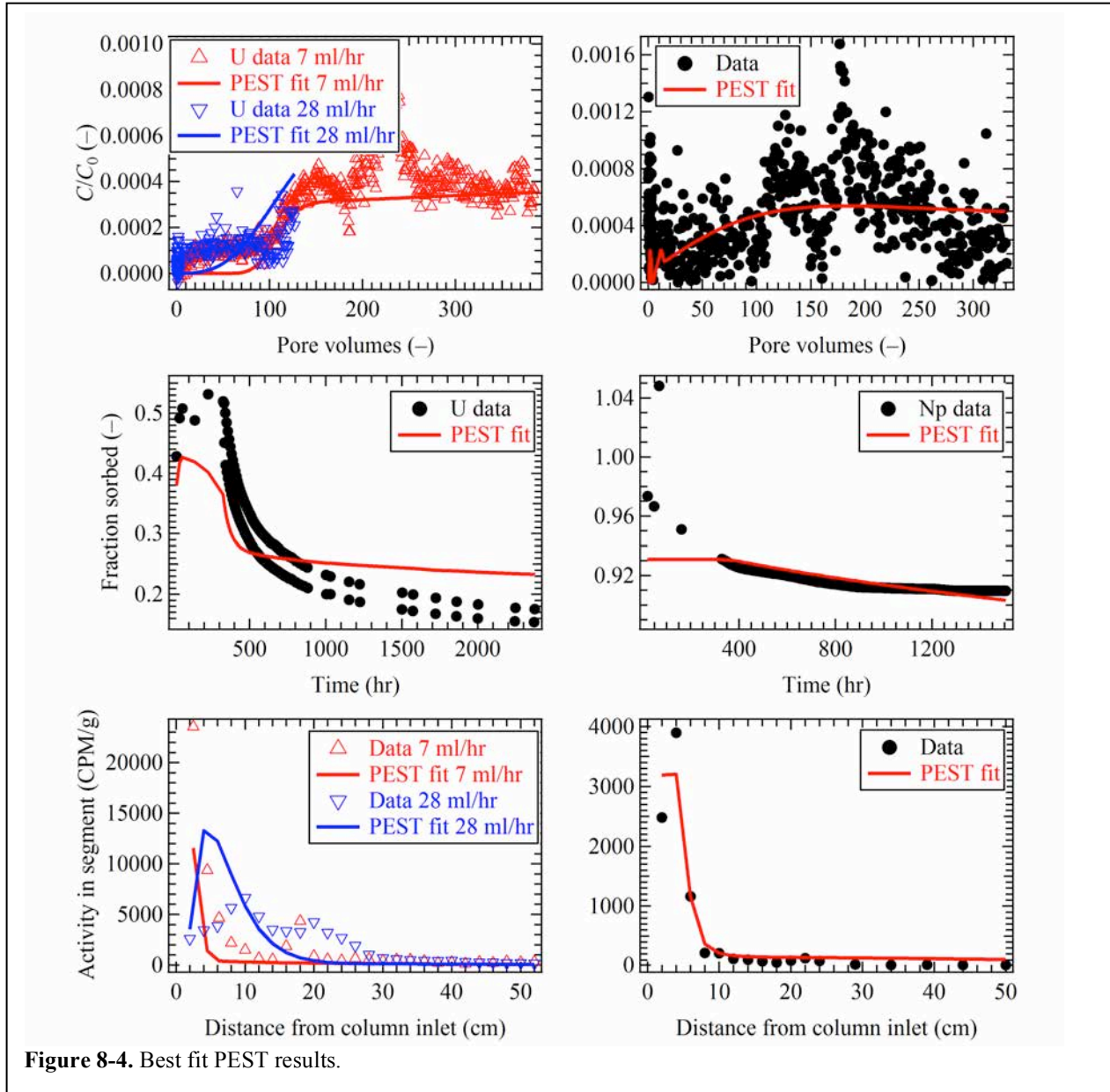


Figure 8-4. Best fit PEST results.

parameter, one for each set supplied to the calibration effort (recall that these were regularized to be equal insofar as the dataset and calibration allow). Note how, in general, identifiability and relative uncertainty reduction are similar, if a parameter is identifiable it can also have its uncertainty significantly reduced. Also, for parameters in the midrange of identifiability, they are more identifiable for second set, which was used to solve equations 8-1 and 8-2 and corresponds to the data in Figure 8-2e. This suggests that the content in Figure 8-2e (post-mortem residual activities) is significant with regard to model parameters.

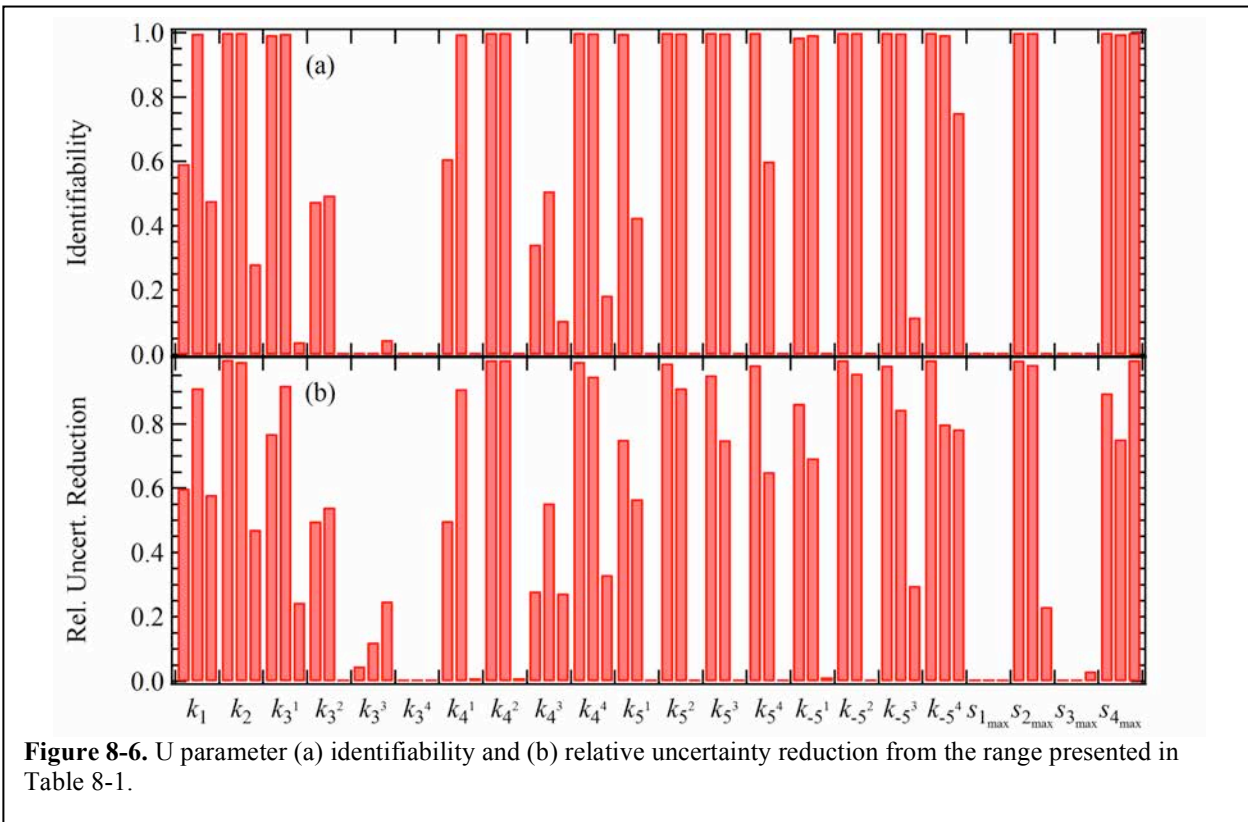
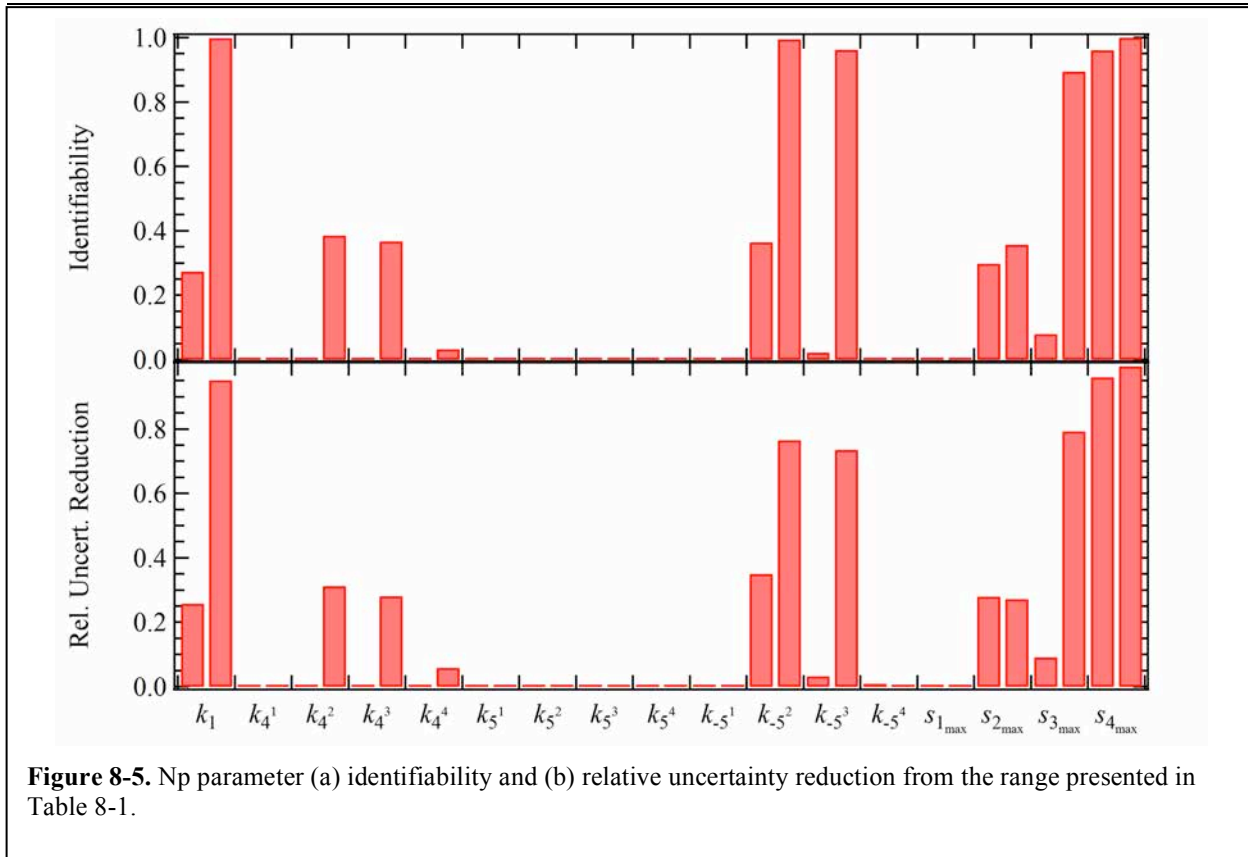
Table 8-2. PEST best-fit sets of parameters (see Figure 8-1 for definition of rate constants).

Neptunium					
Parameter	Solution	Site 1	Site 2	Site 3	Site 4
$k_{1,-1}$ A to B; B to A (1/hr) ^a	10; 0.001				
$k_{2,-2}$ B to C; C to B (1/hr) ^b	1.39, 1.34				
k_3 A to S (ml/g-hr) ^c		10^{-3}	10^{-3}	10^{-3}	10^{-3}
k_{-3} S to A (1/hr) ^d		0	0	0	0
k_4 B to S (ml/g-hr)		0.0101, 0.0098	864, 1190	304, 493	66, 38
k_{-4} S to B (1/hr) ^d		0	0	0	0
k_5 S to C (1/hr)		41, 29	0.028, 0.023	0.0042, 0.0043	0.0015, 0.0017
k_{-5} , S to C (1/hr)		2348, 2753	0.029, 0.033	0.0006, 0.001	6.8×10^{-7} , 7.3×10^{-7}
$S_{i_{max}}$ (μmol/g)		225379, 225377	181, 151	553, 604	3174, 3132
Uranium					
$k_{1,-1}$ A to B; B to A (1/hr) ^e	0.15, 0.28, 0.15				
$k_{2,-2}$ B to C; C to B (1/hr) ^f	0.092, 0.055, 0.066				
k_3 A to S (ml/g-hr)		178, 182, 162	4.8, 6.9, 5.2	6.8, 8.1, 7.7	0.0159, 0.0163, 0.0162
k_{-3} S to A (1/hr) ^d		0	0	0	0
k_4 B to S (ml/g-hr)		0.062, 0.076, 0.072	4025, 1228, 1246	0.078, 0.121, 0.106	22, 8, 6
k_{-4} S to B (1/hr) ^d		0	0	0	0
k_5 S to C (1/hr)		3.4, 3.8, 3.3	0.59, 0.44, 0.43	0.10, 0.18, 0.14 ^g	0.0062, 0.0066, 0.0058 ^g
k_{-5} , S to C (1/hr)		18, 20, 19	0.15, 0.05, 0.09	0.025, 0.051, 0.093	1.2×10^{-4} , 2.8×10^{-4} , 6.3×10^{-4}
$S_{i_{max}}$ (μmol/g)		200105, 202675, 200373	89, 109, 82	11459, 113075, 113253	42826, 51324, 37752

^aNot estimated because the A species was considered absent from the Np chemistry (Arnold et al., 2011, Figure 3-10).
^bForward and reverse rates were assumed equal because B and C were assumed in equilibrium.
^cAssigned negligible values because there is no A species present.
^dIrreversible sorption assumed.
^eForward to reverse ratio fixed to 2:1 (only forward rate, k_1 , estimated).
^fForward to reverse ratio fixed to 1:200 (only forward rate, k_2 , estimated).
^gThese parameter were noted by Arnold et al. (2011, Table 3-4) as being non-unique.

Of the identifiable parameters, it is possible to determine what specific data set (Figure 8-2d, e, and f) had the most information content. The GENLINPRED analysis indicates that for parameter $S_{i_{max}}$ the majority of the uncertainty reduction was for the data in Figure 8-2d, fraction sorbed. Similarly, the data for k_1 was due to the information contained in Figure 8-2e, post-mortem activity. The strength of this analysis is that it allows the modeler to request additional experimental data similar to that in Figure 8-2e to better identify k_1 .

The identifiability and relative uncertainty reduction for the U experiments are shown in Figure 8-6. The three bars for each parameter are for the three different parameter estimates; one each for the 7- and 28-ml/hr data in Figure 8-2a and c and another for the data in Figure 8-2b. For most parameters, there is a reasonably strong identifiability associated with one or two of the data sets (typically a bar or two is high). This indicates which data set informs this parameter. However, as noted by Arnold et al. (2011) there seem to be data set competing against one another to specify a parameter value. This can also be seen in the blue and red curves of Figure 8-4a; the blue curve tends to fall above the data and the red curve below. This means that there is not a single value of the parameter that satisfies both data sets simultaneously (e.g., $k_{5,3}$ and $k_{5,4}$ were noted to be distinct by Arnold et al. (2011) and differ in this calibration even with the regularization constraint). According to the way the three sets of parameters were provided to this analysis, the first bar corresponds to the data set for the 7-ml/hr flow rate in Figure 8-2a, breakthrough, and c, post-mortem activity, the second bar to the 28-ml/hr data sets in Figure 8-2a and c, and the third bar is associated with the data in Figure 8-2b, fraction sorbed. Given this information, it is easy to see which parameters are informed by which data sets. When the first two bars are similar in magnitude, both the 7- and 28-ml/hr flow rates inform the parameters (potentially to disparate values).



When a parameter is not identifiable (e.g., k_{34} and $s_{i_{max}}$), it may be efficient to set it to a constant and not attempt to estimate it given the data set. This could reduce the computational burden for the nonlinear uncertainty analysis.

8.6 Nonlinear Uncertainty Analyses

Now that the parameters have been estimated for each experiment, PEST's NSMC technique was employed to investigate the nonlinear uncertainties of each parameter. However, given the computational expense of this exercise, it is preferable to quantify the distribution of each parameter using as few models calls as possible. While NSMC is already exceptionally parsimonious with regard to model calls, it could be further improved through use of Latin Hypercube Sampling (LHS), which replicates a distribution with fewer random samples as compared to the brute force sampling approach. LHS is a technique whereby a probability distribution is divided into equal intervals (along the x -axis) and a random selection is made from within each interval (instead of a random sample based on the underlying probability distribution function). FORTRAN codes are available to perform LHS (Iman and Shortencarier, 1983); the implementation of one such code in PEST is described in the Appendix.

100 LHSs were drawn for each parameter (34 for Np and 66 for U) where the underlying (truncated) distributions were assumed lognormal, the most probable value is the calibrated value listed in **Error! Reference source not found.2**, and the truncated distribution is limited by the parameter ranges listed in Table 8-1. The 100 final models runs using LHS-generated, calibration-constrained NSMC parameters for Np are shown in Figure 8-7. The calibrated parameters listed in Table 8-2 are shown as red curves while the data are blue circles. Clearly, there is some non-random misfit indicating the existence of structural noise (inability of the model to capture all of the processes of what it is intended to simulate); some of the parameter sets should have undergone additional PEST iterations or have been thrown out. Another approach would be to get an estimate of the posterior parameter covariance matrix. Then, a principle component analysis will yield eigencomponents of this distribution. These will be independent variables; hence LHS can be used to sample them.

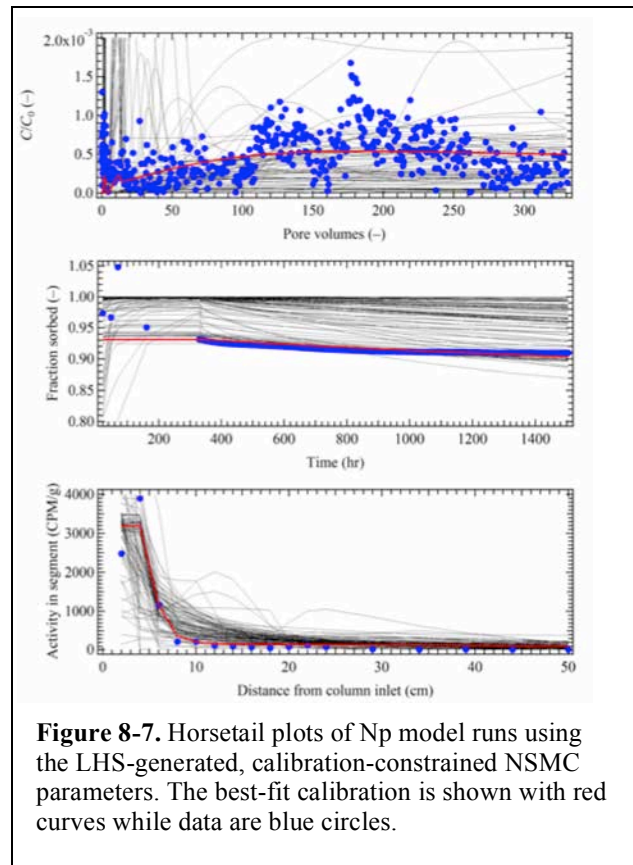


Figure 8-7. Horsetail plots of Np model runs using the LHS-generated, calibration-constrained NSMC parameters. The best-fit calibration is shown with red curves while data are blue circles.

This posterior distribution of LHS eigencomponents would undergo one (or more) iterations of NSMC to pull them back into calibration to yield the final nonlinear uncertainty distributions. This effort may be undertaken in the future.

One of the strengths of this analysis is to determine a calibration-constrained distribution of each parameter to yield its full nonlinear uncertainty distribution. As an example, a histogram of LHSs for the

log transformed k_2 Np parameter is shown in Figure 8-8a. Next, using PEST's PNULPAR routine, the random LHS selections are warped within the null space as described by Doherty (2010, p. 99). Essentially, the differences between the LHS selections and the calibrated parameters (Table 8-2) are calculated. Next, components of these parameter differences that possess a non-zero projection onto the calibration solution space are then removed by computing a set of "projected parameter differences." Then, a new set of "warped" parameter values is then produced by adding the projected parameter differences to the original LHS selections; the result is shown in Figure 8-8b for Np's k_2 . Finally, these warped parameters are provided to PEST and recalibrated for a single iteration (if needed) – see Figure 8-8c. This last step is the classic calibration-constrained NSMC technique (Tonkin and Doherty, 2009), it yields the nonlinear uncertainty for the k_2 parameter. Note how the distribution changes as the analysis progresses. Even tighter results for the bottom plot could have been achieved if PEST was afforded more than a single iteration to bring the model into calibration.

Horsetail plots for the U experiments are shown in Figure 8-9. Clearly, there are some results that do not fit the data well and are not considered calibrated; after all, only a single PEST iteration was used to bring the results back toward calibration. These horsetail plots could be improved by additional NSMC PEST iterations or by discarding parameter sets that could not easily be drawn back into calibration.

Parameter $s_{i_{max}}$, one of the parameters that was difficult to uniquely specify for all data sets simultaneously (see Table 8-2), has distributions as shown in Figure 8-10. The top distribution is LHS generated. The middle distribution was transformed in the solution space by PNULPAR. The bottom distribution was returned from an NSMC iteration of PEST in SVDA mode. Note the final bimodal distribution; this indicates that two distinct values were returned from the

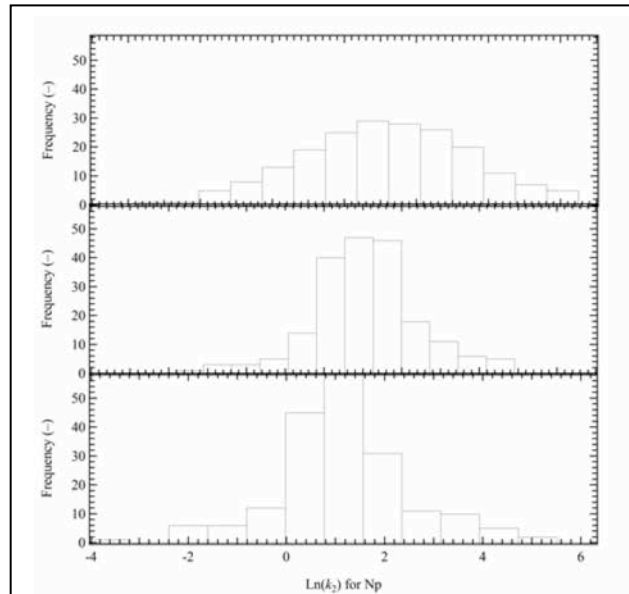


Figure 8-8. Histograms of log-transformed k_2 for Np. Top is the LHS-generated distribution, middle is the distribution after using PNULPAR, and the bottom is the distribution after putting the PNULPAR results through a single iteration of PEST with SVDA.

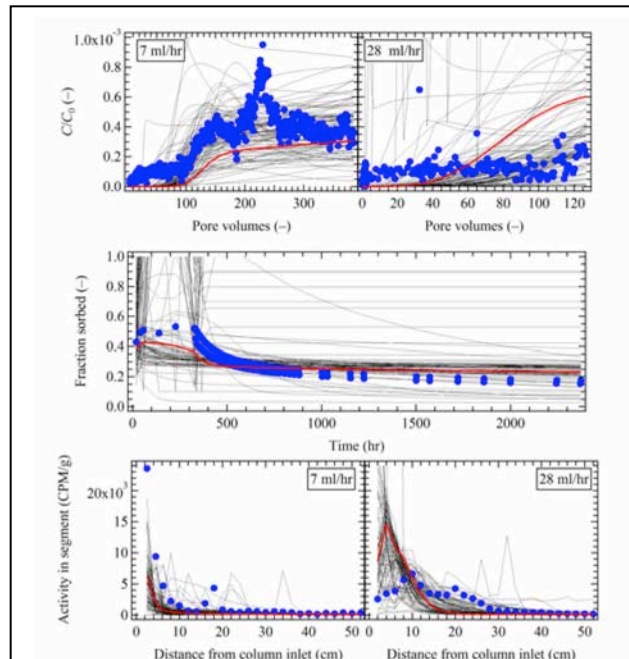


Figure 8-9. Horsetail plots of U model runs using the calibration-constrained LHS-generated NSMC parameters. The best-fit calibration is shown in the red curves while data are blue circles.

calibration process (despite the regularization constraint). Because we are acknowledging parameter non-uniqueness (through both the specification of different parameters for each data set and the NSMC process), it is important to include all parameter values in the nonlinear uncertainty distribution. Certainly if the parameter sets that did not achieve a sufficiently low objective function (after a single PEST iteration) were culled or if more than a single PEST iteration was allowed, then the distributions could have been tightened.

This exercise has demonstrated a new capability in PEST using LHS to generate parameter distributions that are first processed with PNULPAR and then by a single NSMC PEST iteration. Full nonlinear uncertainty distributions of each parameter result. Moreover, in the process of obtaining each nonlinear uncertainty distributions, the linearized uncertainty analysis is also obtained; specifically, the identifiability and uncertainty reduction of each parameter. This information also informs us as to how each data set contributes to the uncertainty reduction of each parameter. This is important information because it allows the modeler to tell the experimentalist just how much information is contained in a data set. This data worth information can help design future experiments and specify if more or less of a certain data type should be collected. In this example, the post-mortem activity data were particularly important, indicating that additional data of this type should be collected.

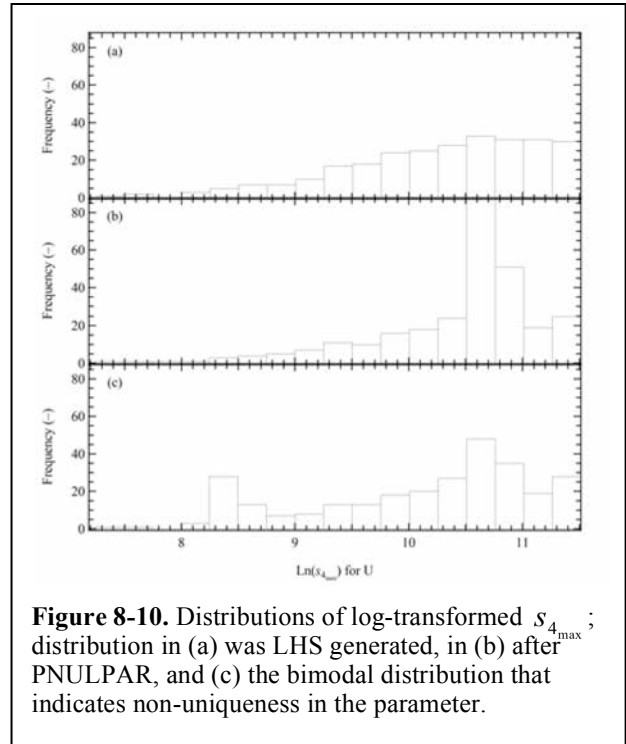


Figure 8-10. Distributions of log-transformed $s_{4_{max}}$; distribution in (a) was LHS generated, in (b) after PNULPAR, and (c) the bimodal distribution that indicates non-uniqueness in the parameter.

Future efforts of parameter uncertainty analysis could include an alternate approach to the one undertaken here where an estimate of the posterior parameter covariance matrix is obtained. Then, a principle component analysis will yield eigenvectors of this distribution. These will be independent variables; hence LHS can be used to sample them. This posterior distribution of LHS eigenvectors would undergo one (or more) iterations of NSMC to pull them back into calibration to yield the final nonlinear uncertainty distributions.

8.7 References

- Arnold, B.W., Reimus, P.W., James, S.C., 2011. Flow and transport in saturated media: FY2011 status report. Department of Energy, Albuquerque, p. 99.
- Davis, J.A., Curtis, G.P., 2003. Application of surface complexation modeling to describe uranium (IV) adsorption and retardation at the Uranium Mill Tailings Site at Naturita, Colorado. United States Geological Survey, Menlo Park, CA.
- Dean, C.A., 2010. Long-term desorption of uranium and neptunium in heterogeneous volcanic tuff materials, Chemical and Nuclear Engineering Department. University of New Mexico, Albuquerque, NM.

- Doherty, J., James, S.C., Reimus, P.W., 2011. Model-based decision making: A new perspective, 13th International High-Level Radioactive Waste Management Conference. American Nuclear Society, Albuquerque, NM, pp. 1-10.
- Doherty, J.E., 2009. Manual for PEST: Model Independent Parameter Estimation, in: Doherty, J.E. (Ed.). Watermark Numerical Computing, Brisbane, Australia, p. 336.
- Doherty, J.E., 2010. Addendum to the PEST Manual, in: Doherty, J.E. (Ed.). Watermark Numerical Computing, Brisbane, Australia, p. 131.
- Doherty, J.E., Hunt, R.J., 2009. Two statistics for evaluating parameter identifiability and error reduction. *Journal of Hydrology* 366, 119-127.
- Iman, R.L., Shortencarier, M.J., 1983. A FORTRAN 77 Program and User's Guide for Generation of Latin Hypercube and Random Samples for Use with Computer Models. Sandia National Laboratories, Albuquerque, NM, p. 57.
- Liu, C., Shi, Z., Zachara, J.M., 2009. Kinetics of Uranium(VI) Desorption from Contaminated Sediments: Effect of Geochemical Conditions and Model Evaluation. *Environ Sci Technol* 43, 6560-6566.
- Liu, C., Zachara, J.M., Qafoku, N.P., Wang, Z., 2008. Scale-dependent desorption of uranium from contaminated subsurface sediments. *Water Resour. Res.* 44, W08413.
- Qafoku, N.P., Zachara, J.M., Liu, C., Gassman, P.L., Qafoku, O.S., Smith, S.C., 2005. Kinetic Desorption and Sorption of U(VI) during Reactive Transport in a Contaminated Hanford Sediment. *Environmental Science & Technology* 39, 3157-3165.
- Tonkin, M.J., Doherty, J.E., 2009. Calibration-constrained Monte Carlo analysis of highly-parameterized models using subspace techniques. *Water Resources Research* 45, W00B10.

Chapter 8 Appendix: PEST NSLHS Utility Codes

PHISTATS

Although it was written to expedite use of the Sandia LHS program with PEST, use of PHISTATS is broader than this. It can be used on its own, or as part of any batch file that undertakes repeated PEST runs. It provides a mechanism for an up-to-date reporting of the status of those runs, and of their ability to lower (or not) the objective function.

PHISTATS is run using the command:

```
phistatsrecfile N
```

where *recfile* is the name of a PEST run record file, and *N* is any integer supplied by the user. If run inside a loop recorded in a batch file, *N* will probably be the index of the loop control variable which, under normal operation, will be incremented after each pass through the loop.

When executed in the above manner, PHISTATS reads the nominated run record file. Note that an extension of “rec” is presumed; if this is omitted it will be added to the user-supplied filename automatically. It then writes the following information to the screen:

- Initial objective function
- Initial contributions to the objective function by all observation groups
- Initial measurement and regularization objective functions (if PEST is run in regularization mode)
- Initial predictive and predictive error terms (if PEST is run in predictive analysis mode).
- All of the above statistics as recorded at completion of PEST execution.

Note that PHISTATS will cease execution with an error message if it is asked to read a run record file that documents the outcomes of a PEST run in which it is run in Pareto mode.

LHS2PEST

General

LHS2PEST provides a linkage between PEST and the LHS program written by Sandia National Laboratories. It facilitates the undertaking of multiple PEST runs, each based on a different set of Latin hypercube parameter value samples generated by LHS.

PEST runs can be undertaken for a number of purposes. If the NOPTMAX control variable is set to 0, then PEST will simply run the model once, calculate the objective function and different components thereof, calculate and record some statistics, and then cease execution. If NOPTMAX is set to -1 or -2 PEST will calculate the Jacobian matrix, this comprising sensitivities of members of the observation dataset to the different parameters. If NOPTMAX is set to a positive number, then PEST will undertake parameter estimation; for each parameter estimation run initial parameter values are Latin hypercube samples of the various parameters.

For NOPTMAX not set to zero, the following should be noted.

- If a model is linear with respect to its parameters, sensitivities recorded in the Jacobian matrix should be independent of parameter values.

- If undertaking parameter estimation, and this process does not employ the SVD assist methodology (do not confuse this with the SVD solution method), consider running PEST with the “/i” switch so that it can re-use the same Jacobian matrix on its first iteration. Presumably this matrix will have been calculated using just a representative set of parameter values. (Note that in the batch file written by LHS2PEST – see below – the command to run PEST is not accompanied by this switch; you must add it to the pertinent command yourself.)

Use of LHS2PEST is predicated on the assumption that a PEST input dataset and corresponding LHS input dataset exist. It is also assumed that the same parameters have the same names in both of these files. (As will be discussed, either of these files can possess other parameters as well.) Adherence to this protocol will require that parameter name lengths be restricted to 12 characters in the LHS input dataset, as this is the character length limit for a parameter name employed by PEST.

It is further assumed that LHS has been run, and that an output file with parameter sample values has thus been recorded. LHS2PEST reads these samples, and builds a set of PEST parameter values files, each recording the values associated with one sample set. These files can be used in similar ways to those written by the RANDPAR utility. In particular, through sequential use of the PARREP utility, these parameter sets can be used as initial values in a sequence of PEST control files. PEST can then use these files to undertake sequential runs for any of the reasons discussed above.

The tasks performed by LHS2PEST depend on the command that is used to run it. These commands, and the tasks that correspond to these commands, are now described.

LHS2PEST – Level 1

The simplest way to run LHS2PEST is using the command:

```
LHS2PEST lhsoutfile parfilebase
```

where *lhsoutfile* is the name of a LHS output file that includes parameter samples and *parfilebase* is the filename base of a set of parameter values files. If run using the above command, LHS2PEST will do the following.

- It reads the names of parameters which are featured in the LHS output file. If any of these names are greater than 12 characters in length, LHS2PEST will report this as an error and then cease execution.
- It reads the Latin hypercube samples associated with these parameters.
- For each Latin hypercube sample set it writes a single PEST parameter value file which contains the values of these samples.

Suppose that *parfilebase* is supplied as “random”. Then the parameter value files written by PEST are named *random1.par*, *random2.par* etc. As many of these files are written as there are sample sets in the LHS output file. Sequence numbers are preserved in writing these files. Hence, in the above example, file *randomN.par* contains values pertaining to the N^{th} Latin hypercube sample generated by LHS.

The following protocols are adopted in writing these parameter value files.

- All parameters are given a SCALE of 1 and an offset of 0.
- The PRECIS and DPOINT control variables are given values of *single* and *point* respectively.

LHS2PEST – Level 2

When run using the command:

```
LHS2PEST lhsoutfile parfile basepestcontrolfile
```

where *pestcontrolfile* is the name of a PEST control file, LHS2PEST reconciles parameters represented within a PEST control file with those represented in the LHS output file. In particular, it informs the user if any parameters cited in the LHS output file are not cited in the PEST control file; it also informs the user if any parameters cited in the PEST control file are not cited in the LHS output file.

When recording parameter value files LHS2PEST adopts the following protocols.

- The only parameters which are recorded in these files are those which are featured in the PEST control file. Hence a parameter that is cited in the LHS output file but is not cited in the PEST control file is not recorded in the parameter value files written by LHS2PEST.
- Where a parameter is cited in the PEST control file, but not featured in the LHS output file, it is provided with the same value in all parameter value files, this being its initial value as recorded in the PEST control file.
- All parameters which feature in both PEST control and LHS output files are given Latin hypercube sample values as recorded in the LHS output file. Note that this occurs regardless of whether they are adjustable, fixed or tied in the PEST control file. provide them with different names in the latter file if you do not want this to happen.
- If a LHS-generated sample for a particular parameter has a value which exceeds the upper bound for that parameter as recorded on the PEST control file, or is lower than that parameter's lower bound, then the user is notified of this. At the same time sampled parameter value is clipped to respect these bounds.
- If a parameter is featured in the PEST control file, but not in the LHS output file, and if that parameter is tied to a parameter whose value is informed by the LHS output file, the value of the tied parameter is adjusted in accordance with the LHS-supplied value for its parent parameter. If, in doing this, its upper or lower bound is transgressed, it is adjusted back to its upper or lower bound and a warning is issued.
- The SCALE and OFFSET value provided to each parameter in LHS-recorded parameter value files is that with which it is provided in the PEST control file.
- Values for PEST control variables PRECIS and DPOINT recorded in the headers to parameter value files are equivalent to those used in the PEST control file read by LHS2PEST.

The parameter value files written by LHS2PEST when run at its level 2 mode of operation are thus perfectly compatible with the PEST control file cited on the LHS2PEST command line.

LHS2PEST – Level 3

To activate LHS2PEST level 3 functionality, it must be run using the following command:

```
LHS2PEST lhsoutfile paramfile basepestcontrolfile batchfile
```

In this case LHS2PEST does everything that level 2 functionality requires. However it also writes a batch file through which PEST can be run repeatedly based on the parameter data file sequence that LHS2PEST also generates. An example batch file is shown below.

```
@echo off
rem #####
rem Delete an existing record file.
rem #####

del /P record.dat
echo > record.dat

rem #####
rem Do all the PEST runs.
rem #####

for /L %%i in (1,1,100) do (
parrep random%%i.par templ.pst t###.pst
del t###.rec
pest t###.pst
copy t###.res t###%%i.res
phistats t###.rec %%i>> record.dat
)
```

A batch file written by LHS2PEST.

The batch file written by LHS2PEST runs PEST repeatedly through a processing loop. This loop is traversed as many times as there are Latin hypercube samples provided in the LHS output file. On each occasion on which PEST is run, the PARREP utility is first run in order to write a new PEST control file which is identical to the PEST control file nominated on the LHS2PEST command line except for the fact that its initial parameter values are those provided by the respective parameter value file, and hence constitute LHS-generated parameter Latin hypercube samples values. This PEST control file is named *t###.pst*. After each PEST run, the PEST residuals file (named *t###.rec*) is copied to file *t###N.rec* where *N* is the run index. Hence a user can inspect the details of model-to-measurement fit calculated on the basis of all Latin hypercube parameter set. If you do not want all of these files saved, comment out or delete the respective line from the batch file. Alternatively, request that other PEST files be saved by adding other commands of a similar type within the processing loop provided in the batch file.

Each PEST run is followed by a PHISTATS run. This gives you the opportunity to inspect a file named *record.dat* (rename this file in the batch file if you wish) at any loop count, and at the end of the loop altogether when all PEST runs have been done. This file informs you of the progression of objective functions that have been calculated on the basis of different Latin hypercube sample sets that have been used up until the time of inspection. At the start of the loop an existing file of this name (i.e. *record.dat*) is deleted. The batch file prompts you for permission to delete this file before it does this so.

When run in level 3 mode, LHS2PEST writes the following message to the screen just before it terminates execution.

```
Note:-
The value for NOPTMAX for all PEST runs initiated through the batch file
will be 0.

If this is not your intention, alter NOPTMAX to an appropriate value in the
PEST control file supplied in the command line.
```

Warning written to screen by LHS2PEST on cessation of level 3 execution.

See the discussion on the NOPTMAX variable at the beginning of LHS2PEST documentation. NOPTMAX is in integer; it is the first variable on the 9th line of the PEST control file.

PEST2LHS

General

PEST2LHS builds an input file for program LHS written by Sandia National Laboratories using information contained within a PEST control file, possibly supplemented by a PEST-compatible parameter uncertainty file. The LHS program can then be run to generate a suite of Latin hypercube samples of parameters featured in the original PEST control file. These samples can then be used by PEST for calculation of objective functions or for more complex tasks such as model calibration based on these initial values. (Creation of a PEST input dataset based on LHS-generated samples can be accomplished using the LHS2PEST program documented above.)

The LHS input file written by PEST2LHS is simple. Of the many options that LHS provides for its input dataset, PEST2LHS supports only a few. The user is advised to alter the PEST2LHS-generated LHS input file him/herself to request options not supported by PEST2LHS if these are required. Because it supports only a few LHS options and employs many defaults, use of PEST2LHS is relatively simple. Adoption of simplicity in its design specifications, accompanied by a recommendation for the user to directly edit the LHS input file written by PEST2LHS him/herself to gain access to more complex LHS functionality, is based on the premise that provision of a complex input dataset to PEST2LHS would be just as difficult (if not more difficult) than supplying a complex input dataset to LHS directly through editing of the latter's input file.

Parameter Probability Distributions

PEST-suite programs which require characterization of parameter uncertainty can receive such characterization through a "parameter uncertainty file". As is documented in the addendum to the PEST manual, this file can provide standard deviations for individual parameters; it can also reference other files which provide covariance matrices for groups of parameters. PEST2LHS, too, can read a parameter uncertainty file (and covariance matrix files cited therein) in order to obtain specifications for the uncertainties of parameters cited within a PEST control file, these being required for specification of probability distributions on the LHS input file which it writes. However its design is such that if it employs variances and covariances read from a parameter uncertainty file, it simultaneously assumes that all adjustable parameters cited in the PEST control file which it reads are described by either a normal distribution (if they are untransformed) or a log-normal distribution (if they are log-transformed).

It will be recalled from PEST documentation that if a parameter is log-transformed then the uncertainty information pertaining to that parameter provided in a parameter uncertainty file must pertain to the log to base 10 of that parameter. As stated above, such information will constitute either the standard deviation of the parameter, or its variance and covariances with other parameters supplied through a covariance matrix file cited in the parameter uncertainty file. To maintain compatibility with other PEST-suite programs, the assumption of base-10 logarithms in the parameter uncertainty file is maintained; PEST2LHS makes the conversion to natural logarithms when writing an LHS input dataset.

If a parameter is cited as untransformed in a PEST control file (i.e. if it has a PARTRANS value of "none" in the "*" parameter data" section of that control file), then the uncertainty information contained in a parameter uncertainty file, or in any covariance matrices cited in that file, must pertain to the native parameter.

As an alternative to obtaining parameter uncertainty information from a parameter uncertainty file, PEST2LHS can calculate parameter uncertainty statistics itself from parameter bounds provided in the

PEST control file. If PEST2LHS is asked to do this, it does not then need to read a parameter uncertainty file at all. Furthermore, if this option for parameter uncertainty characterization is taken, the user can choose between the uniform, triangular and normal probability distributions for expressing that uncertainty. These distributions are assigned on a parameter group by parameter group basis. (Recall that parameter groups are named in the “* parameter groups” section of a PEST control file and that individual parameters are assigned to these groups within the “* parameter data” section of that file.

Regardless of whether parameter uncertainties are supplied through an uncertainty file, or are calculated from parameter bounds, PEST2LHS provides the user with two options for denoting the parameter value at which the probability distribution is at its peak (this coinciding with the mean of a normal probability distribution). The first option is to calculate this parameter value as the midpoint of the interval spanned by a parameter’s lower and upper bounds (or the midpoint of the interval spanned by the natural logs of a parameter’s lower and upper bounds if the parameter is log-transformed in the PEST control file). The second is to use a parameter’s initial value as provided in the PEST control file (or its natural log if the parameter is log transformed) as the parameter value of peak probability. (Note that this is not applicable to the uniform probability distribution as this distribution has no maximum.)

Where PEST2LHS specifies that a parameter is normally or log-normally distributed when recording its probability distribution specifications on an LHS input file, this distribution is actually specified as a bounded distribution. The bounds that are applied to this distribution are the same as those placed on parameter values in the PEST control file. This ensures that Latin hypercube samples do not transgress these bounds. Where a uniform or triangular probability distribution is employed, respect for parameter bounds is built into the probability distribution specifications themselves.

PEST2LHS assigns probability distributions only to adjustable parameters (i.e. to parameters that are neither fixed nor tied to a parent parameter in the PEST control file which it reads). Tied and fixed parameters are therefore not featured in the LHS input file written by PEST2LHS.

PEST2LHS Usage Details

In contrast to many programs of the PEST suite, PEST2LHS does not receive its usage information through command line arguments. This is because it requires more information than can conveniently be provided through a limited number of such arguments. Hence it prompts the user for the information which it needs.

PEST2LHS commences execution with the prompt:

```
Enter name of PEST control file:
```

On having received the name of this file, PEST2LHS checks for its existence, and then reads it. Having done this, it issues the following prompt:

```
There are two options for specifying parameter probability distributions:
```

```
For (log)normal distributions and an uncertainty file - enter 1  
For user-specified distributions with bounds-derived descriptors - enter 2
```

```
Enter your choice:
```

As stated above, PEST2LHS provides the user with two options for specifying parameter uncertainties. The first option is for all of these to be provided through a traditional PEST uncertainty file. The second

is for probability distributions to be provided on a parameter group by parameter group basis. As PEST2LHS behavior is somewhat specific to the selected option, its two different modes of parameter uncertainty specification are now discussed separately.

User-specified distributions

Regardless of which option is selected in response to the above prompt, PEST2LHS's next prompt is:

```
For maximum value of non-uniform distributions:-  
  If halfway between (log) bounds                - enter 1  
  If parameter initial value from PEST control file - enter 2  
Enter your choice:
```

Complete specification of the triangular and normal distributions requires that a parameter value of maximum probability be specified. In the case of the normal distribution, this is also the mean value of the distribution. PEST2LHS can calculate this maximum probability value in either of the two ways specified in the above prompt. In the first case, the peak of the distribution is calculated to correspond to the mean of the parameter's lower and upper bounds as recorded in the PEST control file. In the second case it is associated with a parameter value equal to the initial value for the pertinent parameter as read from the PEST control file. Note that this second option can lead to a non-symmetrical probability distribution.

Where a parameter is log-transformed (which for LHS is decreed as being incompatible with selection of a triangular distribution as the log-triangular distribution option is not supported by LHS) the parameter abscissa calculated by PEST2LHS for the peak value of what LHS refers to as the "underlying distribution" depends on which of the above options is selected. If the second option is selected, then the value of peak probability will be the natural log of the parameter's initial value. If the first option is selected, then the value of highest probability will be the average of the natural logs of a parameter's lower and upper bounds, these being specified in the PEST control file.

PEST2LHS next writes the following text to the screen:

```
Parameter probability distributions must now be provided. This  
must be done on a group-by-group basis.  
Select uniform/triangular/normal distributions as [u/t/n].  
Note that triangular is not allowed if some group members are  
log-transformed.
```

Then, for each parameter group featured in the PEST control file, PEST2LHS asks:

```
Enter distribution for parameter group "param_group" [u/t/n]:  
Enter "u", "t" or "n" as appropriate. PEST2LHS constructs parameter probability distributions in the  
following way.
```

- If a uniform distribution is requested, the distribution extends between the parameter's lower and upper bounds as declared in the PEST control file. If the parameter is log-transformed, PEST2LHS informs LHS that the parameter's distribution is log-uniform. Otherwise it is uniform.

- If a parameter group is endowed with a triangular distribution PEST2LHS first checks whether any member of that group is log-transformed. If any parameter within the group is, in fact, log-transformed, then PEST2LHS informs the user of this and repeats the above prompt. If no group member is log-transformed, then each parameter within the group is endowed with a triangular probability distribution whose bounding zero probability points are the lower and upper parameter bounds (as specified in the PEST control file), and whose peak probability point is either the midpoint of the bounds interval, or the parameter's initial value, as already discussed.
- If the "normal" option is selected in response to the above prompt, then each parameter within the group is awarded either a normal distribution (if it is untransformed) or a log-normal distribution (if the parameter is log-transformed in the PEST control file). If a parameter is untransformed and if in response to a previous prompt the parameter value of maximum probability is selected as the midpoint of the lower-to-upper bounds interval, then the standard deviation of the normal distribution is calculated as a sixth of the distance between the parameter's upper and lower bounds; the bounds are thus decreed to span a probability range of 99.7%. However these are made to span 100% of its probability range by declaring to LHS that the normal distribution is bounded, with the bounds supplied to LHS coinciding with parameter bounds provided in the PEST control file.
- If the normal option is selected and a parameter is log transformed, the abscissa corresponding to the maximum value of the "underlying normal distribution" required by LHS is calculated as the midpoint of the distance between the natural logs of the parameter's bounds (i.e. the average of its natural logged lower and upper bounds), or is calculated as the natural log of the parameter's initial value; see above. If, in response to the pertinent previous prompt, the parameter value of maximum probability is selected as the midpoint of the lower-to-upper parameter bounds interval, then the standard deviation of the "underlying normal distribution" is calculated as a sixth of the difference between the natural logs of the parameter's lower and upper bounds. A log-normal distribution is then specified to LHS, with bounds coinciding with the parameter's natural lower and upper parameter bounds.
- If, in either of the transformed or untransformed normal distribution cases, the parameter value of maximum likelihood is specified as the parameter's initial value (or its log), the standard deviation ascribed to the (log)normal distribution associated with that parameter is equated to a third of the distance between the (log of) the parameter's initial value and (the log of) its lower or upper bound, whichever is further away. The bounded (log)normal distribution whose specifications are supplied to LHS may thus be asymmetric.

Uncertainty File

We begin this subsection by repeating a previous PEST2LHS prompt:

```
There are two options for specifying parameter probability
distributions:
For (log)normal distributions and an uncertainty file - enter 1
For user-specified distributions with bounds-derived
descriptors - enter 2
Enter your choice:
```

As stated above, the PEST2LHS internal algorithm is such that use of a parameter uncertainty file implies selection of a (log)normal distribution for all parameters. The choice between a normal and a log-normal

distribution is made on the basis of the transformation state of each parameter as specified in the PEST control file. On all occasions the (log)normal distribution is bounded, the bounds being those supplied as upper and lower parameter bounds in the PEST control file.

Following the above prompt, PEST2LHS's next prompt is (regardless of which of the above options is selected):

```
For maximum value of non-uniform distributions:-  
  If halfway between (log) bounds                - enter 1  
  If parameter initial value from PEST control file - enter 2  
Enter your choice:
```

The mean of the (log)normal distribution as it applies to each parameter is calculated on the basis of the response to this prompt. If the first of the above options is selected, and if a parameter is untransformed, PEST2LHS calculates the mean of the parameter's distribution as the mean of its upper and lower parameter bounds. If a parameter is log-transformed, the mean of the LHS "underlying normal distribution" (i.e. the distribution pertaining to the natural log of the parameter) is calculated as the mean of the natural logs of the parameter's lower and upper bounds.

If the second of the above options is chosen, the mean assigned to the parameter's normal distribution is the parameter's initial value if the parameter is untransformed. Alternatively, if the parameter is log-transformed, the mean of the "underlying normal distribution" is calculated as the natural log of the parameter's initial value as specified in the PEST control file.

PEST2LHS next asks:

```
Enter name of parameter uncertainty file:
```

The format of this file is described in the addendum to the PEST manual. As therein described, each parameter can be assigned a standard deviation; alternatively, groups of parameters can be assigned a covariance matrix. Where a parameter is untransformed, these apply to native parameters. Where a parameter is log-transformed they apply to the logged (to base 10) parameters.

Where a parameter uncertainty file is provided, PEST2LHS uses standard deviations from that file to assign standard deviations to parameter probability distributions that it provides to LHS. Where a parameter is untransformed, its standard deviation is directly transferred to the LHS input file. Where a parameter is log-transformed, PEST2LHS transfers the standard deviation from the uncertainty file to the LHS input file as the standard deviation of that parameter's "underlying normal probability distribution". However in doing so, account is taken of the fact that the parameter uncertainty file assumes log transformation to base 10 of parameters whereas LHS uses natural logs. Note also that when a parameter features in a covariance matrix cited in the parameter value file, its (log)standard deviation is calculated as the square root of its variance as cited in that file.

Where a covariance matrix is provided for groups of parameters, PEST2LHS evaluates correlations between individual parameter pairs so that these can be recorded on the LHS input file; these correlations can thereby be taken into account in generating Latin hypercube sample sets. Where parameters are log transformed, PEST2LHS calculates correlations pertaining to native parameters from the information provided in a pertinent covariance matrix, notwithstanding the fact that this information pertains to logged (to base 10) parameters. This satisfies LHS input requirements with respect to the CORR keyword.

Correlations supplied to LHS are calculated from native variances/covariances using the usual formula for calculation of correlation coefficients. That is:

$$\rho_{ij} = \frac{\sigma_{ij}}{\sqrt{\sigma_i^2 \sigma_j^2}}.$$

Where necessary, variances and covariances of untransformed parameters are calculated from those of their log-transformed counterparts using the formula:

$$\sigma_{ij} = e^{[(v_i + v_j) + (\delta_i + \delta_j)/2]} (e^{\delta_{ij}} - 1),$$

where v_i and v_j are means of the normal distribution pertaining to the logs of parameters i and j , and δ_i , δ_j , and δ_{ij} are the elements of the log parameter covariance matrix elements pertaining to these parameters. Means are calculated in the manner described above (i.e. as logged parameter range midpoints, or as logs of initial parameter values, according to the user's selection).

In the unlikely event that a covariance matrix is supplied for a group of parameters of which some are log-transformed and some are not, PEST2LHS simply uses covariances from the composite group covariance matrix in order to compute correlation coefficients for parameter pairs. These correlation coefficients are then written directly to the LHS input file.

LHS Input Files

Regardless of the methodology selected for specification of parameter probabilities, PEST2LHS's final prompts are:

```
Enter filename base for LHS files:  
How many parameter sample sets must be generated?  
Enter random number seed (a big integer):
```

Suppose that the user responds to the first of the above responses with the name "file". PEST2LHS will then write an LHS input file named file.dat. In that file it will specify that the LHS sample data output file (this being associated with the LHS keyword LHSOUT) be named file.lsp and that the LHS-generated message file (this being associated with the LHS keyword LHSMSG) be named file.msg.

The other two prompts are self-explanatory.

Chapter 9: Summary and Conclusions

The results and information presented in this document represent significant steps forward in our understanding and descriptive capabilities of the complex chemical and physical processes that occur in naturally heterogeneous systems. These processes transcend scale and space dimensions, and require analysis at a variety of scales using a variety of methods. Stepping forward at a fundamental level requires small scale batch experimentation. Both the plutonium and iodine work presented here demonstrate this circumstance, and both address known inconsistencies and uncertainties relating to plutonium and iodine migration from a geologic repository. These inconsistencies include the current inability to capture colloidal migration in performance assessment modeling, developing chemical relationships as a function of temperature, and the scattered data and interpretation of anion migration in clay systems. The work presented here shows specific evidence of plutonium colloidal interactions with goethite and clays and further constrains potential mechanisms of colloidal migration. Furthermore, using a breadth of clay minerals instead of a single clay mineral has allowed for the observation of an emergent property of clay minerals related only to cation exchange capacity. The presence of ion-pairs in the interlayer space of clay minerals may have significant impacts on ion migration through fine-grained, nanoporous minerals (e.g., clays) and the methods used to describe such migration.

At a much larger scale, column and field tests increase the system complexity and processes involved requiring a different set of analysis tools. A novel procedure is under-development to determine rate-limited sorption and desorption parameters under conditions relevant to uranium transport in granite systems. To date the method results remain untested as the conditions used showed no uranium sorption. These methods will continue to be developed using neptunium. Work at the field scale in Grimsel, Switzerland has allowed for the determination that colloid filtration parameters are not related to system retention time.

At the highest level resides the ability to synthesize the small scale and large scale information into a coherent conceptualization of the waste disposal environment. The work presented here approaches this from two directions, the first being a coupled THMC model description of uranium migration in a clay repository, the second being a mathematical evaluation of model derived parameters estimated from experimental data. The THMC modeling is significant as a fully coupled description of the complex interactions between the thermal-hydrological-mechanical-chemical processes is necessary for repository performance assessment. The model presented here is a critical first step in connecting mechanistic chemistry to the physical processes affecting transport. However, in system level models a wide range of assumed and measured parameters are needed and used. A method for constraining and quantifying the uncertainty of these variables is necessary to stream-line model descriptions using massively parallel simulations. A parameter estimation method was presented here. The added ability of this method is to inform the collection of data to limit parameter uncertainty.